

PROPELLANT SURFACE TEMPERATURE AND PLUME CHARACTERISTICS OF
MICRO-PULSED PLASMA THRUSTERS

BY

ERIK LAWRENCE ANTONSEN

B.S. University of Illinois at Urbana-Champaign, 1997

M.S. University of Illinois at Urbana-Champaign, 2001

DISSERTATION

Submitted in partial fulfillment of the requirements
for the degree of Doctor of Philosophy in Aerospace Engineering
in the Graduate College of the
University of Illinois at Urbana-Champaign, 2004

Urbana, Illinois

UMI Number: 3130872

INFORMATION TO USERS

The quality of this reproduction is dependent upon the quality of the copy submitted. Broken or indistinct print, colored or poor quality illustrations and photographs, print bleed-through, substandard margins, and improper alignment can adversely affect reproduction.

In the unlikely event that the author did not send a complete manuscript and there are missing pages, these will be noted. Also, if unauthorized copyright material had to be removed, a note will indicate the deletion.

UMI[®]

UMI Microform 3130872

Copyright 2004 by ProQuest Information and Learning Company.

All rights reserved. This microform edition is protected against unauthorized copying under Title 17, United States Code.

ProQuest Information and Learning Company
300 North Zeeb Road
P.O. Box 1346
Ann Arbor, MI 48106-1346

© 2004 by Erik Lawrence Antonsen. All Rights reserved.

CERTIFICATE OF COMMITTEE APPROVAL

*University of Illinois at Urbana-Champaign
Graduate College*

April 15, 2004

We hereby recommend that the thesis by:

ERIK LAWRENCE ANTONSEN

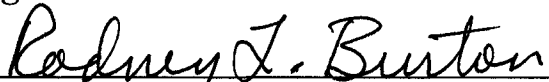
Entitled:

**PROPELLANT SURFACE TEMPERATURE AND PLUME
CHARACTERISTICS OF MICRO-PULSED PLASMA THRUSTERS**

Be accepted in partial fulfillment of the requirements for the degree of:

Doctor of Philosophy

Signatures:




Director of Research



Head of Department

Committee on Final Examination*



Chairperson



Committee Member



Committee Member



Committee Member

Committee Member

Committee Member

* Required for doctoral degree but not for master's degree

Abstract

The micro-Pulsed Plasma Thruster (microPPT) is a device capable of supplying discrete impulses for propulsive maneuvering of small satellites. These devices suffer from low propellant utilization related to late-time propellant ablation, causing a drop in specific impulse and thruster efficiency. The exhaust of these thrusters can also contaminate critical spacecraft surfaces. Current theories by Keidar and Boyd indicate that the defining parameter for propellant ablation is the surface temperature of the solid Teflon™ propellant. All downstream plasma and neutral properties are dependent on this parameter. In this work, the microPPT is investigated to experimentally characterize both the ablation physics and plume characteristics. Infrared photovoltaic detectors using a p-n junction are used to measure the surface temperature of the Teflon propellant in real time. The detector material is Mercury Cadmium Telluride (HgCdTe), chosen because the maximum detector response occurs in wavelengths where a Carbon-Fluorine stretching mode in the solid propellant emits strongly in the infrared. This paper outlines the design, calibration and construction of the infrared thermographic diagnostic. A theoretical treatment of the expected detector output is proposed and validated allowing an estimate of the wavelength dependent emissivity of Teflon in the IR. This diagnostic is applied to an operating microPPT and real-time surface temperature measurements are made after the current pulse ends. This allows analysis of the expected vapor pressure and therefore performance parameters such as thrust, mass loss, and exhaust velocity associated with late-time vaporization. The microPPT plume is characterized using two-color interferometry to simultaneously measure electron and neutral densities during the discharge. As the microPPT operates, the solid propellant recesses into the outer electrode tube, possibly changing thruster performance. Recession shape and depths are measured and electron density measurements as a function of recession depth are made. These data are compared with numerical modeling predictions from the Keidar-Boyd model, which has developed in a parallel effort to create a theoretical tool for predicting spacecraft contamination issues. Predictions from this model compare favorably with the reported data.

This work is dedicated to my friend Michael Dulligan,
And to my brother, Luke Antonsen.

Acknowledgements

There are a huge number of people who contributed to this work. Through time in the laboratory at my side, on the phone or e-mail discussing problems, or simply acting as a support mechanism for me over the many years, countless people have contributed to the compilation that is this research.

The first people who must be thanked are my advisors. Dr. Rod Burton has put up with me as a student at the University of Illinois for almost a decade now. I first met him in my junior year of undergrad education and our working relationship has continued to the present day. His expertise as an engineer and mentor allowed me to develop as an engineer beyond what I thought my capabilities were.

Dr. Greg Spanjers has been dealing with me almost as long. Since our first meeting at Edwards AFB in the spring of 1997, Greg has been a driving force in my education. He has provided encouragement and guidance when I felt lost and useless. His scientific understanding is astonishing, and I consider myself lucky to have been able to work with him so often.

When Dr. Spanjers moved on from Edwards AFB, he asked Dr. Michael Dulligan to keep an eye on me. Mike was a good personal friend and a scientist and mentor of extraordinary ability. Mike was killed along with his instructor in a plane crash in early February 2003 while taking lessons for a twin-engine license. The hole left in my life by his passing will never be filled.

I owe a huge debt of gratitude to Dr. Michael Keidar from the University of Michigan. It is through cooperative work with him that this dissertation was possible. Dr. Keidar and I have had the good fortune of being able to draw from each others results as our respective work continued. His theories influenced the experiments that I conducted, and my results impacted his assumptions and analysis. In short, working with Michael has been great fun and I can only hope that the rest of my career sees that kind of cooperation.

This research was made possible by a great deal of support from the Air Force Research Laboratory at Edwards AFB. While there I worked as an on-site contractor for both Spiral Technologies and ERC Inc. The level of personal support I received while

working at the Electric Propulsion Laboratory at AFRL was amazing. I owe a great debt of gratitude to Dr. Ron Spores. He has been there for me throughout this ordeal. Daron Bromaghim also continuously supported me both financially and through his friendship. I also owe thanks to W.E. Research for access to their tool supplies and technicians.

While at the Electric Propulsion Laboratory, there were a number of people that spent time working with me on experiments. The most notable of these is a young man named Garrett Reed. Garrett kept me sane. When I needed help with my experiments, he was always available and smiling. He is a LabView guru and his programming expertise were crucial to the construction of my diagnostics. He is an extremely hard worker and good friend.

Dr. John Lambros at the University of Illinois gave me my first opportunity to work with photovoltaic detectors and become familiar with these high-speed systems. Dr. Keefer at the University of Tennessee Space Institute had lengthy discussions concerning plasma optical thickness and kept me from biting off more than I could chew. Dr. Iain Boyd from the University of Michigan is an associate of Dr. Keidar's and has been involved in the theoretical treatment of PPTs for a number of years. His assistance was appreciated. Thanks also to Dr. David Ruzic of the Nuclear Engineering department for serving on my dissertation committee.

Paul Adkison and Lt. Greg Cavallero contributed as machinists fabricating a good deal of the support equipment required for these experiments. They also made an obscenely large number of revisions of the calibration apparatus. Their patience is truly appreciated. John Schilling is the resident genius at the EP lab, and I often walked into his office to throw questions at him. His contributions were invaluable and often enabled me to solve problems that I was unsure I'd be able to tackle.

There were a number of summer students who contributed to this research through experimental work in interferometry, IR thermography, and thruster construction and operation. These included Mike Reilly (Chopper), San Gunawardana, and Asher Yap from the University of Illinois, Dave Bennet (Intern Dave or Big Dave) from the University of Michigan, and Benjamin Schmidel (Benji) from Harvey Mudd. Their time and effort was invaluable. Also, Brian Blaine, Diana Connely, Brian Richter, and

Courtney Burgess gave their time and talents to this effort. Many thanks to all of you for all your help.

I also had the good fortune to supervise two cadets from the US Air Force Academy. Josh Arki and David Austin worked hard during their stay at the Electric Propulsion Laboratory. I enjoyed working with them both a great deal. Those two guys will be running the Air Force one day.

Every doctoral student needs a good cop/bad cop duo to keep them on their toes. I don't think a day of work passed where John Asher didn't yell at me to clean up my area or get my act together. He referred to me as "Demo" because he said I was always wrecking something. Luckily that didn't keep him from helping me wire up all the high voltage equipment that I needed. The good cop portion of the team was Bob Gregory. Even when I covered up his nice yellow paint job (with Illinois orange and blue) Bob went real easy on me. He even trusted me to do my own welding occasionally. Many thanks guys.

Tom Glover did instrumentation and helped me with the vacuum chambers I was using. Bruce Chamberlain spent his time coming up with innovative solutions to the problems I encountered. Dave White has the coolest digital camera I've ever gotten to use. It costs more than I do. Dave also freely let me use his tools and technicians, he's the owner of W.E. Research. Dr. Bill Hargus provided a swift kick in the butt when he felt I needed some encouragement. Lt. Christopher Charles contributed time and occasionally beer to make sure I was on track with my work. All of this was greatly appreciated.

The staff of the Aerospace Engineering department were extremely helpful. Lori Ballinger kept tabs on my funding. Angie Pitard helped with reimbursements. Sandee Moore helped with my appointments. Diane Jeffers provided encouragement and moral support. Kendra provided me with the department parking spot when I traveled from Chicago. Many thanks to you.

Now to people who were involved in the work, but also in the social life required to support this kind of commitment. A number of the guys at the EP lab at Edwards are good friends of mine. Our friendships have developed over the seven years I've been working there on and off and I can't imagine my life without their impact. Dave

(Floppy) Kirtley from the University of Michigan is one of the coolest people I have had the good fortune to meet. If I had a tenth of his motivation and drive I would've graduated years ago. My advice to Floppy – the next time someone paints your capacitor rack orange and blue, don't fight it...you're just wasting your time. Stu Bushman (Disco Stu) was actually a teaching assistant for one of my classes at Illinois. He now works at the EP lab and his opinions on life and politics are invaluable, if invariably wrong. Dr. Jimmy Haas has won the admiration of everyone he meets. In fact, all of my friends want to know if Dr. Jimmy is coming out to play for big nights on the town. His bald majesty has the pick of the hotties at Hennessey's Tavern in Hermosa Beach. Finally there is Robar (Scott Engelman). No words can express the connection we have after you backed off the front lawn into my car. We are like brothers, and I always wish the best for you.

My last work thanks go to my grad school friends at Illinois who have helped me work through tough problems and learn new tricks. Jason (Skippy) Merrett helped me learn Matlab and TecPlot. Jason Kamphaus also helped with Matlab as well as other random computer issues that inevitably came up. Ryan Oltman kept me supplied with the latest officially licensed software programs. I am in your debt. Bill Mason, Jennifer Hargens, Chet Hammill, Kishwar Hussein, Bill Hartman and Spaz (Steve Neurauter) spent many lunchtimes listening to me complain. I'm sorry about that. However, I do appreciate all the time we spent playing Halo. Marty Neumann was quite possibly my greatest inspiration. He's a big winner...always doubling down. Finally, for my friend, lab partner, and confidante Fil Rysanek, you are one of the greatest people I've ever met. You also have a really large head. Don't forget to always check the sleeves of your coat...you never know when they'll be filled with shaving cream.

Last are the people who have put up with all my schooling in their personal lives. My parents have put in more time listening and advising than almost anyone else mentioned here. Thank you for believing in me. My brother and sister also helped keep me sane. I'm always thinking of you. I must of course thank Uncle Don for being the only one I trust. And finally, Leslie...who put up with my being gone for almost two years to complete this work. I love you.

Table of Contents

List of Symbols	xii
List of Figures	xvi
Preface	xxi
1. Introduction	1
1.1 Electric Propulsion and Pulsed Plasma Thrusters.....	1
1.2 Motivation for Studies	3
1.3 Summary of Present Experiments.....	7
1.4 Summary of Critical Findings.....	8
1.5 Contents of Dissertation.....	11
1.6 Chapter 1 Figures.....	13
2. Apparatus and Approach	17
2.1 Facilities Description	17
2.2 The Micro-Pulsed Plasma Thruster	18
2.3 Infrared Thermography.....	19
2.3.1 Mercury Cadmium Telluride Detectors.....	20
2.3.2 Optics.....	21
2.3.3 Calibration Apparatus and Method.....	22
2.3.3.1 <i>Calibration Apparatus</i>	22
2.3.3.2 <i>Targeting</i>	24
2.3.3.3 <i>Testing Procedure and Data Acquisition</i>	25
2.3.3.4 <i>Experimental Resolutions</i>	25
2.3.4 Thruster Apparatus and Method	26
2.3.4.1 <i>Thruster Setup</i>	26
2.3.4.2 <i>Plume Measurements</i>	26
2.3.4.3 <i>Thruster Measurements</i>	27
2.3.4.4 <i>Data Acquisition and Reduction</i>	28
2.4 Interferometry	28
2.4.1 Setup	28
2.4.2 Data Acquisition	32
2.5 Other Diagnostics and Sensors	33
2.5.1 Standard Thruster Diagnostics.....	33
2.5.2 DICAM II.....	33
2.5.3 Recession Cone Profiling.....	33
2.6 Chapter 2 Figures.....	34
3. Theory	48
3.1 Infrared Thermography.....	48
3.1.1 Material Emission and Theory.....	48
3.1.2 Teflon Properties.....	51
3.1.2.1 <i>Melt and Viscosity</i>	51
3.1.2.2 <i>Thermal Conduction</i>	52
3.1.2.3 <i>Radiative Properties</i>	53
3.1.2.4 <i>Plasma and Neutral Vapor</i>	54
3.2 Late-time Ablation.....	55
3.3 Keidar-Boyd Plasma Model of the microPPT	56
3.3.1 Plume Description.....	57

3.3.2	Surface Temperature	57
3.3.3	Ablation and Coning	60
3.3.4	Recession Operation	60
3.4	Chapter 3 Figures	62
4.	Experimental Results	72
4.1	Thruster Current and Mass Loss	72
4.2	Infrared Thermography	73
4.2.1	Calibrations	73
4.2.1.1	<i>Voltage vs. Temperature Curve</i>	73
4.2.1.2	<i>Geometrical Uncertainty</i>	75
4.2.1.3	<i>Calibration Uncertainty</i>	76
4.2.2	Teflon Emissivity and Surface Radiation	78
4.2.3	Propellant Surface Temperature	81
4.2.3.1	<i>Noise Sources</i>	81
4.2.3.2	<i>Plume Contribution</i>	81
4.2.3.3	<i>Arc Location</i>	82
4.2.3.4	<i>Surface Temperature Measurements</i>	82
4.2.3.5	<i>Vapor Pressure and Post Pulse Performance</i>	84
4.3	Measured Plasma Properties	89
4.3.1	Electron and Neutral Densities	89
4.3.2	Electron Densities with Propellant Recession	91
4.4	Propellant Recession Profile	91
4.5	Model Results and Comparison	92
4.5.1	Keidar-Boyd Model	92
4.5.1.1	<i>Thruster Plume</i>	92
4.5.1.2	<i>Propellant Ablation and Coning</i>	92
4.5.1.3	<i>Surface Temperature</i>	93
4.6	Chapter 4 Figures	95
5.	Discussion	122
5.1	Infrared Thermography as a PPT Diagnostic	122
5.1.1	Utility and Limitations of IR Theory	122
5.1.2	Issues with Data Collected	123
5.1.2.1	<i>Charring and Surface Topology</i>	123
5.1.2.2	<i>Arc Spoking Issues</i>	124
5.1.3	Diagnostic Limitations	126
5.1.3.1	<i>Calibration</i>	126
5.1.3.2	<i>Thruster Application</i>	128
5.1.4	Surface Temperature During the Pulse	129
5.2	Implications of Experiment and Theory	133
5.2.1	Plume Characteristics	133
5.2.1.1	<i>Flush Propellant Operation</i>	133
5.2.1.2	<i>Recessed Propellant Operation</i>	134
5.2.2	Surface Temperature and Ablation	135
5.3	Chapter 5 Figures	138
6.	Conclusions	142
	References	145

Appendix A	151
Vita	157

List of Symbols

a	speed of sound
a_4	speed of sound where mach number is unity
ACS	attitude control system
AMU	Atomic Mass Unit
Ar^+	Argon ion
B	magnetic field vector
c	speed of light
C	Carbon
C_1	first Planck function constant ($3.742 \times 10^8 \text{ W}\cdot\mu\text{m}^4/\text{m}^2$)
C_2	second Planck function constant ($1.439 \times 10^4 \mu\text{m}\cdot\text{K}$)
C_2F_4	Tetrafluoroethylene
CCD	charge coupled device
CF_2	Carbon Difluoride
CO_2	Carbon Dioxide
c_p	specific heat at constant pressure
D^*	detectivity
DC	direct current
DSMC	Direct Simulation Monte-Carlo
E	energy
EMI	electro-magnetic interference
EO-1	Earth Observer 1
EP	electric propulsion
f	focal length
F	Fluorine
F	molecular flux
G	pre-amplifier gain
Ge	Germanium
HeNe	Helium Neon
HgCdTe	Mercury Cadmium Telluride
i	image distance
I	current
I_E	detector current
I_{in}	amplifier current input
InSb	Indium Antimonide
IR	infrared
I_{sp}	specific impulse
j	current vector
k	thermal conductivity
k	Boltzmann constant ($1.38 \times 10^{-23} \text{ J/K}$)
k_o	optics correction
l	characteristic length of laser exposure to gas
l_p	plasma scale length
l_γ	characteristic length of photon motion prior to reabsorption

L	inductance
L'	inductance gradient
LES	Lincoln Experimental Satellite
LN2	liquid nitrogen
LTE	local thermodynamic equilibrium
LWIR	long-wave infrared
m	magnification
m	molecular weight
M	atomic mass
M	Mach number
MHI	Micropyretics Heaters International
MPD	MagnetoPlasmaDynamic Thruster
N	number laser passes through plasma
n_e	electron density
n_i	ion density
n_n	neutral density
N-S	north-south
o	object distance
p_{eq}	equilibrium vapor pressure
p_c	Teflon characteristic pressure ($1.84 \times 10^{15} \text{N/m}^2$)
p-n	p-type semiconductor and n-type semiconductor junction
P	power
P_i	instantaneous power
PC	polycarbonate
P_E	spectral emissive power
PIC	Particle-in-Cell
PMMA	polymethacrylate
PPT	Pulsed Plasma Thruster
PTFE	PolyTetraFluoroEthylene
q_o	heat
R	resistance
R	Teflon specific gas constant (166.28 J/kg-K)
r_i	central electrode radius
r_o	outer electrode radius
R_p	peak responsivity
SRS	Synchronous Meteorological Satellite
t	time
T	gas temperature
T_c	Teflon characteristic temperature ($20,815 \text{ K}$)
T_e	electron temperature
T_i	initial temperature
T_s	surface temperature
V	voltage
V_o	capacitor voltage
V_{out}	amplifier voltage output
V_{rms}	root-mean-squared molecular velocity

\bar{u}	average exhaust velocity
x	distance
ZnSe	Zinc Selenide
α	ionization fraction
α	thermal diffusivity
α	absorptivity
$\delta\alpha$	ionization fraction uncertainty
δn_e	electron density standard deviation
δn_n	neutral density standard deviation
Δl	change in path length
$\Delta\phi_b$	infrared laser phase shift
$\Delta\phi_r$	blue laser phase shift
Δn_{tot}	total density uncertainty
Δn_{vibs}	uncertainty due to vibrational contributions
Δn_{PPT}	uncertainty due to thruster operating envelope
Δt	small change in time
ϵ	emissivity
ϵ_λ	wavelength dependent emissivity
θ	view cone half angle
θ	electron temperature gradient
λ	wavelength in a vacuum
λ_{mfp}	mean free path
λ_p	threshold wavelength
μ_0	permeability of free space ($4\pi \times 10^{-7} \text{ N/A}^2$)
ϕ	phase shift
ϕ_b	blue laser detector output
ϕ_r	infrared laser detector output
ϕ_e	electron induced phase shift
ϕ_n	neutral vapor induced phase shift
ϕ_{PL}	phase shift induced by physical path length changes
Φ	heat flux
σ	Stephan-Boltzmann constant ($5.67 \times 10^{-8} \text{ W/m}^2\text{K}^4$)
σ	molecular cross-section
ρ	density
ρ_4	local density where mach number is unity
ρ	reflectivity
τ	optical thickness
τ	transmissivity
ω_x	uncertainty in variable x
$\omega_{\Delta x}$	uncertainty in the physical measurement of variable x
ω_{ne}	electron density uncertainty
ω_{nn}	neutral density uncertainty
$\omega_{\Delta\phi_r}$	measurement uncertainty of blue laser phase shift

$\omega_{\Delta\phi b}$	measurement uncertainty of IR laser phase shift
ω_{TC}	thermocouple uncertainty
$\omega_{T\gamma}$	geometric uncertainty
ω_V	voltage uncertainty
ω_T	temperature uncertainty
Ω_c	solid angular area of a small circle
$\int T dt_{EM}$	electromagnetic impulse bit

List of Figures

Figure 1.1: Rectangular, breech-fed PPT from Vondra and Thomassen. ¹⁰	13
Figure 1.2: Comparison of predicted and measured electron density for a 6.35 mm Micro-PPT fired at 6.6 J from Keidar and Antonsen. ^{17,32}	13
Figure 1.3: Photograph of charred micro-PPT with corresponding model prediction of ablation rate through the pulse. The area of lowest ablation rate matches well with the radial char location from Keidar et al. ³²	14
Figure 1.4: Comparison of predicted and measured neutral density for a 6.35 mm Micro-PPT fired at 6.6 J.....	14
Figure 1.5: Data shows significant neutral density for PPT-4 after the pulse using Herriott Cell interferometry from Antonsen. ¹⁹	15
Figure 1.6: Plasma and Late Time Vaporization divergence in a ¼”-diameter, 2–electrode MicroPPT firing at 5 J. 0 mm and 17.5 mm on the left side of the photo refer to the recession depth of the propellant within the tube. The curved rod visible in the plasma pictures is a spark plug used to ignite the main discharge from Spanjers et al. ²⁶	15
Figure 1.7: Herriott Cell measurements for neutral density after the pulse of a microPPT did not have sufficient resolution to distinguish neutral density from Antonsen. ¹⁹ ..	16
Figure 1.8: Vapor pressure of Teflon with surface temperature from Wentink. ^{46,2}	16
Figure 2.1: Three-electrode Micro-PPT layout.....	34
Figure 2.2: Typical micro-PPT circuit with thrust direction shown.	34
Figure 2.3: An unfired MicroPPT face. Outer diameter = 6.35 mm.....	35
Figure 2.4: A two-electrode MicroPPT that has been fired at 7.5 J, 1 Hz for 1 hour.	35
Figure 2.5: Schematic of an HgCdTe detector. ⁵³	36
Figure 2.6: Typical circuitry for HgCdTe detectors. ⁴⁹	36
Figure 2.7: HgCdTe detector responsivity. ⁴⁹	37
Figure 2.8: Wavelength dependent detector responsivity.....	37
Figure 2.9: Responsivity curves for possible InSb detectors. ⁵³	38
Figure 2.10: IR detector experimental layout.	38
Figure 2.11: Optical depth and measurement areas shown for facial measurement and plume measurement.	39
Figure 2.12: Pancake calibration provides Teflon heating with no rear heat source.	39
Figure 2.13: 1/8 th inch thick Teflon is sandwiched between copper plates in the calibration jig. Thermocouples are embedded in the sides to approximately the optical viewing location.	40
Figure 2.14: Thermocouples are embedded in the Teflon close to the area where optical viewing occurs.	40
Figure 2.15: The calibration jig sits on the hotplate and is viewed horizontally through a ZnSe window. The dotted red line shows the optic path.	41
Figure 2.16: Breadboard thruster for creating plasma exposed calibration samples.	41
Figure 2.17: Plasma exposed samples for 500 and 1500 firings.....	42
Figure 2.18: Targeting crosshairs assembled on thruster face.	42
Figure 2.19: Four HgCdTe detectors from the assembly used are shown to scale on the face of a micro-PPT illustrating available spatial resolution with this instrument. ..	43

Figure 2.20: The sparkplug sits more than an inch from the exit plane of the thruster and is off-axis to allow unhindered optical probing of the fuel face.	44
Figure 2.21: Schematic of the (a.) viewable cone for the Plume measurement technique and (b.) target location for the Surface measurement technique.	44
Figure 2.22: a.) 1000 shots with uncharred operation and b.) ~250 shots with charred operation. Charring is typical in low-energy thruster operation.	45
Figure 2.23: Comparison of filtering levels for the zero phase shift low pass filter used. The green trace shows the current pulse.	45
Figure 2.24: Two-color interferometer layout.	46
Figure 2.25: Interferometer post detection processing schematic.	46
Figure 2.26: For two-color interferometry, the laser passes directly in front of the fuel as in the flush case. For recession interferometry, all three cases are measured for comparison.	47
Figure 2.27: Typical ablation profile: 6 J, 6 hours, 1 Hz.	47
Figure 3.1: Several Planck distribution curves for blackbody emission at relevant temperatures.	62
Figure 3.2: Infrared spectrum of polytetrafluoroethylene, 0.005 cm film thickness. ⁵⁵ ...	62
Figure 3.3: Teflon polymer (a.) has an asymmetric C-F stretching mode (b.) absorbing energy at 8.4 μm	63
Figure 3.4: Estimated Teflon emissivity for 2-12 μm	63
Figure 3.5: Expected fraction of total emission to reach the detector. The cone is defined by the ZnSe viewport diameter.	64
Figure 3.6: Transmission response for ZnSe (a.) and Ge (b.) viewports. ⁵⁸	64
Figure 3.7: Predicted detector calibration for a Black Body and Teflon.	65
Figure 3.8: Teflon above melt temperature changes from white to transparent and retains a high viscosity.	66
Figure 3.9: Conductive heating into the surface of a micro-PPT at 20 μs from Eqn. 17. Average power of .203 MW used.	67
Figure 3.10: Heat transfer laterally across the surface of a micro-PPT in 200 μs due to conduction alone.	67
Figure 3.11: Schematic of the near Teflon plasma layers from Boyd and Keidar. ³¹	68
Figure 3.12: Electron density (a. and c.) and neutral density (b. and d.) experiment and predictions for $\theta=0.4$ (a. and b.) and $\theta=0.5$ (c. and d.). ²⁷	69
Figure 3.13: Surface temperature prediction for a 6.35 mm diameter micro-PPT. ³² Note that the units are in error, temperature is given in $^{\circ}\text{C}$	69
Figure 3.14: Intensified images showing arc behavior at a.) 2.3 J, b.) 5.55 J, and c.) 6.73 J. Capacitance is 0.417 μF	70
Figure 3.15: Anode spotting is predicted at high voltages when the anode voltage drop reaches zero from Keidar. ³⁶	70
Figure 3.16: Model of arc constriction due to high discharge voltage. The red lines denote the arc coverage area. From Keidar. ³⁶	71
Figure 3.17: Ablation rate dependence on current density increase due to discharge non-uniformity in the azimuthal direction from Keidar. ³³	71
Figure 4.1: Typical current trace for microPPT operation in these tests (4.35 J).	95
Figure 4.2: Comparison of measured and calculated current with linearly varying resistance.	95

Figure 4.3: Power deposition from the capacitor using the current and estimated resistance.....	96
Figure 4.4: Energy deposition during a typical microPPT firing.....	96
Figure 4.5: Mass Loss per pulse from average mass loss over varying number of shots at 4.35 J.....	97
Figure 4.6: Teflon surface after a.) 100 shots, b.) 1000 shots, and c.) 12000 shots at 4.35 J.....	97
Figure 4.7: A calibration run where the Teflon extruded out of the optical hole. It is easy to identify where the signal is disrupted.	98
Figure 4.8: Teflon a.) flows and b.) extrudes though the calibration hole. In one case c.) it remained flat.	98
Figure 4.9: Calibration curves for cases where deformation occurs (blue) and does not (red).....	99
Figure 4.10: Calibration tests for virgin and plasma exposed Teflon.....	99
Figure 4.11: Plasma exposed calibration curves for varying plasma exposures.....	100
Figure 4.12: Teflon plate used for calibration tests showing typical thermocouple location for testing and a centered thermocouple to characterize the temperature gradient.	100
Figure 4.13: A heating test with a centered thermocouple shows a measured difference of $\sim 6^{\circ}\text{C}$ when compared with the standard testing location.....	101
Figure 4.14: ANSYS results for temperature gradients assuming steady heat flow in and steady radiation out of the top and bottom surfaces. A maximum difference of 8° is shown.....	102
Figure 4.15: Difference between virgin and plasma exposed Teflon calibrations along with T^2 fits. Representative data points shown.....	103
Figure 4.16: Experimental calibration data with T^2 fits shown with theoretical predictions of the calibration using the Teflon emissivity estimate.	103
Figure 4.17: Estimated a.) virgin Teflon emissivity and b.) plasma exposed Teflon emissivity for 2-12 μm wavelengths.....	104
Figure 4.18: Detector voltage comparison for the Teflon emissivity estimate from plasma exposed Teflon and a grey body with emissivity 0.113.....	104
Figure 4.19: Detector noise in both channels is caused by current spikes in the sparkplug (yellow). The sparkplug causes EMI that is unavoidable at these low detector voltages.	105
Figure 4.20: A typical thruster firing with optical shield in place to block detection of the IR emission and show just the electrical noise.	105
Figure 4.21: Plume signals observed at varying distances from the fuel face.....	106
Figure 4.22: Plume and surface response with energy deposition over time.....	106
Figure 4.23: Five voltage measurements viewing the thruster face illustrate signal repeatability during the pulse with variation after ~ 30 ms.	107
Figure 4.24: Comparison of surface and plume measurements in a micro-PPT. 4.35 J.	107
Figure 4.25: The thruster face a.) before conditioning and testing and b.) after testing. The targeting location is shown on the right. The following data corresponds to the surface conditions of this face.....	108
Figure 4.26: 14 consecutive shots on a microPPT at 4.35 J not reduced.....	108
Figure 4.27: 14 shots from Figure 4.26 with 11-point smoothing shows trends, but also still has significant noise.....	109

Figure 4.28: 14 shots are filtered with a 300 kHz cutoff frequency. These data are also shown in the temperature domain.....	109
Figure 4.29: Measurement from pulse 20. During current reversal it is unknown whether the surface is measured. Therefore acceptable data begins at 20 μ s.....	110
Figure 4.30: Cooling curves from 14 pulses shown together.	110
Figure 4.31: Average of the 14 pulses in Figure 4.30 with typical uncertainty bars calculated by standard deviation.....	111
Figure 4.32: Single pulse cooling data from pulses 19 and 20 showing individual measurement uncertainty for these cases.....	111
Figure 4.33: Measurement of the cooling curve allows calculation of the Teflon vapor pressure after the pulse.....	112
Figure 4.34: Post-pulse impulse bit contribution from neutral Teflon vapor pressure is calculated using the pressure shown in Figure 4.33.	113
Figure 4.35: Expected post pulse neutral density for Pulse 20 is calculated using the Ideal Gas Law.	113
Figure 4.36: Total number of molecules and mass evaporated based on the surface temperature measurement of Pulse 20.	114
Figure 4.37: Separation of electron and neutral density for a 6.35 mm DIA MicroPPT with 0.415 μ F capacitance fired at 6 J.	114
Figure 4.38: Ionization fraction calculated from electron and neutral densities.....	115
Figure 4.39: Measurements of electron density for the cases shown in Figure 2.26. 6.35 mm microPPT fired at 6 J with 0.415 μ F capacitor.....	115
Figure 4.40: The dependence of the recession depth on the radial position within the tube after 6 h of firing and comparison with experimental profile. 6 J.....	116
Figure 4.41: Electron (a) and neutral (b) density distribution. Model prediction is in red.	117
Figure 4.42: Model predictions for electron density (with and without ion reflection) and neutral density for propellant recession of 50 mm. The experimental results are shown in black for comparison.	118
Figure 4.43: Ablation depth after a single pulse. ³³	118
Figure 4.44: Surface temperature predictions both within and outside a theoretical arc spoke.	119
Figure 4.45: The predictions shown in Figure 4.44 are compared with the averaged measurements from Figure 4.31. Note that valid experimental data begins at 25 μ s.	120
Figure 4.46: Comparison of predicted surface temperature a.) within an arc constriction to pulse 20 which showed the highest cooling temperature of the data set. Part b.) shows the prediction far from the arc constriction location with Pulse 19 which showed the lowest cooling temperature of the data set.....	121
Figure 5.1: Schematic showing an attempt to keep Teflon from flowing during calibration using a horizontal orientation for the calibration apparatus. The ZnSe window was inadvertently heated and began emitting in the IR. This invalidated the calibration.	138
Figure 5.2: Unfiltered data for Pulse 20 shows data clipping above 25 mV during the pulse. This was done intentionally to increase the measurement resolution for post-	

pulse cooling data. However, this makes peak data values unreliable during the pulse when filtering is applied. 138

Figure 5.3: Schematic showing the viewable cone locations and orientations within the plume for plume emission measurements and surface temperature measurements. The focal point of the viewable cone is located at 1 mm and 3 mm away from the propellant face. The surface measurement sees emission from the plume during the pulse. 139

Figure 5.4: Six measurements at the 1 mm plume location and six at the 3 mm plume location are shown early in the pulse. The repetitive nature of the plasma emission is clear. 139

Figure 5.5: The emission minimums from Figure 5.4 are shown with uncertainty bars. 140

Figure 5.6: Thruster face showing the viewable cone of a plume measurement above the surface (red). If the arc spokes a.) outside of the viewable cone, the emission measurement will be minimized. If it spokes b.) within the viewable cone, the emission measurement will be maximized. 140

Figure 5.7: Due to high noise levels, varying the filtering frequency results in a number of values for the voltage when the current passes through zero. This makes it difficult to discern whether the surface is actually being measured. 141

Figure 5.8: Using the 500 kHz cutoff frequency, the minimums during the pulse are plotted along with the prediction from the K-B model. These may be indicative of surface temperature during the pulse. 141

Preface

The experiments described in this work are part of an ongoing effort at the University of Illinois which began in 1997 with work on a modified Herriott Cell designed to increase the resolution of laser interferometry for measuring exhaust densities in Pulsed Plasma Thrusters. The Electric Propulsion Laboratory of the Air Force Research Laboratory at Edwards Air Force Base funded this research, and a parallel numerical modeling effort at the University of Michigan in order to develop an understanding of spacecraft contamination effects due to the operation of these thrusters. To date the experimental work has contributed to four refereed journal articles, eight conference papers at international conferences and one Master of Science Thesis. These works are referenced throughout this paper and have been presented at the AIAA/ASME/SAE/ASEE Joint Propulsion Conference, the AIAA Plasmadynamics and Lasers Conference, the International Electric Propulsion Conference, the APS Division of Plasma Physics, and the High Temperature Plasma Diagnostics Conference.

1. Introduction

1.1 Electric Propulsion and Pulsed Plasma Thrusters

Electric propulsion (EP) differs from chemical rocket propulsion in several areas. Where chemical rockets require the energy from the combustion of high energy, often toxic materials, EP requires only electrical power to accelerate its propellant. This has several distinct advantages over the more common chemical rockets. Electric systems operate at significantly higher specific impulses (I_{sp}) than chemical systems, often limited only by the available power. (Specific Impulse is the total impulse a rocket generates per unit of propellant weight. The higher the specific impulse, the less propellant a rocket uses to generate a certain total impulse.) In terms of launch systems for large satellites, this can mean a downgrade to a smaller launch vehicle or much larger on-orbit payload mass fraction. Since these rockets do not operate on the stored energy in the propellant, inert substances can be used for fuel. Reduction of costs from handling of toxic materials such as hydrazine (a common liquid rocket fuel) is also an incentive for electric propulsion.

Electric thrusters are generally classified by 3 types of acceleration mechanisms.¹ Electrothermal rockets such as arcjets and resistojets use ohmic heating from the arc to heat the propellant and then gasdynamically expand it through a nozzle. These rockets are closest in principle to conventional rockets and typically operate at the lowest I_{sp} levels. Electrostatic devices include ion engines and Hall effect thrusters and operate by applying an electric field to accelerate highly ionized plasmas. Finally, electromagnetic thrusters such as magnetoplasmadynamic rockets (MPDs) use magnetic fields to accelerate a plasma by means of a $\mathbf{j} \times \mathbf{B}$ force.

Many electric thrusters have been flight-qualified and used on-orbit. Pulsed Plasma Thrusters (PPTs) were the first electric propulsion device flown and have since seen operational use on several satellites.² Arcjets were the first used in a commercial capacity and have flown at power levels up to 30 kW.³ Ion engines provide North-South (N-S) stationkeeping for commercial telecommunications satellites and recently flew on the Deep Space 1 mission.⁴ Hall effect thrusters developed in Russia are seeing a

substantial commercial push in the U.S.⁵ Widespread use of electric rockets shows increasing acceptance of this field, but significant research remains in the areas of theoretical modeling, increasing performance, and understanding spacecraft interactions. This research focuses on Pulsed Plasma Thrusters.

A pulsed plasma thruster (PPT) is a pulsed electric rocket that provides short bursts of thrust by discharging a capacitor-driven arc over a solid surface. The surface then ablates to provide both current carriers for the arc and propellant for the rocket. The standard design for the PPT is a bar of Teflon held between two rectangular electrodes with an ignitor plug mounted in the cathode shown in Figure 1.1. In general, PPTs can be broken down into rectangular and coaxial geometries with either breech-fed or side-fed fuel bars. Their attraction as a propulsion option on small satellites is their design simplicity and use of solid, non-toxic propellant.

The history of PPTs shows significant research and several demonstration flights dating back to 1964 when the Soviet Union launched the Zond-2 spacecraft towards Mars. The PPTs on this spacecraft were the first electric propulsion thrusters flown.² After the Zond-2 flight, several flight applications occurred in the US including the Lincoln Experimental Satellite 6 (LES-6) which set the stage for rectangular PPT usage in future decades. The LES-6 thrusters provided attitude control for 10 years on orbit. More research led to the development of the LES 8/9 thrusters that were flight qualified, but never flew due to circuitry problems.⁶ PPTs have also been flight demonstrated on the Synchronous Meteorological Satellite (SRS) in 1974,⁷ the three spacecraft TIP/NOVA series in 1981,⁸ and the Earth Observer 1 (EO-1) satellite in 2000. A significant amount of research was done on these thrusters, and many diagnostics were performed to understand the basic physics of the thruster operation.⁹⁻²²

The most recent addition to the PPT family of thrusters is the microPPT. This is a coaxial, three-electrode PPT invented²³⁻²⁵ at the Air Force Research Laboratory. It retains many of the features of standard PPTs, but because of circuitry changes the micro-PPT demonstrates significant savings in system mass. Studies indicate that the micro-PPT can provide full ACS at 1/5th the dry mass of conventional torque rods and reaction wheels for a 150 kg class spacecraft.²⁶

1.2 Motivation for Studies

This research is geared towards improving the understanding of Teflon™ ablation physics within these thrusters. In recent years research has focused on improving the efficiency of these thrusters, but little progress has been made. In fact, over the past 30 years research has failed to produce significant improvements in the overall performance of PPTs. Part of this is due to an incomplete understanding of the physical processes at work in these thrusters. There is still very little understanding of key areas such as the ablation process, transition from solid to plasma, and chemical description of the exhaust. Typical efficiencies of PPTs remain below 10%.² A critical source of this inefficiency is the poor use of propellant in the device. In 1971, Vondra et al. reported estimates from Faraday cup measurements in the plume of the LES 8/9 thruster showing a 10% ionization fraction.²¹ Discrepancies between the mass-average velocity and measured velocities of ions and neutrals suggested there was a significant portion of the total propellant being consumed but not used for thrust. As little as 10% of the propellant may be used to create thrust, the remaining 90% being wasted in the form of small ionization fraction during the current pulse and late time vaporization after the pulse.¹²

In order to improve this efficiency and harness the full potential of these thrusters, it is necessary to gain a more complete understanding of the physics behind their operation and propellant consumption. One of the key unknowns is the ablation process involved in this type of thruster. This process governs both the microscopic details of plasma development as well as macroscopic thruster operation in terms of propellant efficiencies, specific impulse, impulse bit, and even spacecraft contamination. The governing parameter for ablation is the surface temperature of the propellant. The process of heat transfer between the arc and the Teflon, along with the cooling of the propellant after the pulse, control the total mass ejected per pulse.

Initial experimental inquiries into propellant temperature focused on the effects of steady state thruster operation since techniques were not available to examine surface temperature on a real-time scale. Kamhawi and Turchi used thermocouples to measure the temperature of the entire thruster including electrodes and Teflon propellant.¹³ Their results showed that the propellant temperature rose to a steady state value determined by the radiation characteristics of the thruster body. Additionally, the propellant surface

temperature near the anode was significantly warmer than near the cathode. It is significant to note that they were unable to measure temperature during thruster firings because of adverse affects the arc was having on the thermocouple operation.

Their research was furthered by an investigation into propellant temperature effects by Spanjers *et al.*¹² Spanjers buried thermocouples in the Teflon of XPPT-1 at varying distances from the fuel face. The results correlated increases in propellant temperature with an increase in total propellant consumption, which indicated a decrease in thruster I_{sp} and efficiency. The temperature increases showed no effect on thrust, indicating that propellant surface temperature was the governing factor in the late-time vaporization losses. Spanjers hypothesized that active cooling of the propellant would result in increased specific impulse and thruster efficiencies. As a follow-up on that research, steady-state temperatures over sustained operation of the microPPT have been measured on the outer electrode. In their research, within the first 4 hours of steady-state operation, the temperature near the exit-plane of the microPPT rose from 22 °C to 65 °C.¹⁴

Unfortunately, assessment of thruster and propellant temperatures during steady state operation has significant limitations when used for analysis on a shot-to-shot basis. PPTs and microPPTs experience starting transients and modified behavior as operation normalizes. During repetitive pulsing, it can take ~1000 pulses for a steady state temperature to be achieved. During this time mass lost per pulse varies in amount for both propellant and electrode material. For the microPPT, there is increasing evidence that the performance changes as a result of sustained operation due to propellant recession into the outer electrode tube.

Experimental work has also contributed to the development of numerical thruster modeling. While there are a number of modeling approaches that match thruster operating trends, a highly detailed description is required to allow prediction of contamination effects and description of the plasma generation process. Because of the effects mentioned above, time-averaged measurements cannot give the level of detail required to validate models that predict the physics on the basis of individual pulses. For this reason, the Keidar-Boyd models are considered.

In recent years, accruing experimental evidence has enabled the development of numerical models capable of predicting the behavior of PPTs and microPPTs on a single pulse basis. Several of these attempts^{27,28} have focused on end-to-end (plasma generation to plume far-field) model development for both electrothermal^{29,30} and electromagnetic³¹ PPTs. A consistent indication from the modeling effort is that plume properties depend very heavily on the upstream conditions including the ablation characteristics such as propellant surface temperature. In fact, one model by Keidar and Boyd has predicted the trends that may explain the temperature effects observed by Spanjers.³⁶ The development of these models along with their validation indicates that the physical understanding of thruster operation is approaching a point where we are able to predict both micro- and macroscopic properties of the plume and ablation. This has ramifications for understanding and improving both thruster performance and spacecraft contamination issues. Throughout this paper, the experimental data are compared with predictions from the Keidar-Boyd Model.

Early microPPT models by Keidar and Boyd were first validated by experiments in interferometry when the predicted electron densities during the pulse matched well with measurements.³² Figure 1.2 shows this comparison. At the same time, analysis of a failure mode known as ‘charring’ was being investigated and modeled. These same models were applied to the charring problem and indicated possible causes including low surface temperature in the charred regions that led to decreased ablation, and carbon ion backflux from the arc. Figure 1.3 shows good correlation between a prediction of a zone of low ablation rate and char location on a microPPT.³² These early validations indicated two important principles: first, the Keidar-Boyd models held promise for use as a tool for describing the physics of PPT operation and spacecraft interaction. Second, surface temperature is the key parameter required to describe the ablation process and validate the models.

The next experimental step used two-color interferometry to resolve both neutral and electron densities during the pulse. Early measurements of neutral density had large uncertainties that only showed the trend of the measurement, but the predictions from the first model were clearly inaccurate. Figure 1.4 shows this comparison.¹⁷ This lack of agreement was due to the inclusion of assumptions of local thermodynamic equilibrium

and Saha equilibrium within the transition from solid to plasma. The model was then updated to include non-equilibrium physics in the transition regions. The initial two-color measurements had a large uncertainty and new measurements are required to validate the model updates.

Analysis of the plume during the pulse only addresses half of the problem. Past interferometry measurements on standard PPTs have shown neutral vapor presence after the pulse.¹⁶ In addition to the late-time neutral vapors measured, there is a loss of propellant due to particulate ejection. This has been witnessed in a number of experiments and is likely a significant contributor to total late-time mass loss. Figure 1.6 shows false-color pictures of both the neutral vapor and particulate ejection portions of the discharge.²⁶

To investigate the neutral vapor generation, a Herriott Cell was added to an interferometer to increase resolution of the instrument by 18X.^{18,19} It produced measurements of neutral density out to 200 μ s after the pulse on the co-axial PPT-4.^{19,20} Figure 1.5 shows this neutral density measurement along with vibrational uncertainty for the instrument as a function of time. Late-time measurements for PPT-4 are different than standard PPTs and microPPTs because they include a timeframe required for transportation of the neutral vapor from the thruster chamber to the exit plane where the laser beams are located. Therefore similar measurements on other thrusters would expect to see a neutral density peak earlier. However, the PPT-4 measurements illustrate a need to investigate the late time neutral vapor generation that does not contribute to thruster performance. When the Herriott Cell was applied to the microPPT, an increase in resolution of 13X was attained, but this was not enough to resolve neutral density after the pulse of such a small discharge. Figure 1.7 shows that the interferometry measurements taken after the microPPT pulse fail to resolve a neutral density signal.¹⁷

With the failure of interferometry to provide an avenue for studying late-time ablation and an understanding that surface temperature is the key parameter in this problem, we propose a new approach: Measure the surface temperature of the Teflon propellant in real-time. Research in the fracture dynamics community relies heavily on infrared photovoltaic detectors to characterize temperature rise near the tips of fast-propagating cracks in solid materials.³⁹⁻⁴⁴ The time-frame under observation for these

experiments is similar to timeframes during which a microPPT discharge is observed. It is a claim of this paper that real-time propellant surface temperature measurements can be accomplished using the same techniques. The relationship between surface temperature and Teflon vapor pressure is well known at high temperatures (Figure 1.8). Through this relationship, surface temperature governs ablation rate in these thrusters and becomes critical in calculation of total mass loss, available charge carriers, and late-time ablation. These extend the influence of T_s to plasma resistivity, ionization fraction, current density, and the feedback process of ablation from arc radiation and particle convection. Surface temperature is the defining parameter for thruster operation and analysis, which until now has been un-measurable in real-time for these thrusters.

The Keidar-Boyd models currently in development²⁷⁻³⁵ calculate plasma generation and plume far-field development for the purpose of predicting thruster performance and the effects of pulsed ablative thruster operation on hardware such as solar panels and electrical and optical equipment common to earth-orbiting satellites. These models develop through a symbiotic relationship with experiments performed on these thrusters. Therefore the experiments described here have proven critical to the development of a theoretical understanding of the ablation process and thruster operation in general.

1.3 Summary of Present Experiments

Several experiments are presented here to increase understanding of the ablation process and operation of microPPTs. The proposed experiments fill gaps in knowledge that are currently outstanding in microPPT operation and theory. These data are also encouraging for the validation of the Keidar-Boyd Model. Development and validation of current ablation and plume models hinges on experiments performed on a thruster where the propellant has not recessed into the outer electrode tube. For a full experimental description, the thruster must be investigated in all expected operating conditions. For the microPPT, this includes a description of propellant recession into the tube and plume properties that account for exhaust flow through the tube. With these in mind, the following experiments are performed.

- The bulk of this research concerns development and use of a real-time surface temperature measurement diagnostic using infrared detectors. This paper describes the design, calibration, and operation of a Mercury Cadmium Telluride photovoltaic detector for measuring the surface temperature of Teflon propellant used in the microPPT. The results of this diagnostic are used to critically evaluate the validity of theoretical predictions of surface temperature and its effects.
- Two-color interferometry is used to measure electron and neutral densities during the pulse to evaluate the validity of the non-equilibrium physics that have been recently introduced to the Keidar-Boyd models. This is also used to calculate the ionization fraction during the microPPT pulse.
- High-speed pictures are taken during the microPPT pulse to locate anode spots and evaluate current distribution in the microPPT discharge.
- Measurements of recession coning patterns are made for comparison with long time-frame predictions of propellant ablation by the Keidar-Boyd model.
- Single-color interferometry measures the electron densities while the propellant is recessing to investigate the predictive ability of the models when propellant recession occurs.

Using these experiments we provide an experimental description of microPPT operation that is used to help refine theoretical description of the processes involved. The development of infrared detectors for the surface temperature measurements attained here provides a new direction for photovoltaic technology use and a new tool for analysis of ablation problems and plasma-wall interactions.

1.4 Summary of Critical Findings

This section presents a list of the critical findings presented in this dissertation. Three areas of research have been impacted by the experiments performed here. The first

is the field of infrared thermography. The development effort here is the first attempt to use infrared thermography to investigate plasma-wall interactions, and to the best of our knowledge the first attempt to characterize the infrared emission of heated Teflon. Advancements in the field of Infrared Thermography include:

- A new calibration procedure was created for materials with wavelength dependent emissivity and high transmissive character. This allows application of emissive temperature measurements to materials that until now have been difficult to characterize.
- Using data from infrared spectroscopy and infrared thermography, a method of estimating the wavelength-dependent emissivity has been developed.
- These experiments are the first application of high-speed thermography to discharge physics for analyzing plasma-wall interactions of which we are aware.
- The first microsecond time-scale measurements of propellant surface temperature on an operating microPPT are presented here. Although data during the pulse of the microPPT is not resolved due to plasma interference, the cooling curve of the propellant is characterized immediately after the pulse.
- Measurement of the surface temperature in real-time demonstrates that it is possible to perform time-dependent mass flow measurements from hot Teflon.

The second field that has been advanced since the Antonsen Master of Science (MS) thesis¹⁹ is interferometry and characterization of microPPT plumes. The MS thesis describes development of the Herriott Cell for an interferometer to increase system resolution and a first attempt to use two-color interferometry in a standard PPT plume. The advancements made since that point include:

- Two-color interferometry applied to the microPPT to measure electron and neutral densities simultaneously during the pulse.
- The Herriott Cell was applied to a microPPT in an attempt to measure neutral densities after the pulse. This attempt was unsuccessful, but demonstrated the need for a new approach to the late-time ablation problem.
- Recession operation is investigated through measuring plume electron densities while the Teflon was recessed. This allows measurements of polarity effects on the electron density.

The data presented here has also provided the Keidar-Boyd numerical model with a high level of feedback and validation throughout its development. In that respect, this research is one of the key legs of Keidar's theories. The theory is currently a repository of knowledge for describing the physics of Teflon ablation, plasma generation, and plume far-field behavior. Although the current model geometrically describes the microPPT, the physics involved are applicable to any Teflon ionization problem. Advancements to the Keidar-Boyd model enabled by this research include the following:

- Keidar's original theory was partially validated by electron density alone. However, two-color interferometry highlighted a shortfall in the ability of his theory to describe thruster operation. This is perhaps the most significant example of experiment helping to shape theory presented in this paper.
- Measurements of coning profiles from operating thrusters provide a validation of Keidar's predictions of recession ablation and current densities around the central electrode.
- High-speed, intensified images of the microPPT face during thruster firings provide evidence of anode spotting. Keidar has been able to calculate when spotting should occur and has initiated a new phase in his theory addressing arc constriction.
- Comparison of predicted propellant recessed electron densities with measurements directed theoretical development to include electrostatic ion reflection from the outer electrode while acting as the anode.
- Predictions of surface temperature near and far from a current constriction give an expected range of temperatures for propellant cooling after the pulse considering ablation as the main heat loss mechanism. This prediction shows good agreement with the cooling curves measured through infrared thermography. This lends credence to both the experiment and theory. The differences between experiment and prediction suggest the inclusion of radiation losses and thermal conduction would improve the level of agreement.

1.5 Contents of Dissertation

This dissertation is divided into sections discussing Apparatus and Approach, Theory, Experimental Results, Discussion, and Conclusions. Section 2 describes the facilities used for the experiments. The construction, calibration, and operation of the infrared diagnostic are detailed here. A brief summary of the interferometer is provided with references for more in-depth description of that experiment. Other sensors and diagnostics are detailed for complete evaluation of the experimental processes used. Finally, the data acquisition system is described for the IR and interferometry experiments.

Section 3 on theory discusses the theory and calculations behind the infrared temperature diagnostic development and thermal analyses of Teflon. Impact of plasma and neutral vapors on the diagnostic is discussed here. This section also discusses several models being considered for description of the ablation process, propellant cooling after the pulse, and thruster performance as a function of surface temperature. These models are evaluated in light of experimental results in the following sections.

Section 4 shows experimental results. First, the calibration of the infrared detector to heated Teflon is shown. The uncertainties are calculated and both plasma and surface temperature contributions are detailed. It is shown that surface temperature measurements are valid after the current pulse has ended. These measurements are then used to calculate Teflon vapor pressure and estimate performance due to Teflon ablation as the propellant cools.

Measurements of the electron and neutral densities during the pulse of the microPPT are taken and the ionization fraction is calculated. Measurements of the coning profile are also taken and high-speed intensified images of the microPPT pulse are used to locate anode spots. Finally, Keidar-Boyd model predictions are shown and compared with the experimental measurements of surface temperature, electron and neutral densities, recession propellant profile, and recession electron density.

Section 5 discusses issues with the data collection for the surface temperature measurements and explores sources of uncertainty. The utility and limitations of the thermographic theory are investigated. Material effects and arc spoking are examined to illustrate the limitations of the surface temperature diagnostic. The overall utility of IR

thermography as a thruster diagnostic is considered with respect to its limitations. The Keidar-Boyd model is discussed in more detail and the implications of comparisons with interferometry and coning profiles are considered. Finally, assumptions required for performance calculations are evaluated.

Section 6 presents the conclusions of this research. Future directions are discussed for improving the surface temperature diagnostic and possible means of achieving real-time surface temperature measurements during the discharge of a microPPT are discussed.

1.6 Chapter 1 Figures

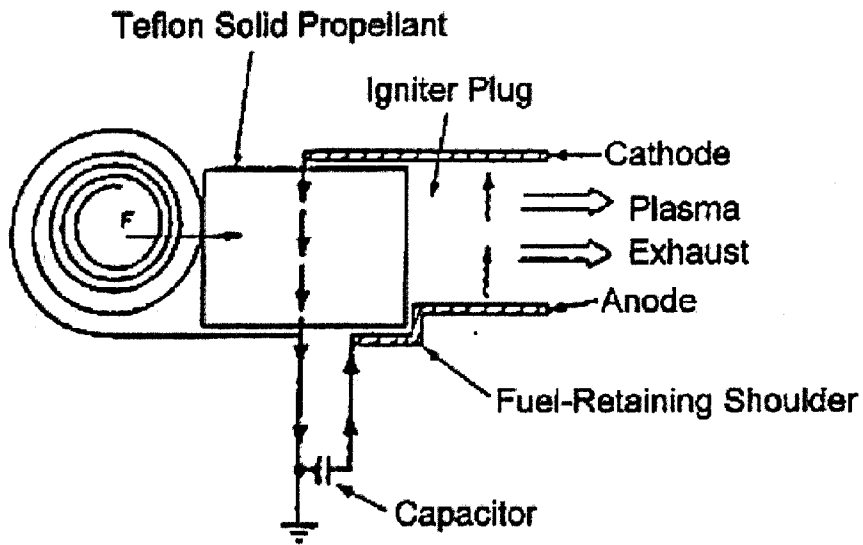


Figure 1.1: Rectangular, breech-fed PPT from Vondra and Thomassen.¹⁰

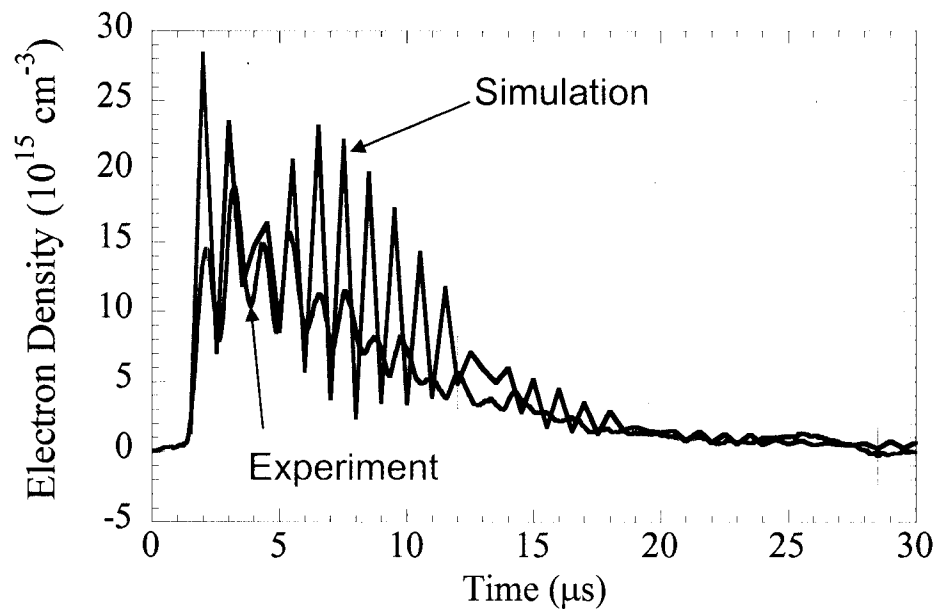


Figure 1.2: Comparison of predicted and measured electron density for a 6.35 mm Micro-PPT fired at 6.6 J from Keidar and Antonsen.^{17,32}

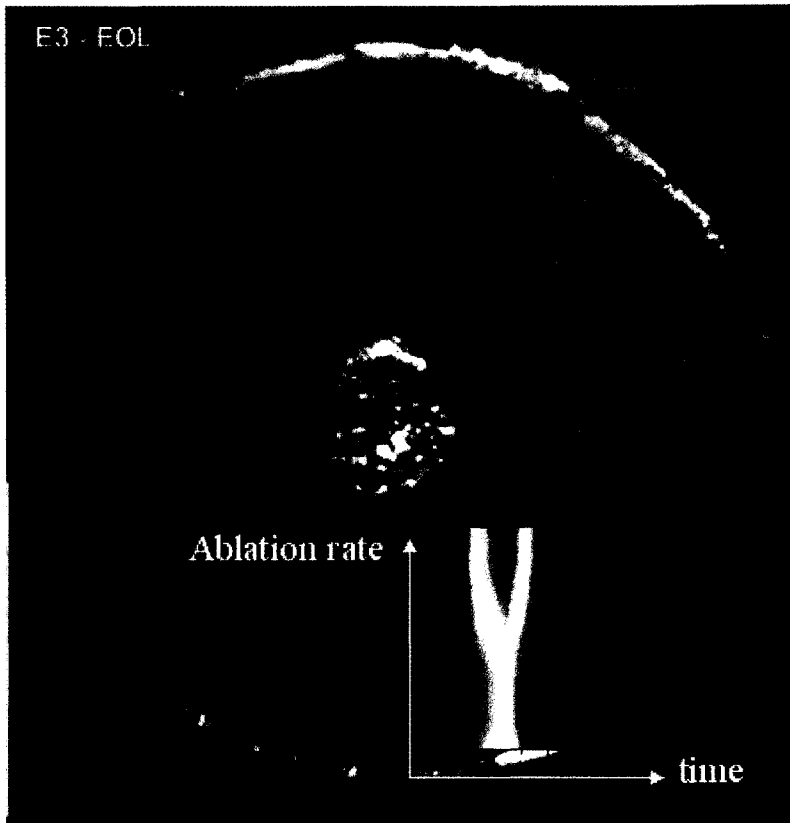


Figure 1.3: Photograph of charred micro-PPT with corresponding model prediction of ablation rate through the pulse. The area of lowest ablation rate matches well with the radial char location from Keidar et al.³²

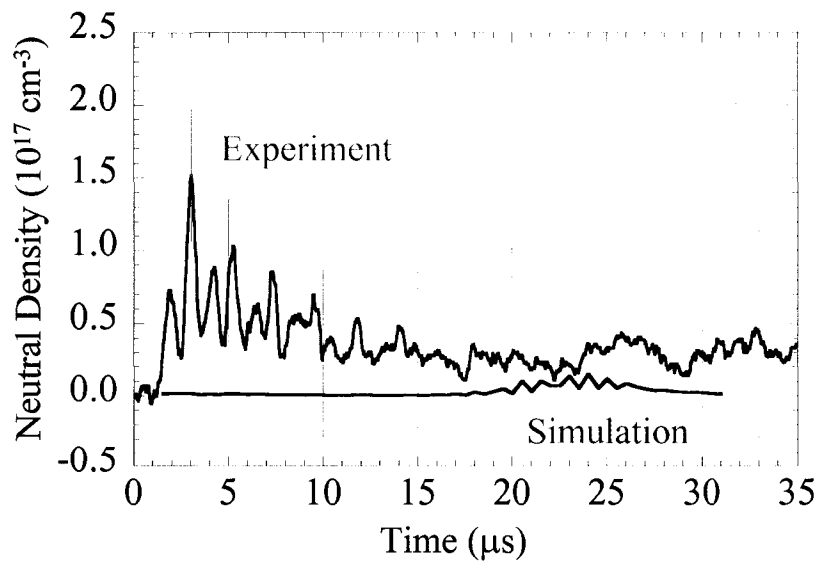


Figure 1.4: Comparison of predicted and measured neutral density for a 6.35 mm Micro-PPT fired at 6.6 J.

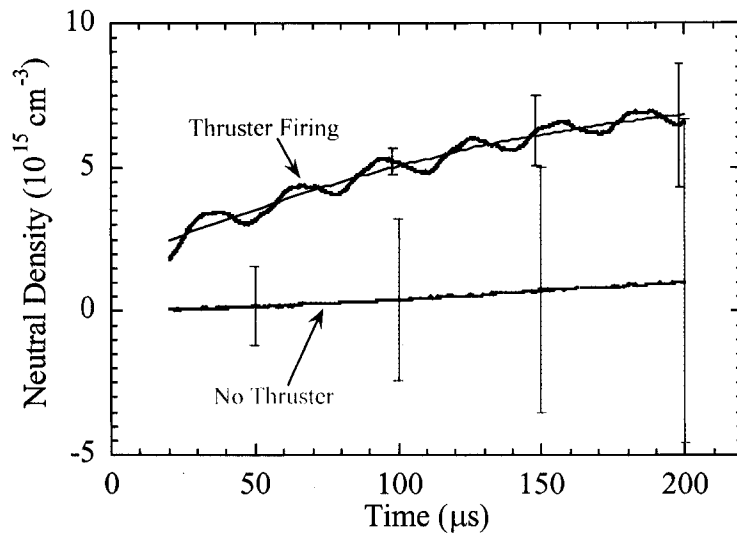


Figure 1.5: Data shows significant neutral density for PPT-4 after the pulse using Herriott Cell interferometry from Antonsen.¹⁹

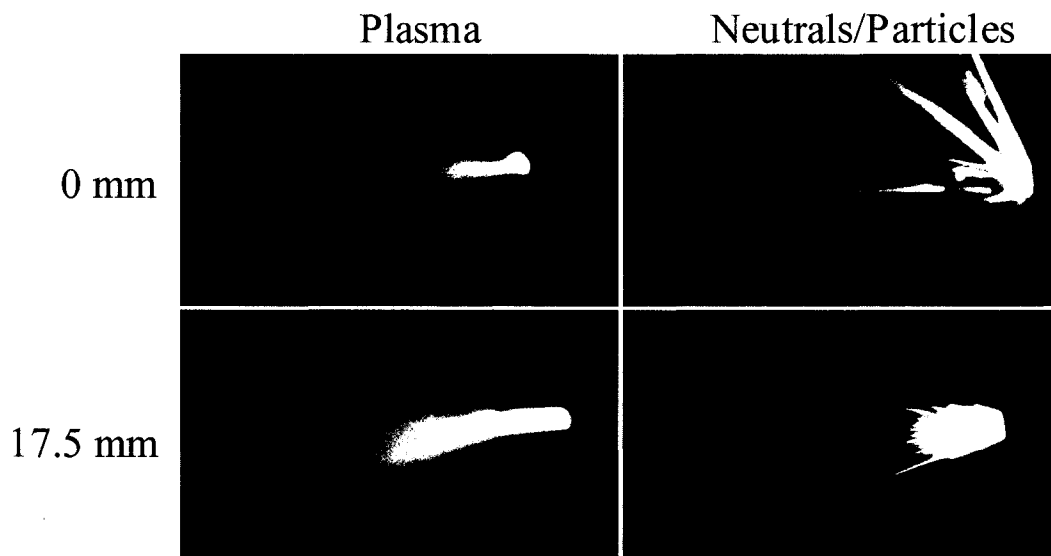


Figure 1.6: Plasma and Late Time Vaporization divergence in a $\frac{1}{4}$ "-diameter, 2-electrode MicroPPT firing at 5 J. 0 mm and 17.5 mm on the left side of the photo refer to the recession depth of the propellant within the tube. The curved rod visible in the plasma pictures is a spark plug used to ignite the main discharge from Spanjers et al.²⁶

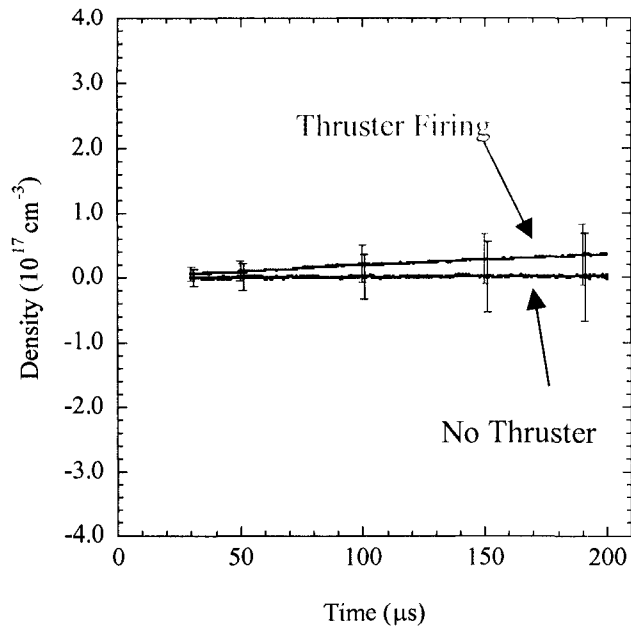


Figure 1.7: Herriott Cell measurements for neutral density after the pulse of a microPPT did not have sufficient resolution to distinguish neutral density from Antonsen.¹⁹

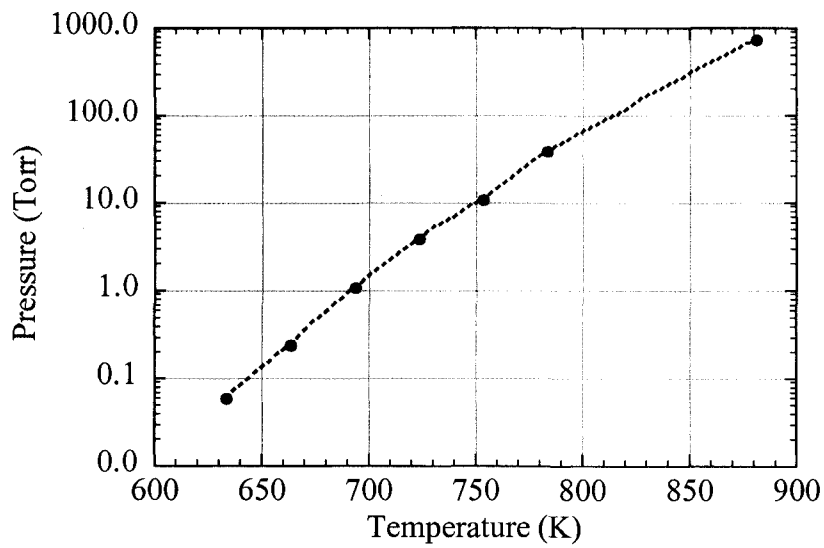


Figure 1.8: Vapor pressure of Teflon with surface temperature from Wentink.^{46,2}

2. Apparatus and Approach

2.1 Facilities Description

Data is taken at the Electric Propulsion facility at the Air Force Research Laboratory, Edwards AFB, CA. Three vacuum chambers were used for testing. Tank 5 A is a 2.1-m³ vacuum tank that has 2 Varian 182, 4400-Watt diffusion pumps backed by a Varian SD-1400 mechanical pump. The tank is roughed from a pump train using a Stokes 412H-12 (300 CFM) located outside the building. These Stokes pumps provide roughing and diffusion pump backing for 4 separate tanks. A small mechanical pump was used to back the Tank 5 A diffusion pumps and was vibrationally isolated from the tank using bellows and a vibration mount to prevent transmission of high frequency pumping noise through the floor. The tank windows are Bk7 glass. This tank is also electrically isolated with power sources under the tank floating with respect to the laboratory ground.

Two bell jars, an 18-inch and a 24-inch with a single collar extension are used for IR thermographic testing with the Micro-PPTs. Viewing is performed through Zinc Selenide (ZnSe) windows to meet the special infrared needs of the diagnostic. The 24 inch system is used for calibration tests because the Micropyretics Heaters International (MHI) model HP220-HIGHBO hotplate⁴⁷ used for calibration fits within this diameter. This hotplate is adjustable up to 1400 °C and capable of 3000 W. For some calibration tests a modified top is provided for the 24" bell jar. Using this top, the optical system requires top-down viewing into the tank, so a stainless-steel reinforced lid with a welded half-nipple is placed atop a rubber gasket for sealing. Pressures of 30 μTorr have been achieved. The half nipple seats a 4" conflat flange where the ZnSe window is placed. Cooling is provided for operation with the hotplate by an Endocal RTE 4 refrigerated circulating bath pumping ethylene glycol through copper tubing pressed onto the steel structure. Both bell jars are pumped by Varian 300-SF turbopumps backed by an SD-301 mechanical roughing pump. The second calibration configuration uses the 2.75 inch conflate ports on the side of an extension collar for optical access to the calibration setup and thruster face.

A possible source of error is collection of photons emitted from sources other than the target. To create a thermally isolated environment, the detector and Newtonian telescope are enclosed in large cardboard sheets. Cardboard faces inward providing a diffuse reflection mechanism within the enclosure, and aluminum foil is attached to the outside of the sheets to reflect away any ambient radiation that could skew the signal.

Interferometric testing used two lasers. A LaserPhysics 150M, 488-nm, 150-mW Ar⁺ laser is used. The second frequency was provided by a Spectra Physics 127 HeNe laser. This laser is capable of operating at either 633-nm or 1152-nm. The photodiode detectors are Analog Modules models 712A-9 and 712A-5-NI. The Bragg cell is an Isomet model 1201E-1 with oscillator model 21A-2.

2.2 The Micro-Pulsed Plasma Thruster

The three-electrode microPPT is shown schematically in Figure 2.1. An arc is initiated between the pin and intermediate electrode creating seed plasma for initiation of the main discharge between the intermediate and outer electrode. In these studies, a two-electrode testbed (Figure 2.2) is used as an approximation of the main discharge simplifying the operation of the experiment and focusing on the physics of the main discharge only. All testing is performed on 6.35 mm diameter micro-PPTs with a central electrode diameter of 1.64 mm. The outer diameter of the Teflon dielectric is 5.46 mm.

Figure 2.3 shows the fresh face of an unfired micro-PPT. The fuel face forms a flat exit plane for thruster operation. In contrast, Figure 2.4 shows a thruster that has been fired at 7.5 J for 1 hour at 1 Hz (3600 shots). Some deformation of the fuel face is evident as a result of the large number of shots at high energy for this device. These pictures illustrate the small variations in fuel topography that can be expected from shot to shot for this device. The micro-PPT uses a small amount of propellant ($\sim 4 \mu\text{g}/\text{J}$) and as such, the topographical variation of the face during a single shot is negligible ($0.6 \mu\text{m}$ at 7.5 J for even ablation). This ablation topography is discussed below in regards to the optical depth of the detector system.

Variations in the fuel face topography and chemistry are a motivating factor for a surface temperature measurement. One failure mode of these thrusters is charring, which is high carbon content black material that gathers on the fuel face in specific locations

and correlates with low energy-to-area ratio thruster operation. Modeling predictions (Figure 1.3) show low surface temperature and ablation rates in the areas where the char accumulates along with an increased backflux of carbon ions.³² Scanning Electron Microscopy (SEM) X-ray analysis of a charred section of fuel indicates an atomic carbon signature 3x higher than that found in virgin Teflon. Correspondingly, the fluorine signature is 20% lower than in virgin Teflon.⁴⁸ This becomes a failure mode because the char material is conductive and can short the gap between the electrodes. The result is an inability to fire the thruster. Practically, the solution to this problem is to find an operating regime where this failure mode is not present. Proper selection of the energy-to-area ratio for thruster operation eliminates this problem, but for a complete understanding of this problem an investigation of the surface temperature must be performed.

2.3 Infrared Thermography

The development of this experiment is based on high-frequency measurements of infrared emission from the hot Teflon propellant to measure the surface temperature. Description is given here of the hardware required to accomplish this measurement. After hardware description, an explanation of experimental procedure used to calibrate the detector output to an actual temperature is given. Finally, a description of the data collection methods and data acquisition for thruster measurements is discussed.

Photovoltaic cells are used for two reasons. First, they provide an emissive measurement method capable of response times in the sub-microsecond timeframes typical of microPPT arcs. The alternative is photoconductive cells, which are limited to sub-megaHertz bandwidths. Non-emissive means such as thermocouples and thermistors are also unable to achieve the response times required, and they have an additional constraint. All non-emissive measures require contact with the propellant surface, which means exposure to the high-voltage breakdown. This creates a number of electronic noise issues and often results in an inability to carry out measurements.

2.3.1 Mercury Cadmium Telluride Detectors

Photovoltaic detectors operate by means of a p-n junction converting radiant energy from photons of certain wavelengths into electric current. The photovoltaic diode operation is characterized by a logarithmic proportionality to light current input and a fast response determined by the external circuitry involved. Figure 2.5 shows a schematic of a single HgCdTe detector. Photons with energy higher than the semi-conductor bandgap energy change the conductivity by exciting electrons into a conduction band. A bias current is applied and the output is sent to a pre-amp. In this case, the detector rise time is ~ 40 ns. The system circuitry is shown in Figure 2.6. The bias current can be adjusted to change the relative responsivity and noise level, however for these experiments, the factory bias setting of -5 mV was used exclusively.

Detector response is a wavelength-dependent phenomenon where peak responsivity (R_p) for the detectors defines the maximum of a responsivity curve. For these detectors, R_p is 8.2 A/W as measured by Fermionics.⁴⁹ Using this value and normalizing the relative responsivity (D^*) shown in Figure 2.7 to a percentage of the maximum value, the wavelength dependent detector response can be calculated. Figure 2.8 shows this result. Note that where possible (7-12 μm), the actual calibration curve from the factory is input instead of the general response shown in Figure 2.7. The general response data is used for 2-7 μm since the factory calibration curve didn't show these values.

For the initial studies into feasibility of the fast-response infrared diagnostic, a linear array of 4 Mercury Cadmium Telluride detectors was purchased from Fermionics.⁴⁹ With DC to 10-MHz bandwidth, this detector from Fermionics is capable of seeing both sub-microsecond temperature shifts and slow decays back to room temperature. Detector responsivities for HgCdTe and Indium Antimonide (InSb) are shown in Figure 2.7 and Figure 2.9 respectively. The HgCdTe detector is chosen for its broad range of responsivity over 2-12 μm wavelengths because the main source of Teflon emission is at 8.4 μm .⁴⁶ Additionally, the InSb detectors are less sensitive to lower temperatures due to their lack of response to wavelengths exceeding 6 μm . The linear array is a vertical design with detector active areas of 80 μm x 80 μm square and a pitch

of 20 μm between detectors. This array is housed in an LN2 dewar to minimize thermal radiation from the detector housing.

2.3.2 Optics

The optics for infrared detection use a 15.2-cm diameter gold coated concave spherical mirror with a 30.5-cm focal length and a 50-mm diameter gold coated flat mirror. These act as a Newtonian telescope following the optic equation³⁷

$$\frac{1}{f} = \frac{1}{i} + \frac{1}{o} \quad (1)$$

and magnification equation

$$m = -\frac{i}{o} \quad (2)$$

which provide the proper distance for an inverted 1:1 image on the detector. In these equations, f is focal length, i is image distance, and o is object distance. This provides a distance of 61 cm from the mirror to both the target and the detector. The 50-mm flat mirror is generally placed about 36 mm from the spherical mirror to complete the Newtonian telescope. Figure 2.10 shows a schematic of this layout for clarity.

Figure 2.11 shows a close-up view of the optic effects on the measurement area. The large mirror provides a cone of measurement, the apex of which is the 1:1 image of the detector array on the fuel surface. Theoretically, light emission is collected from everywhere within the cone provided the photon vector is oriented toward the detector. Practically, an optical depth is defined over which emitter proximity to the focal point will contribute a significant number of photons. Determination of this optical depth is performed during optical alignment and targeting using a micrometer translation stage to move the detector in and out of the focal point while the tungsten wire is heated. The drop-off in signal from the maximum at the focal point defines the acceptable optical depth characterized as ± 1 mm.

2.3.3 Calibration Apparatus and Method

Calibration methodology has undergone a number of iterations. Due to the transmissivity of Teflon in the long-wave infrared (LWIR), valid calibration must exclude any undesirable heat sources within the extended viewable cone behind the Teflon sample being measured. Initial attempts to calibrate failed to address this problem, and showed abnormally high voltage to temperature curves. Once this problem was understood, the calibration method was modified to allow the optical cone of the detector to look through a thin sheet of Teflon. A bonus of this technique is that the application of heat to the Teflon closely resembles that of the arc, with heat only applied to the top surface from which IR measurements are made. It is also important to note that sheets of 0.125" thick Virgin Electrical Grade Teflon purchased from McMaster-Carr are used for calibrations. It is not clear whether this has the same level of impurities as the Teflon in the microPPTs used for testing.

2.3.3.1 Calibration Apparatus

Extensive measures have been taken to verify that the calibration curve reflects only the emission from Teflon and excludes other heat sources. Initial versions of the calibration heated Teflon by resting it on a copper hot plate with a temperature range of room temperature to 1400 °C. The optics viewed the Teflon from above. Since Teflon is quite transmissive in the wavelength range of interest, there was no way to verify that emission from the heat source behind the Teflon was not significantly transmitting through the Teflon and skewing the signal. To circumvent this source of error, the calibration setup is modified to look through the Teflon with no heat source behind it. Figure 2.12 shows this schematically. A 3.175 mm thick sheet of Teflon is sandwiched between two copper plates with optical access holes 5.38 mm in diameter in both copper plates. Three K-type thermocouples are drilled into the sides of the Teflon sheet and embedded close to the point where the IR detector is imaged. The Newtonian telescope images the detectors at 1:1 magnification onto the Teflon surface. Figure 2.10 shows a schematic of the calibration apparatus and optics, and Figure 2.13 shows a photo of the calibration apparatus used. Figure 2.14 shows the apparatus with the back removed highlighting the thermocouples embedded in the Teflon sample. The baseplate of the

apparatus is seated on a Micropyretics Heaters International (MHI) hotplate as shown in Figure 2.15. Two copper plates are hinged to form a triangle of reflective metal that reflects heat back at the calibration apparatus. Optical access for the Newtonian telescope is provided through a 25.4 mm conflat viewport made of Zinc Selenide (ZnSe). Figure 2.15 also shows a view of the detector optical setup. Heat is transferred through the baseplate to the front copper plate which then heats the front side of the Teflon. Data from the thermocouples and detectors are recorded by a data logger at 1 or 2 second intervals. A typical calibration takes about 10 hours. A slow heating scheme is used to increase accuracy by reducing transient thermal effects.

Possible problems with this approach include Teflon thermal expansion out of the viewing hole, resulting in emission levels that are not proportional to the temperatures measured. This becomes a limiting factor for experimental calibration and is discussed below. Temperatures above this limit are theoretically calculated using the thermographic theory developed in Section 3.1.1.

Another problem is Teflon surface condition. When the microPPT operates at low energy-to-area ratios, surface char can develop which has different emissive characteristics. While this case can be guarded against through selection of proper discharge energy, there still exists the possibility that a clean plasma exposed surface will exhibit different emissive characteristics than a virgin Teflon surface. A demonstration of the effects of the plasma on a clean surface is necessary to determine if the exposure affects the calibration curve, and thus the emissivity of the Teflon propellant. This is performed using a thruster breadboard shown in Figure 2.16. The copper electrodes are separated by 6 mm with a Teflon sheet 3.75-mm thick placed under the electrodes. Some charring develops around the edges of the electrodes during operation at 4.35 J, but the Teflon surface between the electrodes is kept clean. Two samples exposed to plasma are shown in Figure 2.17. These have been exposed to 4.35-J discharges for 500 and 1500 firings. Using this method, clean plasma exposed samples ranging from 100 pulse exposures up to 1500 pulse exposures are created for calibration comparison. These are also compared to calibrations with virgin Teflon.

2.3.3.2 Targeting

Targeting the detector assembly is a meticulous process that involves two steps. The first step uses the imaging optics to create an image of the target on the front window of the detector. This gives a rough location that is off-target only slightly in 3 dimensions. The detector is mounted on 3 dial micrometer optical mounts yielding full control of the detector positioning. Since the actual detector array is located 8 mm behind the front pane of the ZnSe dewar window, the detector is moved forward the appropriate distance. Additional control of the targeting is provided with mirror tilt on the spherical and flat mirrors.

The second stage of targeting procedure uses a targeting crosshairs consisting of two strands of 0.080-mm tungsten wire. This targeting jig is shown in Figure 2.18. The crosshairs are strung vertically and horizontally, and placed in front of the calibration jig or micro-PPT face such that the cross-point can be used for the targeting location. The horizontal filament is heated by first applying ~ 1.2 A of current. This heat source is located by the detector in DC operation by adjusting the vertical control of the flat and/or spherical mirror. Then the vertical wire is heated, and the horizontal control of the mirrors are adjusted until the signal is maximum. Finally, the forward and backward direction of the detector mount is adjusted until the signal is a maximum.

Once the optics are targeted they are locked in place. The distance from the spherical mirror to the target location is known from the optics equation, and easily measured. For multiple calibrations, an infrared emitter is placed behind the calibration jig, located appropriately at the focal point of the optics. The entire jig is then moved laterally until the emitter is located through the Teflon. For utility, a small wire is strung across the belljar marking the appropriate distance from the large spherical mirror. The calibration jig is then moved laterally along this wire until the heat signature from the emitter is found. For thruster tests, the focal point of the optics is located with targeting crosshairs as described above. The thruster face is then located behind the crosshairs such that the detector targets the point of interest.

2.3.3.3 Testing Procedure and Data Acquisition

After the calibration is targeted, the tank is closed and brought to vacuum (~ 30 μ Torr). The output signal from the infrared detectors is sent through an external pre-amplifier supplied by Fermionics. Figure 2.6 shows the basic circuitry for the pre-amplifier. The output from the pre-amplifiers is run into an Agilent HP34907A data-logger through 50 Ω terminators for impedance matching. The data-logger records the voltage from the relevant channels every 2 seconds. The hotplate is turned on and the sample is heated slowly (over 2-4 hours) to 700-800 K. The hot plate is then switched off and the sample is allowed to cool slowly back to room temperature. LabView™ code reads the thermocouple and detector voltages simultaneously throughout the process.

2.3.3.4 Experimental Resolutions

Voltage resolution for the detector is determined by measuring the standard deviation of the voltage hash on the detector channel outputs in real-time. This accounts for the bias setting on the detector and is measured to be ± 0.5 mV for minimum resolution. This resolution limit sets the minimum signal that can be measured at >0.5 mV which corresponds to a minimum resolvable temperature of about 132 °C from the calibrations discussed below. This is much worse than past testing and in large part is due to the small solid angle available in the calibration setup used. For example, testing performed by Li and Lambros⁴⁴ suggests a temperature resolution of 0.1 K for Polymethacrylate (PMMA) and Polycarbonate (PC). This resolution estimate requires explanation. Because of the non-linear nature of the calibration curves, the optimal temperature response range is expected to be at the peak temperatures observed. At 800 K, the voltage resolution is ± 11 K.

Spatial resolution of the detector is defined by the active area of the detector (6.4×10^{-9} m²) as imaged 1:1 on the face of the micro-PPT. Figure 2.19 shows the detector image to scale. For these experiments this means that only a tiny portion of the fuel face is being measured per detector. A single 80 μ m x 80 μ m detector is used to characterize the operation of the diagnostic. For each detector of this size, it is unlikely that there will be meaningful temperature gradients across the size of the active area. However, when measurements are made on an operating thruster, the presence of arc

spoking may mean that the measured temperature cannot be extrapolated to the rest of the fuel face.

2.3.4 Thruster Apparatus and Method

2.3.4.1 Thruster Setup

The micro-PPT circuitry layout is shown in Figure 2.2. A 2.95 μF capacitor is charged to 1-10 J. Discharge initiation is provided by a spark plug placed in front of and below the thruster face. The sparkplug is a small version of a two-electrode microPPT operated by a sparkgap circuit. The plug is passed through an insulated feedthrough into the tank and positioned ~ 2.5 cm from the fuel face without blocking the view of the optics. Figure 2.20 shows the typical sparkplug location for testing. Once the plug has provided seed plasma, the main discharge is initiated and current passes between the electrodes. A portion of the ablated mass is accelerated electromagnetically, and as the plasma cools, it is assumed that the resistance increases linearly from 25 $\text{m}\Omega$ to 60 $\text{m}\Omega$ until the current reversal ceases. Current reversal typically occurs over about 20-25 μs with inductance estimated around 190 nH. The resistance and inductance estimates are determined by fitting the current measured by a Rogowski coil and are discussed in Section 4.1.

2.3.4.2 Plume Measurements

To experimentally characterize the emission from the plasma and neutral vapor above the fuel face, IR measurements are taken with the detector optical cone targeted to a point in front of the central electrode and traversing across the exit plane of the thruster. The view cone in this orientation does not intersect the surface of the microPPT. Figure 2.21a shows the cone apex targeted schematically to illustrate this configuration. By measuring emission from the plasma and neutral vapors without a heated background, the contribution of the plasma and neutral vapor can be characterized. If the plume contribution ends when the current pulse ends, then the surface can be measured after that time without emissive interference from the exhaust. To characterize this, measurements across the fuel face are made with the focal point of the optics located at 1 mm, 3 mm, 5 mm, and 7 mm in front of the fuel face. When these measurements are compared to fuel

face measurements, an assessment concerning optimal viewing time during the pulse is made. Repeated tests have shown that after the current reversal stops, there is no measurable detector signal. These results will be discussed below, but here it is sufficient to state that after the current pulse ends, plasma and vapor emission contribution also ends and a clear surface measurement can be obtained.

2.3.4.3 Thruster Measurements

Figure 2.21b shows the target location for a typical thruster measurement using a single detector. In this case, the targeting is performed as described in Section 2.3.3.2. As discussed above, after the current pulse has ended surface temperature measurements are able to characterize the cooling curve of the propellant. Propellant surface temperature is measured in real-time for single pulses. The input signal from the Rogowski coil on the thruster is used as a trigger for the start of data acquisition. For the single detector element, a point is selected halfway between the electrodes and multiple firings are recorded. Data acquisition and reduction are discussed in the next sub-section, but first a small discussion of experimental requirements for accurate measurements is required.

The ability of the diagnostic to determine the true surface temperature depends on a number of conditions being met. First, the optics must be the same for thruster measurements as they are for calibration. If this is not met, then the calibration will not apply to the thruster measurement and a systematic error is created. This error is avoided in these experiments by locking the optics after calibration and locating the focal point with the targeting wires discussed above. The thruster face is then positioned behind the targeting wires.

The second condition is that the calibration surface must have the same roughness as the thruster surface. For this reason, calibrations were performed with Teflon that had been exposed to the same plasma conditions found in thruster operation. The calibration procedure is discussed in Section 2.3.3.1. To match the calibration, the thruster must operate in a regime where charring does not occur. If charring does occur, it must be verified both before and after testing that the targeting location covers an area that is char-free. Figure 2.22 shows the difference between charred and uncharred operation for

1000 shots in a. and 250 shots in b. From this picture it is apparent that a significant difference in emissivity between clean Teflon and charred Teflon exists.

2.3.4.4 Data Acquisition and Reduction

During thruster testing data is taken by a Tektronix 460A oscilloscope with input impedance set to $50\ \Omega$ to match the calibration measurements. This data is recorded by LabView directly from the oscilloscope through a GPIB connection to a computer. The file format is accessible to MS Excel or any text editor. Data taken on an operating thruster can experience some noise issues. The source of this noise is electromagnetic and is discussed below. The noise issue is addressed through either filtering or smoothing. A low-pass digital filter is applied to the data to omit noise with frequencies above 300 kHz. This digital filter is a zero phase-shift Butterworth filter applied through MatLab.⁴⁵ Figure 2.23 shows a comparison of an unfiltered data file (yellow) with filtering at 700 kHz and 300 kHz cutoff frequencies. The 700 and 300 kHz curves follow the original data signal. 300 kHz is the lowest cutoff frequency used for these data. The second method is an 11-point smoothing routine that accomplishes some noise reduction without phase-shifting the data.

2.4 Interferometry

The interferometry experiments here used a 6.35 mm diameter microPPT with a 0.417 μF capacitor. These experiments are conducted using a pulse energy of 6 J unless otherwise noted. For statistical purposes, a minimum of 20 pulses is used to characterize the uncertainties.

2.4.1 Setup

The interferometer setup (Figure 2.24) consists of two lasers, an infrared 1152-nm and a blue 488-nm. Each of these are split into separate beams in a Bragg Cell that induces an acousto-optic modulation at 40 MHz in higher order beams. The zeroth order beam is unchanged in frequency. This modulation process involves passing the light through a crystal and acoustically vibrating the crystal such that a refractive index wave is created. This causes the crystal to act as a sinusoidal grating. A laser entering this grating will be diffracted into several order beams. The zeroth order beam is selected as

the scene beam and a first order beam becomes the reference beam. This is chosen so that modifying the power to the Bragg cell will serve to increase the scene beam intensity relative to the reference beam. Generally, through large numbers of optics the scene beam is much lower in intensity at the detector than the reference beam which is confined to the optics table outside the tank.

After the Bragg cell, the beams are separated by the diffraction angle. This is a function of the acoustic frequency, acoustic velocity, and optical wavelength and is about 5 degrees in this application. In order to separate the beams, about a meter of path length is provided before combining the two frequencies and deflecting the combined scene beam into the vacuum tank. The scene beam is sent into the tank through a BK7 glass window and reflected off a single mirror in tank. The scene beam passes directly across the exit plane of the thruster, then back through the window. The beam diameter is 6 mm. It is then sent through two beamsplitters and recombined with the reference beams. Each reference beam is matched almost exactly in path length from the Bragg cell to the recombining beamsplitter. This matching must be within 10% of the coherence length of the laser. The coherence length is the maximum path length difference over which the 2 beams will interfere. For the Argon-ion laser, that coherence length is 10 cm and the path lengths are matched to less than 1 mm through the use of rail mounted micrometer mounts. For the HeNe, the coherence length is 30 cm. The recombining beamsplitters are wavelength-tuned to ensure that equal amounts of scene and reference beam are passed to the detection equipment. Recombination at the beamsplitter requires accurate matching of the vectors of the beams. Both beams must match at the beamsplitter surface and follow exactly the same direction. Allowing for a long path between the beamsplitter and the photodetector is helpful in ensuring accurate alignment. Following recombination at the beamsplitter, the recombined beam passes through a line filter matching the appropriate wavelength, and an achromatic lens to focus onto the detector element. If the signal is still too intense for the detector, a dual polarizer is used to lower the light intensity incident on the detector. Spatial resolution is roughly the beam diameter at the thruster crossing (~6 mm).

The interferometer is sensitive to several phenomena involved in the thruster operation. The phase change in the interferometer scene beam at the detector can be written as¹⁸

$$\phi(t) = \phi_e(t) + \phi_n(t) + \phi_{PL}(t) \quad (3)$$

where the first term represents phase change due to the plasma electron density, the second term neutral density, and the third term physical changes in the path length difference between the two beams. The phase shift due to the electron and neutral densities can be written (MKS-radians)¹⁶

$$\phi_e(t) = -2.8 \times 10^{-15} \lambda \int n_e dl \quad (4)$$

$$\phi_n(t) = \frac{3.9 \times 10^{-29}}{\lambda} \int n_n dl \quad (5)$$

where λ is the laser wavelength (m), n_e and n_n are the densities (m^{-3}), and the integral is performed over a characteristic path length through the probed region. The interferometer measures a line-averaged density, and requires assumptions concerning scale lengths and symmetry to reduce the measurement to a local density. These include the definition of a characteristic path length over which the plasma density is assumed constant. The final term in equation 3 includes changes in the path length which are dominated by vibrations physically moving the optic components and air currents affecting local density and temperature gradients within the path of the reference and scene beams. This can be written as

$$\phi_{PL}(t) = \frac{2\pi\Delta l}{\lambda} \quad (6)$$

The Δl in Eqn. 6 represents the effective increase in optical path length for all of the environmental influences (vibration, air density, air temperature, and gradients). The dominating effect here is the vibrational differences between the optics table (where the laser and detection equipment are located) and the in-tank optics table supporting the in-tank mirror. The $1/\lambda$ dependence in Eqn. 6 is the same for neutrals in Eqn. 5.

A second wavelength can be used to separate electron and neutral densities during the discharge. The separation is accomplished by integrating Eqns. 4 and 5 along the exposed path length (the thruster diameter is used here) and solving for

$$n_e = \frac{\Delta\phi_r \lambda_r - \Delta\phi_b \lambda_b}{-2.8 * 10^{-15} Nl [\lambda_r^2 - \lambda_b^2]} \quad (7)$$

$$n_n = \frac{\frac{\Delta\phi_r}{\lambda_r} - \frac{\Delta\phi_b}{\lambda_b}}{3.9 * 10^{-29} Nl \left[\frac{1}{\lambda_r^2} - \frac{1}{\lambda_b^2} \right]} \quad (8)$$

where λ_r and λ_b are the infrared and blue laser wavelengths (m) respectively, $\Delta\phi_r$ and $\Delta\phi_b$ are the measured phase shifts for the infrared and blue lasers (radians), N is the number of passes through the plasma experienced by the scene beams, and l is the characteristic length (m).

For two-color density measurements made here, the beams are both focused onto the detector active area using long focal length lenses. The effect of this is to significantly reduce uncertainty associated with the beam dispersion over large path lengths. Because the path lengths can reach 5 m in length, the beam diameter can be over 1 cm at the detector location. The detector active area is 0.5 mm². It is possible for the two beam colors to be measuring two different locations within the thruster plume. By focusing onto the active area, a much larger portion of the beam diameter is sampled and both detectors are forced to sample similar areas of the plume.

Two-color measurements can be used to determine the ionization fraction during the arc. The assumptions of complete dissociation and single ionization are made. Considering that the electron temperature is probably no more than 2 eV, this is probably a good assumption. The ionization fraction is then calculated by

$$\alpha = \frac{n_e}{n_e + n_n} \quad (9)$$

where the single ionization assumption translates to $n_e = n_i$.

For the recession measurements, only electron density is measured using the 1152 nm laser. Figure 2.26 shows the experimental layout for the recession measurements. A

control case with the fuel flush against the laser is measured (top case). The propellant is then recessed into the tube a distance of 50 mm and the laser is passed across the exit plane. Figure 2.26 shows the recessed case in the middle of the three cases. The final case shows the propellant flush with the thruster exit plane, but the exit plane is removed from the laser by 50 mm.

2.4.2 Data Acquisition

The data acquisition system for the interferometer consists of Analog Modules photodiodes with amplifiers and a demodulating circuit. The demodulating circuit includes two mixers (Mini-circuits model ZAD-1), a 90° phase shifter (model ZCSQ-2-50), a power splitter (model ZSC-2-1), and low-pass (<10.7 MHz) and band-pass (40 MHz) filters. This circuit separates the phase shift signal into sine and cosine with information from the Bragg cell. These signals are then sent to a Tektronix TDS 460A oscilloscope to be captured by a computer. Figure 2.25 demonstrates this arrangement.

At the computer the data is reduced using two MS-DOS Fortran codes written by Spanjers. The first, called *tran40*,⁵⁰ takes the output signal from the demodulating circuit and puts it into sine and cosine data files for quadrature analysis. This program can handle either the two signals from a single wavelength interferometer or four signals from a 2-color interferometer. After the signal is formatted by the *tran* program, a program called *tquad40e*⁵⁰ is used to perform numerical quadrature on the output signals. There is an 11 point smoothing process built into *tquad40e* to remove some of the extraneous high frequency noise. The reduced data are sent to a single file in ASCII format.

For multiple thruster firings required by standard testing, each shot is reduced and a program called *stat40*⁵⁰ is used to evaluate 20 to 40 data shots and calculate the average and positive and negative standard deviations. This code yields a single file in ASCII format and is used solely to reduce data reduction time.

2.5 Other Diagnostics and Sensors

2.5.1 Standard Thruster Diagnostics

Thruster current is measured using a self-integrating Rogowski coil from Ion Physics Corporation.⁵¹ The model used is CM-1-MG which can handle up to 50,000 A. For the sparkplug current, model CM-10-MG is used. High voltage is measured with a Tektronix P6015A passive high-voltage 1000:1 probe.

Mass loss is measured using a Mettler Toledo AX105 Delta Range scale. This scale has a sensitivity of ± 0.1 mg. Pre-test mass is measured, then testing is performed with the total number of pulses recorded. After the test, post-test mass is measured and the total mass lost is divided by the total number of pulses to give a time-averaged mass per pulse. Note that this does not discriminate between Teflon and electrode mass loss.

2.5.2 DICAM II

The DICAM II is a high-speed charge coupled device (CCD) camera capable of gate times in the nanoseconds with variable gain and delay. Made by the Cooke Corporation,³⁸ this camera is used to image the face of the micro-PPT on the microsecond time-scale to assess plasma emission in the visible portion of the spectrum.

2.5.3 Recession Cone Profiling

It is possible to measure the cumulative effects of the ablation process by measuring the profile of the propellant cone as it recedes into the tube of the outer electrode. A thruster is pulsed in a steady operating mode at 1 Hz, 6 J for 6 hours. One side of the thruster is soaked in nitric acid, which removes the copper tubing while leaving the Teflon intact. With half of the Teflon tube exposed, the Teflon is shaved away with a razor exposing the conical recession pattern shown in Figure 2.27. Reference lengths are measured from the copper tube lip back to the closest point of remaining Teflon and across the Teflon diameter. This yields the axes shown in Figure 2.27. The DataThief⁵² program is used to pick off the curve of the recession in a high-resolution picture.

2.6 Chapter 2 Figures

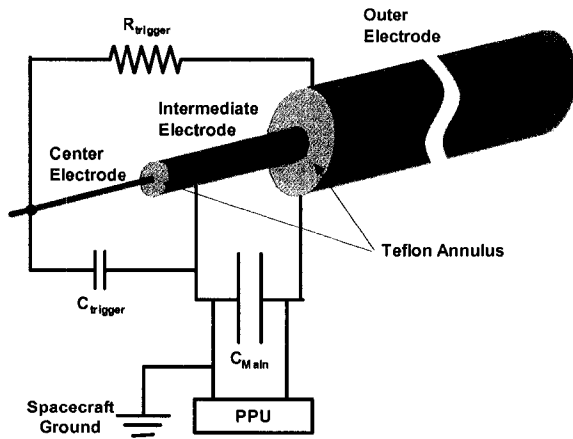


Figure 2.1: Three-electrode Micro-PPT layout.

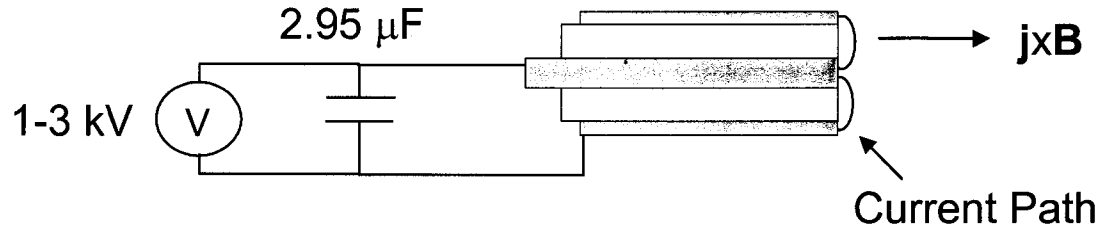


Figure 2.2: Typical micro-PPT circuit with thrust direction shown.

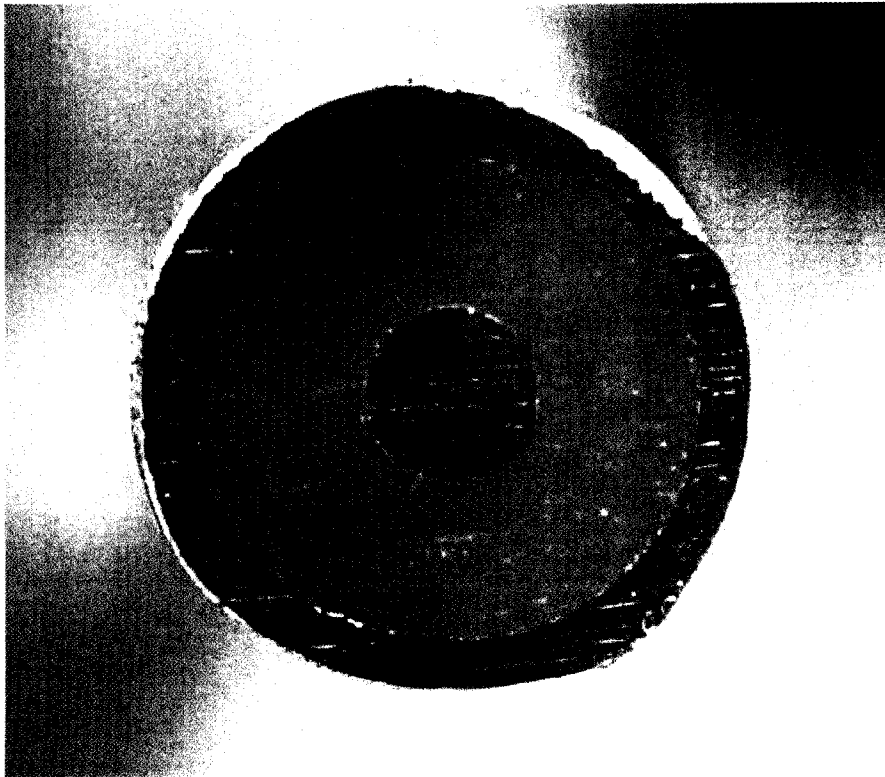


Figure 2.3: An unfired MicroPPT face. Outer diameter = 6.35 mm.

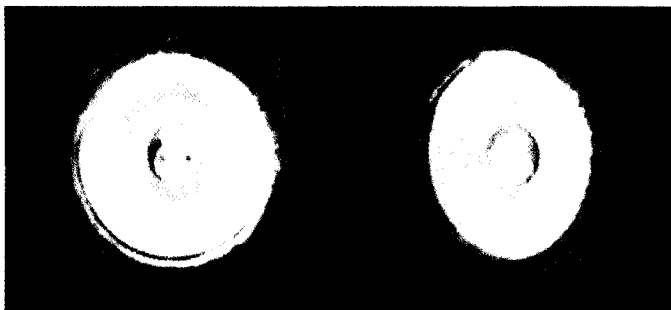


Figure 2.4: A two-electrode MicroPPT that has been fired at 7.5 J, 1 Hz for 1 hour.

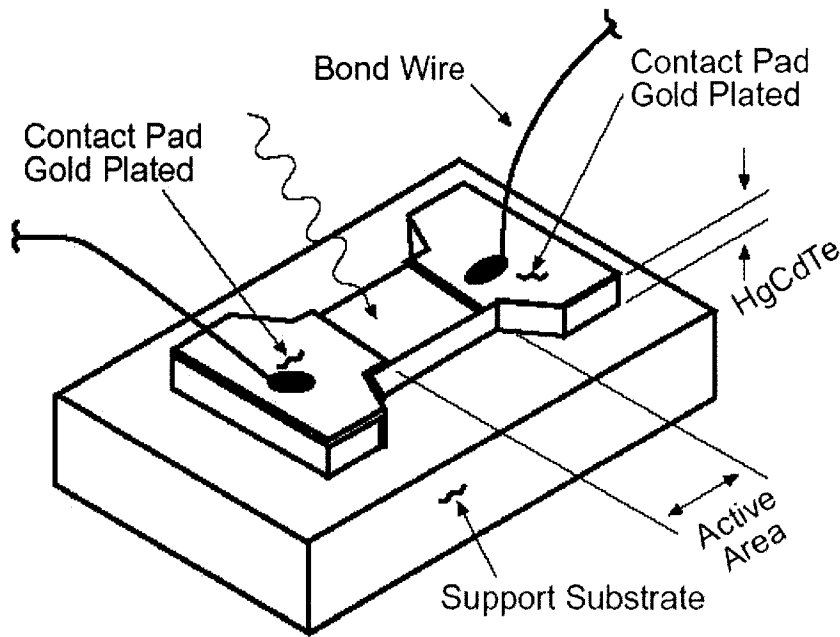


Figure 2.5: Schematic of an HgCdTe detector.⁵³

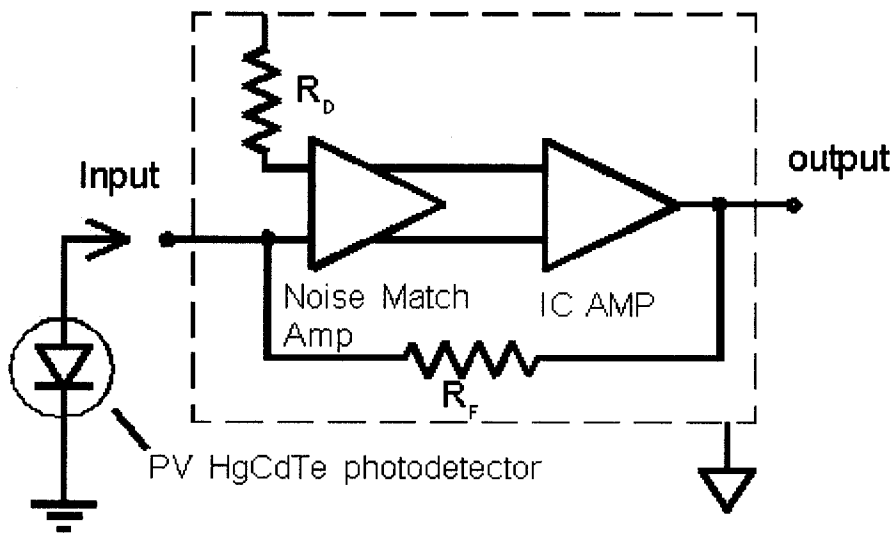


Figure 2.6: Typical circuitry for HgCdTe detectors.⁴⁹

Typical Detectivity vs. Wavelength

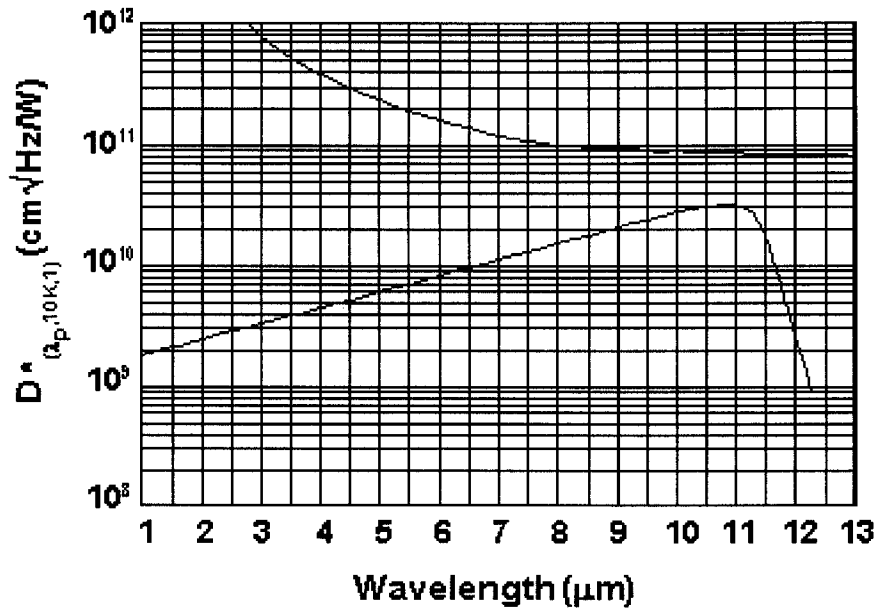


Figure 2.7: HgCdTe detector responsivity.⁴⁹

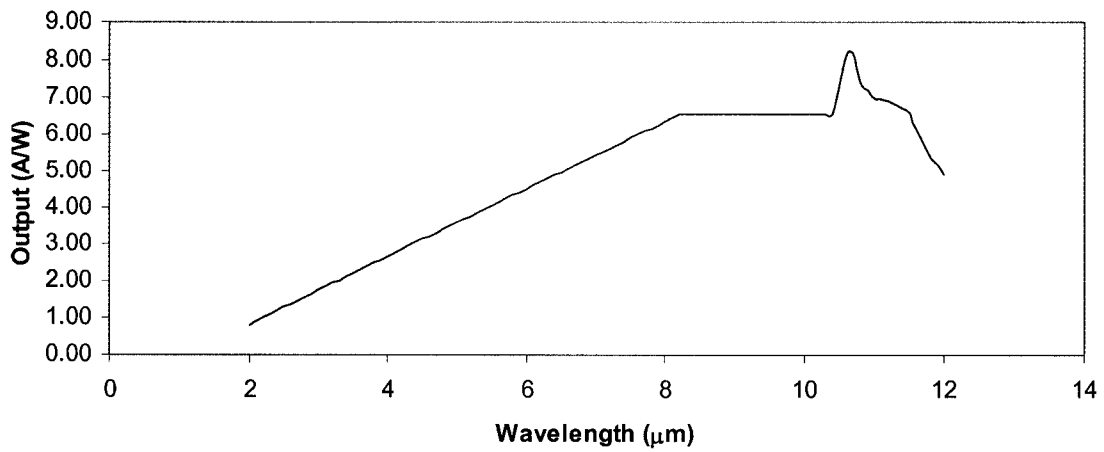


Figure 2.8: Wavelength dependent detector responsivity.

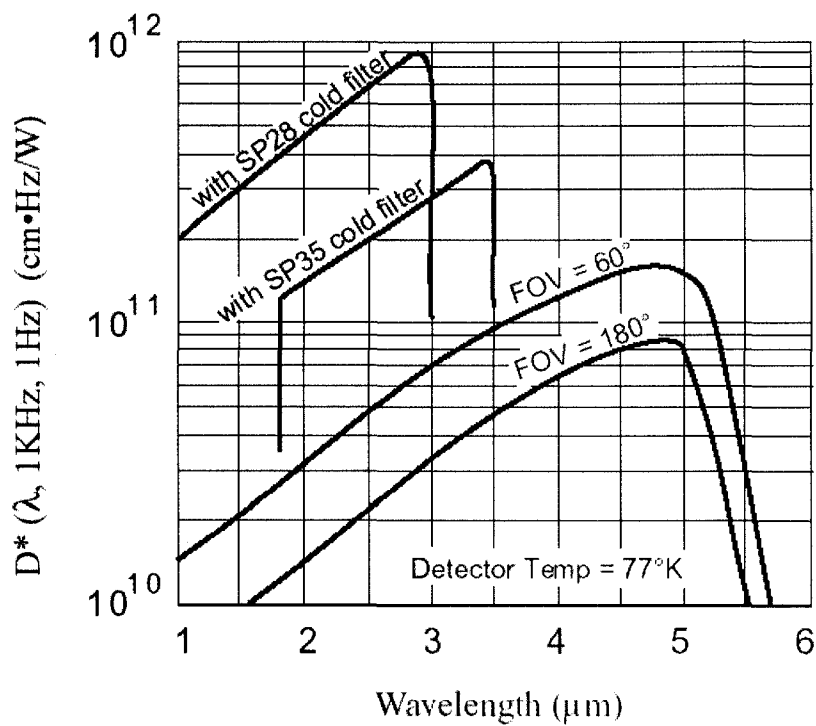


Figure 2.9: Responsivity curves for possible InSb detectors.⁵³

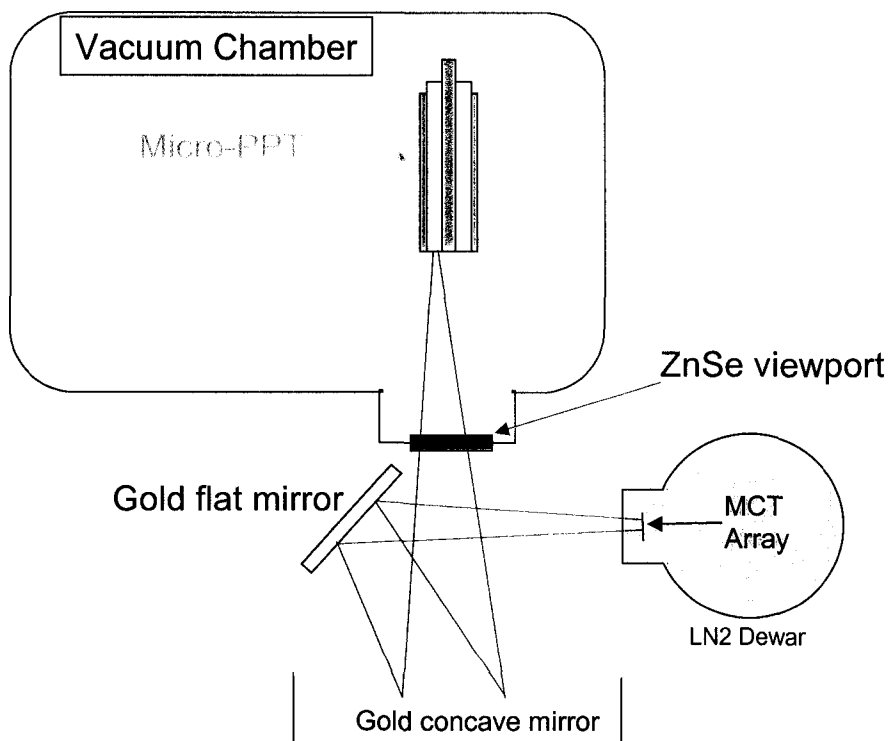


Figure 2.10: IR detector experimental layout.

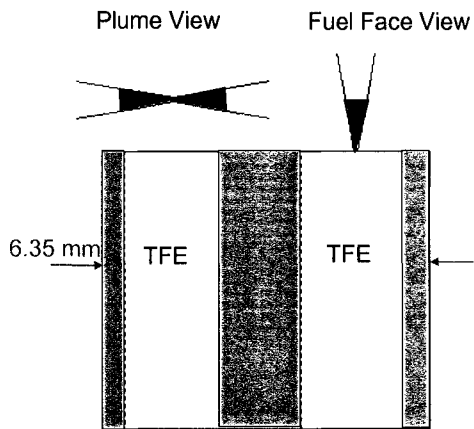


Figure 2.11: Optical depth and measurement areas shown for facial measurement and plume measurement.

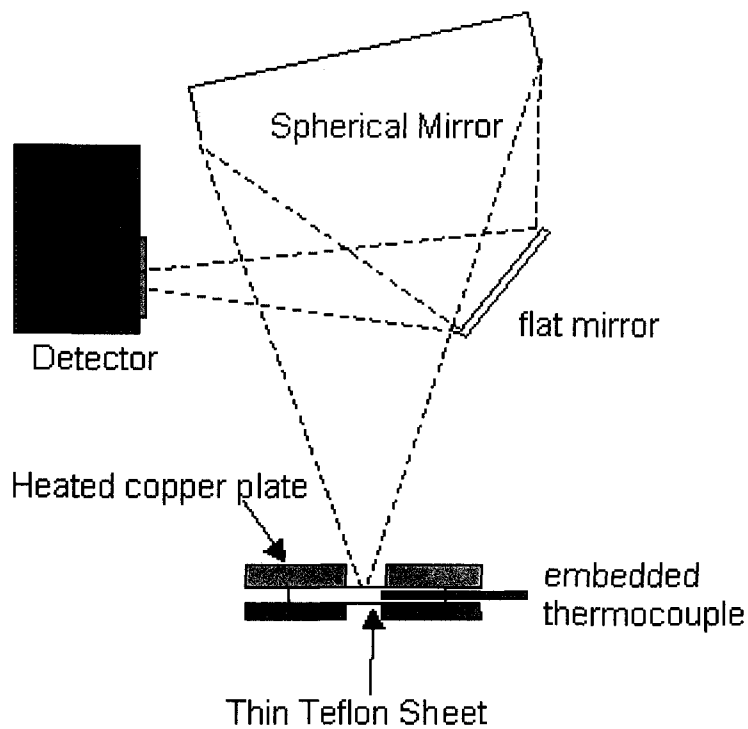


Figure 2.12: Pancake calibration provides Teflon heating with no rear heat source.

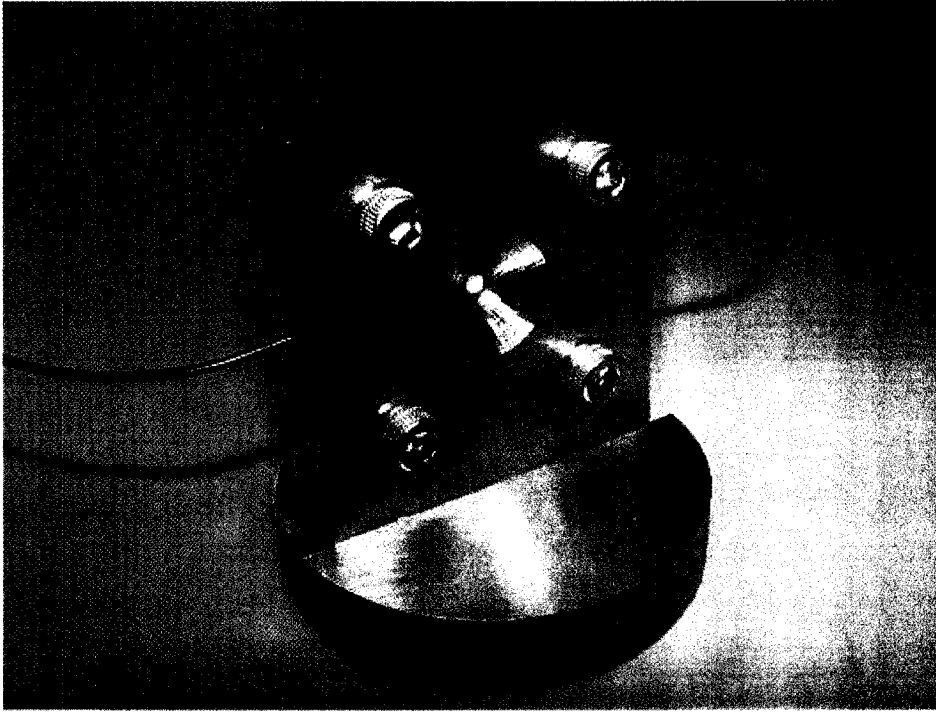


Figure 2.13: 1/8th inch thick Teflon is sandwiched between copper plates in the calibration jig. Thermocouples are embedded in the sides to approximately the optical viewing location.

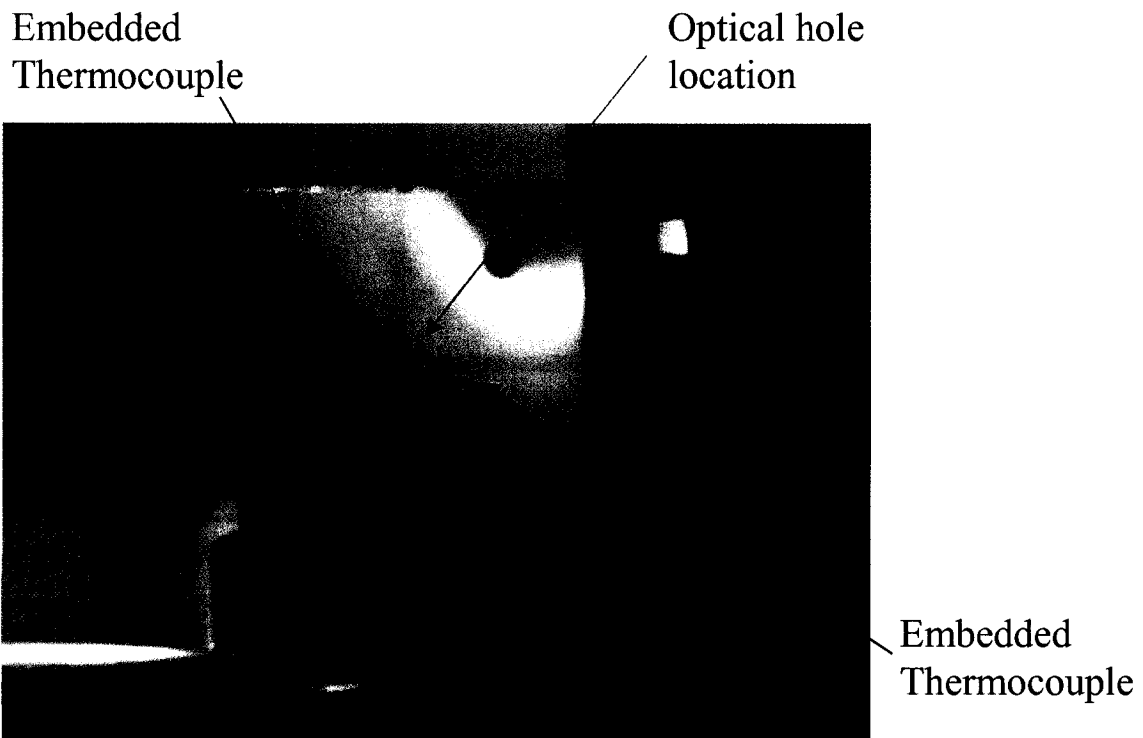


Figure 2.14: Thermocouples are embedded in the Teflon close to the area where optical viewing occurs.

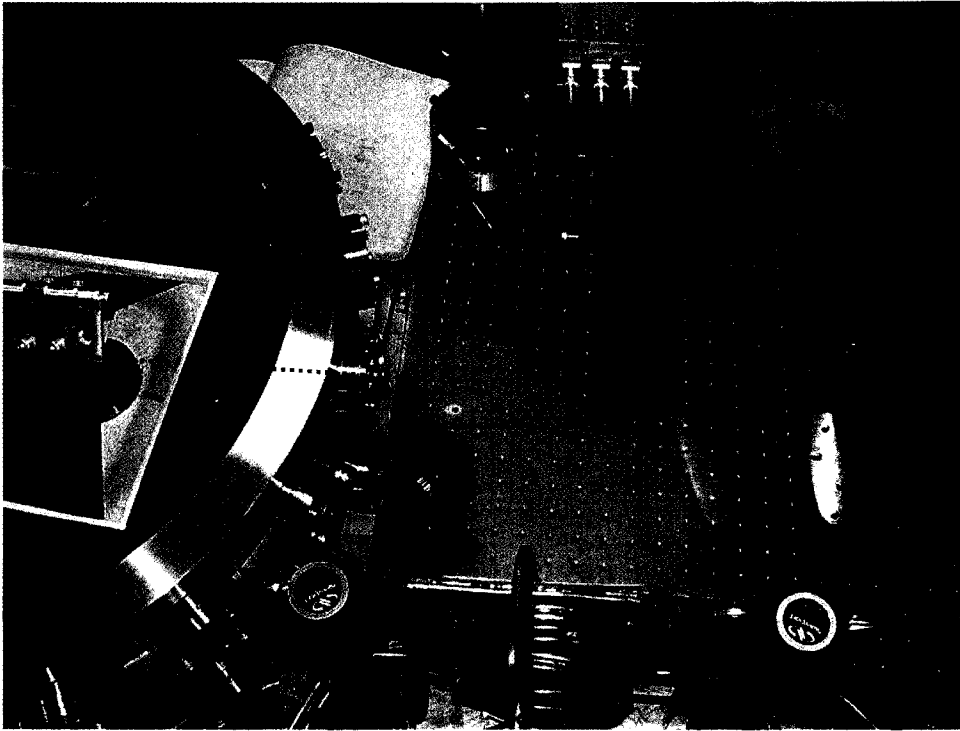


Figure 2.15: The calibration jig sits on the hotplate and is viewed horizontally through a ZnSe window. The dotted red line shows the optic path.



Figure 2.16: Breadboard thruster for creating plasma exposed calibration samples.

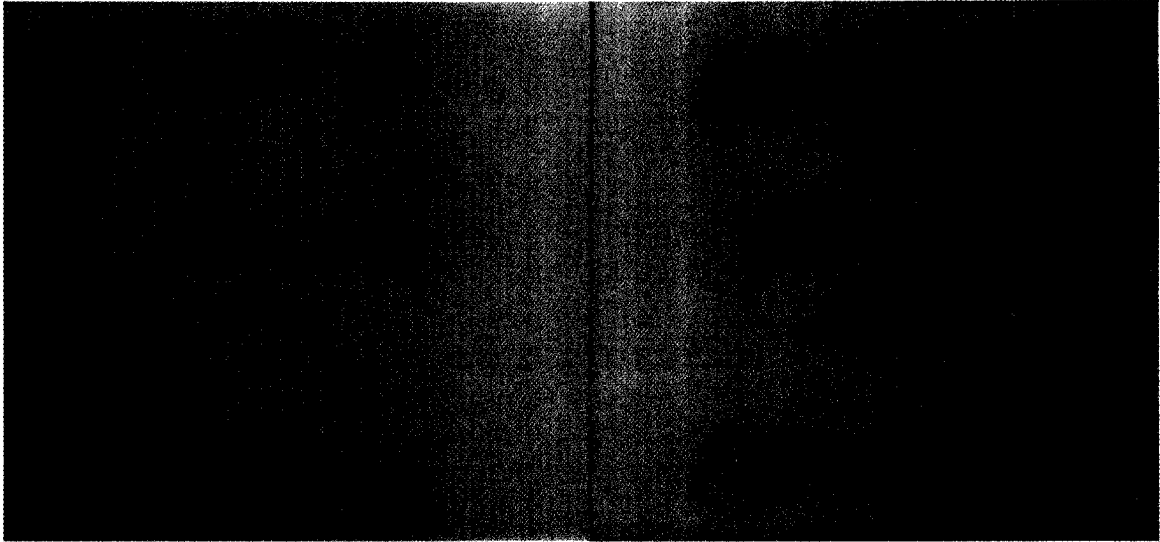


Figure 2.17: Plasma exposed samples for 500 and 1500 firings.

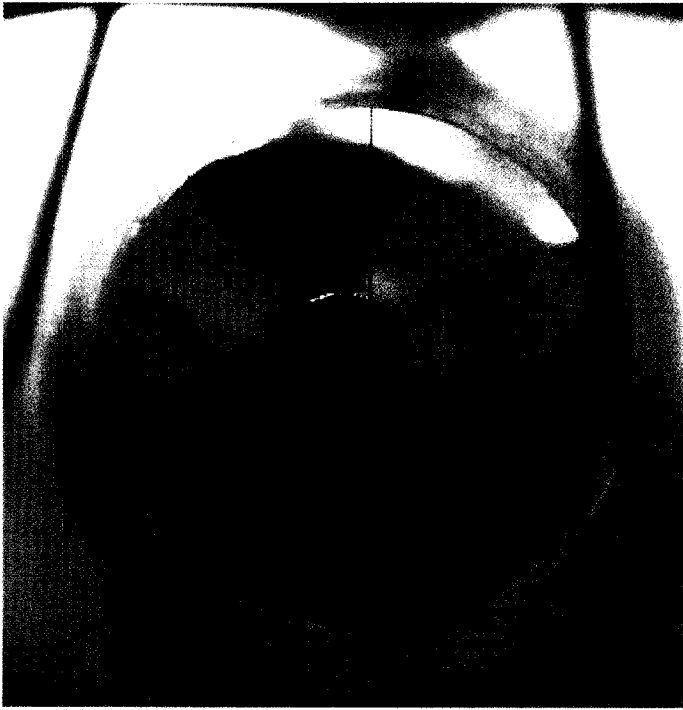


Figure 2.18: Targeting crosshairs assembled on thruster face.

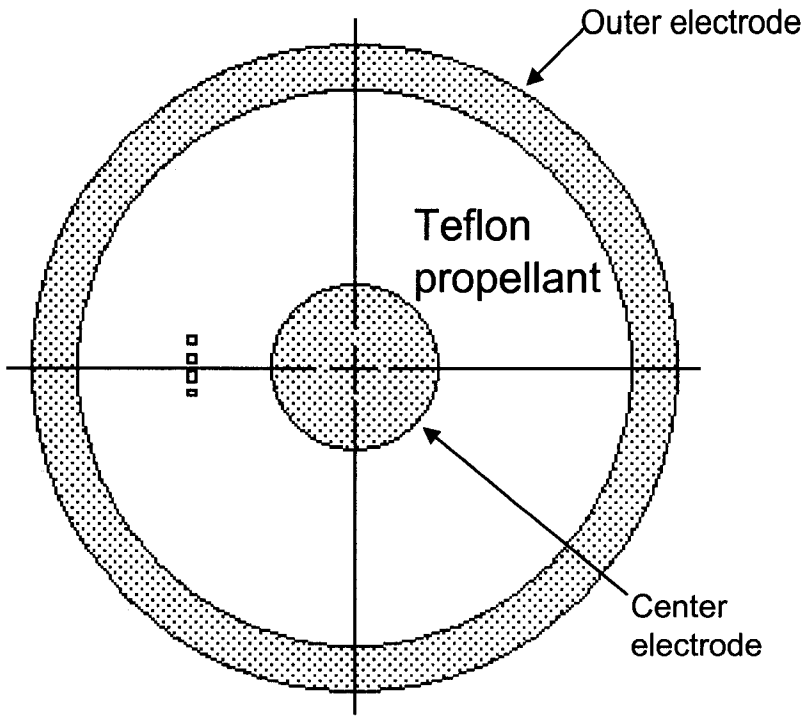


Figure 2.19: Four HgCdTe detectors from the assembly used are shown to scale on the face of a micro-PPT illustrating available spatial resolution with this instrument.

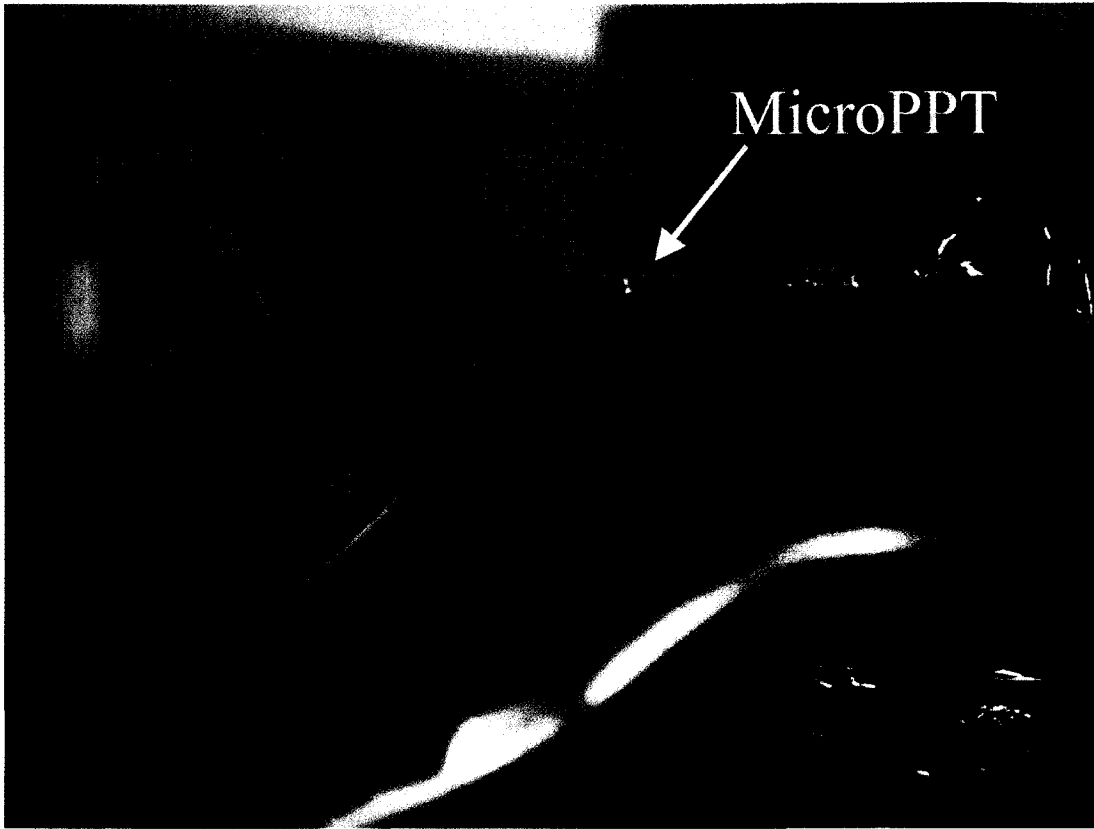
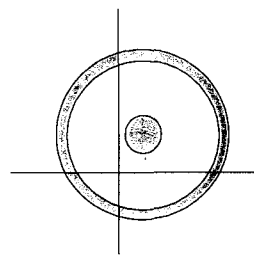
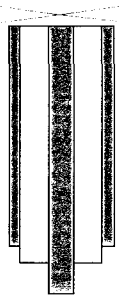


Figure 2.20: The sparkplug sits more than an inch from the exit plane of the thruster and is off-axis to allow unhindered optical probing of the fuel face.

a. Plume Measurement b. Surface Measurement

viewable cone



target location

Figure 2.21: Schematic of the (a.) viewable cone for the Plume measurement technique and (b.) target location for the Surface measurement technique.

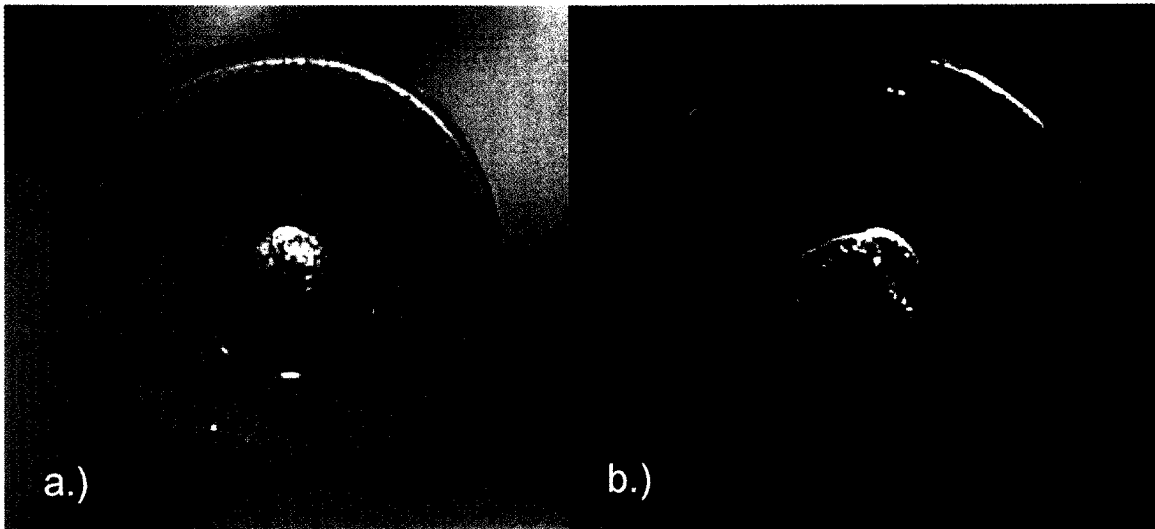


Figure 2.22: a.) 1000 shots with uncharred operation and b.) ~250 shots with charred operation. Charring is typical in low-energy thruster operation.

Comparison of cutoff frequency at 300 kHz and 700 kHz

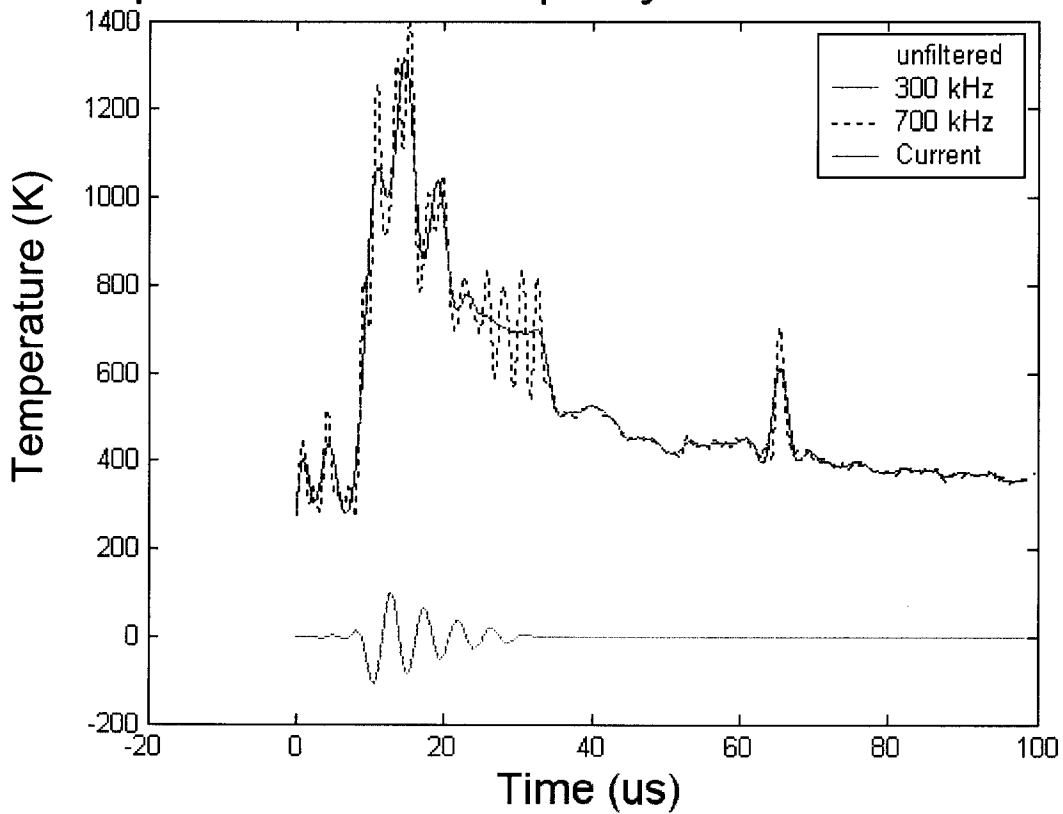


Figure 2.23: Comparison of filtering levels for the zero phase shift low pass filter used. The green trace shows the current pulse.

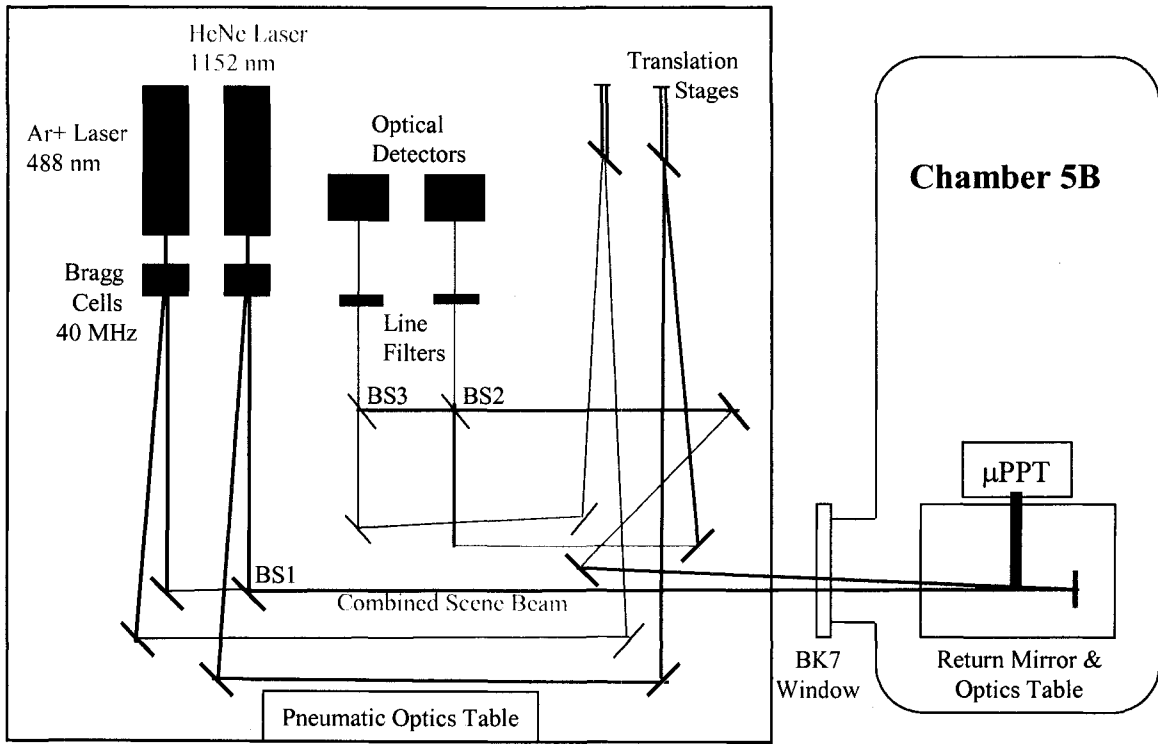


Figure 2.24: Two-color interferometer layout.

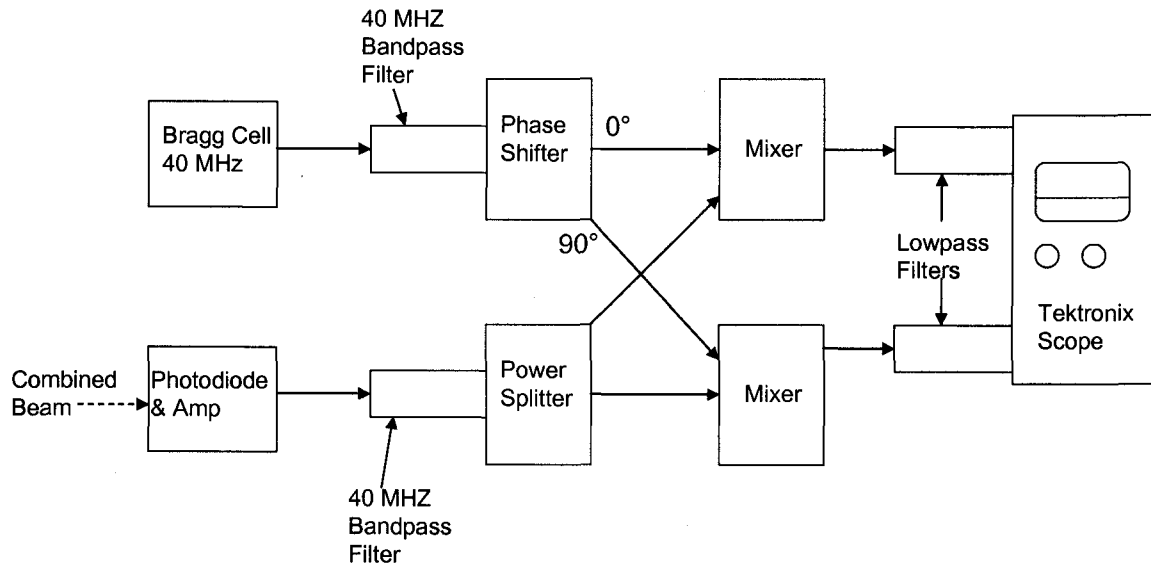


Figure 2.25: Interferometer post detection processing schematic.

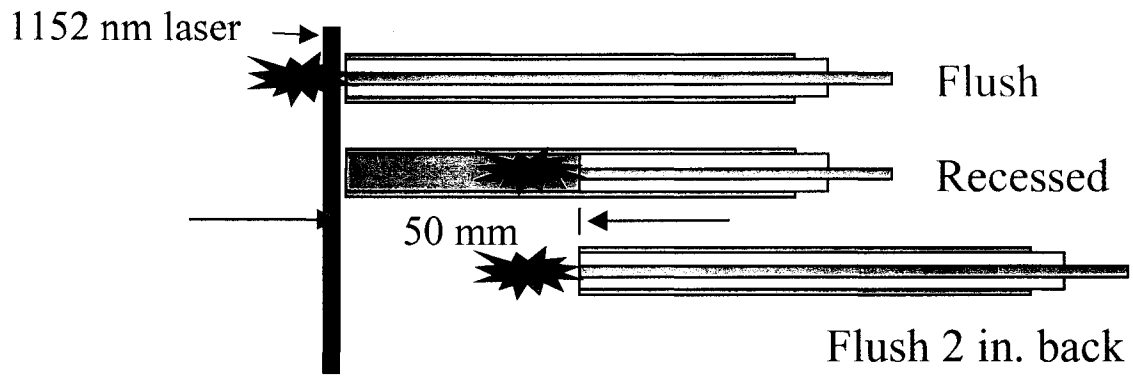


Figure 2.26: For two-color interferometry, the laser passes directly in front of the fuel as in the flush case. For recession interferometry, all three cases are measured for comparison.

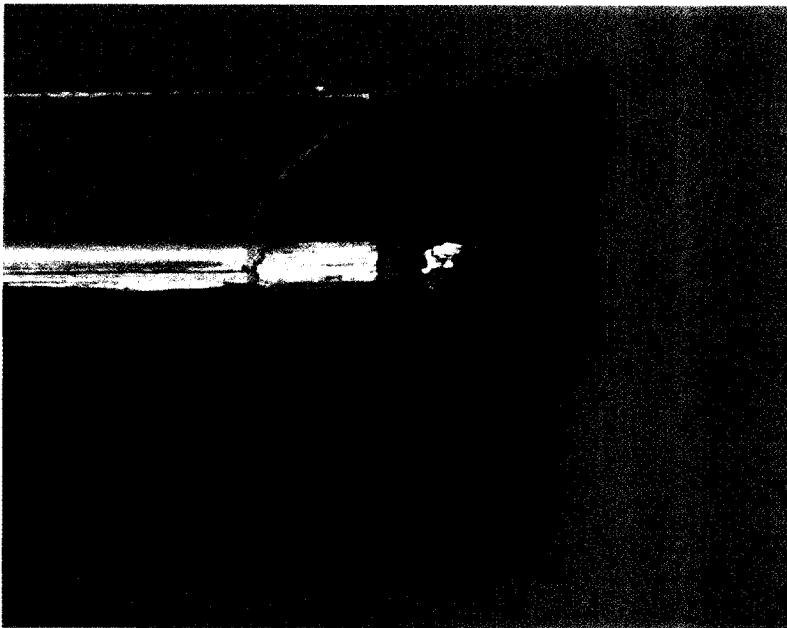


Figure 2.27: Typical ablation profile: 6 J, 6 hours, 1 Hz.

3. Theory

3.1 Infrared Thermography

3.1.1 Material Emission and Theory

The key principle for this diagnostic is that all materials above absolute zero temperature emit radiation. The distribution of that radiation depends on the temperature of the body and is described by the Planck function⁵⁴

$$P_E = \frac{C_1}{\lambda^5 \left(e^{\frac{C_2}{\lambda T}} - 1 \right)} \quad (10)$$

where C_1 is $3.742 \times 10^8 \text{ W}\cdot\mu\text{m}^4/\text{m}^2$, C_2 is $1.439 \times 10^4 \mu\text{m}\cdot\text{K}$, λ is the radiation wavelength (μm), and T is the material temperature (K). This equation yields spectral emissive power for a blackbody. Traces of this power output at several relevant temperatures are shown in Figure 3.1.

In understanding the source of Teflon emission it is useful to predict an expected detector output from calibration with a Teflon sample. The starting point is to determine what the expected emission from Teflon looks like. Figure 3.2 shows the transmissivity of a thin film of Teflon.⁵⁵ This transmissivity is determined using IR spectroscopy, where radiation of the appropriate wavelengths is exposed to a thin film (0.005 mm) and a spectral intensity drop is measured through the film. For any material,⁵⁶

$$\rho + \alpha + \tau = 1 \quad (11)$$

where ρ is the reflectivity, α is the absorptivity, and τ is the transmissivity. Areas of high absorption correspond to areas of high emission since energy is absorbed and emitted equally by the stretching and bending modes of the C-F bonds in the Teflon molecules (Figure 3.3). The reflectivity of Teflon in the wavelengths of interest is unknown, but from Eqn. 11 it can be assumed that any reflectivity will decrease the amount of emission. Therefore, if the reflectivity is not included in any prediction of the detector response, an overprediction of the total emission should be expected. We proceed with

this overprediction expected in the final estimates. Eliminating the reflectivity and setting absorptivity equal to emissivity (ϵ) converts Eqn. 11 to

$$\epsilon = 1 - \tau \quad (12)$$

which allows an estimate of the wavelength dependent emissivity for Teflon. An emissivity estimate is shown in Figure 3.4. Using this estimate, an expected spectral emissive power for the 2-12 μm range can be calculated.

A first order determination of the expected total emission and response can be obtained by combining the Planck distribution for Teflon with the wavelength dependent detector responsivity and integrating over the range of wavelengths (2-12 μm). This gives an expected detector current output calculated by

$$I_E = \int D^* R_p \epsilon_\lambda P_E d\lambda \quad (13)$$

where D^* is the normalized wavelength dependent responsivity, R_p is the peak responsivity, ϵ_λ is the wavelength dependent emissivity, and P_E is the spectral emissive power calculated by Eqn.10.

Equation 10 yields the total power emitted from the specimen, however, only a fraction of that power is observed by the detector. Assuming 1:1 imaging, with a detector view angle limited by the flat mirror (50.8 mm DIA) the half angle of the viewable cone is 3.05° (Figure 3.5). The angular area of a hemisphere is 2π , and the angular area of a small circle of angular radius θ is given by⁵⁷

$$\Omega_c = 2\pi(1 - \cos\theta) \quad (14)$$

The ratio of the circle solid angle to the hemispherical solid angle is simply $(1 - \cos\theta)$, which is the ratio of the power received to the power emitted.

For a realistic calibration prediction, the effect of the optics on total intensity is considered. The Newtonian telescope uses two gold mirrors with a reflectivity of $\sim 99\%$

in the relevant wavelength range. Additionally, since the calibration will be performed at vacuum, the transmissivity of the viewport material must be included. The materials considered are Zinc Selenide (ZnSe) and Germanium (Ge) because the transmission properties allow decent transmission in the wavelengths of interest. Figure 3.6 a. and b. show the transmissivity of Ge and ZnSe respectively.⁵⁸ The window on the LN2 dewar is ZnSe provided by the manufacturer. The optical viewport on the vacuum chamber is ZnSe, chosen to maximize the total emission in the IR. The full optical response is defined as a constant, k_o , which is the multiplied value of all mirror reflectivities and window transmissivities. The value of k_o for this experiment is 0.48. Multiplication of the ultimate detector output by this constant corrects for losses in the optical system.

Since the optics provide an imaging system, the detector is operated with a 1:1 magnification of the detector element onto the surface of the specimen. Only emission coming from within the viewable cone (the apex of which is the detector image) can be sensed. The detector active area limits the total number of photons collected from the optics, therefore the active area, A , must be taken into account. Each detector is a square with $80 \mu\text{m}$ to a side for an area of $6.4 \times 10^{-9} \text{ m}^2$.

Finally, the amplifier has a transimpedance factor ($V_{\text{out}}/I_{\text{in}}$), of 20000 V/A. This is the gain of the pre-amplifier and is denoted here as G . The combined end result for estimating detector voltage out becomes

$$V = k_o G A (1 - \cos\theta) \int_{\lambda} D^* R_p \epsilon_{\lambda} P_e d\lambda \quad (15)$$

Using Eqn. 15 and remembering the omission of Teflon reflectivity in the estimation of the emissivity, a calculation for the output voltage from this detector measuring heated Teflon can be made. Figure 3.7 shows this calculation along with the predicted black body output voltage against temperatures expected in typical micro-PPT operation. Since we expect an overprediction for the Teflon response, a calibration curve must be obtained to demonstrate the deleterious effects of the assumptions up to this point. This process is discussed in section 2.3.3, but the predictions shown indicate the expected trends in this measurement and likely temperature resolution.

3.1.2 Teflon Properties

The properties of Teflon are discussed here with regards to material behavior during calibration and experiments. The melt temperatures and viscosity can pose physical limitations during the calibration procedures. Also, thermal conduction between detector elements is discussed as well as depth of heat transfer into the material. The radiation properties including transmissivity and emissivity affect the operation and validity of the infrared diagnostic. Finally, the radiation contribution of plasma and neutral vapors is discussed in terms of photon transmission and optical depth.

3.1.2.1 Melt and Viscosity

During the calibration procedure, a Teflon sheet is raised to high temperatures over several hours. This can be a source of concern as melting and flowing out of the calibration device can change the viewing angle of the surface as well as surface roughness. A theoretical treatment of this is very limiting, since physical data on Teflon above 380°C is not available. High-temperature behavior is discussed here, but since the temperatures experienced in calibration are much higher than available data, only experimental testing can determine the physical limitations that will be encountered.

Teflon has a first melt point of 342 °C and a second melt point of 327 °C.⁵⁹ This refers to the first time Teflon temperature is raised after the original fabrication process. The temperature must go above 342 °C to reach a truly amorphous polymer configuration. Once this has been reached after the original molding process, the crystalline structure is modified such that a second melt temperature applies. This fact becomes significant when considering the differences in calibration measurements between virgin Teflon and Teflon that has been exposed to a high temperature plasma environment. When the material does melt, the viscosity remains extremely high (10^{10} - 10^{12} Poise at 380 °C)⁶⁰ and the color changes from white to semi-transparent. Figure 3.8 shows this change. This block was placed in an oven with a K-type thermocouple supporting its weight and heated above 420 °C. Notice that the edges of the block are white indicating faster cooling along the edges. Also apparent are bubbles formed below the surface of the Teflon. The origin of these is suspected to be from porosity due to the sintering process in creation of the PTFE. From this information, there is little concern

about Teflon liquid flowing during the operation of this thruster, and although there are obvious changes in surface conditions as a function of temperature, an experimental calibration takes these into account.

3.1.2.2 Thermal Conduction

Teflon thermal response must be considered in terms of whether the fuel will quickly transmit heat laterally across the surface and how deeply heat will be transferred. The thermal diffusivity is defined by⁵⁶

$$\alpha = \frac{k}{\rho c_p} \quad (16)$$

where k is the thermal conductivity (0.167 W/m °C), ρ is the density (2160 kg/m³), and c_p is the specific heat (1200 J/kg °C). For Teflon, this value is 6.4x10⁻⁸ m²/s. The transient solution for heat flow into a semi-infinite solid is⁵⁶

$$T - T_i = \frac{2q_o}{kA} \sqrt{\frac{kt}{\rho c_p}} e^{-\frac{\rho c_p x^2}{4kt}} - \frac{q_o x}{kA} \left(1 - \operatorname{erf} \sqrt{\frac{\rho c_p x^2}{4kt}} \right) \quad (17)$$

where $T - T_i$ is the temperature rise, A is the area (Teflon surface, 6.45x10⁻⁴ m²), q_o is the heat input in Watts, x is the distance from the heat source, and t is the timeframe observed (pulse duration, 10 μs). The average power from current measurements during a 20 μs pulse typical to this experiment is 0.203 MW. This is not the same as the power transferred to the surface from the arc, but without an estimate of efficiencies, this is the best estimate available. Solving for the temperature difference at varying distances from the source indicates that a depth of 5 μm from the source sees no conducted heat transfer in the pulse timeframe. Figure 3.9 shows the conducted heat at 20 μs after the start of the pulse for the depths indicated. The y-axis scale is cut off at 1000 K since Teflon that experiences temperatures above that are likely to ablate during the pulse.

Lateral conduction of heat away from the targeted area is a concern both during and after the pulse. The 1-D heat transfer equation is used. This is given as:

$$\frac{\partial}{\partial x} \left(k \frac{\partial T}{\partial x} \right) = \rho c \frac{\partial T}{\partial \tau} \quad (18)$$

Using central differencing, this can be discretized to:

$$\rho c \frac{T(t+1) - T(t)}{\Delta t} = k \frac{T(x+1) - 2T(x) + T(x-1)}{\Delta x^2} \quad (19)$$

Holding the temperature at $x=0$ at 1000 K, and calculating with a Δx of 1 μm and a Δt of 2 μs , it is shown that at 200 μs , the heat conduction has not extended past 20 μm from $x=0$ for Teflon conductive characteristics. Figure 3.10 shows this result. This has implications in surface temperature resolution. Since the detector pitch is $\sim 20 \mu\text{m}$, it is important to know whether neighboring sensors will pick up conductive heating in the timeframes of interest. The temperature rise at a neighboring sensor image is less than .001 degrees due to conduction alone after 200 μs . This effect is negligible when compared to the hundreds of degree rises in this experiment and is well below the resolution of these detectors.

3.1.2.3 Radiative Properties

The emissivity of Teflon is a poorly known value. Available information from the literature suggests the emissivity of Teflon varies significantly with wavelength, reaching unity at about 8.4 μm .⁴⁶ However, the emissivity below 4 μm is very low. The bulk of the emission is distributed between 4 and 10 μm . Since the peak response of the HgCdTe detectors lies in this regime, the detector material provides an ideal choice in terms of matching actual Teflon emission from molecular stretching and bending modes with the detector response discussed above.

However, the detector choice does lead to a different problem. Considering that the emission peak for a hot blackbody $\sim 800\text{-}1000 \text{ K}$ resides in the sub-4- μm regime the ideal detector for these temperatures is InSb, which loses response at longer wavelengths where the bulk of Teflon emission occurs. Unfortunately, InSb detectors have poor response to lower temperatures (500 K and below) removing the ability to define a late-time cooling curve. Finally, since these temperatures are only expected at the peak in surface temperature (if at all), and since there is a possibility that we are not yet able to

detect the surface during the early part of the discharge this problem is not yet a concern and the choice of HgCdTe detectors stands.

Another concern is the transmissivity of the Teflon itself and the optical focus of the detector system. Figure 3.2 shows the transmissivity of Teflon plotted against infrared wavelengths. Of clear concern is the fact that from 2.5 to 7.5 μm the transmissivity averages 70%. This means that the calibration method must remove any source of infrared emission from behind the Teflon during testing. In the case of actual thruster firing, heat deposition occurs only on the front face of the propellant and on a microsecond timescale. There are no heat sources behind the Teflon face during thruster operation.

3.1.2.4 Plasma and Neutral Vapor

The intent of the IR measurement is to determine the surface temperature immediately after the pulse. However it is interesting to consider more ambitious measurements during the discharge. Measurement of the surface temperature during current reversal may not be possible due to emission encountered from plasma and neutral vapor situated above the Teflon face. As the surface is heated during the arc, both plasma and neutral vapors above the surface exist at high temperatures and may be capable of emission within the measurement range of the detectors. Determination of whether surface emission may be viewed is dependent upon the optical thickness of the plasma and neutrals. Calculation of wavelength dependent optical thickness is beyond the scope of this inquiry, but a more simple optical thickness calculation is possible.

Presence of plasma may hinder photon collection by re-absorption of the radiated photons. The magnitude of this effect is estimated by calculating the optical thickness as the non-dimensional ratio of the plasma scale length to the characteristic length of photon motion prior to reabsorption.

$$\tau = \frac{l_p}{l_\gamma} \quad (20)$$

Therefore an optical depth much less than 1 indicates a high likelihood for photons generated within the plasma to reach the edge without reabsorption and be available for collection by the diagnostic optics.

The plasma optical thickness for a Doppler broadened line⁶¹ is given by (CGS units)

$$\tau = 1.76 \times 10^{-13} \lambda \left(\frac{Mc^2}{kT_e} \right)^{\frac{1}{2}} N_e l_p \quad (21)$$

where M is the atomic mass (averaged to 16.7 AMU or 2.77×10^{-23} gm), c is the speed of light, k is the Boltzmann constant, T_e is the electron temperature, N_e is the number density, and l_p is the plasma depth. Inserting typical values for a micro-PPT ($N_e = 1 \times 10^{16}$ cm⁻³, estimated $T_e = 11500$ K (1 eV), $l = 0.635$ cm (using the thruster diameter), 6 μ m wavelength), gives $\tau = 8 \times 10^4$. This suggests that the plasma is optically thick. Emission from the Teflon surface is likely to be reabsorbed by the plasma and not reach the detector. The optical thickness of the plasma may limit the usefulness of the diagnostic to after the conclusion of the plasma discharge. Note that this analysis for optical depth presumes that the transitions in the solid Teflon at the propellant face will be very close to the line transitions in the plasma. If these transitions are at significantly different wavelengths, the plasma may be more optically thin than indicated by these calculations.

Fortunately, there is an experimental means of determining whether the surface emission can be independently collected during and after the pulse. Both plasma and neutral vapor emission can be accounted for experimentally by measuring the total emission in the viewable cone in an area where they are present. By targeting across the surface of the thruster over the central electrode, the plasma and vapor contribution can be assessed. This method characterizes the gaseous emission throughout the pulse and is described in depth in Section 2.3.4.2.

3.2 Late-time Ablation

In section 1.2, reference was made to studies by Kamhawi¹³ and Spanjers¹² which characterized thermal issues in PPTs. Both of these studies noted elevated propellant base temperature between pulses when the thruster operates repetitively for long timeframes. The thruster system comes to a thermal equilibrium determined by the radiation characteristics of the thruster housing. Spanjers noted an increase in propellant consumption with the increase in propellant base temperature, however no increase in thrust. By varying the power (and therefore the propellant temperature), Spanjers showed

a 25% increase in thruster efficiency when the propellant steady state base temperature dropped from 135 °C to 42 °C. The resulting hypothesis is that the base temperature of the propellant governs the late-time ablation process. If this is true, then both the I_{sp} and the thruster efficiency can be partially controlled by controlling the propellant base temperature.

Thermocouple testing on microPPTs showed a steady state temperature of 65 °C for typical sustained operation (a rise of 40 °C). It is likely that this modest rise in base temperature does contribute to the ablation process, but it is difficult to quantify at this point. It is possible that control of this modest rise in base temperature would result in an increase or decrease in surface temperature after the pulse that may be detected by infrared thermography. This prospect is investigated further below.

3.3 Keidar-Boyd Plasma Model of the microPPT

The Keidar-Boyd Model (K-B Model) is an end-to-end (plasma generation to plume far field) model specifically addressing the geometry of the microPPT with regards to thruster performance and spacecraft contamination issues. Development of this model has progressed with significant input from experiments performed here and in related past research. As it stands, this research is one of the key supports for the theoretical description of the physical processes involved in PPT operation. Because of the significant cooperative work between the experimental and theoretical processes, this is likely the best validated theoretical description of a Teflon capacitive discharge in existence. Development and details of the Keidar-Boyd Model are given in references 30-35. The K-B model is reviewed here for completeness.

Three models are employed to investigate the complete discharge of the micro-PPT. Figure 3.11a shows a schematic of the total theory. The first model is a first-order ablation model that characterizes Teflon loss to the arc. The second is a description of the Teflon transition through neutral vapor to plasma in several sublayers. Figure 3.11b shows a schematic of this portion including the Knudsen layer (the layer in which a half-range Maxwellian distribution of vaporized atoms turns into a full-range Maxwellian) and a non-equilibrium hydrodynamic layer. These layers are electrically neutral, however near the surface there is a space charge negative sheath. Finally, there is a

Particle-in-Cell (PIC) description of the plume to far field. These models use a fluid description of the electrons, a direct simulation Monte Carlo (DSMC) model of the neutrals, and a PIC description of the ions.

The ablation and plasma generation models provide boundary conditions for the plasma plume model.³³ This allows for a consistent description of the plasma flow from the Teflon surface into the near plume. Because of this fact, the plume properties depend very heavily on the upstream conditions including surface temperature.

3.3.1 Plume Description

In early iterations, electron density proved to be a robust prediction even using local thermodynamic equilibrium (LTE) conditions (Figure 1.2). However, initial neutral density predictions showed no similarity to experimental measurements (Figure 1.4). It was hypothesized that the interaction of the Knudsen and hydrodynamic layers with the Teflon surface was a key parameter in the generation of neutral vapor during the arc. When Saha equilibrium in the Knudsen layer is taken out of the equation and replaced by non-equilibrium physics, the prediction of neutral density during the arc begins to resemble the experimental data.²⁷

Figure 3.12 shows early attempts to include non-equilibrium physics in the model. Parts a. and b. show the electron and neutral densities compared with experiment for a parameter θ value of 0.4. Parts c. and d. show the same for $\theta = 0.5$. The physical meaning of θ is an electron temperature gradient from the plasma bulk to the propellant surface. It is the ratio of the electron temperature at the beginning of the ionization layer to the electron temperature in the plasma bulk. The inclusion of this factor of θ suggests that the large uncertainties in the experimental measurements used for comparison are limiting the usefulness of the measurements. Therefore, new two-color measurements presented in Section 4.3.1 with much smaller uncertainties are compared with the model predictions to show the present accuracy of the model's plume description.

3.3.2 Surface Temperature

The surface temperature is calculated during the pulse using particle convection to the surface as the main heat transfer mechanism from the arc. Radiation in the ultraviolet

may play an important role in heating and is not fully considered in these models. This is discussed in more depth in Section 5.2.2. Figure 3.13 shows a prediction of the surface temperature as a function of thruster radius for a 6.35 mm diameter micro-PPT.³² This prediction assumes a symmetric current distribution angularly across the thruster face. The peak temperature reached during the pulse is ~ 900 K dropping to ~ 820 K by the end of the current pulse at 12 μ s. Radial non-uniformity reflects the increased current density experienced near the central electrode. Since the rate of Teflon ablation depends exponentially on the surface temperature, small changes in this parameter dictate significant changes in ablation rate which correspond to variations in the amounts of current carriers, ionization fraction, and neutral vapor generation throughout and after the discharge.

Unfortunately, while the arc is present, the IR diagnostic has not been proven able to measure surface temperature. Therefore, the post-pulse cooling curve is of greater interest given the experimental limitations. Post-pulse cooling is currently calculated using heat lost through ablation only. It is possible that this will under-predict the rate of cooling by neglecting heat lost through radiation from the surface and thermal conduction into and across the propellant face.

This post-pulse surface temperature governs neutral vapor contributing to late-time ablation. As discussed above, there is a possibility that a rise in propellant base temperature can contribute to late-time ablation. Keidar evaluates the Spanjers theory and shows that additional mass loss can be expected between pulses depending on the base temperature. For a base temperature of 330 °C, an additional 4 μ g would be lost per second.³⁶ This is comparable to the total ablated mass per pulse in steady state operation of the microPPT for a 4.35-J discharge. Keidar suggests that the base temperature can affect neutral particle flux from the surface, but does not affect plasma generation or ion flux during the discharge. To effect any significant increase in neutral flux from the surface, however, the base temperature must rise almost 200 °C. This level of temperature rise has not been shown to occur in the microPPT. A modest rise to ~ 65 °C has been measured. Experimentally this temperature was measured on the outer copper electrode, and it is likely that the Teflon surface could have a higher temperature than that measured at the thermocouple location.

Prediction of the surface temperature up to this point has generally assumed an azimuthally symmetric current sheet during the microPPT discharge. This would conveniently allow any measurement of T_s to also be assumed azimuthally symmetric. At low energies, the development of char seems to follow this pattern (Figure 1.3). However, DICAM pictures of an operating microPPT at varying energies (Figure 3.14) suggest that as the energy increases, the arc attachment to the outer electrode may become localized by the appearance of anode or cathode spots. Angular localization of the arc is called arc spoking. It is a constriction of the current due to increased magnetic field strength at high currents and minimization of arc resistance due to ohmic heating. This behavior has ramifications for both measurement and prediction of surface temperature. Keidar investigates this phenomenon and predicts that anode spotting will occur at high discharge voltages while low voltages result in a diffuse discharge. Figure 3.15 shows this as a function of anode voltage drop. This allows prediction of when spoking conditions exist and seems to be supported by the limited experimental data available.

The consequences of spoking for surface temperature and ablation rate are explored. When the current constricts, it is assumed to do so in a linear fashion between the electrodes. Figure 3.16 shows a schematic of such a constriction.³⁶ Within this constriction, the current density rises significantly, leading to an increase in ohmic heating of the plasma (proportional to the square of the current density). The result is an increase in heat flux to a localized area of propellant, which leads to locally high surface temperature and ablation rate. Because the surface temperature directly underneath the arc is dominated by particle convection, this area experiences the highest temperatures on the propellant face. Away from the arc, the heat transfer due to particle convection is minimal and the surface temperature is dominated by radiation from the arc. This results in significantly reduced temperature predictions for this region. These temperature differences are significant because they provide an expected range of surface temperatures dependent on arc proximity. In Section 4.5.1.3 these predictions are explored and compared to measurements of surface temperature from IR thermography.

3.3.3 Ablation and Coning

When a symmetric current sheet is assumed, the surface temperature and near-field plasma properties are strongly non-uniform in the radial direction. This is due to high current densities experienced near the central electrode. Using this assumption, the Keidar-Boyd model predicts a single pulse ablation profile that looks like a cone with the apex at the center electrode. Multiplying this by the total number of pulses yields an ablation profile that should describe the propellant shape after a large number of pulses. This prediction is compared with experimental measurements in Section 4.5.1.2.

Azimuthal non-uniformities in current density (spoking) have an impact on ablation rate. Localized increases in heat flux lead to locally high surface temperature and ablation rate. However, the surface area exposed to this increase is smaller which also affects total ablation rate during the pulse. Keidar uses a current density enhancement factor due to the non-uniformity to predict the affect on total ablation rate. Figure 3.17 shows this dependence. A stronger arc constriction covers smaller total area causing the asymptotic increase in ablation rate.

3.3.4 Recession Operation

Recession of the propellant into the outer electrode tube presents a new set of parameters to consider in terms of plasma and fluid flow through the tube. For both plasma and neutral vapor, there will be a time-of-flight delay for material exiting the thruster as the propellant recesses. For neutral vapors, the density within the tube could conceivably be affected by formation of a boundary layer along the inner wall of the tube. However, the measurable exit plane densities are lowered significantly by axial expansion of the vapor through the tube. For this reason, experimental measurements of neutral density are much more difficult to obtain compared with flush propellant operation. Therefore, while Keidar predicts neutral density at the exit plane of a recessed thruster, these are not evaluated experimentally.

Measurements of electron density are achievable, however, and therefore discussion of the plasma behavior in the tube is relevant. The Debye length for plasma densities (10^{16} cm^{-3}) and temperatures (1-2 eV) typical to a microPPT discharge is on the order of 0.1 μm . Such a small Debye length suggests that electron behavior will be a

close approximation of ion behavior in the exhaust. The question of tube effects on ion behavior is important. There are two possible expected behaviors that can affect the predictive capability of the model. It is possible that ions moving within the tube with non-zero radial velocity can impact the tube wall. The velocity of the ions can be large enough (and the sheath voltage small enough) that the ions will pass their charge to the wall and neutralize there. The other possibility is that the ions could electrostatically reflect from the outer tube when it acts as the anode. This result would present a larger electron density magnitude at the exit plane of the thruster than if the ions neutralized at the wall. The implications of this could extend beyond the accurate predictive ability of the Keidar-Boyd model. If the ion reflection hypothesis holds true, it could suggest that a non-reversing current pulse where the outer tube is the anode could increase total thruster ion flux, and therefore act to increase the thrust in recessed operation.

3.4 Chapter 3 Figures

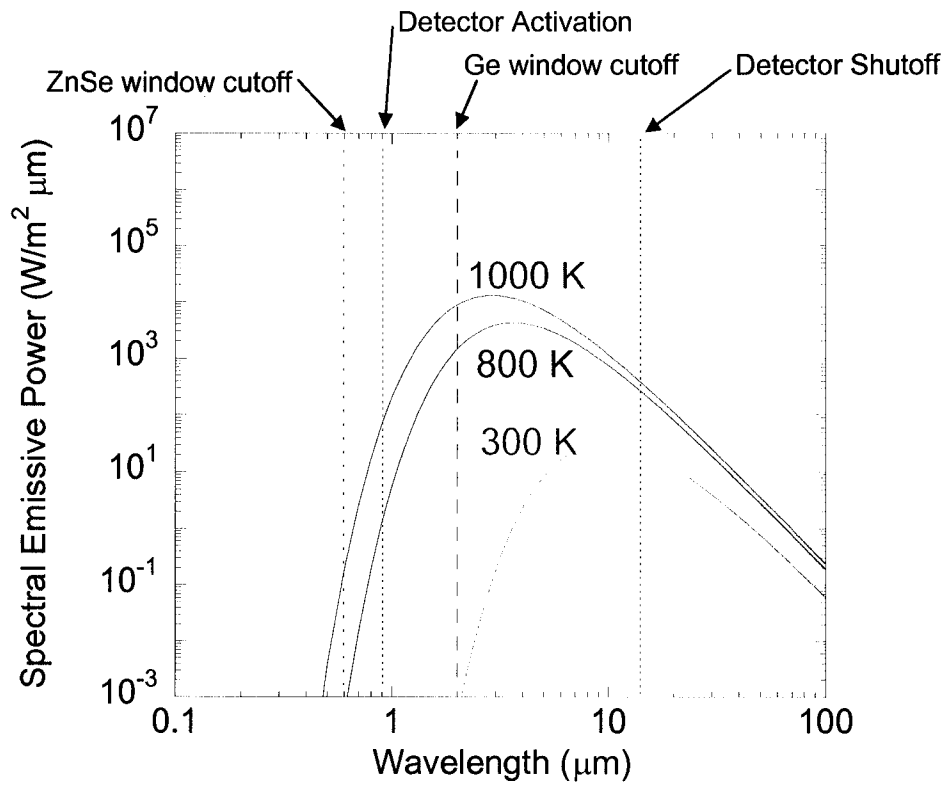


Figure 3.1: Several Planck distribution curves for blackbody emission at relevant temperatures.

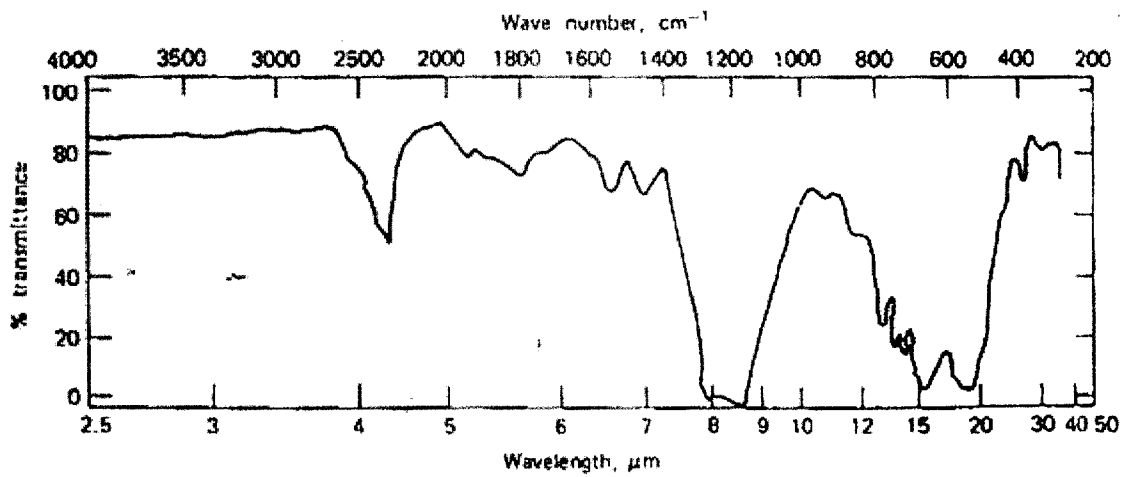


Figure 3.2: Infrared spectrum of polytetrafluoroethylene, 0.005 cm film thickness.⁵⁵

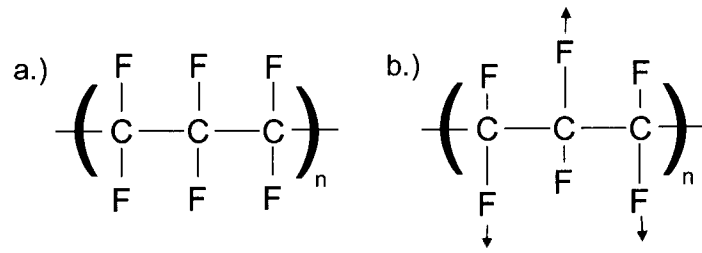


Figure 3.3: Teflon polymer (a.) has an asymmetric C-F stretching mode (b.) absorbing energy at 8.4 μm .

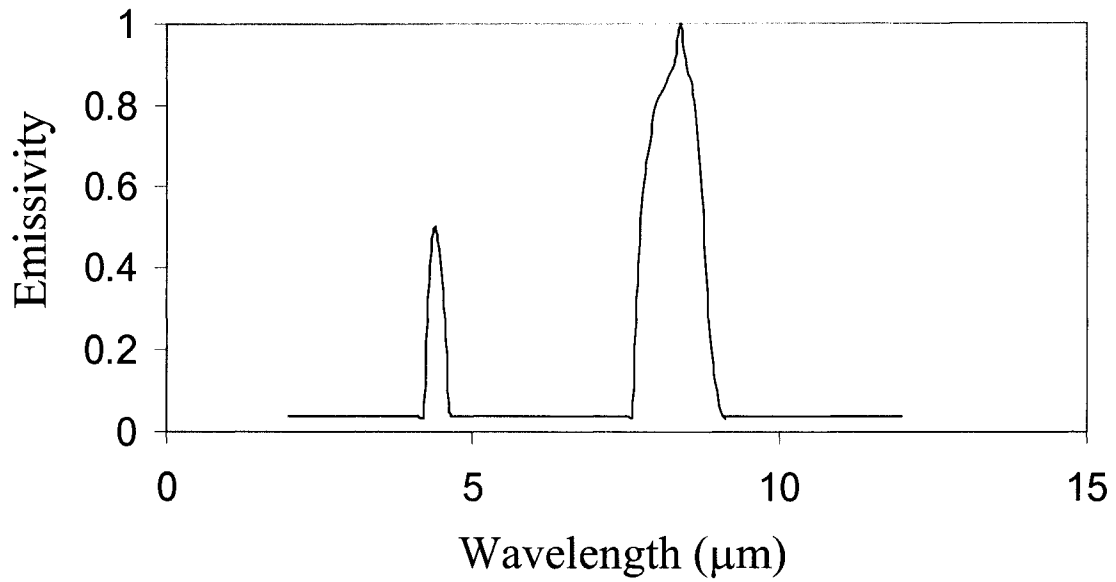


Figure 3.4: Estimated Teflon emissivity for 2-12 μm .

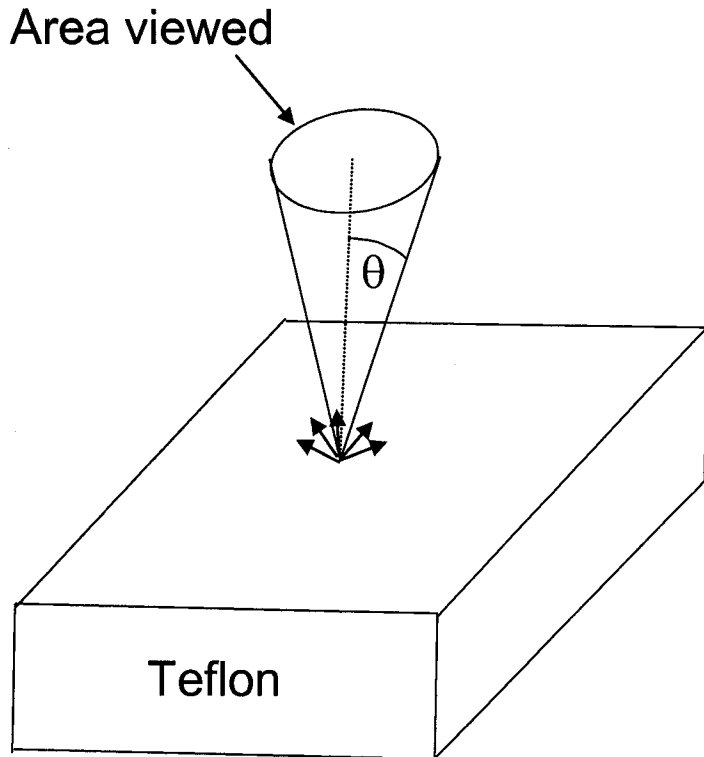


Figure 3.5: Expected fraction of total emission to reach the detector. The cone is defined by the ZnSe viewport diameter.

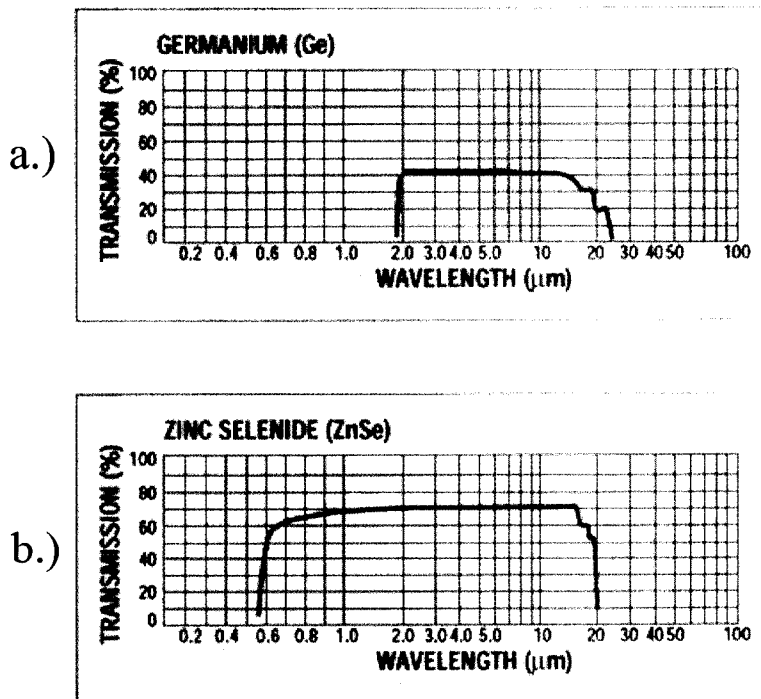


Figure 3.6: Transmission response for ZnSe (a.) and Ge (b.) viewports.⁵⁸

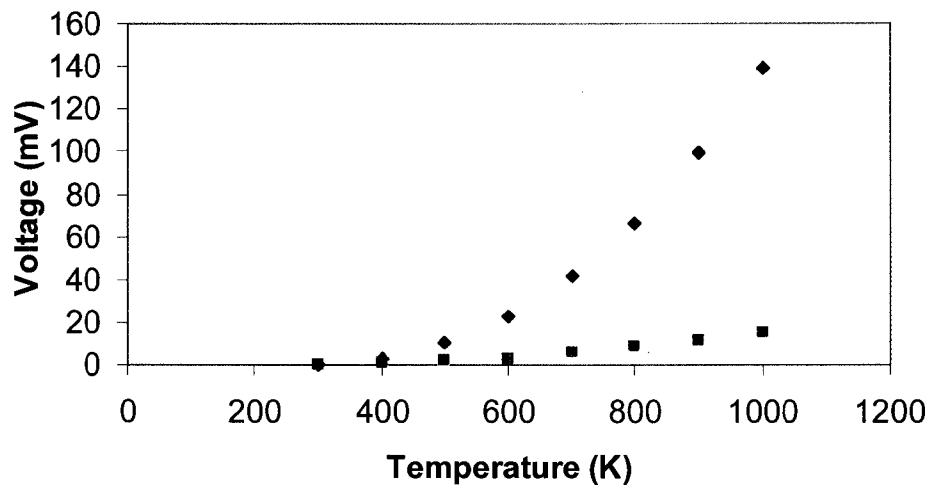


Figure 3.7: Predicted detector calibration for a Black Body and Teflon.

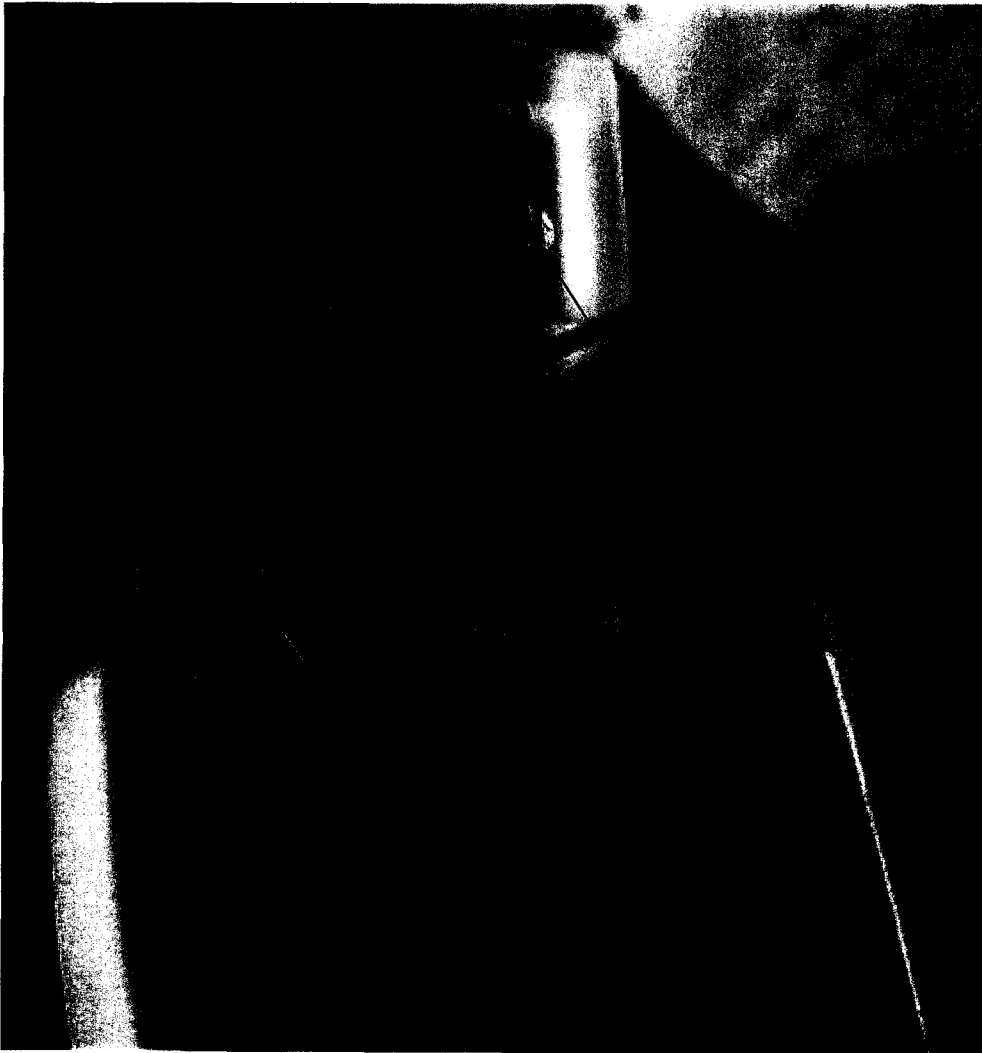


Figure 3.8: Teflon above melt temperature changes from white to transparent and retains a high viscosity.

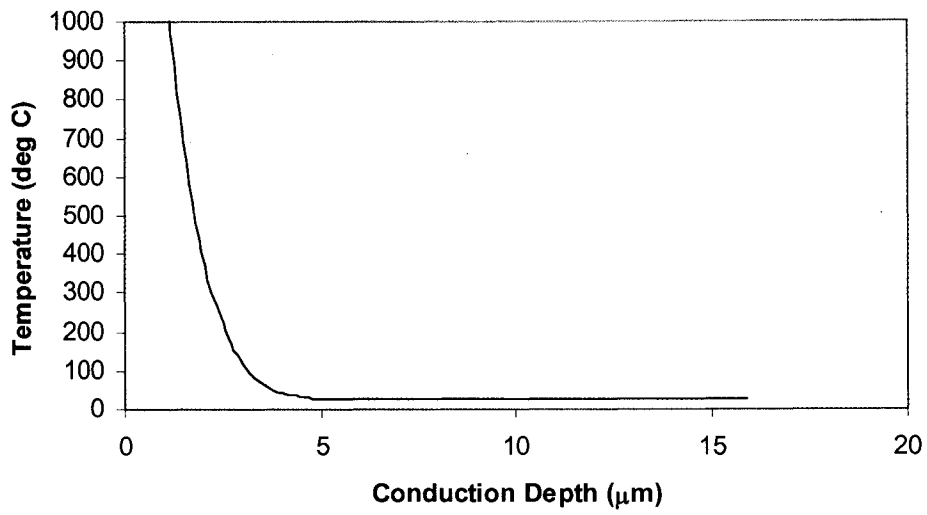


Figure 3.9: Conductive heating into the surface of a micro-PPT at 20 μs from Eqn. 17. Average power of .203 MW used.

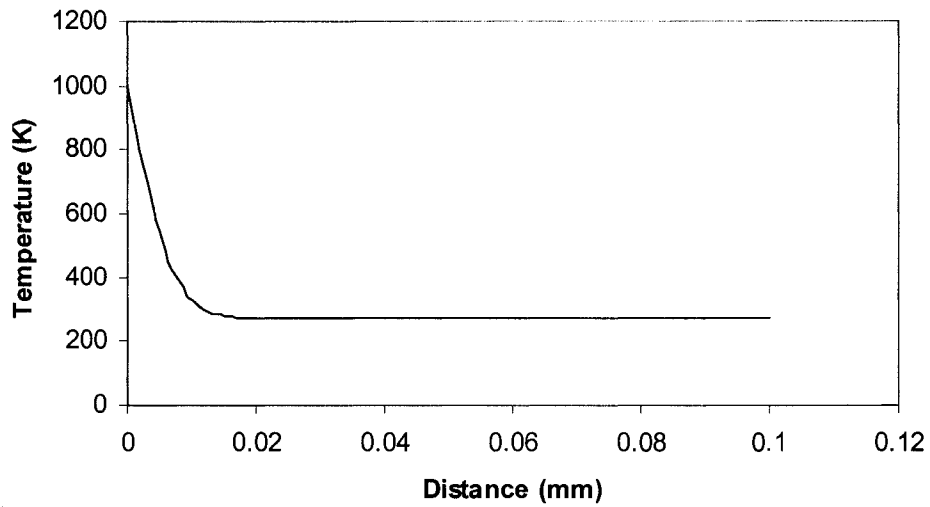
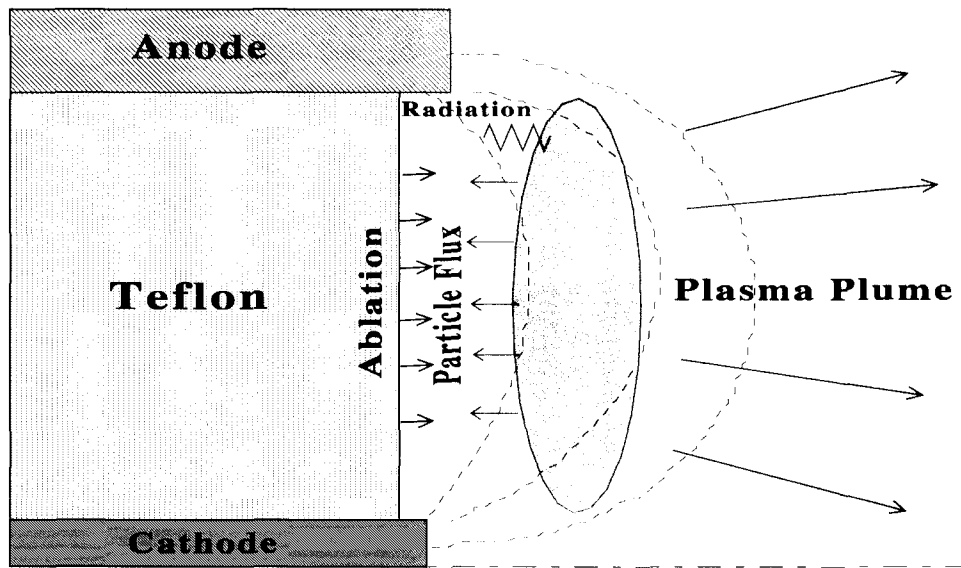
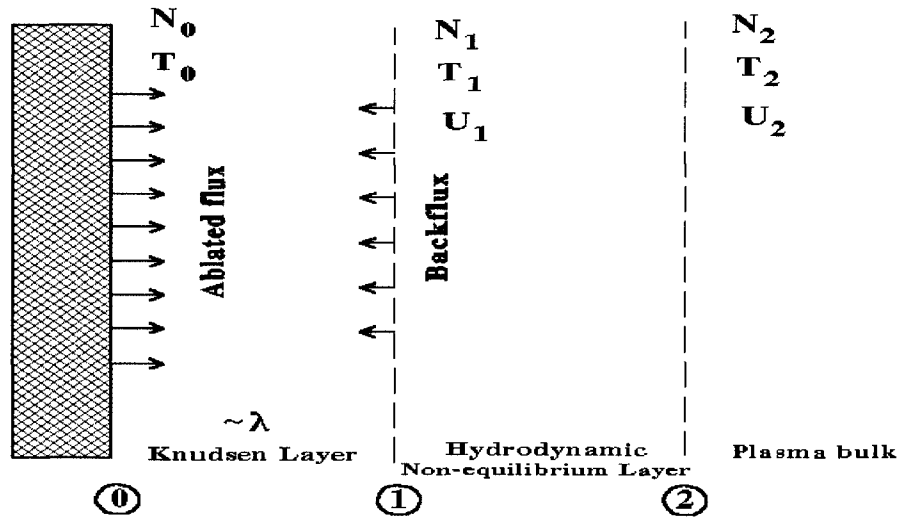


Figure 3.10: Heat transfer laterally across the surface of a micro-PPT in 200 μs due to conduction alone.



a.



b.

Figure 3.11: Schematic of the near Teflon plasma layers from Boyd and Keidar.³¹

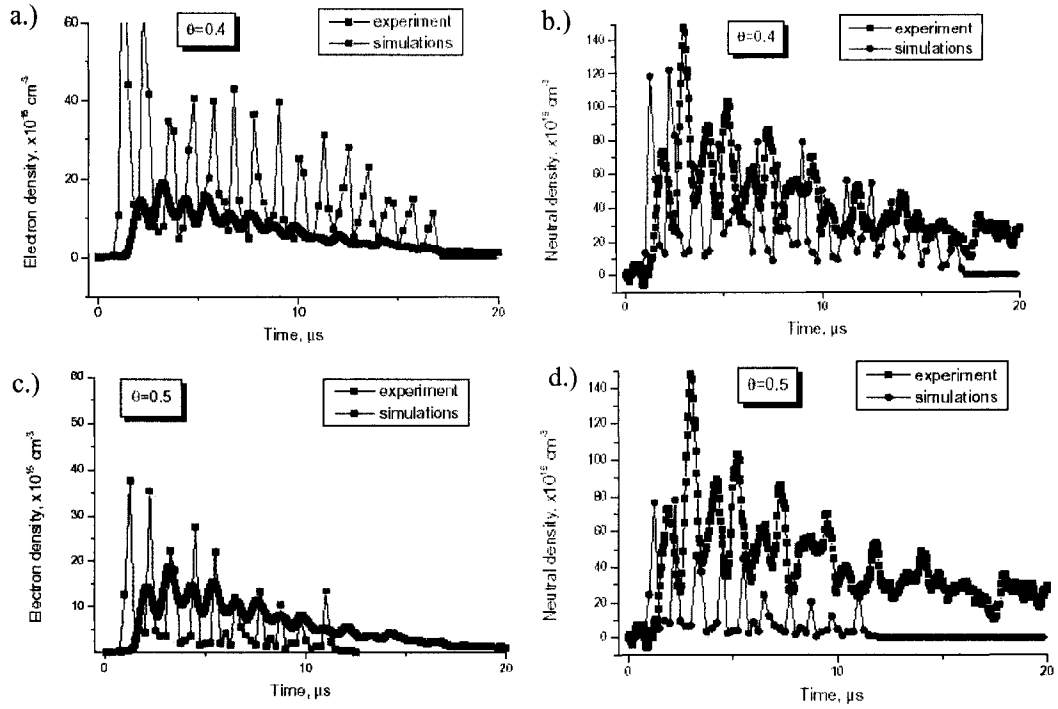


Figure 3.12: Electron density (a. and c.) and neutral density (b. and d.) experiment and predictions for $\theta=0.4$ (a. and b.) and $\theta=0.5$ (c. and d.).²⁷

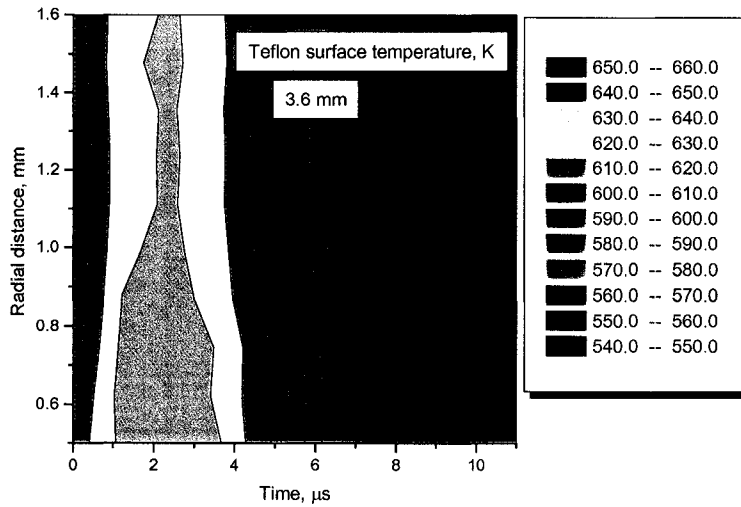
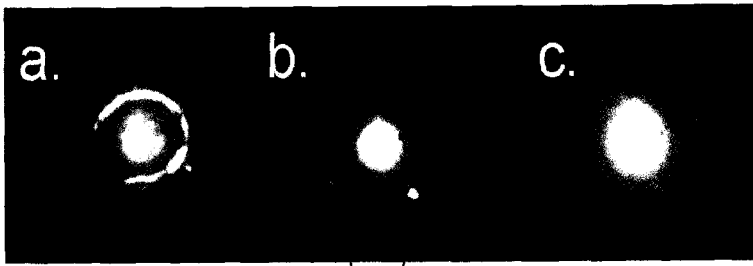


Figure 3.13: Surface temperature prediction for a 6.35 mm diameter micro-PPT.³² Note that the units are in error, temperature is given in $^{\circ}\text{C}$.



Anode spots

Figure 3.14: Intensified images showing arc behavior at a.) 2.3 J, b.) 5.55 J, and c.) 6.73 J. Capacitance is $0.417 \mu\text{F}$.

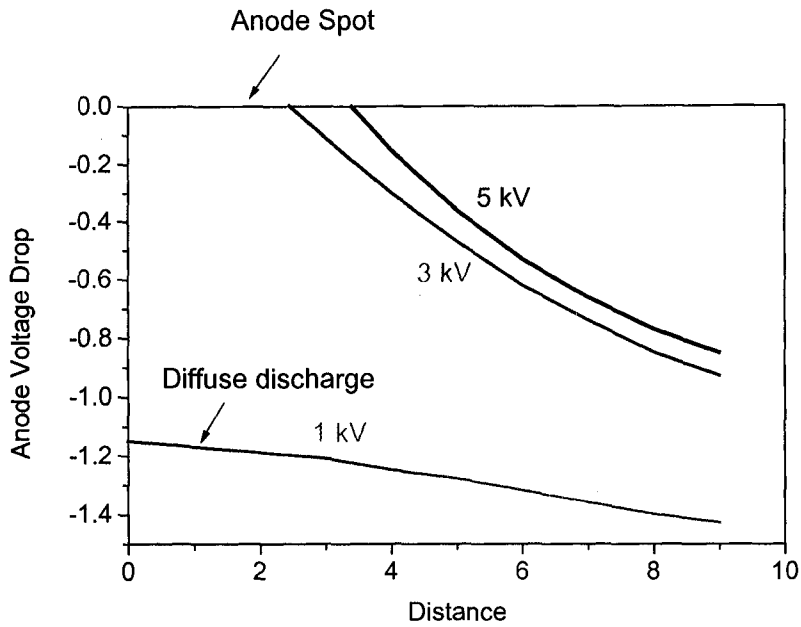


Figure 3.15: Anode spotting is predicted at high voltages when the anode voltage drop reaches zero from Keidar.³⁶

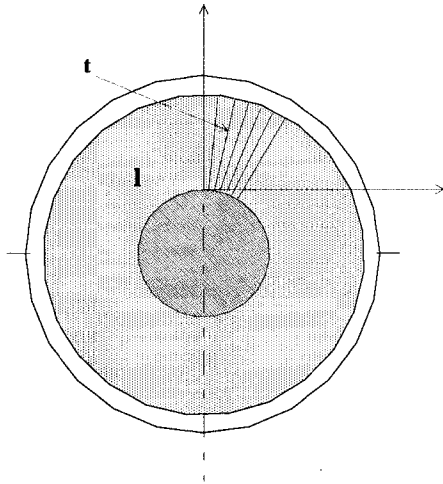


Figure 3.16: Model of arc constriction due to high discharge voltage. The red lines denote the arc coverage area. From Keidar.³⁶

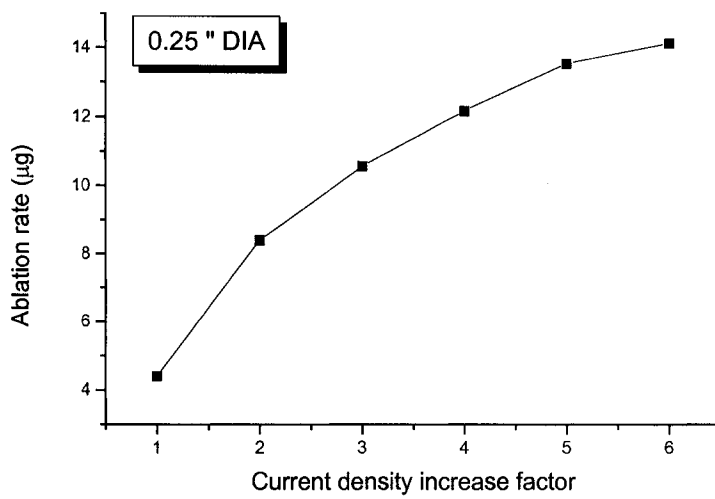


Figure 3.17: Ablation rate dependence on current density increase due to discharge non-uniformity in the azimuthal direction from Keidar.³³

4. Experimental Results

4.1 Thruster Current and Mass Loss

Measurements of the thruster current and mass loss are shown and analyzed here. Figure 4.1 shows the current pulse for a microPPT pulse representative of that used during the surface temperature measurements. At the point where the current passes through zero, the power into the arc is zero. Electron and neutral densities as well as the emission measurements in the plume follow the peaks and valleys of the power deposition during the pulse, although the densities do not go to zero when the current goes to zero between reversals.

Typical RLC circuit equations are used to analyze the current trace obtained with the Rogowski coil to estimate resistance and inductance, and consequently power and energy deposition. This analysis starts with the current,

$$I = \frac{V_o}{\omega L} e^{-\frac{R}{2L}t} \sin(\omega t) \quad (22)$$

where V_o is the initial voltage, L is the inductance, R is the resistance, t is time, and ω is

$$\omega = \sqrt{\frac{1}{LC} - \frac{R^2}{4L^2}} \quad (23)$$

with capacitance C . It is determined that a linearly increasing resistance fits the experimental data well. For the current trace measured with a self-integrating Rogowski coil, the curve-fit parameters are $V_o = 1.8$ kV, $C = 2.98$ μ F, and $L = 185$ nH. To match the current pulse, the resistance must vary from 30 to 60 m Ω in the 20 μ s of the pulse duration. Figure 4.2 shows the current pulse along with a fit calculated using the linearly increasing resistance. This allows calculation of the arc power using $P=I^2R$ and integration with time provides the instantaneous energy deposited. The power deposition is in the megawatt range over the short duration of the pulse and is shown in Figure 4.3. The average of this power over the pulse duration is 0.203 MW. If the instantaneous power is integrated over time, the energy deposition through the duration of the pulse can be calculated. Using a Riemann Sum, the energy is then equal to

$$E = \sum_i P_i \Delta t \quad (24)$$

where i is indexed over the total number of points in the data file. For any point in time, the total energy deposited is calculated by summing up to that point. Figure 4.4 shows the energy deposition as a function of time along with the current waveform. Essentially all of the energy in the capacitor has been delivered by 20 μ s after pulse initiation. Beyond this point there is no longer an energy source for creating electrons in the plasma. Since the ion-electron collision time (a good estimator of the plasma neutralization time) is very short, it is reasonable to assume that the bulk of the fluid above the surface is neutral gas vaporizing from the Teflon surface.

Mass loss per pulse is typically averaged over a large number of shots to determine a steady state mass loss. However, over the small total shot numbers used in these experiments, the mass loss per pulse varies significantly. Figure 4.5 shows the mass lost per pulse averaged over 100, 1000, and 12000 shots. The large drop in average mass loss may be due to increased erosion from the copper electrodes while reaching steady-state operating conditions. This does show a limitation of the time-averaged measurement method that may be circumvented using the time-resolved surface temperature measurement. Differences in the Teflon surface for these three cases are shown in Figure 4.6. In cases such as these where surface charring is not encountered, the actual surface of the Teflon becomes smoother as the thruster face is burned in. However, for too many firings, the face can take on a conical shape distorting the optic view of the surface slightly. To avoid this, all measurements are made in the 100 – 1200 shot range on a microPPT.

4.2 Infrared Thermography

4.2.1 Calibrations

4.2.1.1 Voltage vs. Temperature Curve

The first requirement to demonstrate a valid calibration curve is to show that the heating and cooling curves for V vs. T match. The reason for this requirement is that if the thermocouples are measuring close to the location of the emission measurement, and

there are no changes to surface condition during the test, both curves should demonstrate the same emission. Reasons why the two curves might not match include Teflon expansion out of the viewing hole (which causes a change in the optical path), targeting errors, material depositing on the surface of the Teflon causing a change in emissivity, or possibly a permanent change in emissivity due to thermal cycling of the Teflon. A single test showing a heating and cooling curve matchup indicates that there are no significant natural changes to the Teflon emissivity due to thermal cycling. Because of this, failure to match heating and cooling curves indicates an error in the calibration process attributable to one of the other problems.

If the Teflon has expanded out of the calibration hole, the emission measurement will show a lower-than-expected voltage for the temperatures measured. Figure 4.7 shows a calibration test where the Teflon extruded out of the optical view hole (Figure 4.7c.) during the test. This is a common failure mode for calibration tests, but it is also easily identifiable. When the Teflon extrudes, the location being measured cools rapidly and the emission angle changes showing a sharp drop in voltage (Figure 4.7a.) that is not reflected in the temperature measurement (Figure 4.7b.). This failure mode can occur through Teflon extrusion or simply Teflon flow out of the calibration jig. Figure 4.8 shows three pictures of experimental calibrations where the Teflon behaved differently during the tests. In case a.), the Teflon flowed out of the calibration hole while case b.) extruded out of the hole. Case c.) shows an example of a calibration test that stayed flat. The voltage vs. temperature curve for two of these cases (a. and c.) are shown in Figure 4.9. In the case where the Teflon flows out of the hole, the view angle and cooling properties of the area being measured by the detector change significantly. The result is that while the calibration during heating is correct, the calibration during cooling very obviously fails. While the temperature keeps increasing, the voltage drops significantly. This is a consequence of the thermocouple measurement location no longer coinciding with the position being measured by the detector. It is important to note that the failure in this mode is easily identifiable and that the heating curves are still valid up to that point. In the case of the valid cooling curve (Figure 4.9, red curve), the portion that doesn't match is a consequence of the LN2 dewar running out of liquid nitrogen.

Section 2.3.3.1 described the apparatus and means for measuring the emissive difference between virgin and plasma exposed Teflon. Figure 4.10 shows a number of tests indicating that there is a difference between virgin and exposed Teflon, but not a significant difference between Teflon exposed to 100 shots of plasma and that exposed to 1500 shots of plasma. The blue traces are the virgin cases and the red traces are the plasma exposed cases. There is a single virgin case that falls well below the other two shown, and it is suspected that the Teflon started to flow in that test skewing the signal. However, since a definite failure in that test was not recorded, it is considered in the uncertainty calculations below.

For the case of only plasma-exposed tests, Figure 4.11 shows small deviation up to about 450 °C. This demonstrates that the optimal surface temperature exposure times are between 100 and 1500 shots on the face of the microPPT. Beyond 1500 shots, the surface can start deforming to a natural cone shape changing the optics of the system. Before 100 shots, it may still be measuring in the virgin Teflon regime.

Fitting the curves with a T^2 fit, the virgin Teflon case is fit by $V = 3.5 \times 10^{-5} T^2$ and the plasma exposed case is fit by $V = 2.87 \times 10^{-5} T^2$. Figure 4.15 shows selected calibration data points with the relevant T^2 fits. In the discussion sections below, consideration is given to actual theoretical predictions of the calibration curve along with the data fits.

4.2.1.2 Geometrical Uncertainty

The calibration hole is 5.38 mm diameter. The hottest point on that circle is the outer edge, which is in contact with the copper plate. As heat transmits inward through conduction, the center of the circle represents the lowest temperature point in the Teflon due to conduction time and the presence of energy loss through radiation. The thermocouples are located just below the Teflon surface adjacent to the edge of the copper hole.

The geometric uncertainty in the calibration curve is primarily associated with how well the thermocouple measurement location matches with the actual surface temperature at the point of detector measurement. The thermocouples cannot measure the exact same location as the detector (since their different material would perturb the

effective emissivity). The uncertainty associated with the distance between the focal point of the optics and the thermocouple joint is assessed using two different methods.

The first method for determining the temperature difference is experimental. One of the three thermocouples is drilled into the center of the hole while the other two remain at the edges. This is shown schematically in Figure 4.12. During a calibration, this cannot be done because the detector can pick up emission from the hot sheath of the thermocouple. A typical heating cycle for calibration is performed and the difference in thermocouple temperatures is monitored. Figure 4.13 shows the results of this test. Throughout the heating stage, the difference between the centered thermocouple and the two in test locations was ~ 6 °C.

The second method used is thermal analysis using ANSYS™ code.⁷¹ The Teflon cylinder located beneath the optical viewing area is modeled with a constant temperature load of 808 K applied to the top corner of the cylinder. This is a higher temperature than is typically attainable in calibration tests. The front and back circles are allowed to radiate into space with a grey body emissivity of 0.1, an approximation of the average emissivity between 2 and 12 μm . A temperature map of this model at steady state is shown in Figure 4.14 indicating that the difference between the heated area and the very center location is around 8°C. The steady state assumption is used because heating during calibration tests can last up to 5 hours and is applied slowly to minimize transient thermal effects.

Since the detector focal point is targeted somewhere within the optical circle, it is assumed that the more conservative of these two estimates will apply in the uncertainty calculations for calibration of the detector. Therefore a ± 8 °C (± 8 K) uncertainty due to geometrical differences (measurement locations of thermocouples and optics) is used.

4.2.1.3 Calibration Uncertainty

An upper temperature limit using this technique so far has currently been experienced around 770 K. The cause of the limit is Teflon deformation at elevated temperatures. This deformation changes the viewing angle of the Teflon and therefore alters the optical path sufficiently to change the light collection and change the calibration curves. If the Teflon does not deform, the heating and cooling curves in the

calibration should match. This has been observed in cases at lower temperatures without deformation. Using the current calibration apparatus, Teflon deformation limits the calibration to about 750 K.

The heating curves shown in Figure 4.10 are analyzed for average and standard deviation. The root-mean square standard deviation is combined with the ± 0.5 mV limitation of the detector to define a voltage uncertainty shown in Figure 4.15 for representative data points. Also shown are temperature uncertainties using the same method based on the thermocouple uncertainty. For the K-type thermocouples used, uncertainty is ± 2.2 K or $.0075T$, whichever is larger. The ± 8 K uncertainty due to geometrical differences is included here.

From the fit determined in section 4.2.1.1, the temperature in Kelvin is given by

$$T = \sqrt{\frac{V}{2.87 * 10^{-5}}} + 273.15 \quad (25)$$

where the V is the voltage in milliVolts. Total uncertainty can be calculated by using the relations from Wheeler and Ganji.⁶³ The uncertainty in any variable x is calculated here using the root of the sum of the squares method. Its most general form is

$$\omega_x = \left[\sum_{i=1}^j \left(\omega_{\Delta x_i} \frac{\partial R}{\partial \Delta x_i} \right)^2 \right]^{1/2} \quad (26)$$

In this case, x becomes temperature or voltage, and Δx_i are the uncertainties associated with the physical measurements made by the diagnostics. R is the relevant function and ω is the uncertainty of the denoted parameter.

For the voltage measurements made by the detector, Eqn. 26 expands to

$$\omega_v = \sqrt{\left(\omega_{\Delta V} \frac{\partial V}{\partial \Delta V} \right)^2 + \left(\omega_{V_i} \frac{\partial V}{\partial V_i} \right)^2} \quad (27)$$

where $\omega_{\Delta V}$ is the uncertainty in the voltage measurement and ω_{V_i} is the statistical standard deviation from multiple calibration tests in the same configuration. The partial derivative for the both uncertainty terms is simply $\frac{\partial V}{\partial V}$ which is 1.

For temperature, these uncertainties are plugged in and Eqn. 26 is expanded to become

$$\omega_T = \sqrt{\left(\omega_{\Delta V} \frac{\partial T}{\partial \Delta V}\right)^2 + \left(\omega_{\Delta T_{TC}} \frac{\partial T}{\partial \Delta T_{TC}}\right)^2 + \left(\omega_{\Delta T_\gamma} \frac{\partial T}{\partial \Delta T_\gamma}\right)^2} \quad (28)$$

where $\omega_{\Delta V}$ is the uncertainty in the voltage measurement, $\omega_{T_{TC}}$ is the uncertainty in the thermocouple measurements, and ω_{T_γ} is the uncertainty due to geometrical differences in measurement locations. The partial derivative for the thermocouple, geometric uncertainty, and standard deviation terms is simply $\frac{\partial T}{\partial T}$ which is 1. Evaluation of Eqn. 28 yields the temperature uncertainty for the calibration made in the present experimental configuration. In Figure 4.15, these uncertainties have been calculated and are shown on the selected data points with bars.

4.2.2 Teflon Emissivity and Surface Radiation

Experimental calibration curves allow a comparison of predicted detector response with actual measurements. Using Eqn. 15, an estimate for the Teflon emissivity, ϵ_λ , can be calculated. Using the IR transmission spectrum from Teflon shown in Figure 3.2, several vibrational features can be identified. Between 15 and 20 μm , there is a vibrational bending mode, which contributes to emission outside the scope of this diagnostic. At 8.4 μm there is a vibrational stretching mode where the emissivity reaches unity. This mode is within the detectable range of the detectors and is the largest contributor to total signal recorded. Figure 3.3 shows the Teflon polymer (a.) and the stretching mode (b.) that produces this signal. While the 8.4 μm signal is the largest contributor to total detectable emission, there is an overtone at 4.4 μm produced by

superposition of the stretching and bending modes in the molecule. This peak cannot be neglected since it occurs at higher energies and can contribute significantly at higher temperatures. The final contributor in the 2-12 μm range is referred to here as background emission. Since there are no other peaks in this range, the background emission is the result of non-zero reflectivity in the infrared.

Figure 3.4 shows the prediction of virgin Teflon emissivity in the 2-12 μm wavelength region without accounting for experimental calibration. This theoretical prediction is fit to the experimental Teflon calibration curve from above taking into consideration the vibrational peaks identified by IR transmission spectroscopy. It is important to distinguish that the emissivity shown here is only an estimate and cannot be taken as verified. The true emissivity is likely temperature dependent, for which this model fails to account. Additionally, the same level of agreement with the experimental calibrations can be reached by varying the width of the major emission lines and background emissivity level used in the model.

Since the outside evidence guiding the selection of this emissivity curve provides a high level of agreement with experimental measurements, there is justification for using this model to predict surface temperature beyond the experimental upper limits. While Teflon undergoes physical changes at 327 $^{\circ}\text{C}$ and 342 $^{\circ}\text{C}$, there is no evidence to suggest a change in the major emissive structures at 4.4 and 8.4 μm since these are the result of vibrational modes present in the Polytetrafluoroethylene monomers even after the polymer has completely unzipped.

Figure 4.16 shows the calibration data from Figure 4.15 for both virgin and plasma exposed Teflon along with new lines showing the theoretical detector output using the emissivity estimate from above. The most significant result is that the small degree of disagreement between virgin Teflon and plasma exposed Teflon can be explained completely through a small change in background emissivity. Figure 4.17 a. and b. show the difference in background emissivity required to match the observed difference in calibration. For the virgin case, the background emissivity is set at 0.04. Keeping the major emissive structures constant and reducing the background emissivity to 0.01 results in good agreement between the experimental data for plasma exposed Teflon and the modeled calibration. This degree of agreement between virgin and plasma

exposed Teflon calibrations suggests that there is very little emissive contribution that cannot be traced to the C-F stretching mode.

This estimate of the emissivity in the infrared region of the spectrum allows an estimation of the total radiative heat flux from the Teflon surface. The heat transferred away from the Teflon by radiation is described by the Stephan-Boltzmann relation:

$$\Phi = \epsilon\sigma T^4 \quad (29)$$

where Φ is the heat flux in Watts, ϵ is a constant grey-body emissivity, σ is the Stephan-Boltzmann constant, and T is the surface temperature. The Stephan-Boltzmann relation is achieved by integrating the Planck function (Eqn. 10) across all possible wavelengths. It is possible to use the Planck function to describe heat flux away from the surface, but without a wavelength dependent emissivity estimate for wavelengths outside the range investigated here, that calculation would be incomplete. Instead, the Stephan-Boltzmann relation for a grey body can be used to estimate the total heat flux away from the surface. A grey body emissivity estimate is given using the Teflon emissivity calculation shown in Figure 4.17b to generate a voltage vs. temperature curve for expected temperatures. The Planck function is then used with equation 15 to calculate a voltage vs. temperature curve for a grey body. This grey-body emissivity is varied until a close match is achieved with the experimentally-validated curve. Figure 4.18 shows the comparison achieved with a grey body emissivity of 0.113. This average emissivity can be used to calculate heat lost from the surface through radiative emission. It is important to note that although this emissivity estimate does have some basis in experimental results, the lack of information about Teflon radiative behavior for wavelengths shorter than 2 μm means that this estimate could be incomplete at high temperatures (above 700 K). This radiation calculation will be used below to estimate total heat loss from the surface during the cooling period after the pulse.

4.2.3 Propellant Surface Temperature

4.2.3.1 Noise Sources

The real-time surface temperature measurements inevitably contain a certain amount of electro-magnetic interference, or electrical “noise”. The source of this noise has been identified as the sparkplug which provides seed plasma for initiation of the main discharge. The sparkplug is a 0.141 inch diameter micro-PPT operated through a Unison⁶² sparkgap and capacitive circuit designed to cause a voltage spike to the surface of the unit. Exciter boxes have also been used in an effort to remove the source of noise from this system, but the variants used cause excessive noise before the thruster discharge making it difficult to trigger the recording electronics. The current through the sparkplug is measured using a self-integrating Rogowski coil. Figure 4.19 shows the sparkplug current in yellow along with channels 2 and 4 from the IR detector. The spikes witnessed in the sparkplug current trace throughout the timeframe shown are mirrored by similar spikes in the detector voltages. This is the case in all data taken. In essence, the sparkplug is acting as an RF transmission antenna with the electro-magnetic noise being picked up by the detector circuitry. At the low voltage levels used in this experiment, typical filtering and shielding techniques are ineffective at removing this noise from the measurement.

Using the optical shield discussed above, data are taken without emission measurement for comparison. Figure 4.20 shows a typical data shot without an emission measurement highlighting a significant noise contribution during the pulse. This shot shows a measurement zero in all areas where electronic noise is not present. Note that even the noise at 60 μ s is present in this pulse. A possible solution to this noise problem is to operate with an optical scheme that significantly increases the output voltage, thus increasing the signal-to-noise ratio for the measurement. For future work, a revised optical configuration is suggested to allow for a larger signal-to-noise ratio that would alleviate this problem.

4.2.3.2 Plume Contribution

By measuring the plume emission alone we are able to infer what the contribution of the plasma is during the discharge. By noting where the plume contribution ends, a

timeframe for possible surface viewing can effectively be determined. Figure 4.21 shows measurements with the IR detectors with the focal point located at varying distances above the fuel face. This geometry is shown in Figure 2.21a. For these data, the focal point is located at 1, 3, 5, and 7 mm above the fuel face. Of note is the magnitude increase from 1 to 3 mm. This is a repeatable signal increase. Also, the signal from the plume drops to zero throughout the discharge by 5 mm from the fuel face indicating that the plume expansion at that distance has limited the total emission to below that which the detectors can sense. These measurements are all in terms of voltage since calibration with the plasma and neutral vapor is not available. However, they show a significant result. The plume signal stops contributing to the total emission at or before the end of the current pulse. This justifies the use of the detectors for surface temperature after the current pulse is complete.

4.2.3.3 *Arc Location*

The spatial resolution of the detector in these experiments is limited to the detector size as imaged on the propellant face. Since the optics are configured for 1:1 magnification, the detector only sees 80- μm x 80- μm of surface area. This is a small fraction of the total propellant area exposed to the effects of the arc. Figure 3.14 shows DICAM images of a microPPT firing at a.) 2.3 J, b.) 5.55 J, and c.) 6.73 J. These firings used a 0.417 μF capacitor with the central electrode as the cathode. The discharge voltages are then a.) 3300 V, b.) 5200 V, and c.) 5700 V. The trend observed is that at low discharge voltages, there is a greater likelihood of a symmetrical discharge across the propellant face. At the higher energies the emission suggests that anode spots form on the outer electrode which indicates the possibility of current constriction across portions of the propellant face. This has implications for the surface temperature measurements taken here. These are discussed in Section 5.1.2.2.

4.2.3.4 *Surface Temperature Measurements*

Uncalibrated measurements of the fuel face emission demonstrate that it is possible to view the actual Teflon emission after the current ends. Figure 4.22 shows a typical measurement of the fuel face shown with the most significant measurement in the plume (focus located 3 mm above the surface). The blue line shows the subtraction of

the two and the green line demonstrates energy deposition during the arc. Note that at $\sim 40 \mu\text{s}$ (86% energy deposited) the signal from the plume ends. However, the view of the fuel face still shows an appreciable signal out to $\sim 100 \mu\text{s}$. This is a key point in validating this diagnostic. After the plume has stopped contributing to the signal, there is sufficient signal remaining to suggest that an actual surface temperature measurement is being made. An 11-point smoothing scheme is applied to the data to remove as much high-frequency noise as possible.

Additionally, an indication of the repeatability of this signal is shown in Figure 4.23. Five firings are co-plotted under the same conditions. During the timeframe where there is significant contribution from the plasma, the peak structure and magnitudes are the same for every shot. However, after the plasma has died down, the response varies significantly. From one perspective, this behavior is to be expected in terms of spoking properties within the thruster itself.

Figure 4.24 shows a smoothed set of data illustrating the obvious ability of the detector to see the fuel face after the pulse has ended. The current trace in yellow ends just as the surface signal in blue becomes readable. Also, the plume signal (red) fails to contribute measurable emission after the current pulse ends. This is consistent with all data sets showing that once the current has stopped flowing in the thruster, emission from the plasma and noise attributed to thruster EMI stop contributing to the voltage read at the detector.

A single set of data is analyzed here to demonstrate the data reduction process used. Figure 4.25 shows the surface conditions before conditioning and after testing. The thruster was conditioned for 200 pulses while the detector was shielded from viewing the face. After conditioning, the testing took some 50 additional shots. Figure 4.26 shows a set of 14 consecutive data shots from this test in the voltage domain without reduction. These data show significant noise during the pulse with some indication of the general measurement trend after the pulse. This may be caused by sparkplug noise. There is a second noise blip around $60 \mu\text{s}$ after initiation of the pulse. To see the general trends in the data, an 11-point smoothing routine is run on the measurements. Figure 4.27 shows the smoothed data highlighting acceptable data after the discharge has completed around $26 \mu\text{s}$.

Figure 4.28 shows the same 14 shots converted to the temperature domain and digitally filtered with a low-pass filter cutting off frequencies above 300 kHz. This filter removes the bulk of the noise both during and after the pulse, although the noise at 60 μs shows up as a bump on the measurement.

Figure 4.29 shows the pulse with the highest surface temperature at 26 μs (pulse 20), and co-plots this data with the current trace. Since the optical thickness of the plasma is insufficiently described, it is impossible to make any definitive conclusions regarding measurements taken while the plasma is present. Therefore all data before the end of the current pulse are disallowed. Figure 4.29 shows surface temperature uncertainty bars that are calculated using the procedure described in Section 4.2.1.3. The line drawn at 26 μs shows where acceptable data begins.

Figure 4.30 shows data from 20 μs to about 90 μs . This set shows the transition to acceptable data along with the spread of results obtained through the 14 pulses observed. These measurements are averaged together and the standard deviation is calculated. The standard deviation becomes another term in the uncertainty calculation from Eqn. 28. The average and total uncertainty of the 14 pulses is shown in Figure 4.31.

Figure 4.32 shows the cooling curves of two individual pulses (Pulses 19 and 20). These two are selected because they are near the coolest and highest temperatures observed during the set. A significant temperature difference is observed between the individual pulses. This difference is attributed to unpredictable changes in the surface-discharge arc location from shot-to-shot. This problem is discussed in Section 5.1.2.2.

4.2.3.5 Vapor Pressure and Post Pulse Performance

Surface temperature data can be used to calculate a Teflon vapor pressure leading to an estimate for mass loss and expected impulse bit. Figure 4.33 shows the current pulse and surface temperature for shot 20. The timeframe 25-40 μs is expanded and a pressure calculation is shown. The natural vapor pressure of heated Teflon is given by Wentink⁴⁶ (Figure 1.8) and later described by Turchi.^{64,2} The mathematical description of this curve is

$$p_{\text{eq}} = p_c e^{-T_c/T_s} \quad (30)$$

where p_{eq} is the equilibrium vapor pressure of Teflon, p_c and T_c are characteristic pressure and temperature values respectively, and T_s is the surface temperature. In this case, $p_c = 1.84 \times 10^{15} \text{ N/m}^2$ and $T_c = 20,815 \text{ K}$.⁶⁴ Combining this estimate of the vapor pressure with the measured surface temperature gives a time dependent pressure calculation relevant to neutral vapor generation after the pulse. Since the pressure is logarithmically dependent on the surface temperature, small changes in temperature data can result in large differences in pressure. The uncertainty shown is based only on the uncertainty in the temperature measurement. There is no information available for the pressure measurement uncertainty from the Wentink experiments.

The pressure can be used to calculate the impulse bit gained from the post-pulse neutral vapor generation. Assuming a symmetrical current sheet, the exposed Teflon propellant area is $2.13 \times 10^{-5} \text{ m}^2$. Combined with the pressure, this gives an instantaneous force on the propellant face due to the vapor pressure. Integrating this through the measurement time yields the impulse accumulated through the ablative cooling process. Figure 4.34 shows this with typical error bars. The total calculated impulse bit from post-pulse neutral generation is $1.1 \pm 0.5 \text{ } \mu\text{N}\cdot\text{s}$ with the largest contribution occurring before $40 \text{ } \mu\text{s}$.

The ideal gas law can be used to calculate the total number of particles liberated per unit volume.

$$n = \frac{p_c}{kT_s} e^{-T_c/T_s} \quad (31)$$

where k is the Boltzmann constant ($1.38 \times 10^{-23} \text{ J/K}$). Figure 4.35 shows the post-pulse neutral density calculated from Eqn. 31. Assuming that after the current pulse each particle liberated is a CF_2 monomer, the average particle mass is 50 AMU. Multiplying this value by Avogadro's number gives a molecular weight of $8.3 \times 10^{-23} \text{ grams/particle}$. Using calculations for thermal evaporation common to particle vapor deposition⁶⁵, the surface temperature and vapor pressure can be related to a molecular flux through⁶⁵

$$F = \frac{p_{eq}}{\sqrt{2\pi mkT_s}} \quad (32)$$

where m is the molecular weight, k is the Boltzmann constant, p_{eq} is the equilibrium vapor pressure, and T_s is the surface temperature. This relationship is derived from the

Clausius-Clapeyron equation. The molecular flux, F , is the number of molecules liberated from the surface per unit area per unit time. Using the data from Pulse 20 above and assuming that the surface temperature measured is representative of the total surface temperature, the molecular flux can be multiplied by the propellant surface area and integrated through time to yield a total molecular evaporation and therefore a total post-pulse mass loss. Figure 4.36 shows the integration of the mass loss (and molecular evaporation) through time with typical uncertainties. The total mass lost through post-pulse evaporation is $1.2 \pm 0.6 \mu\text{g}$. If this is compared with the average mass lost per pulse after 12,000 pulses from Figure 4.6c ($5.2 \mu\text{g}/\text{pulse}$), then the post pulse mass as a percentage of the total mass lost is $23 \pm 11\%$. The mass loss from the 12,000-pulse case is used because the mass loss from the 100 and 1000 pulse cases likely reflect starting transients. Note that the assumption of the measured surface temperature across the propellant face does not necessarily apply well due to arc spoking. When the averaged temperature and uncertainties from Figure 4.31 are used, the mass loss drops to $0.0176 \pm 0.046 \mu\text{g}$. This discrepancy is discussed further in Section 5.

It is also useful to estimate an exhaust velocity for these neutral particles evaporated after the pulse. It is assumed that since there is no energy source after the pulse, the surface temperature (T_s) is also the temperature of the evaporated gas just above the surface. Using the atomic mass from above, the specific gas constant, R , is calculated as $166 \text{ J/kg}\cdot\text{K}$. Assuming that the Teflon vapor is a thermally and calorically perfect gas and that the gas temperature is the same as the Teflon surface, the speed of sound for that gas is $a = \sqrt{\gamma RT}$. If the CF_2 molecule is assumed to not vibrate, then it has 3 translational and 3 rotational degrees of freedom. This gives a ratio of specific heats of $\gamma = (6+2)/6$ or 1.33. Estimating the diameter of the CF_2 molecule as $\sim 3 \text{ \AA}$, the cross sectional area, σ , is calculated as $7.07 \times 10^{-20} \text{ m}^2$. Since this is a neutral gas, a billiard ball approximation for the cross-section applies. Using the neutral density calculated from Eqn. 31, a mean free path can be calculated using

$$\lambda_{\text{mfp}} = \frac{1}{n_n \sigma} \quad (33)$$

At the start of Pulse 20, the mean free path is 8.7 μm . Taking the thruster diameter (0.00635 m) as a characteristic length, the Knudsen number is then about 10^{-3} , well within the collision-dominated regime. At about 40 μs the Knudsen number reaches 1, suggesting that a kinetic gas description may apply thereafter. However, because the neutral vapor is dense until then, a fluid dynamic centered expansion wave approximation is used to estimate the expected exhaust velocity.

It was suggested by Burton to use the Method of Characteristics as applied to unsteady flow by Anderson⁶⁶ to describe a centered expansion wave. Along a characteristic, the value of

$$u + \frac{2a}{\gamma - 1} = \text{const.} \quad (34)$$

where u is the expansion wave velocity and a is the local speed of sound. This can be modified to give a ratio of the local sound speed anywhere in the flow to the location where the local wave velocity is equal to the sound speed (Mach number = 1). This is given by

$$\frac{a}{a_4} = 1 - \frac{\gamma - 1}{2} \left(\frac{u}{a_4} - 1 \right) \quad (35)$$

where a_4 denotes the location of unity Mach number. Taking the surface temperature as the gas temperature at the surface and averaging from 25 until 40 μs , an average gas temperature of 740 K is calculated. Using isentropic relations, the gas temperature at the point where $M=1$ is calculated as 635 K. This translates to an a_4 value of 375 m/s. Eqn 35 can be manipulated through the isentropic relations to give a density ratio of

$$\frac{\rho}{\rho_4} = \left[1 - \frac{\gamma - 1}{2} \left(\frac{u}{a_4} - 1 \right) \right]^{\frac{2}{\gamma - 1}} \quad (36)$$

where ρ is the local gas density and ρ_4 is the density where $M=1$. A density weighted average for the expansion wave velocity can be calculated by numerically integrating

$$\bar{u} = \frac{\int \rho u dx}{\int \rho dx} \quad (37)$$

where the integral of ρdx gives the total mass. The technique used to perform this integral is to use the following relation from Anderson, which is a property of the Method of Characteristics

$$x = t \left(u - a_4 + \frac{\gamma - 1}{2} u \right) \quad (38)$$

where t is the time and x is the axial location of the local wave velocity. The integrals in Eqn. 37 can be transformed into velocity integrals by taking the derivative of Eqn. 38. This gives

$$dx = t \frac{\gamma + 1}{2} du \quad (39)$$

When this is substituted into the two integrals in Eqn. 37, the integral is performed from a_4 to u_{\max} . The time term is a constant in both integrals and therefore drops out. Since the background pressure is a vacuum, the density will decrease as the gas expands allowing a transition to supersonic velocities without a source of energy. Ultimately, the numerical solution to Eqn 37 is $\bar{u}=1.75a_4$. Using a_4 from above, the average velocity from the centered expansion wave approximation is ~ 655 m/s. This yields an I_{sp} of ~ 60 s for the post-pulse exhaust contribution. Combining this with the mass loss estimated from Eqn. 32, a total impulse bit from the post pulse ablation can be calculated again. The impulse bit estimated from this technique is 0.8 ± 0.4 $\mu\text{N}\cdot\text{s}$. This is within the uncertainty of the impulse bit calculated from the surface pressure of 1.1 ± 0.5 $\mu\text{N}\cdot\text{s}$.

These impulse bit values can be compared with the calculated electro-magnetic impulse bit. The electromagnetic impulse bit¹ is calculated by

$$\int T dt_{EM} = \frac{1}{2} L' \int I^2 dt \quad (40)$$

where I is the current measured with the rogowski probe and L' is defined by

$$L' = \frac{\mu_0}{2\pi} \left(\ln \frac{r_o}{r_i} + \frac{3}{4} \right) \quad (41)$$

where μ_0 is the permeability of free space ($4\pi \times 10^{-7}$ H/m) and r_o and r_i are the outer and inner electrode radii respectively. Using the current pulse measured for Pulse 20 yields an expected electro-magnetic (EM) impulse bit of 19 $\mu\text{N}\cdot\text{s}$. There is also an electro-thermal (ET) impulse bit contributed during the pulse from neutral vapor. Without

accurate thrust data for the 6.35 mm microPPT or surface temperature data during the pulse, this is difficult to estimate, but it is likely to add significantly to the total impulse bit. Assuming no ET contribution, the late-time neutral vapor generated can contribute a maximum of 8% of the total thrust. This is probably a significant overprediction and is discussed further in Section 5.

4.3 Measured Plasma Properties

4.3.1 Electron and Neutral Densities

Figure 4.37 shows the results of two-color interferometry for the case of a 6 J discharge with a 0.417- μF capacitor. At 2 μs , peak electron density is $8.7 \pm 1.0 \times 10^{16} \text{ cm}^{-3}$ and peak neutral density is $9.8 \pm 1.8 \times 10^{17} \text{ cm}^{-3}$. This data demonstrates the measurements and instrument resolutions achievable with this diagnostic. Also shown is a current pulse for these measurements. The densities shown are averaged over 20 firings of the microPPT with uncertainties determined by the standard deviations of those firings. From this two-color data is calculated ionization fraction (Figure 4.38) by assuming single ionization and using Eqn. 9. The ionization fraction oscillates slightly around 0.09. The uncertainty increases as the density signals decrease, but early in the pulse, it is ± 0.018 .

The uncertainties for these measurements and calculations are determined starting from Eqn. 26. Modifying this general form to accommodate two-color interferometry leads to

$$\omega_{n_e} = \sqrt{\left(\omega_{\Delta\phi_r} \frac{\partial n_e}{\partial \Delta\phi_r}\right)^2 + \left(\omega_{\Delta\phi_b} \frac{\partial n_e}{\partial \Delta\phi_b}\right)^2} \quad (42)$$

$$\omega_{n_n} = \sqrt{\left(\omega_{\Delta\phi_r} \frac{\partial n_n}{\partial \Delta\phi_r}\right)^2 + \left(\omega_{\Delta\phi_b} \frac{\partial n_n}{\partial \Delta\phi_b}\right)^2} \quad (43)$$

where ω_{n_x} is the total uncertainty for a given density measurement, $\omega_{\Delta\phi_i}$ is the uncertainty limitation due to the detector, n_x is density (n_e for electrons, n_n for neutrals), and $\Delta\phi_i$ is phase shift ($\Delta\phi_r$ for the infrared frequency, $\Delta\phi_b$ for the blue frequency). This reduces to the uncertainty equations for n_e and n_n (in MKS-radians). Plugging in $\pm 0.5^\circ$ for $\omega_{\Delta\phi_r}$ and

$\omega_{\Delta\phi b}$ gives a single shot uncertainty for electrons $\omega_{ne} = \pm 2.80 \times 10^{14} \text{ cm}^{-3}$. Likewise, for the neutrals, $\omega_{nn} = \pm 1.14 \times 10^{16} \text{ cm}^{-3}$.

Although this serves as adequate for single firings of the micro-PPT, actual analysis typically takes multiple numbers of pulses to characterize the operating envelope of these thrusters since they are dominated by shot-to-shot irreproducibility. The total uncertainty from a statistical viewpoint is

$$\Delta n_{tot} = \sqrt{(\Delta n_{vib})^2 + (\Delta n_{PPT})^2} \quad (44)$$

where Δn_{vibs} is the uncertainty due to vibrations and Δn_{PPT} is the shot-to-shot variation of the PPT in question. Typically PPT operation results in the shot-to-shot uncertainty defining an operating envelope for the thruster. This is where focusing of the beams onto the detector active area plays a significant role in reduction of uncertainty. On a shot-to-shot basis, if the detectors are forced to sample the same location in the plume, a more accurate measurement of the relative phase shifts for the different laser frequencies is obtained. The end result is an uncertainty that is much improved over that shown in Figure 1.2 and Figure 1.4.

After about 50 μs , mechanical vibrations begin to catch up to the thruster irreproducibility and can grow to overwhelm any neutral signal after the pulse. The Herriott Cell was introduced to combat this effect by increasing the signal-to-noise ratio of the system. It has failed to produce results on a micro-PPT to this point. For this reason, only measurements of densities within the timeframe of the pulse are presented.

Finally, the uncertainty in calculated ionization fraction is given by

$$\delta\alpha = \sqrt{\left(\delta n_e \frac{n_n}{(n_e + n_n)^2}\right)^2 + \left(\delta n_n \frac{-n_e}{(n_e + n_n)^2}\right)^2} \quad (45)$$

where the δn_e and δn_n are the electron and neutral density uncertainties defined by standard deviations over at least 20 firings.

4.3.2 Electron Densities with Propellant Recession

Measurements of electron density are shown in Figure 4.39 for flush and recessed propellant locations. The red curve shows measurements from the flush case as shown in Figure 2.26. The green curve shows the electron density measurements when the propellant is recessed 50 mm into the outer tube. The blue curve shows the case where spherical expansion of the exhaust is permitted for 50 mm with the propellant flush with the thruster exit plane. For all three cases, the central electrode is the high voltage cathode with firing occurring at 6 J. The significant difference in magnitude between the blue and green traces indicates that propellant recession into the outer electrode tube does increase directed plasma flux away from the propellant face. It also indicates that although there is an initial delay time associated with the distance from the propellant face to the exit plane of the microPPT, the electron density pulse fades with the end of the current pulse. This is true for both recession and flush propellant locations.

4.4 Propellant Recession Profile

As the thruster is repetitively fired, the Teflon propellant recesses back into the outer electrode tube. The profile of this recession is roughly conical due to increased current density near the central electrode. Figure 2.27 shows a cutaway of a microPPT fired at 6 J for 6 hours at 1 Hz. The outer copper electrode was removed using nitric acid, and the Teflon was then shaved away carefully using a razor blade. The axis shown is from the Datathief program⁵² to attempt measurements of the actual ablation profile. Figure 4.40 shows these measurements along with a prediction by Keidar's model.³³ Agreement is fairly close, the red and black curves are the experimental measurements from both above and below the central electrode. The green is the prediction by Keidar. The experimental measurements have some uncertainty not shown due to positioning of the axes on the picture. This uncertainty in the y-direction is $\sim\pm 0.3$ mm. The x-direction is more accurately measured with an uncertainty of $\sim\pm 0.1$ mm. Both the predicted depth and profile are close to those measured experimentally.

4.5 Model Results and Comparison

4.5.1 Keidar-Boyd Model

4.5.1.1 Thruster Plume

Development and details of the Keidar Boyd Model (K-B Model) are given in references 30-35. Figure 4.41 shows predictions from the K-B Model for a.) electron and b.) neutral density during the discharge of the microPPT compared with the experimental measurements shown in Figure 4.37. The experimental uncertainties have been reduced significantly allowing a more exact comparison with theoretical predictions. Presently, both electron and neutral density predictions show a peak structure that follows power deposition to the arc. Simulation matches the experimental measurements extremely well indicating that any further refinement of the theory must move to description of small details that are not being modeled quite correctly.

Predictions of recession electron density are shown in Figure 4.42 compared with measurements from interferometry. In this plot, several hypotheses are being tested against the experimental data. The green trace shows an expected neutral density which is not measured experimentally. The red trace shows electron density with an assumption of ion reflection from the outer tube when it is the anode. The blue trace is the electron density using ion neutralization against the outer tube throughout the discharge. The black trace is the experimental data shown in Figure 4.39 (green trace). The delay times are close, but the assumption of ion neutralization against the outer tube causes significant underprediction of the electron density magnitude throughout the pulse. In the case where ion reflection from the anode is assumed, the electron density magnitude matches well with experiment. However, the electron density signal does not decay at the same time as experimental data. The implications of this are discussed in Section 5.2.1.2.

4.5.1.2 Propellant Ablation and Coning

Modeling of the ablation process typically assumes a symmetric current sheet across the face of the thruster. The K-B model states that Joule heating is the primary source of heat flux to the propellant. Since the current density is highest at the central

electrode, the ablation profile will depend on the radius. The calculated ablation depth for a single pulse (Figure 4.43) shows this dependence. The expected recession depth is at a maximum near the central electrode. By multiplying this ablation depth by the number of pulses, the total recession depth is calculated.

Figure 2.27 shows a cutaway of a microPPT fired at 6 J for 6 hours at 1 Hz. Figure 4.40 shows these measurements along with a prediction by Keidar's model.³³ Agreement is fairly close, the red and black curves are the experimental measurements from both above and below the central electrode. The green is the prediction by Keidar. The experimental measurements have some uncertainty not shown due to positioning of the axes on the picture. This uncertainty in the y-direction is $\sim\pm 0.3$ mm. The x-direction is more accurately measured with an uncertainty of $\sim\pm 0.1$ mm. Both the predicted depth and profile are close to those measured experimentally.

4.5.1.3 *Surface Temperature*

Figure 4.44 shows a K-B Model prediction of the surface temperature both near and far from a theoretical arc spoke location. "Near" refers to surface temperature from an area that was directly underneath the current constriction. "Far" refers to a distant section of propellant face that only sees radiation effects. These two predictions then provide the maximum and minimum temperatures expected during the cooling phase. They also constitute an expected distribution of cooling curves based on proximity to the arc location.

Figure 4.45 shows comparison of both curves to the averaged data shown in Figure 4.31 above. The expected cooling corridor from the prediction is close to the statistical spread of the experimental data. Of particular importance is immediately post-pulse the experimental and predicted surface temperatures are close to the same range. The experimental cooling profile is similar to the predicted profile, but cools faster. The K-B Model uses only ablation as a heat removal mechanism from the propellant face. By omitting radiation from the surface and thermal conduction into the surface, their prediction cools at a slower rate than is measured. The experimental data suggests that radiation and thermal conduction mechanisms should be included for a more accurate cooling curve prediction.

Keidar's specific predictions concerning surface temperature near and far from arc constriction can be evaluated by comparison with single pulses that mark the highest and lowest temperatures measured. It is thought that a temperature measurement made in a location directly under the constriction will have the highest temperature post-pulse cooling curve and that one far from the constriction (i.e. heated only by radiation) will have the lowest temperature cooling curves observed. Any spread between these values reflects changes in proximity to the actual constriction location. Figure 4.46 shows comparison of a.) the highest temperature cooling curve from the data set (pulse 20 shown in Figure 4.32) compared with the surface temperature predicted for an area covered by the arc constriction. Part b.) shows a comparison of the lowest temperature cooling curve from the data set (pulse 19 from Figure 4.32) compared with the surface temperature predicted for an area far from the arc constriction. The difference in these measurements suggests that the arc was moving randomly around the propellant face during testing. This is not conclusive proof. Two-dimensional imaging of the propellant face in the LWIR would be required to positively assess constriction location on a shot-to-shot basis. However, since there is no other evidence available on the spoke locations during firing, the theoretical predictions are the only viable check that the diagnostic is measuring expected temperatures in real-time.

4.6 Chapter 4 Figures

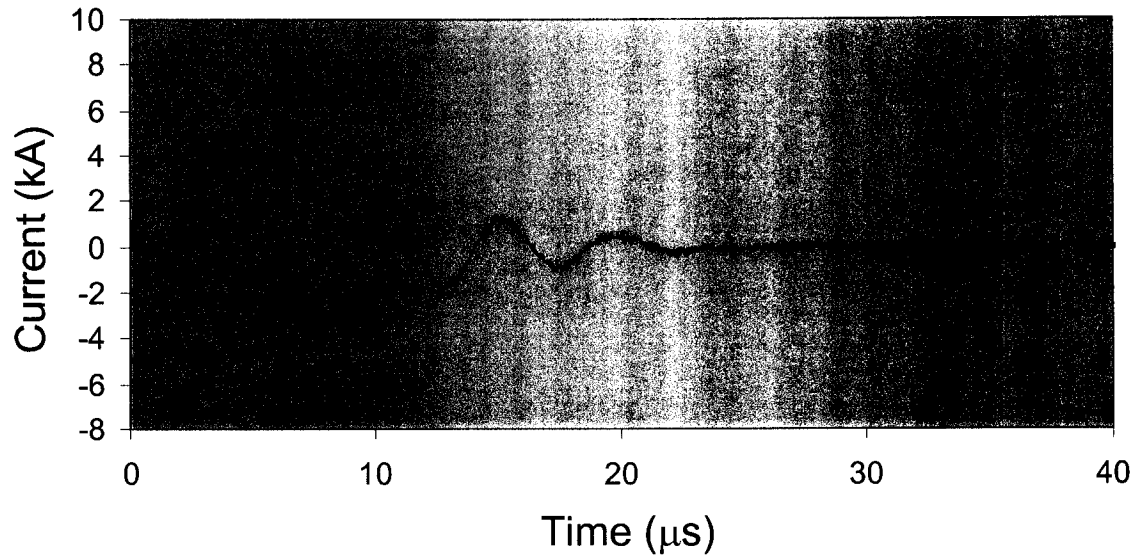


Figure 4.1: Typical current trace for microPPT operation in these tests (4.35 J).

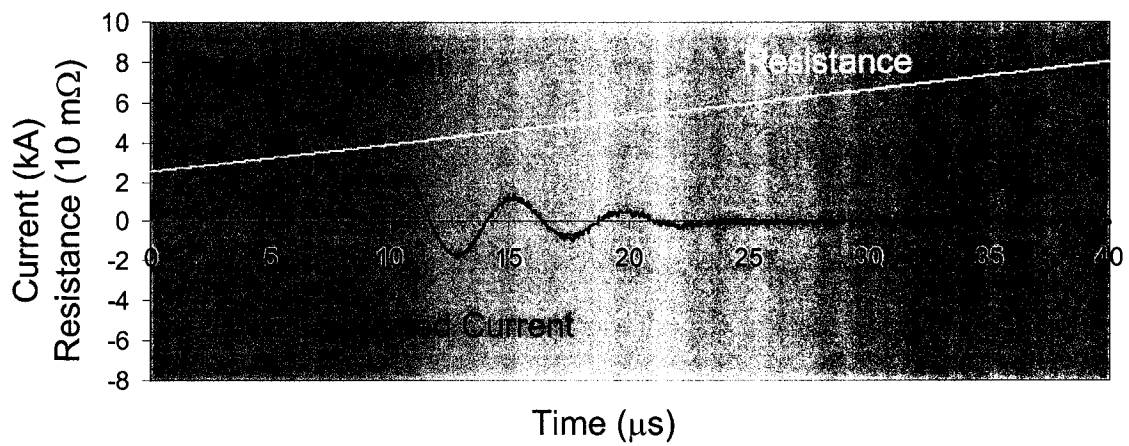


Figure 4.2: Comparison of measured and calculated current with linearly varying resistance.

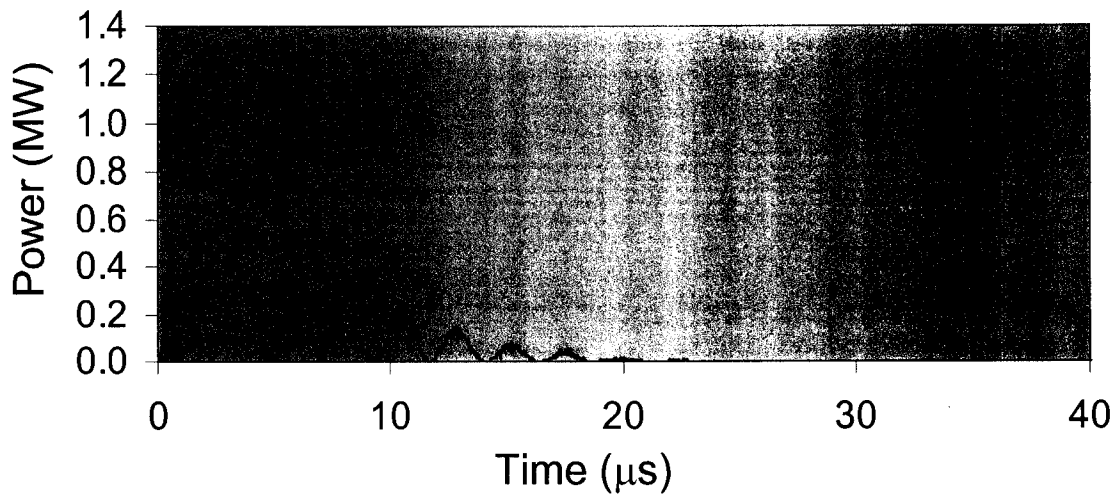


Figure 4.3: Power deposition from the capacitor using the current and estimated resistance.

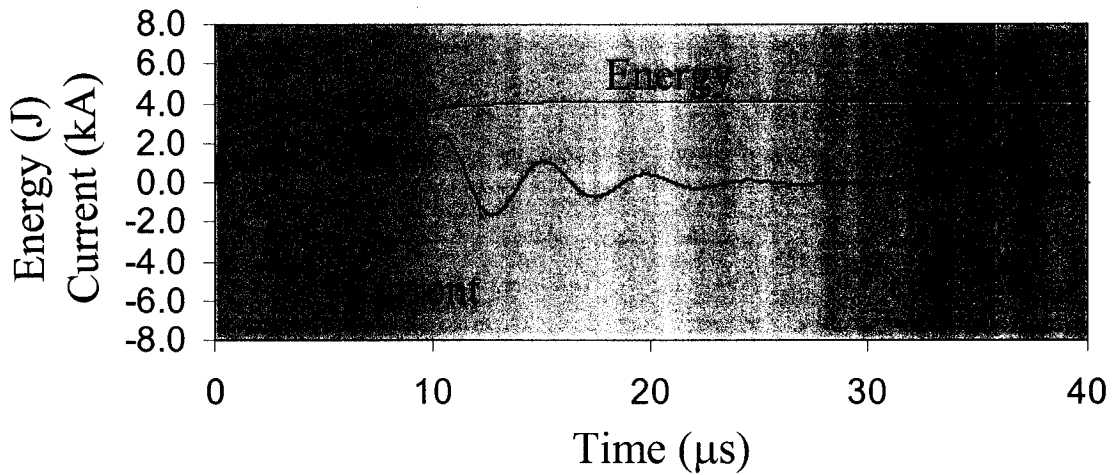


Figure 4.4: Energy deposition during a typical microPPT firing.

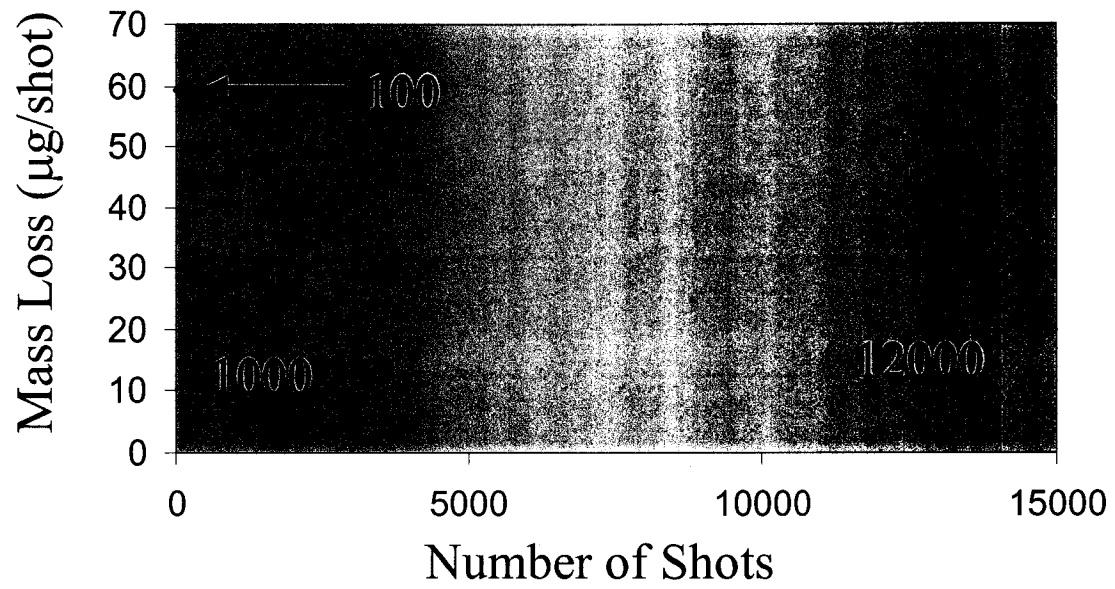


Figure 4.5: Mass Loss per pulse from average mass loss over varying number of shots at 4.35 J.

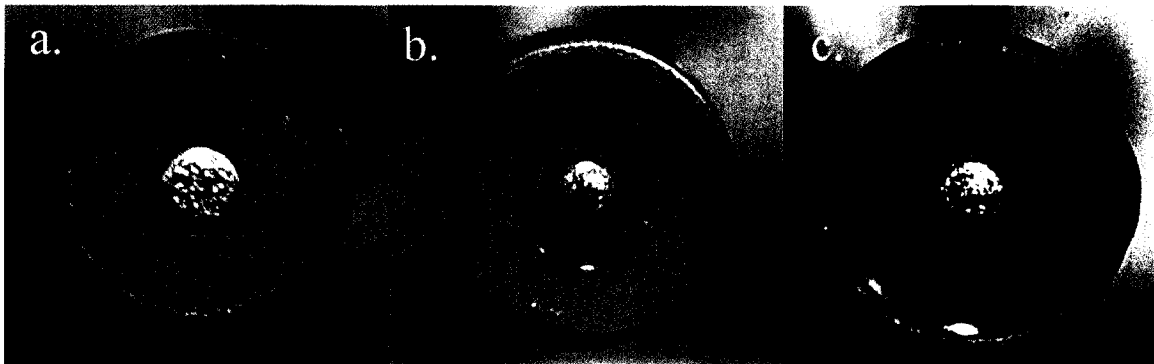


Figure 4.6: Teflon surface after a.) 100 shots, b.) 1000 shots, and c.) 12000 shots at 4.35 J.

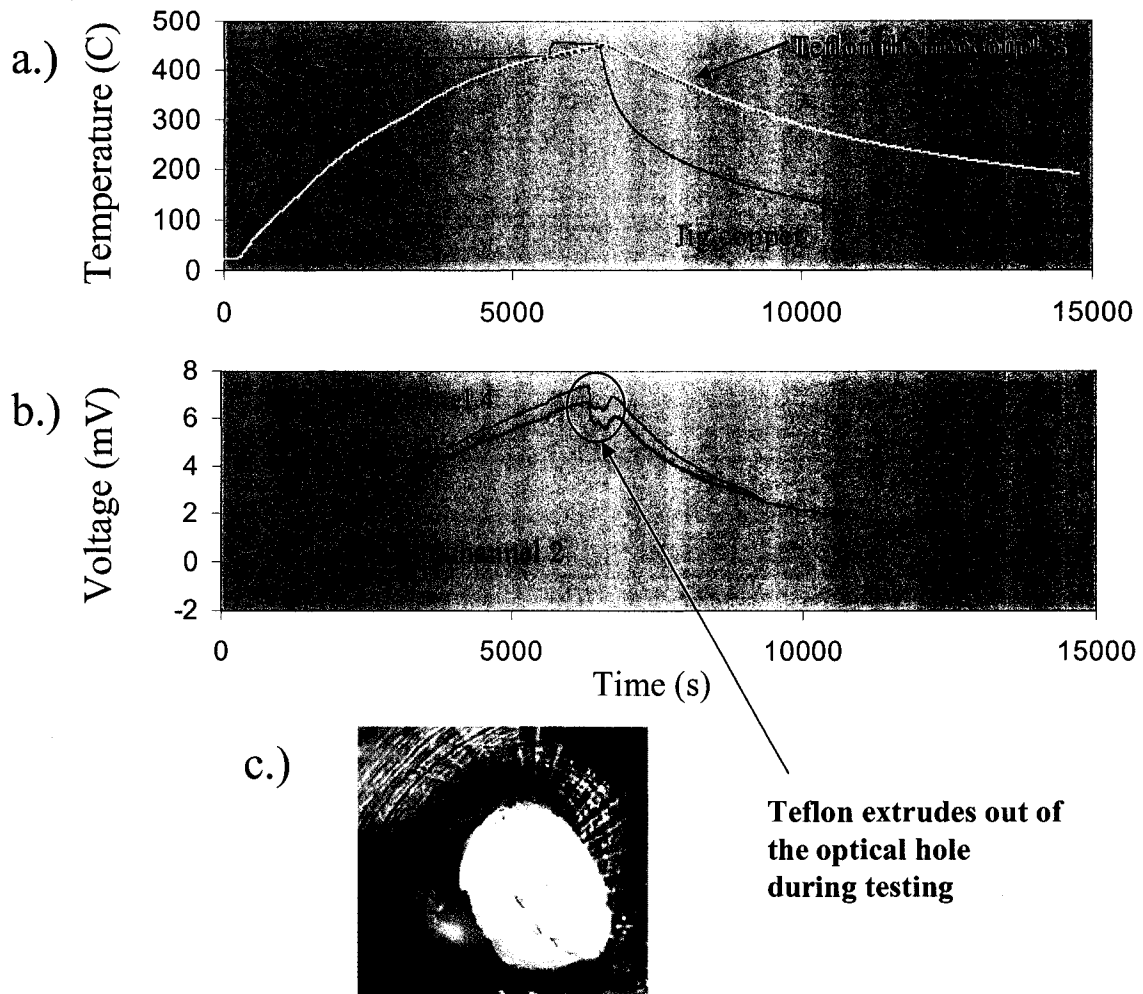


Figure 4.7: A calibration run where the Teflon extruded out of the optical hole. It is easy to identify where the signal is disrupted.

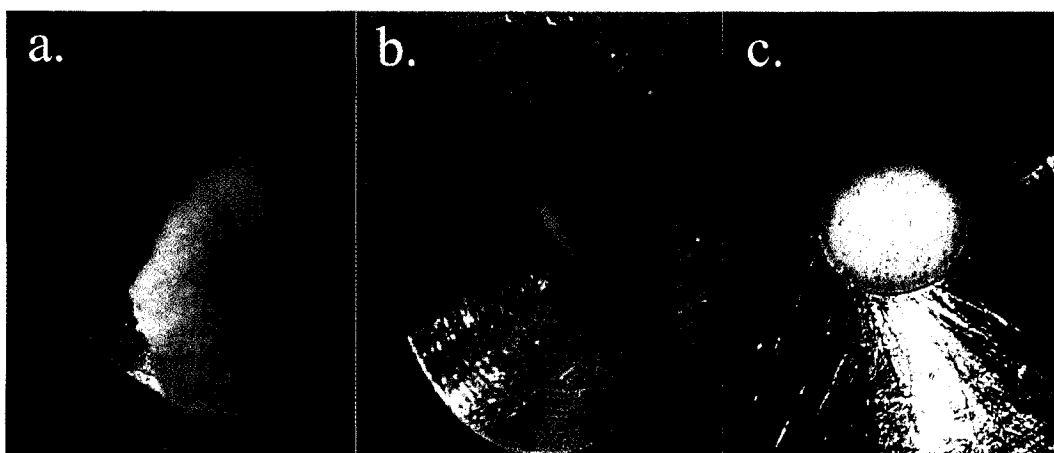


Figure 4.8: Teflon a.) flows and b.) extrudes through the calibration hole. In one case c.) it remained flat.

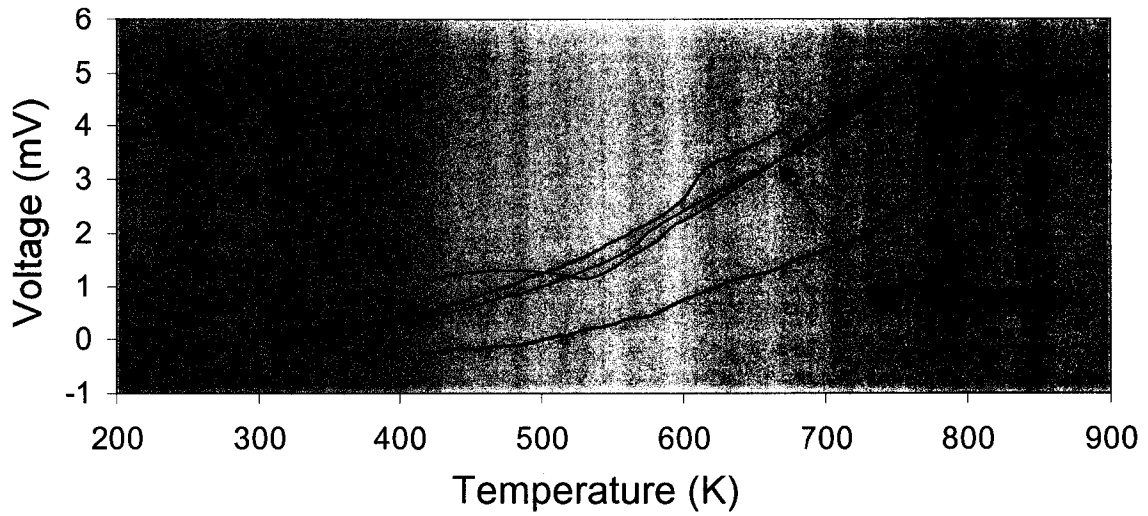


Figure 4.9: Calibration curves for cases where deformation occurs (blue) and does not (red).

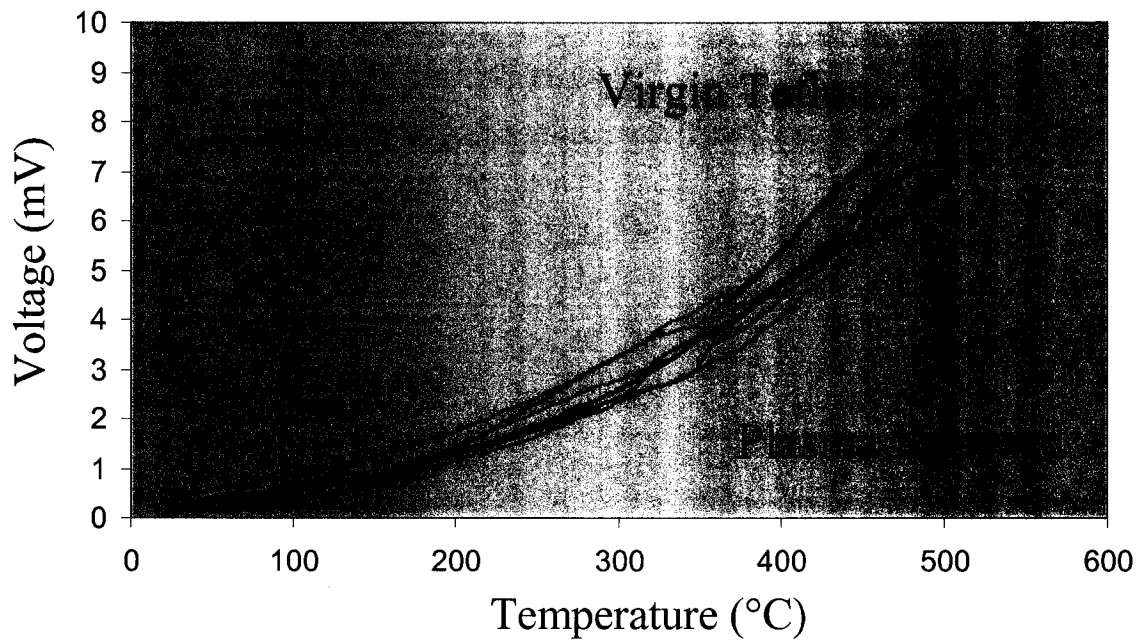


Figure 4.10: Calibration tests for virgin and plasma exposed Teflon.

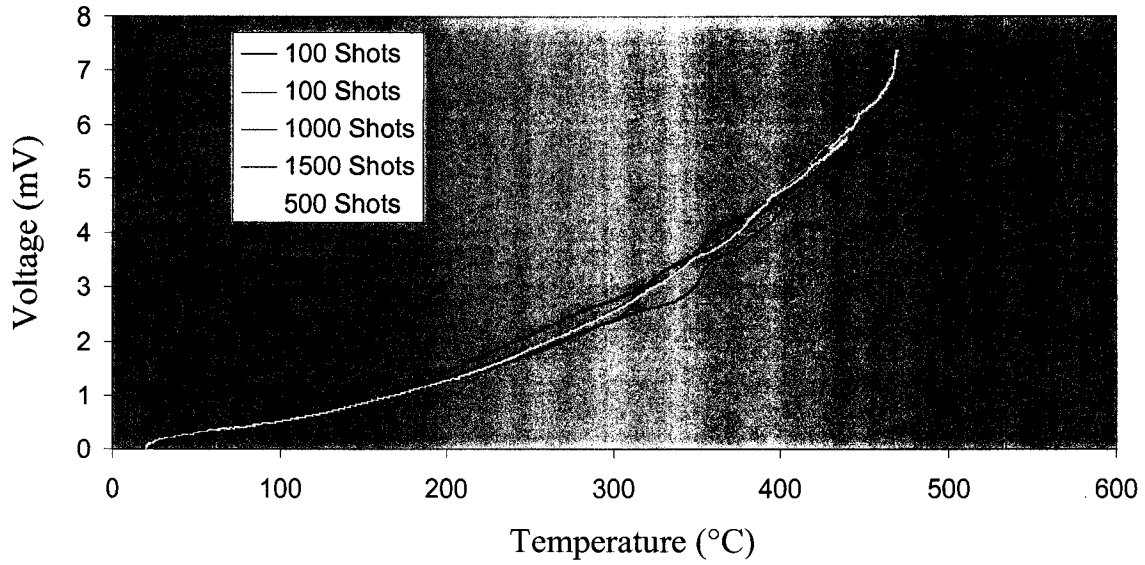


Figure 4.11: Plasma exposed calibration curves for varying plasma exposures.

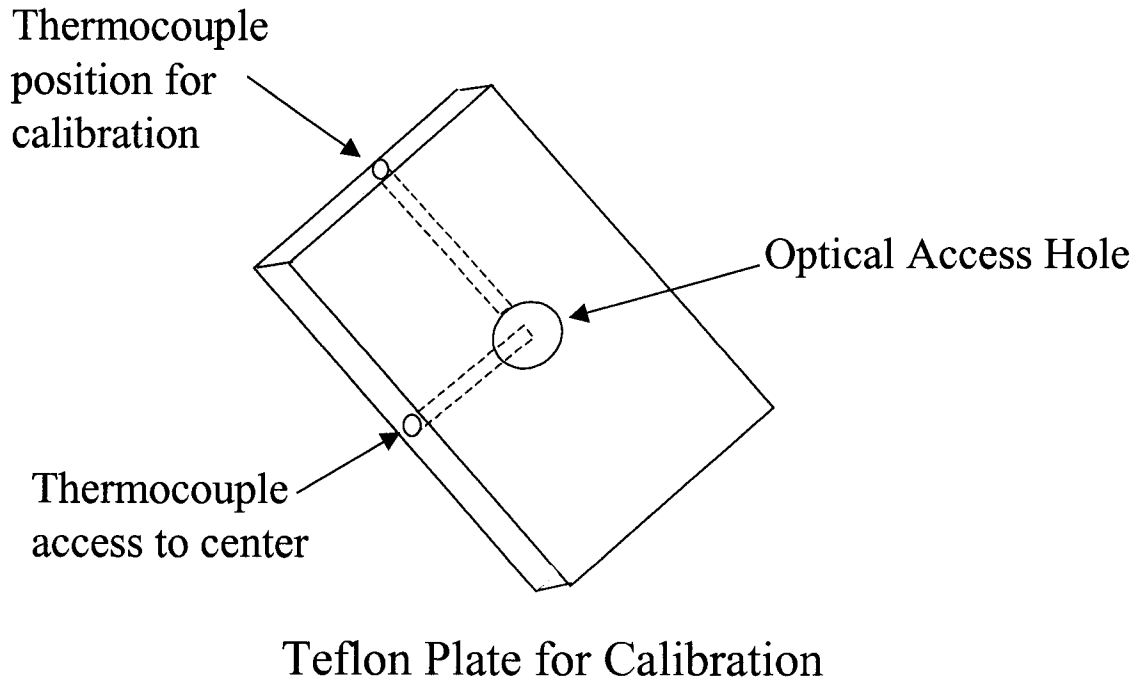


Figure 4.12: Teflon plate used for calibration tests showing typical thermocouple location for testing and a centered thermocouple to characterize the temperature gradient.

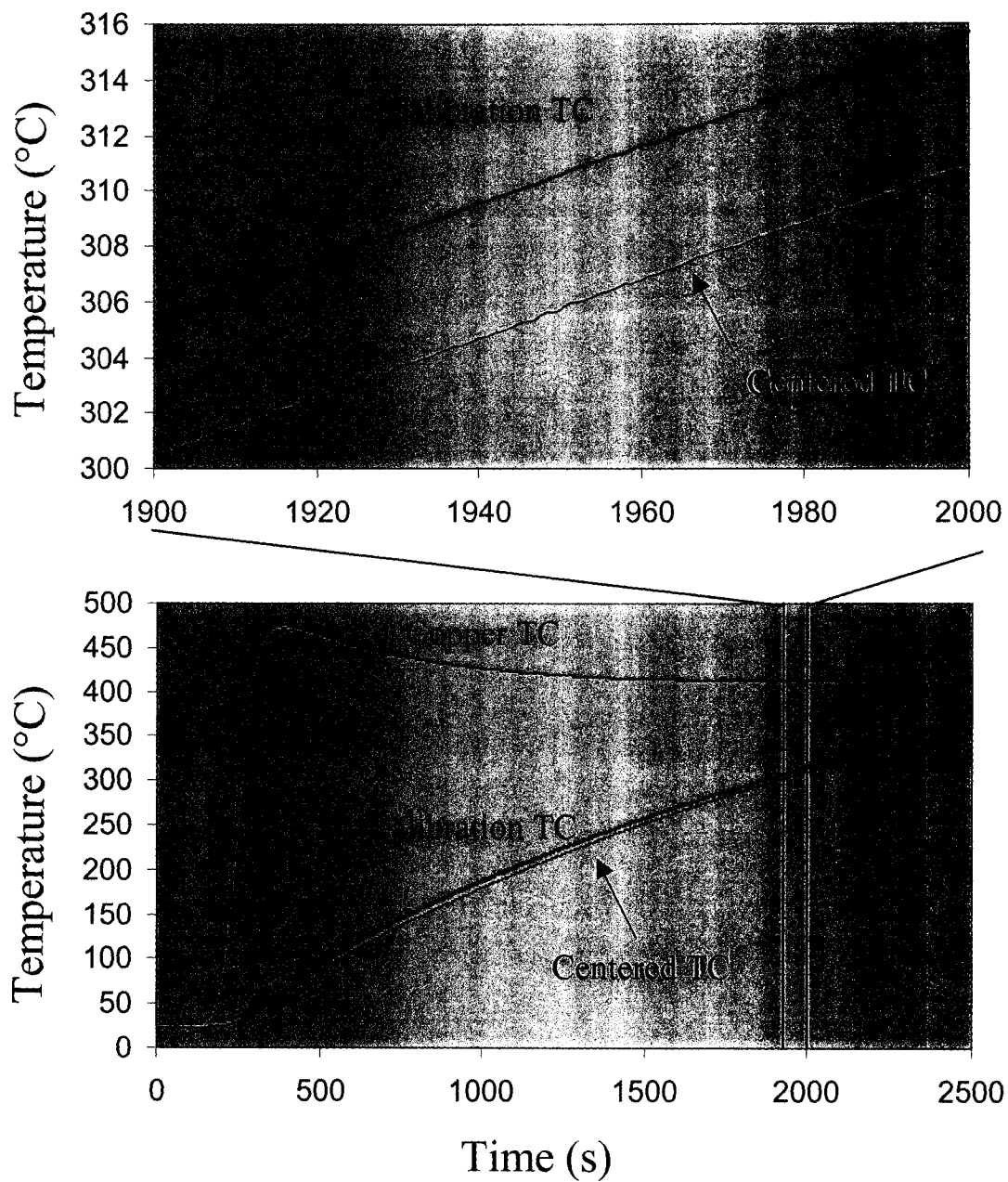


Figure 4.13: A heating test with a centered thermocouple shows a measured difference of $\sim 6^{\circ}\text{C}$ when compared with the standard testing location.

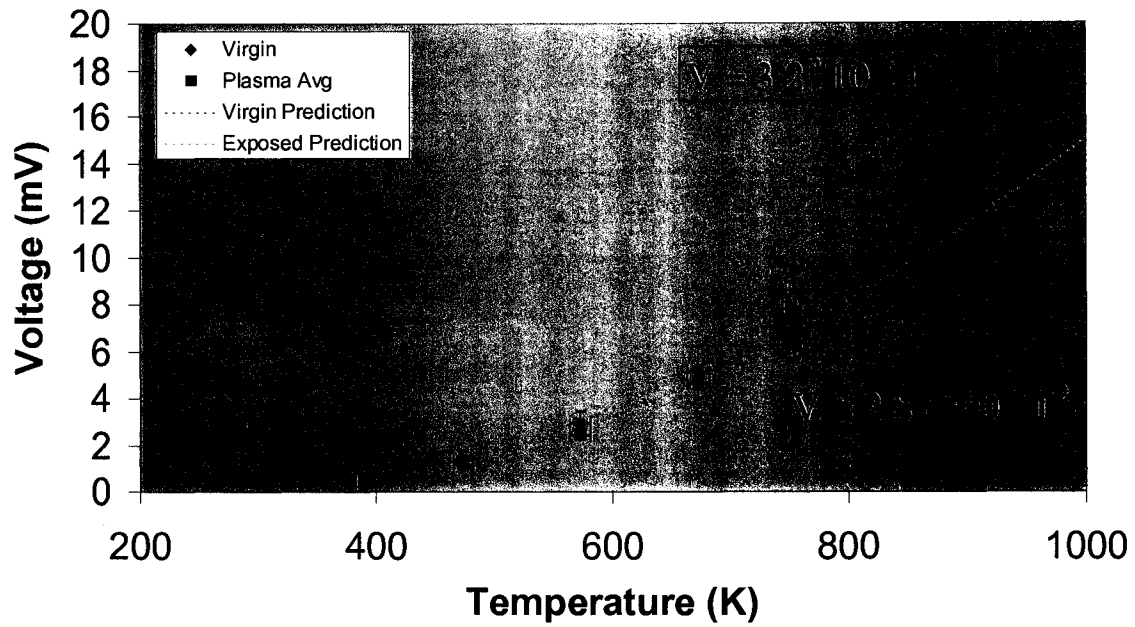


Figure 4.15: Difference between virgin and plasma exposed Teflon calibrations along with T^2 fits. Representative data points shown.

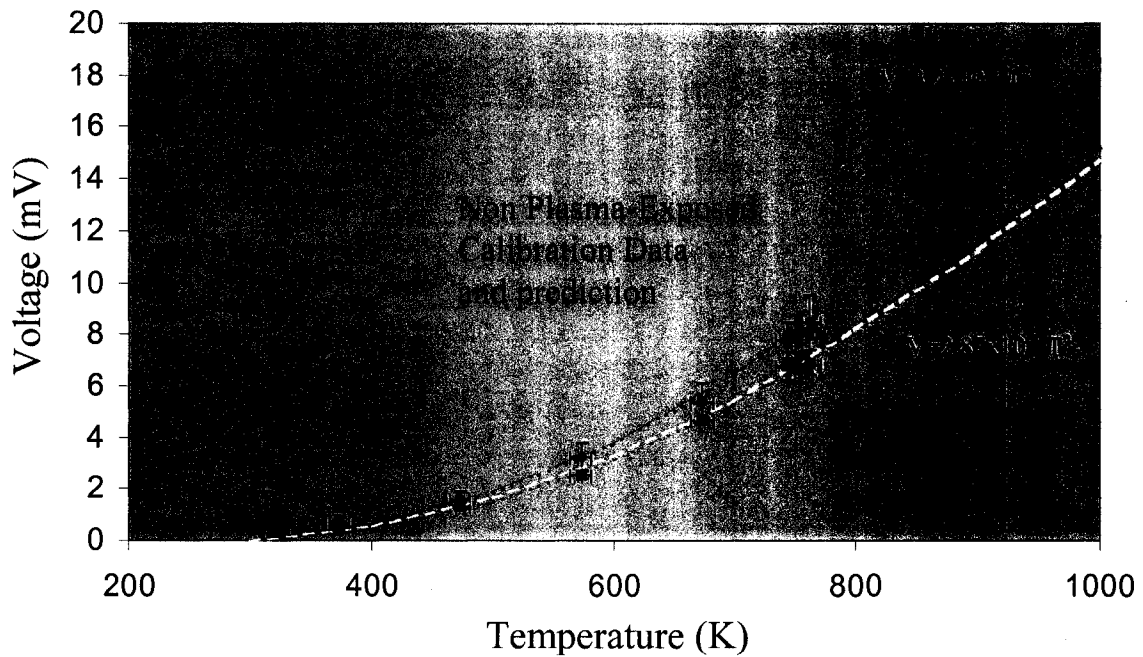


Figure 4.16: Experimental calibration data with T^2 fits shown with theoretical predictions of the calibration using the Teflon emissivity estimate.

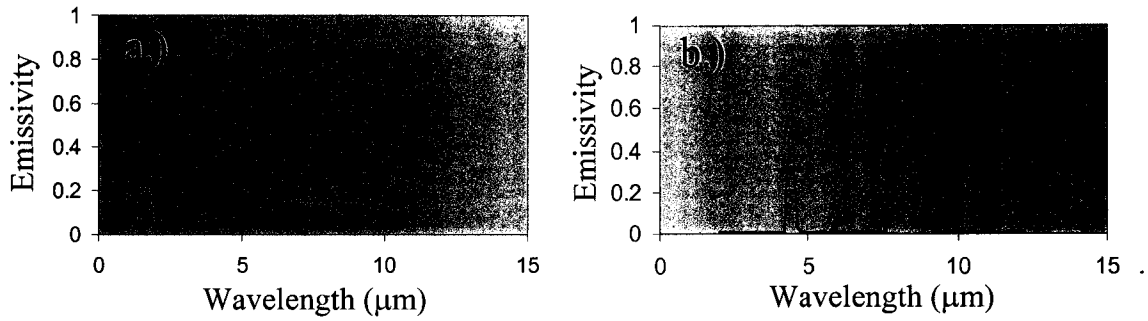


Figure 4.17: Estimated a.) virgin Teflon emissivity and b.) plasma exposed Teflon emissivity for 2-12 μm wavelengths.

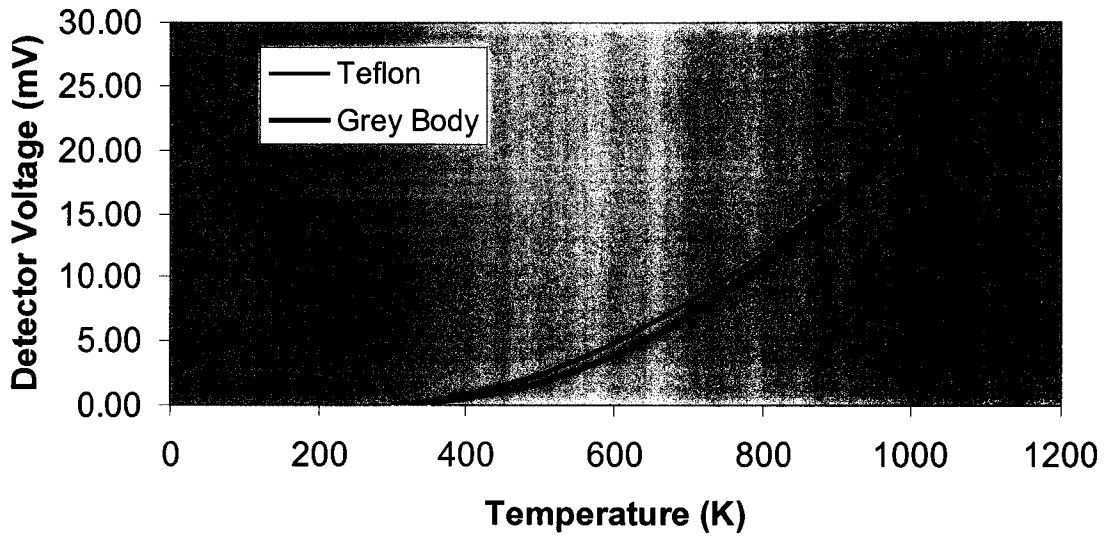


Figure 4.18: Detector voltage comparison for the Teflon emissivity estimate from plasma exposed Teflon and a grey body with emissivity 0.113.

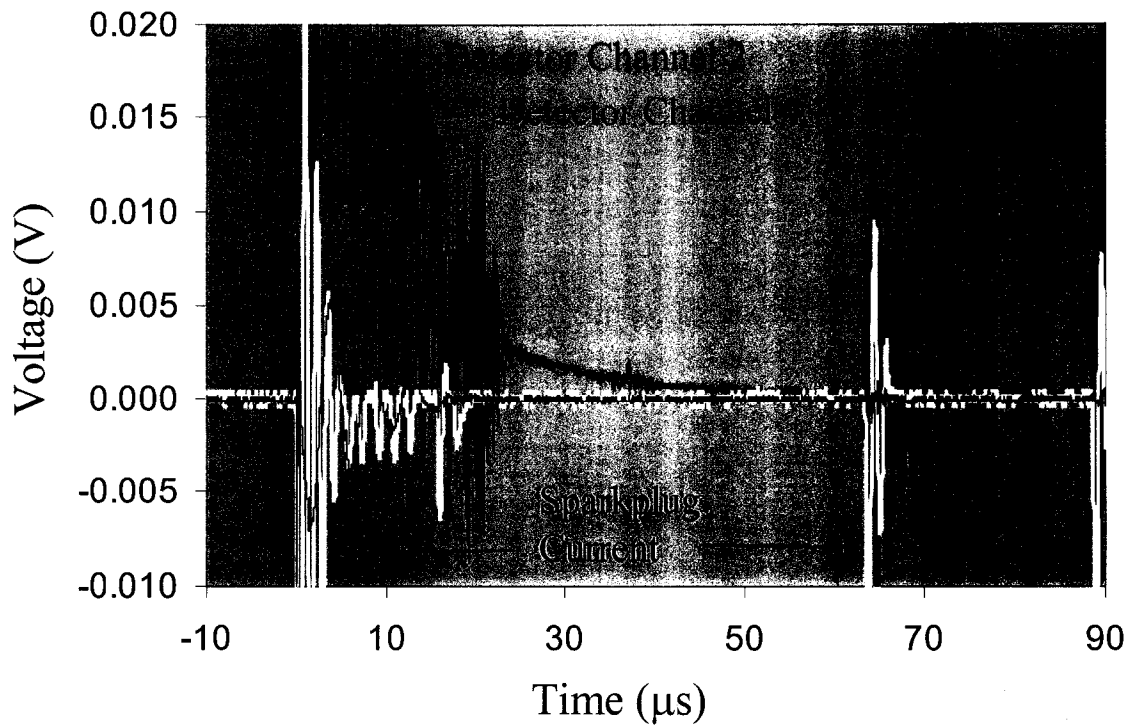


Figure 4.19: Detector noise in both channels is caused by current spikes in the sparkplug (yellow). The sparkplug causes EMI that is unavoidable at these low detector voltages.

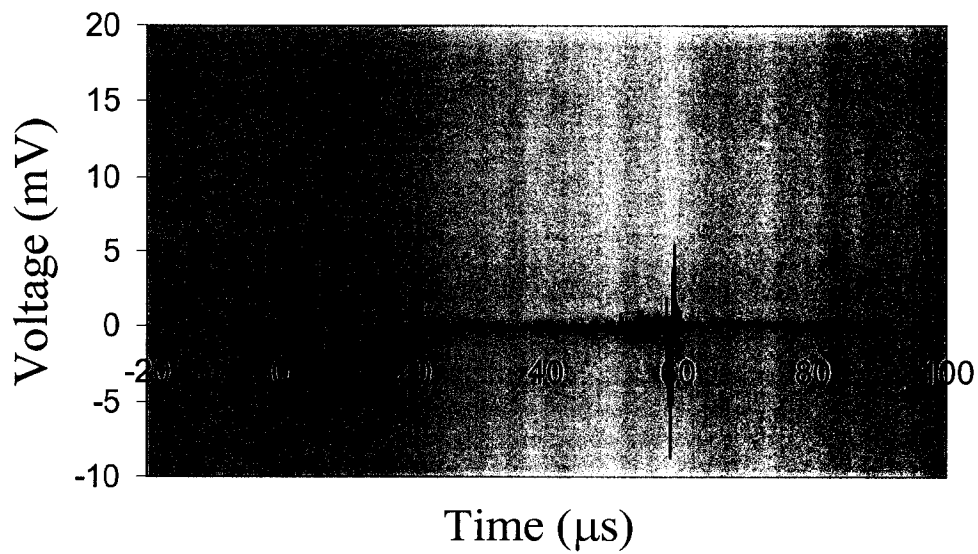


Figure 4.20: A typical thruster firing with optical shield in place to block detection of the IR emission and show just the electrical noise.

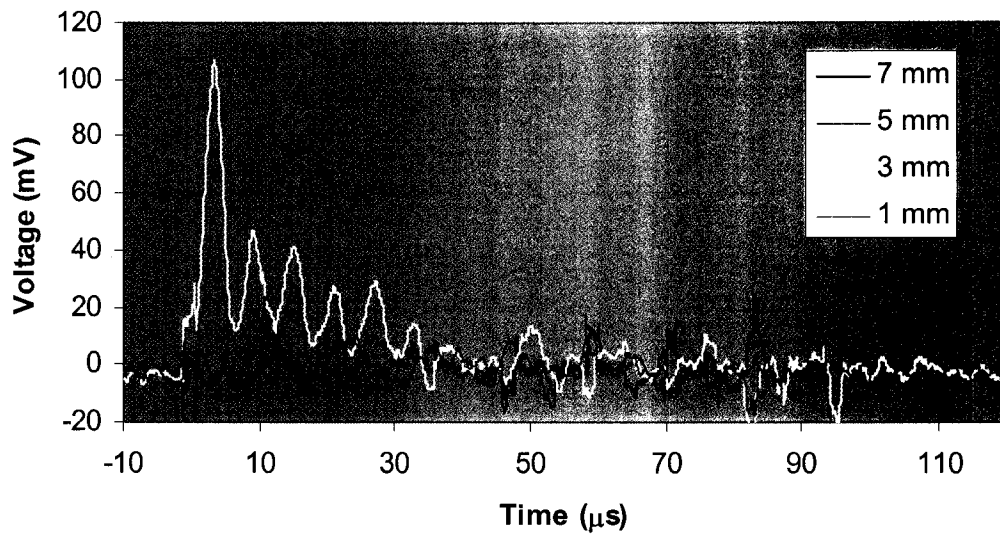


Figure 4.21: Plume signals observed at varying distances from the fuel face.

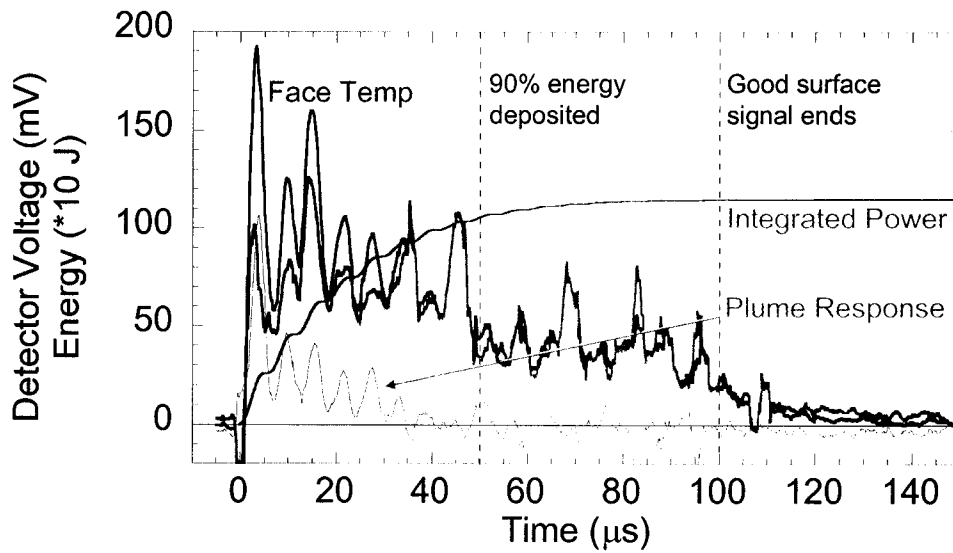


Figure 4.22: Plume and surface response with energy deposition over time.

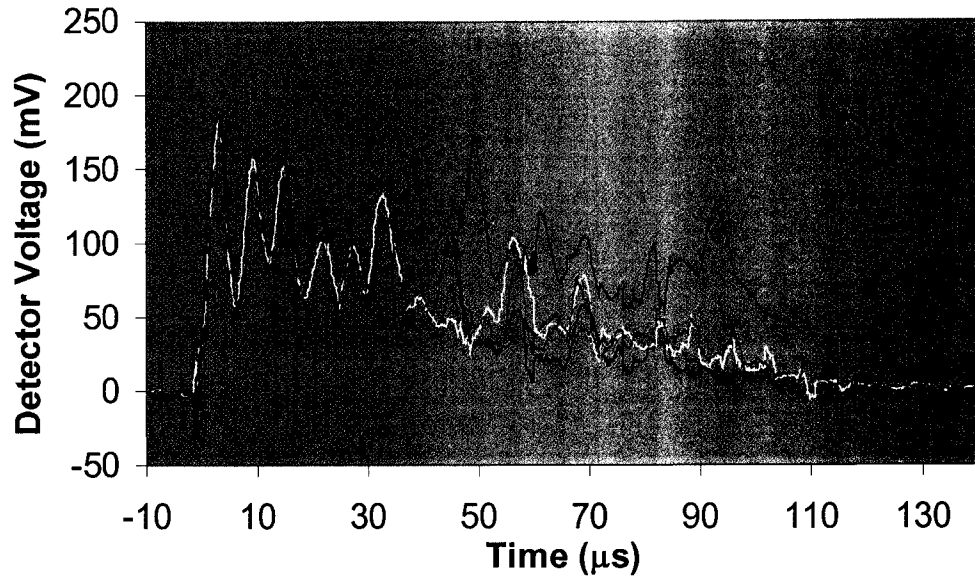


Figure 4.23: Five voltage measurements viewing the thruster face illustrate signal repeatability during the pulse with variation after ~30 ms.

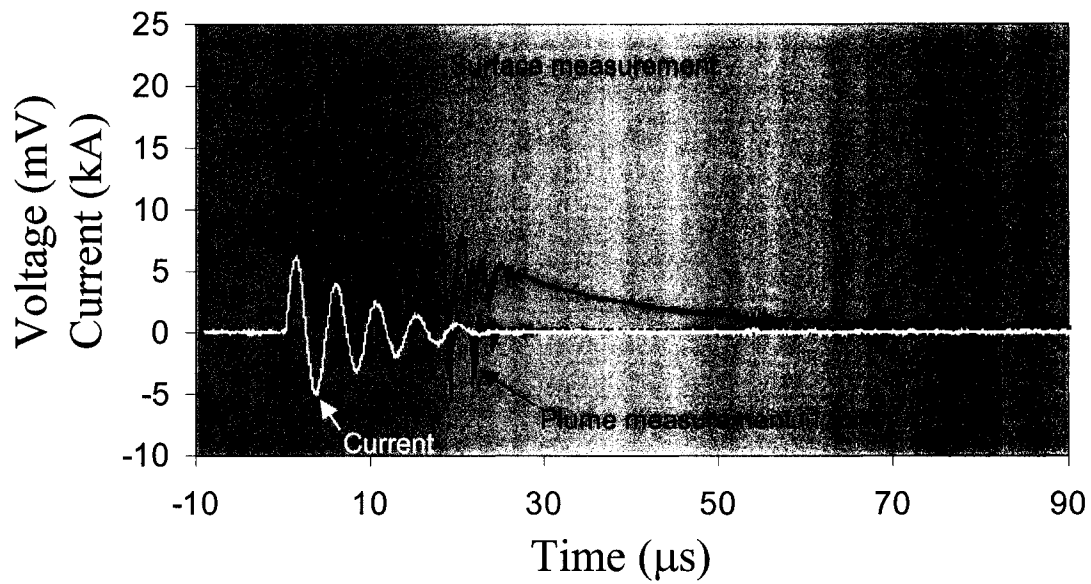


Figure 4.24: Comparison of surface and plume measurements in a micro-PPT. 4.35 J

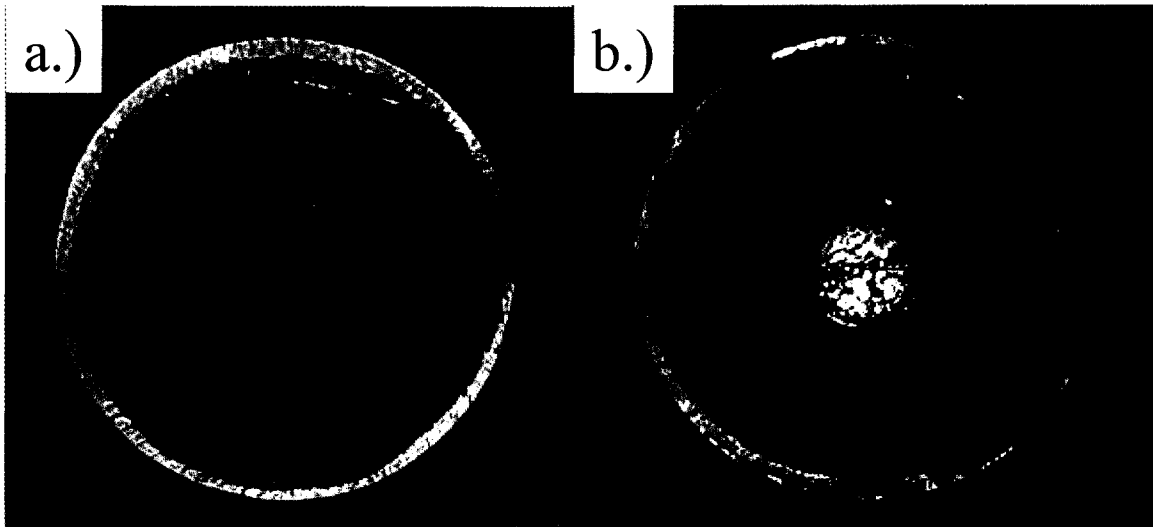


Figure 4.25: The thruster face a.) before conditioning and testing and b.) after testing. The targeting location is shown on the right. The following data corresponds to the surface conditions of this face.

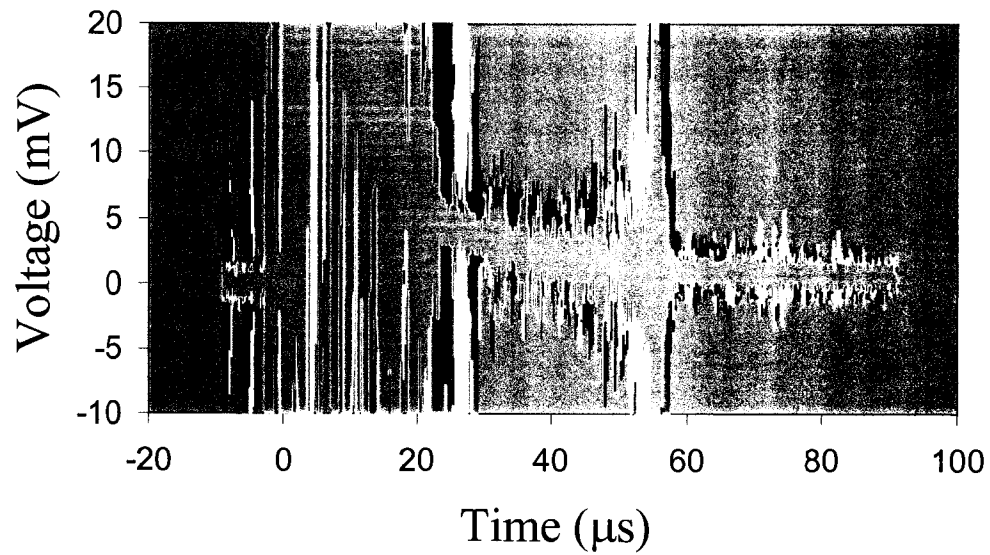


Figure 4.26: 14 consecutive shots on a microPPT at 4.35 J not reduced.

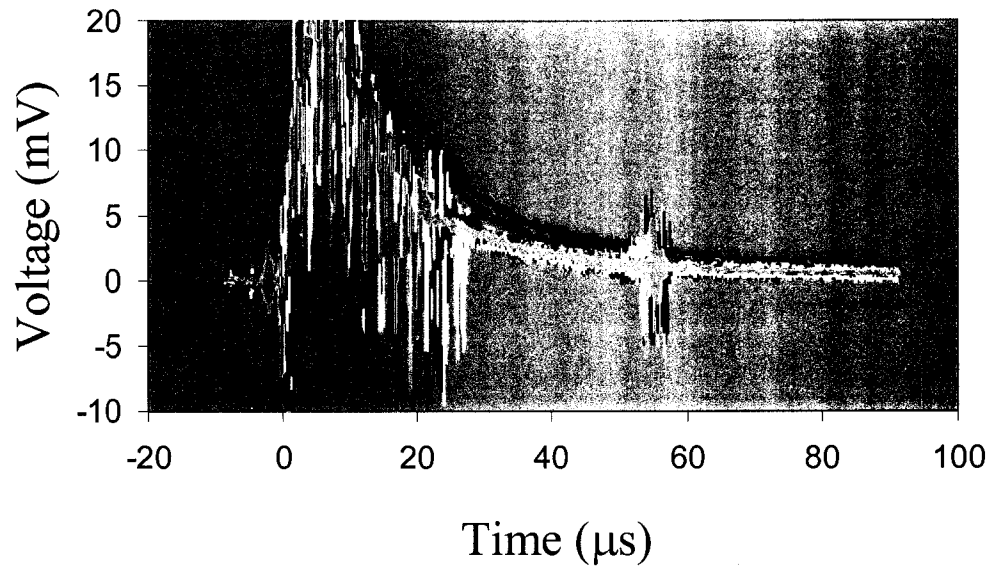


Figure 4.27: 14 shots from Figure 4.26 with 11-point smoothing shows trends, but also still has significant noise.

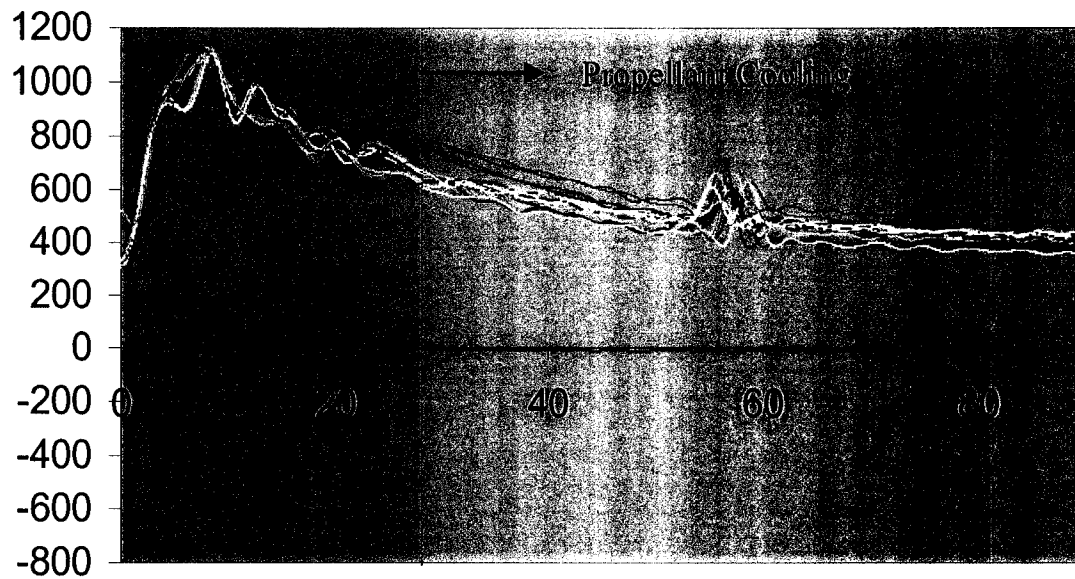


Figure 4.28: 14 shots are filtered with a 300 kHz cutoff frequency. These data are also shown in the temperature domain.

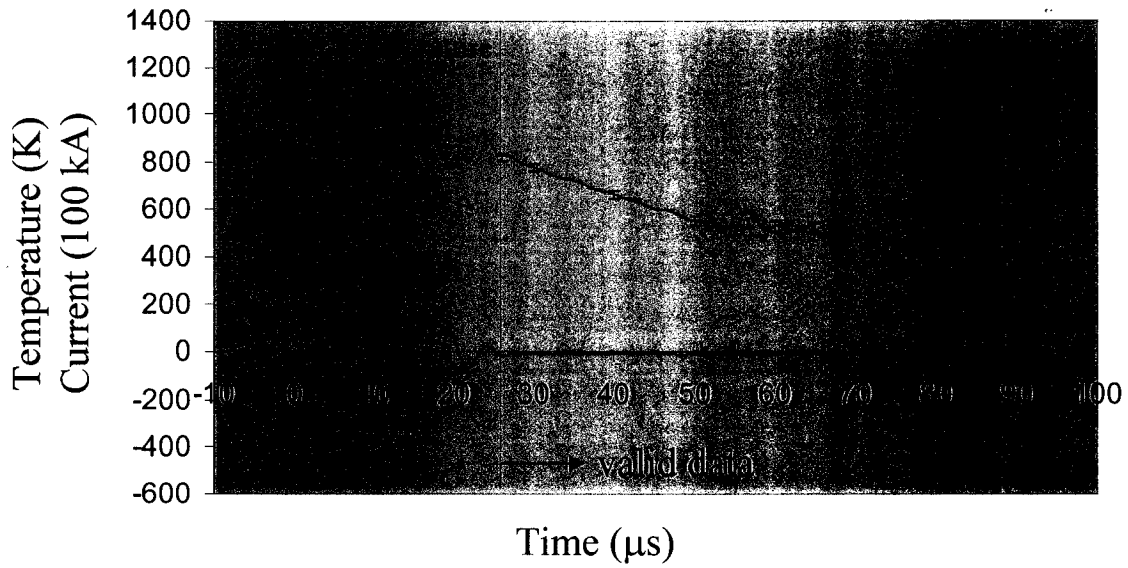


Figure 4.29: Measurement from pulse 20. During current reversal it is unknown whether the surface is measured. Therefore acceptable data begins at 20 μ s.

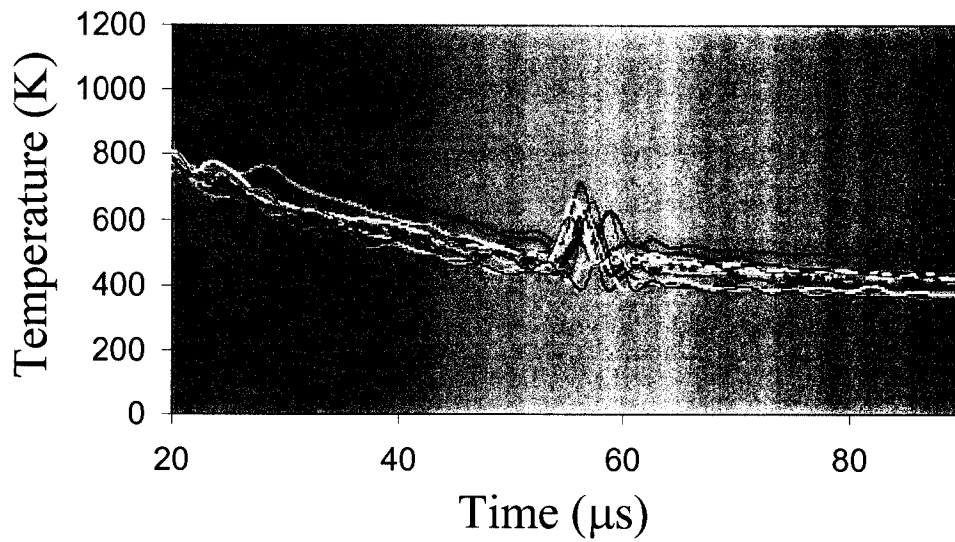


Figure 4.30: Cooling curves from 14 pulses shown together.

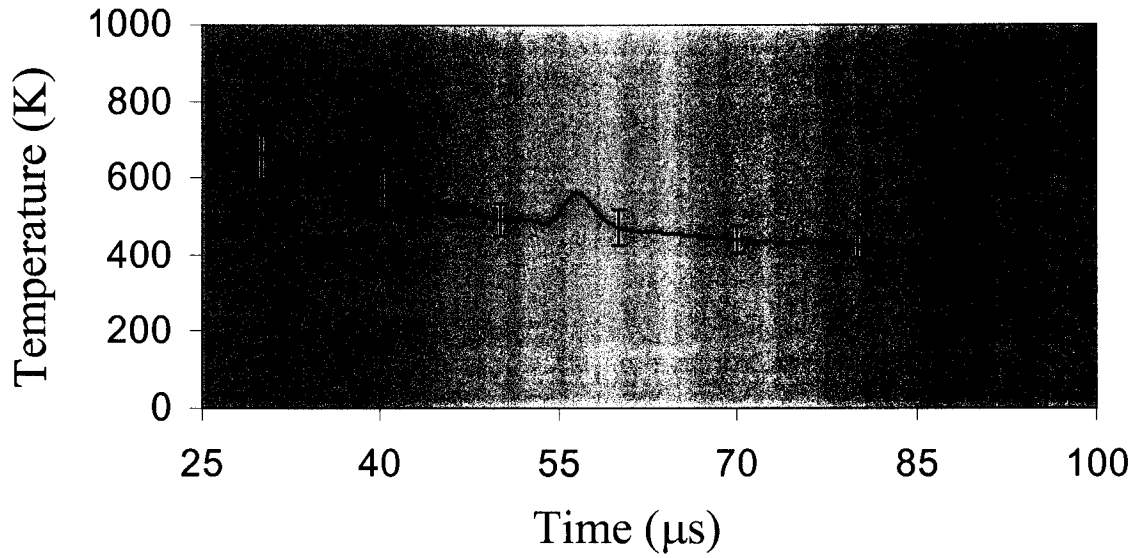


Figure 4.31: Average of the 14 pulses in Figure 4.30 with typical uncertainty bars calculated by standard deviation.

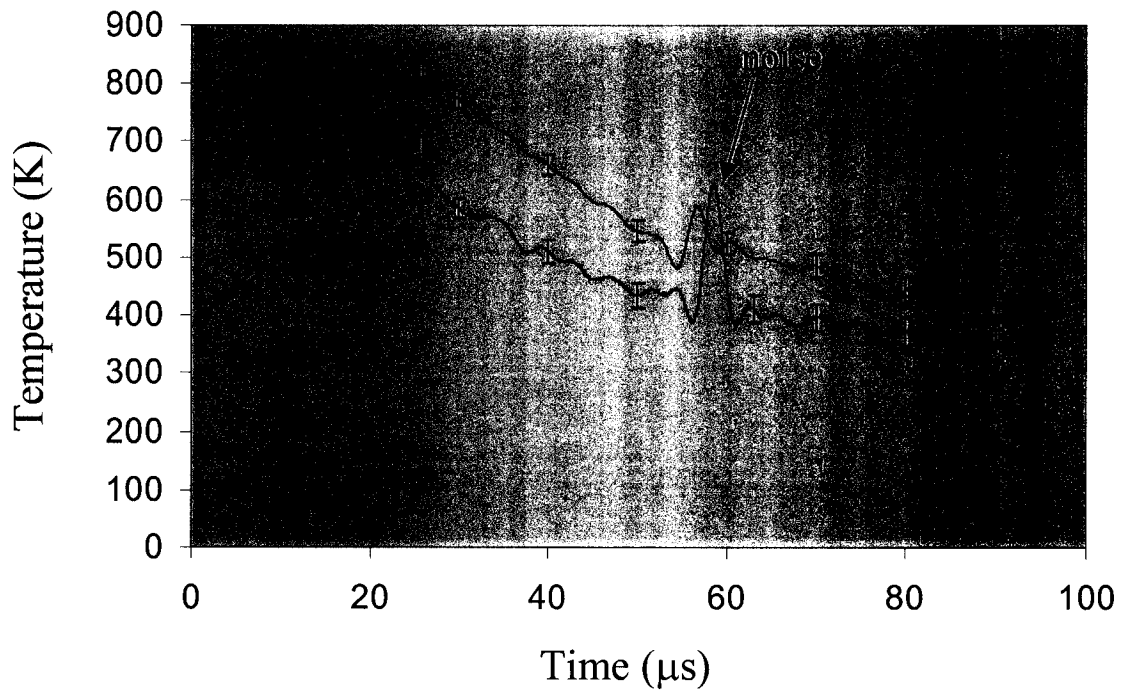


Figure 4.32: Single pulse cooling data from pulses 19 and 20 showing individual measurement uncertainty for these cases.

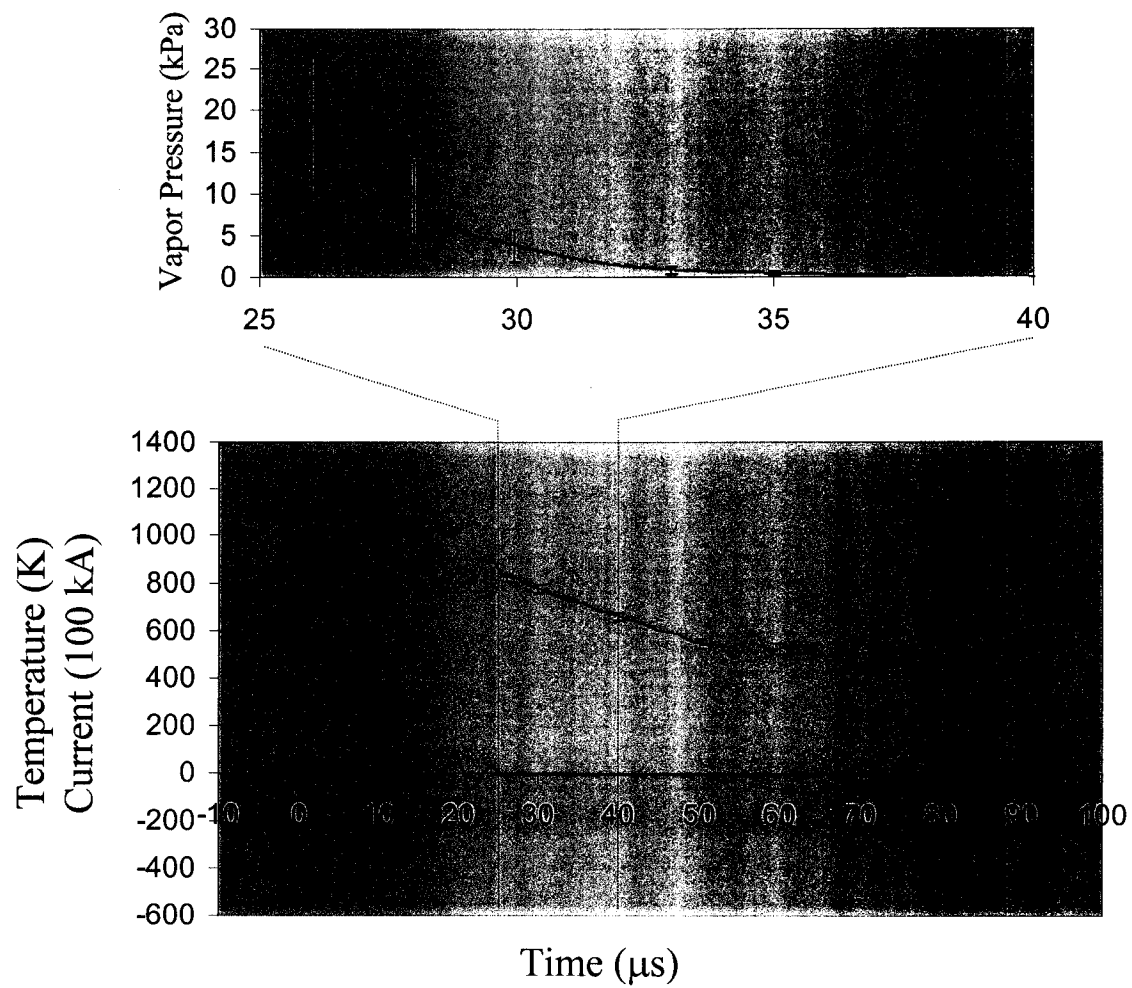


Figure 4.33: Measurement of the cooling curve allows calculation of the Teflon vapor pressure after the pulse.

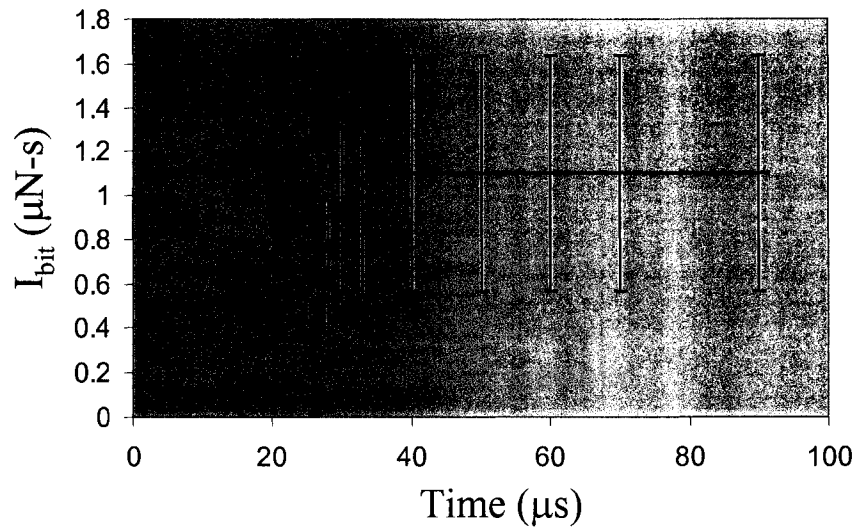


Figure 4.34: Post-pulse impulse bit contribution from neutral Teflon vapor pressure is calculated using the pressure shown in Figure 4.33.

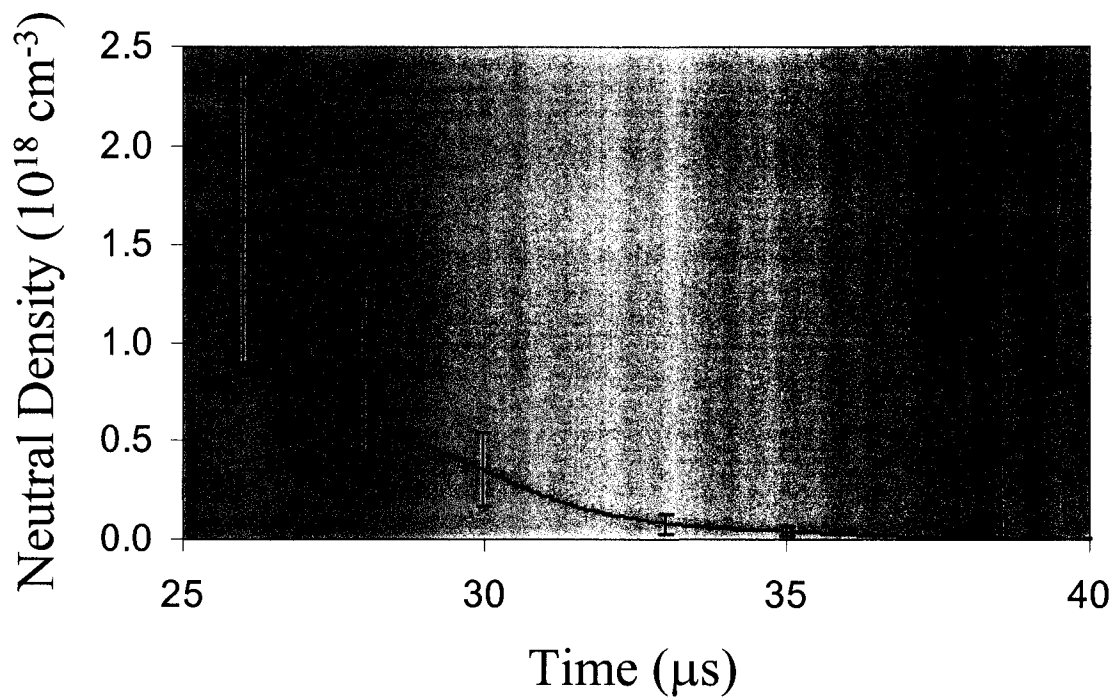


Figure 4.35: Expected post pulse neutral density for Pulse 20 is calculated using the Ideal Gas Law.

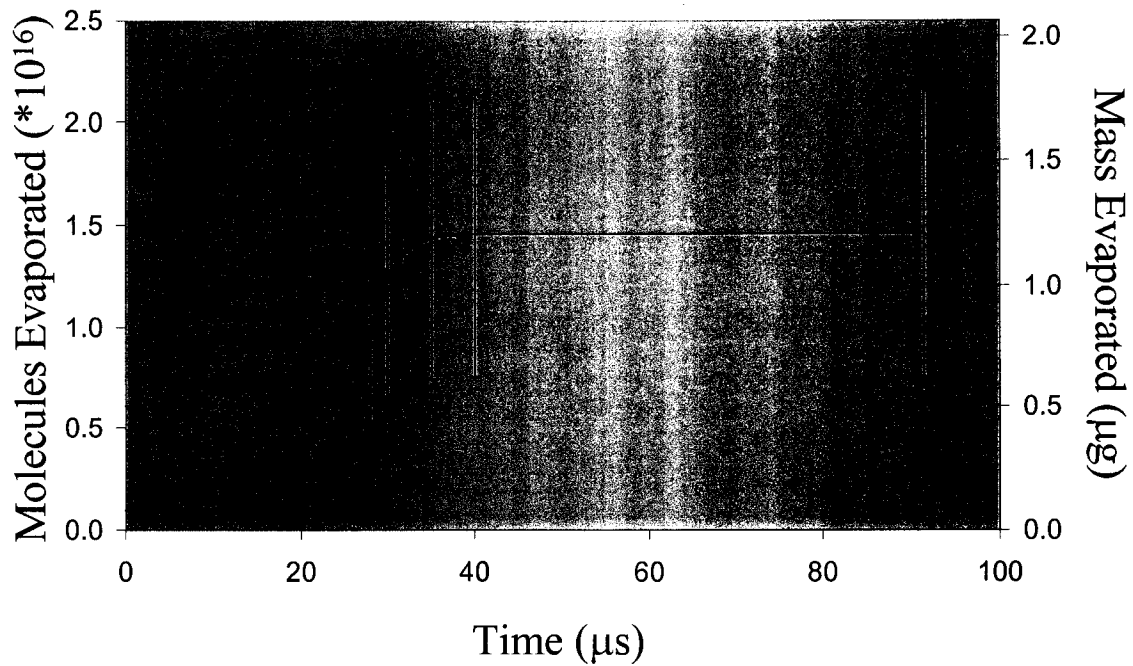


Figure 4.36: Total number of molecules and mass evaporated based on the surface temperature measurement of Pulse 20.

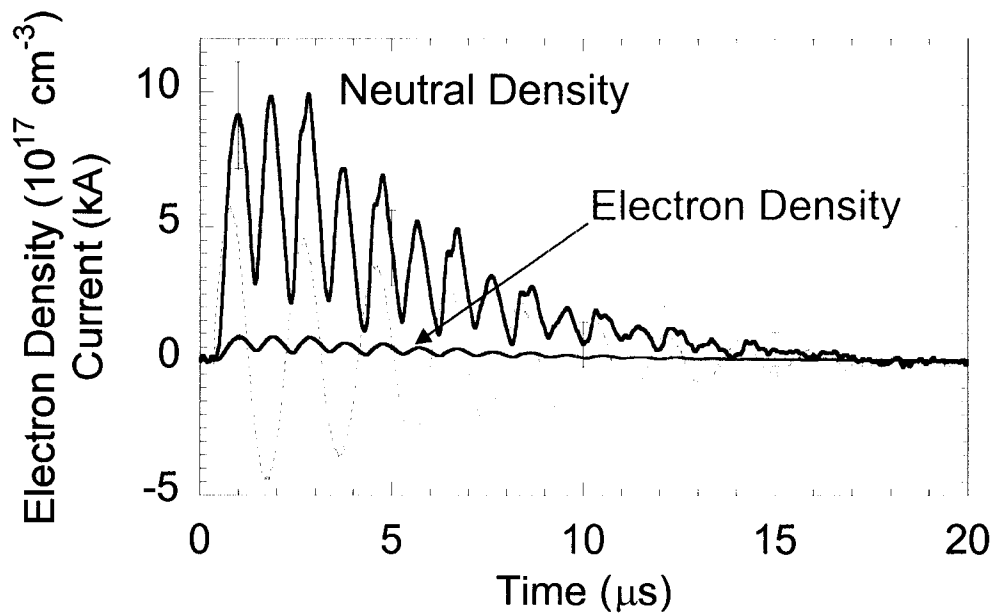


Figure 4.37: Separation of electron and neutral density for a 6.35 mm DIA MicroPPT with 0.415 μF capacitance fired at 6 J.

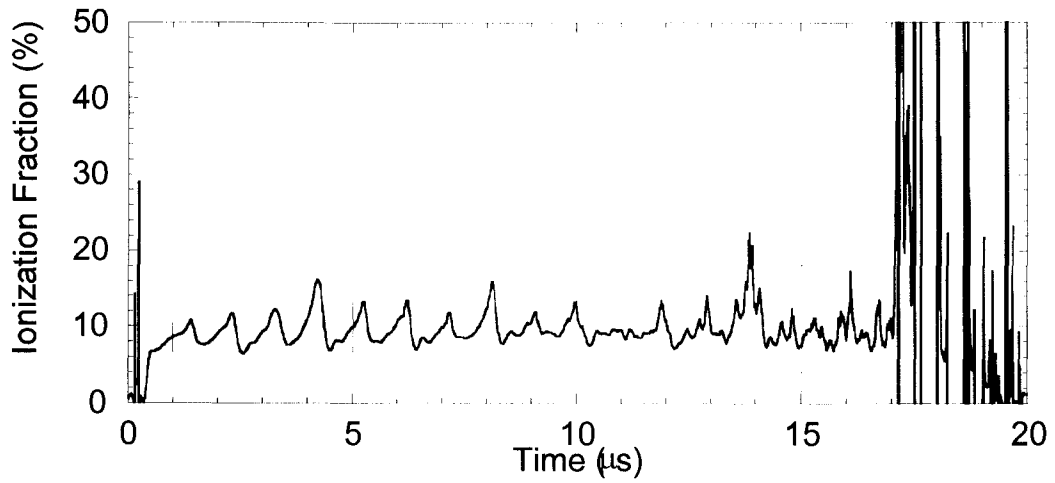


Figure 4.38: Ionization fraction calculated from electron and neutral densities.

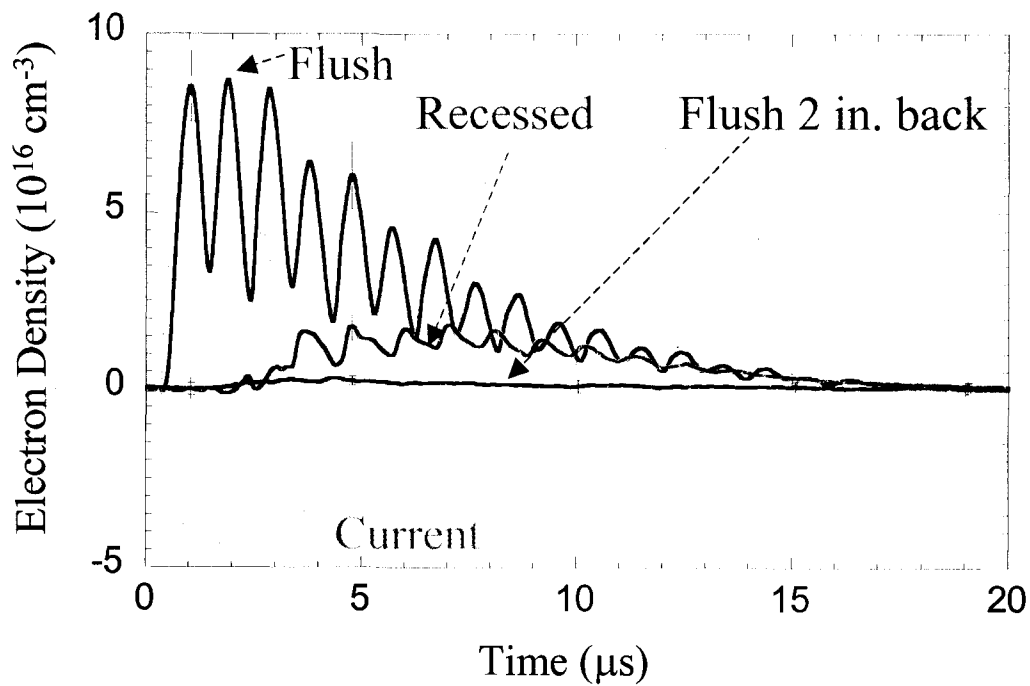


Figure 4.39: Measurements of electron density for the cases shown in Figure 2.26. 6.35 mm microPPT fired at 6 J with 0.415 μ F capacitor.

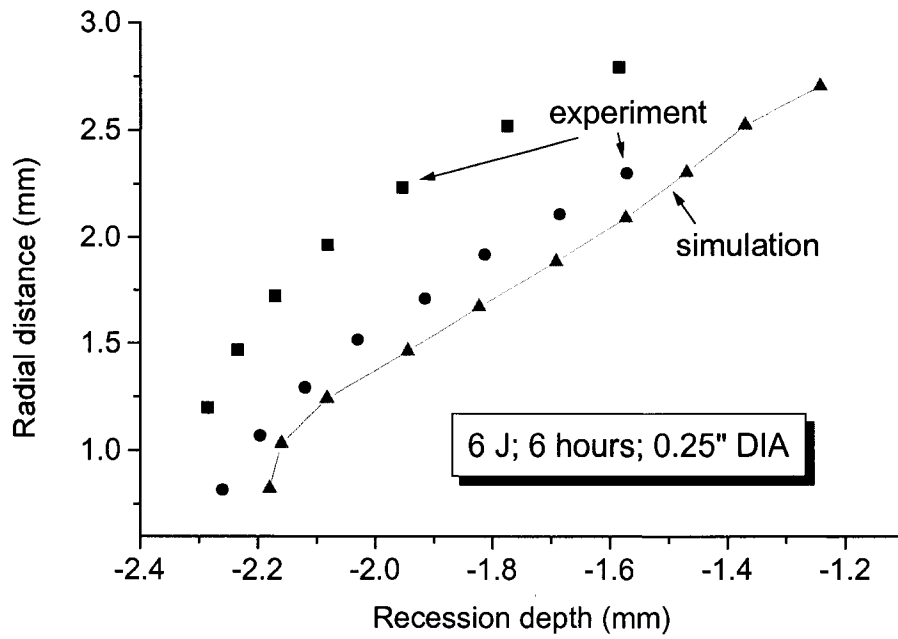


Figure 4.40: The dependence of the recession depth on the radial position within the tube after 6 h of firing and comparison with experimental profile. 6 J

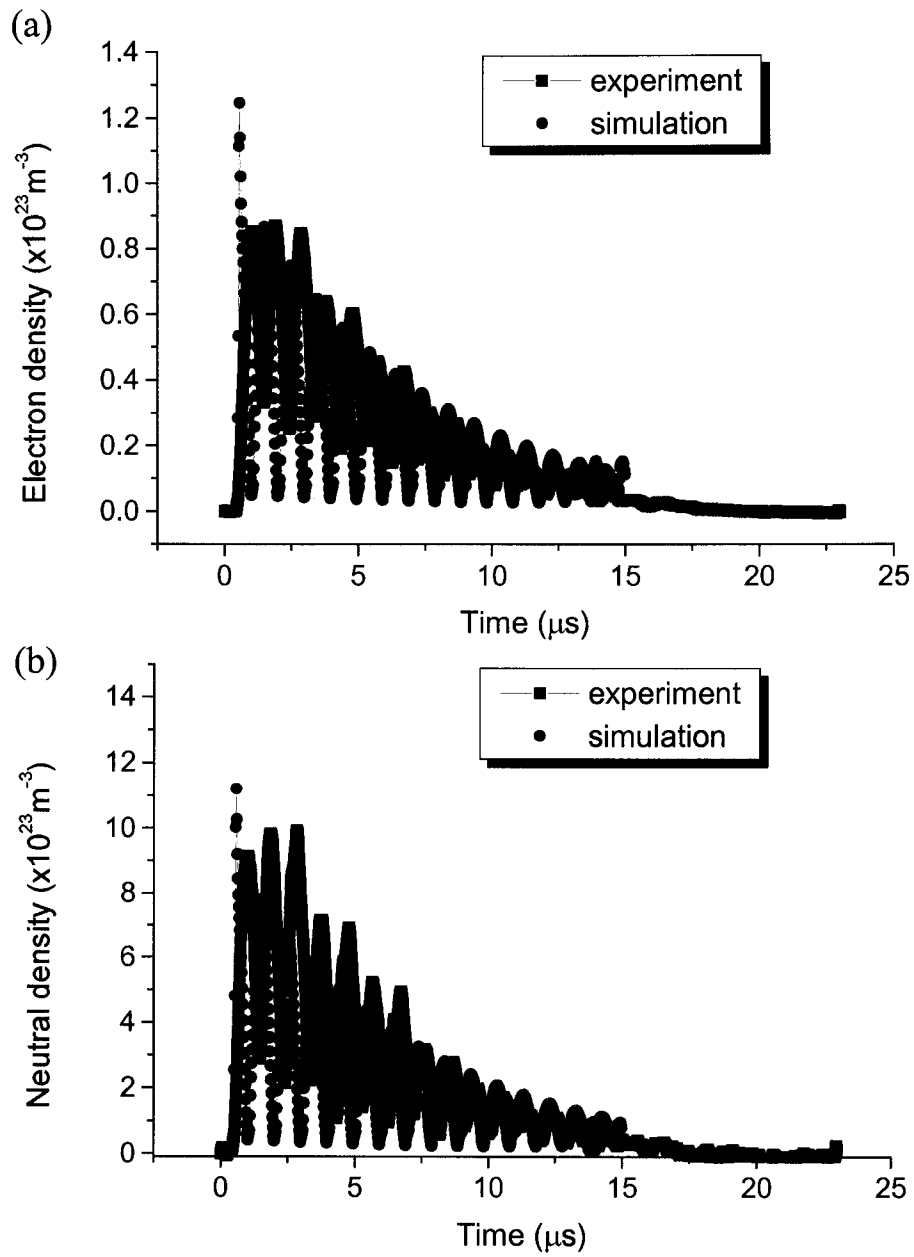


Figure 4.41: Electron (a) and neutral (b) density distribution. Model prediction is in red.

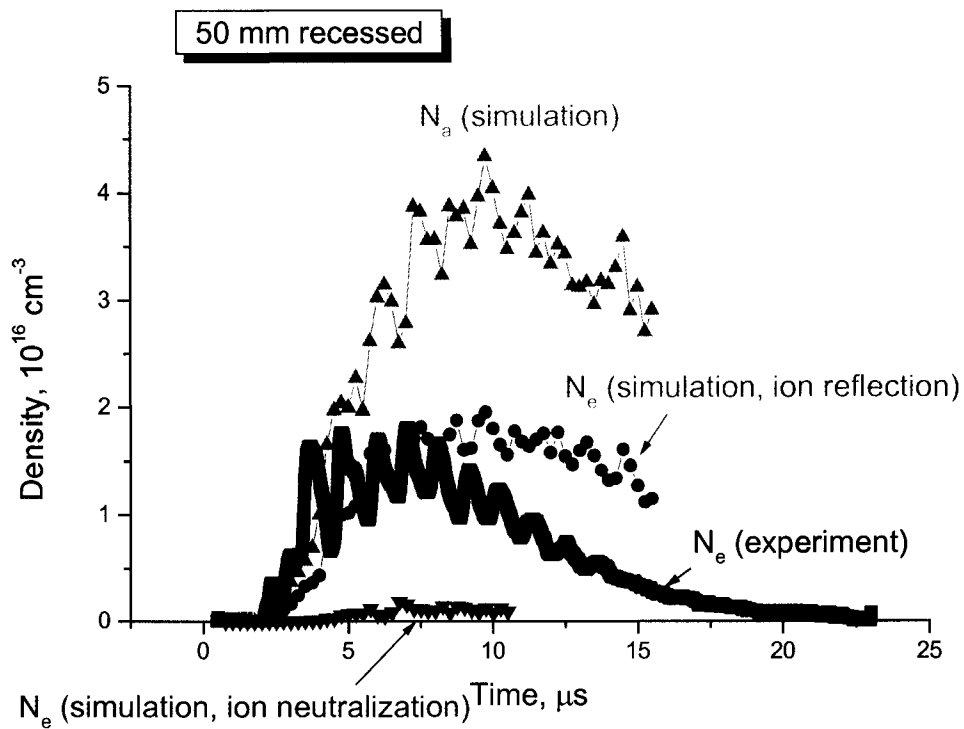


Figure 4.42: Model predictions for electron density (with and without ion reflection) and neutral density for propellant recession of 50 mm. The experimental results are shown in black for comparison.

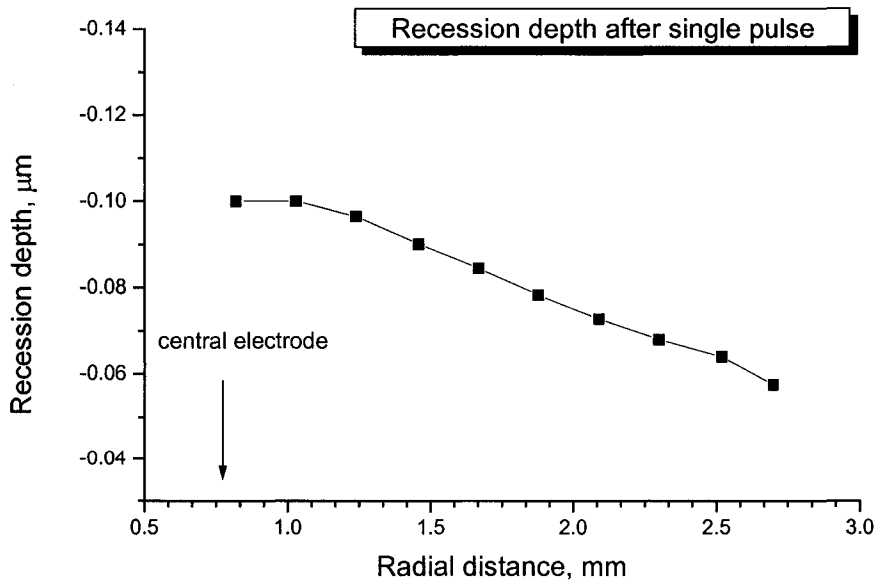


Figure 4.43: Ablation depth after a single pulse.³³

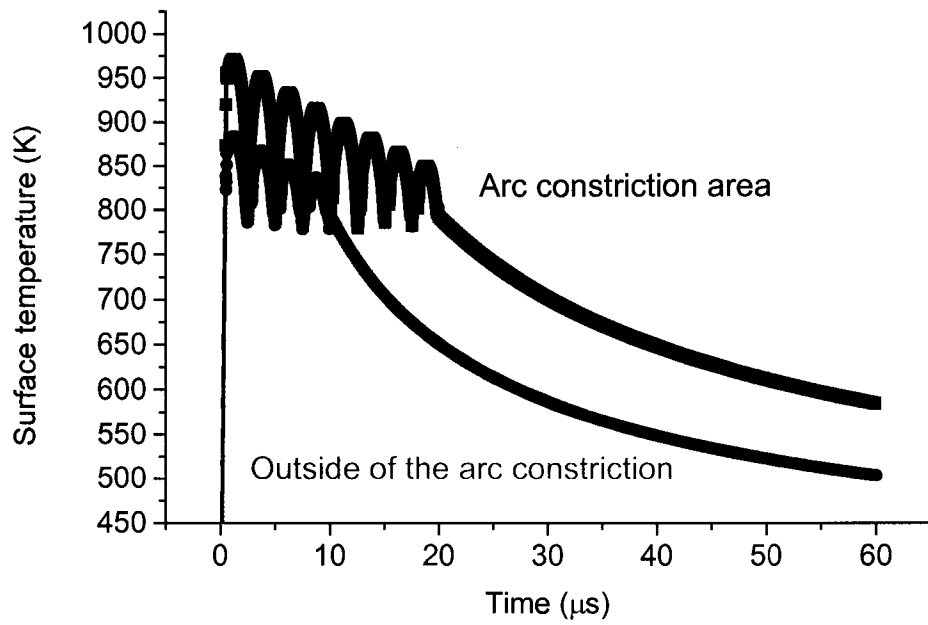


Figure 4.44: Surface temperature predictions both within and outside a theoretical arc spoke.

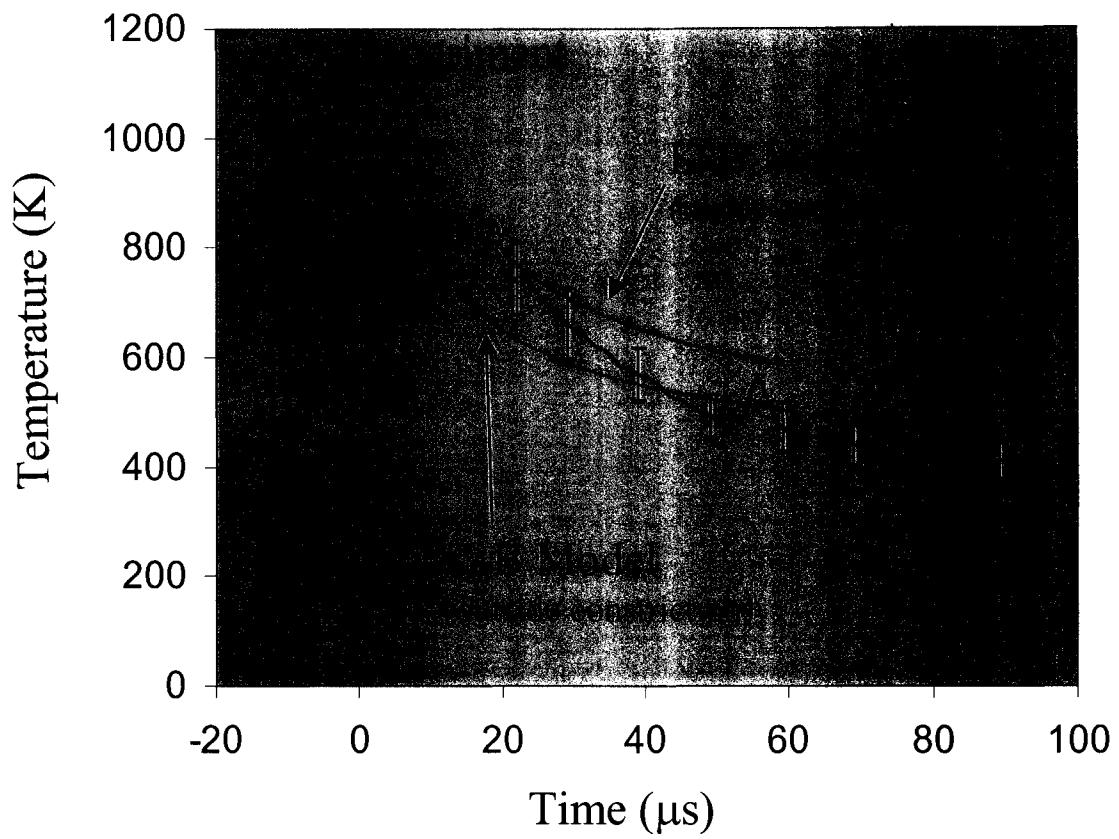


Figure 4.45: The predictions shown in Figure 4.44 are compared with the averaged measurements from Figure 4.31. Note that valid experimental data begins at 25 μs .

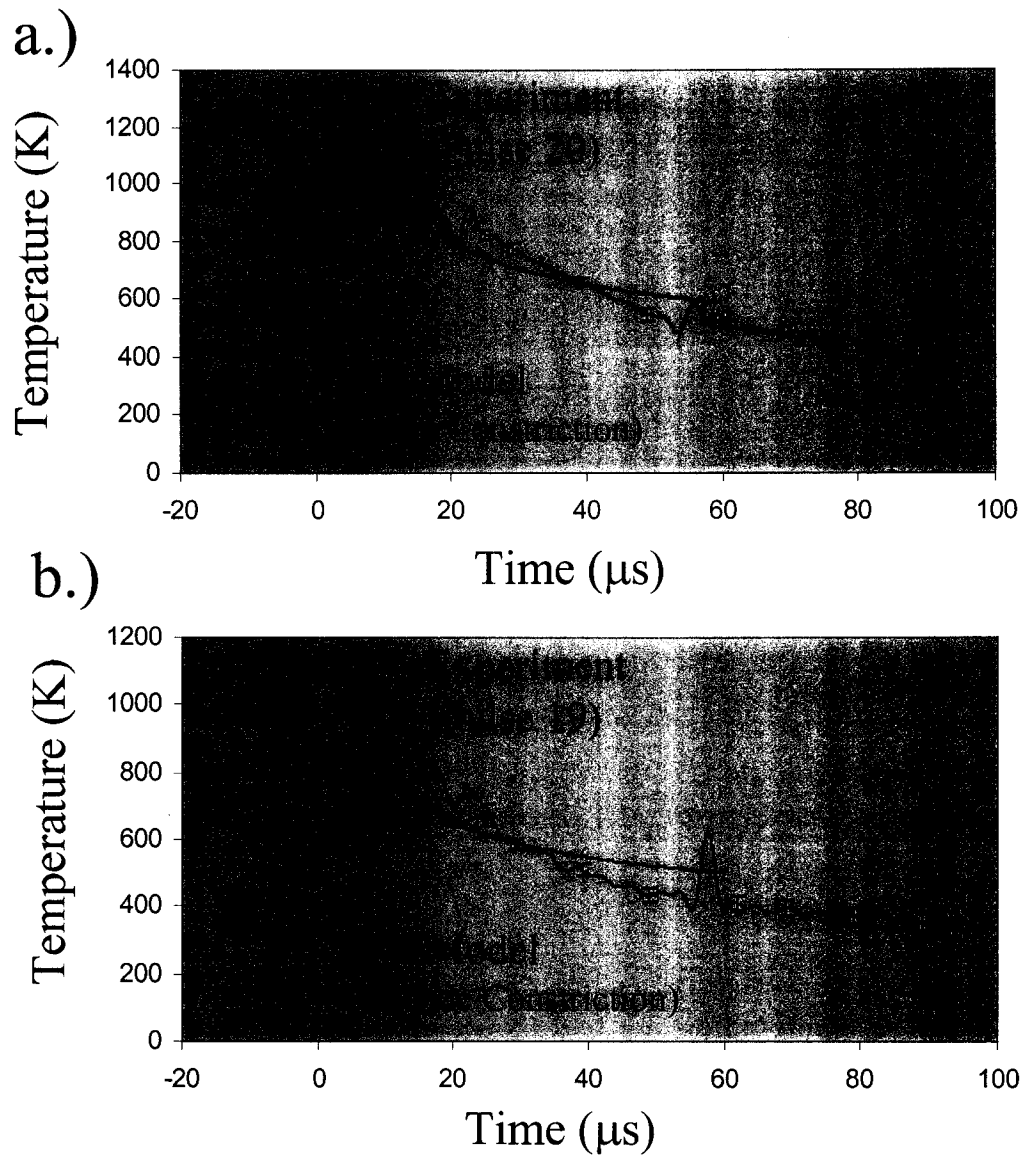


Figure 4.46: Comparison of predicted surface temperature a.) within an arc constriction to pulse 20 which showed the highest cooling temperature of the data set. Part b.) shows the prediction far from the arc constriction location with Pulse 19 which showed the lowest cooling temperature of the data set.

5. Discussion

5.1 Infrared Thermography as a PPT Diagnostic

The results from above show that IR photovoltaic detectors are currently capable of measuring surface temperature in real-time after the current pulse of a PPT ends. Theoretical predictions match experimental calibrations with heated Teflon and the cooling measurements on operating thrusters agree with temperatures expected after the pulse. This section discusses the utility and limitations of the theory derived to describe detector voltages, the known issues with data collected here, and physical limitations of the diagnostic.

5.1.1 Utility and Limitations of IR Theory

The ability to predict the voltage output of the HgCdTe detectors hinges on obtaining an estimate of the material emissivity over all wavelengths being measured. All other parameters that contribute to the signal magnitude are easily measured. For many materials, a wavelength dependent emissivity is not available. This is true for Teflon, and only the availability of the IR spectroscopy data from DuPont allowed an estimate of the emissivity to be made. Note that the emissivity of Teflon is also probably temperature dependent, but with the information available, no estimate of that dependence can be made.

The thermographic theory summed up by Eqn. 15 highlights possible methods to improve the diagnostic significantly. The main deficiency in these experiments is the extremely low signal voltage. It is so low that normally un-intrusive noise sources such as the sparkplug become major contributors to the noise. To increase the signal-to-noise ratio, several techniques are available.

The detector active area can be made slightly larger enabling more photon collection. However, this is limited by the fact that the detector rise-time is inversely proportional to the active area. Minor improvements are available through this change, but time-response can be negatively affected if the active area becomes too large. Likewise, differently doped detector materials can provide somewhat higher responsivity

in the wavelengths of interest, but the HgCdTe detectors used here are likely the best available for this application.

Significant increases in signal magnitude can be achieved by increasing the viewable solid angle determined by the Newtonian telescope. While we use a 6-inch concave mirror to maximize photon collection, the limiting factor is actually the diameter of the ZnSe window on the side of the vacuum tank. Because of this limitation, the value of θ in Eqn 15 has been limited to $\sim 3^\circ$. If θ is increased to 15° through use of a larger window, then a 10x increase in signal-to-noise ratio can be achieved. This would bring the expected voltage signals during calibration out of the 10 mV range and up into the 100 mV range. Sparkplug noise would cease to be a concern, and the temperature uncertainty for the diagnostic would decrease significantly.

5.1.2 Issues with Data Collected

5.1.2.1 Charring and Surface Topology

One of the main concerns when operating this diagnostic is the condition of the surface being measured. When the thruster is operating in the expected regime, no surface char develops. However, in the cases where char does develop, even slightly, the calibration based on clean Teflon fails to apply. Char changes both the emissivity (black vs. clean white) and the surface roughness. In light of this, every effort must be made to prevent char from occurring during testing.

The Teflon samples created for calibration to a plasma-exposed surface are operated in a different geometry than the microPPT. While this is not expected to be an issue, the microPPT does experience some operational differences that can affect temperature measurements. The microPPT experiences an elevated current density around the central electrode due to its geometry. This results in the formation of a small concavity in the Teflon immediately surrounding the central electrode early in the operational life of the microPPT. The beginnings of this can be seen after 50 pulses. When the IR detectors are targeted at the fuel face, they must not be focused within this region. The concavity formed effectively changes the viewing angle rendering the calibration useless. Likewise, it can take as many as 5,000 pulses for this concavity to extend across the entire fuel radius. For this reason, this diagnostic is limited to

temperature measurements on the microPPT between 20 and 5,000 pulses. On a standard parallel plate PPT, the IR diagnostic is more universally applicable because the propellant face tends to remain relatively flat. However, even parallel plate PPTs show significant Teflon deformation during extended operation. Therefore, it is critical that the thruster surface must be both flat and in clean (uncharred) condition before and after the application of this diagnostic to ensure accurate temperature measurements.

These requirements limit the usefulness of the IR diagnostic in its current form. As it stands, this diagnostic cannot be used to measure surface temperature when the propellant face is recessed into the outer electrode of the microPPT. Char temperature could conceivably be characterized by calibration, but the char amount and shading (on a scale between Teflon white and carbon black) will vary the emissive contribution significantly.

This is also the case with the copper of the center and outer conductors. Temperature measurements could be calibrated to the copper, but great care must be exercised to be sure that the emissivity of the copper does not change during the pulse. Generally this disallows using a large number of pulses for a statistical sampling since the copper becomes pitted and can change from shiny to dark over 10-20 pulses. For single pulse characterization, copper temperatures can be achieved.

5.1.2.2 Arc Spoking Issues

MicroPPT operation, and indeed the operation of any PPT is typified by an expected level of non-repeatability from pulse to pulse. In past experimental measurements of any type, most data are averaged over large numbers of pulses with standard deviations demonstrating the operating envelope for the property being investigated. While this statistical approach is attractive as a possible method for characterizing the operational envelope for thruster surface temperature, limitations in the spatial resolution of the detector require a careful assessment of whether such a description is appropriate.

An obvious reason for caution is that operation of the microPPT is typified by an asymmetrical current sheet that can condense into a plasma spoke during repeated firing. Figure 3.14 shows DICAM pictures of three individual firings with the camera

integration over 20 μs . The three cases are at different energies, but illustrate different possibilities for current distribution over the face of the microPPT. If we assume that emission is an indicator of current location, then a.) seems to show a broadly distributed current path over a significant portion of the propellant face. Picture b.) is at a higher energy, and consistent with greater magnetic field strength, indicates spotting on the outer electrode, possibly denoting arc spoking over much smaller total propellant areas. Picture c.) is at an even higher energy, and while possible anode spots are still observed, it is likely that arc attachment is largely occurring on the outside of the outer electrode. Non-uniform distribution of the current path over the face of the microPPT presents a challenge for interpreting surface temperature results. There are generally two heating mechanisms at work in a microPPT. Particle convection from the arc to the walls, which can be ions, neutrals, or monomers, is expected in the region over which the arc is passing. The other heating method is radiation from the arc to the surface.

It is expected that radiative heating will act over larger distances from the spoke location than particle convection. However, the relative magnitudes of radiative and convective heating are not well understood. It is tempting to use Wien's law to describe the peak radiation wavelength from an arc at 1 eV, but if molecular radiation in the UV contributes significantly, then such an analysis is incorrect.

There are a number of physical reasons that may lead to discharge non-uniformity including current constriction and cathode and anode spot appearance. Keidar et al. calculated some effects of spoking on ablation rates. Figure 3.17 shows that for a 6.35 mm microPPT, the ablation rate is strongly dependent on the current increase. However, the ablation rate is also not uniform. For a single pulse, Keidar also predicts the ablation as a function of the thruster radius. Figure 4.43 shows this prediction. Note that the variation in depth is about 0.4- μm maximum due to the increased current density near the central electrode. Figure 4.6 a.) and b.) show a close up of the surface after 100 and 1000 firings and indicate a relatively flat fuel face near the outer electrode with the beginnings of a cone situated around the central electrode. There is no evidence of radial canals due to arc spoking. This indicates that any spoking that occurs likely distributes around the fuel face over multiple firings or that the superheated Teflon flows to fill in such voids during pulsing. These fairly even ablation profiles show that as the fuel is ablated in the

microPPT, there is not preferential ablation that contributes in the short term to significant changes in the landscape of the propellant. Over a long timeframe, the propellant begins to recess into the tube. This is evidenced in Figure 4.6c showing the initial recession after ~12,000 firings. The even recession patterns indicate that preferential spoking does not occur.

The data shown in Figure 4.45 matches fairly well with Keidar's predictions of propellant cooling profiles both near and far from the arc constriction. This suggests that for the number of shots taken, the arc may be distributing randomly around the propellant face from shot-to-shot. Keidar's predictions form a corridor of expected cooling curves, and the measured corridor formed by the experimental average and uncertainties match well. Since there is no other experimental information available on arc constriction, the temperature predictions of the model are the best available resource for validating the diagnostic. At the very least, the diagnostic is measuring very close to the expected temperature range considering ablation as the main source of cooling.

5.1.3 Diagnostic Limitations

5.1.3.1 Calibration

A major limitation of the diagnostic is the ability to calibrate only up to about 770 K. This upper limit is imposed by Teflon deformation and flowing at high temperatures in the calibration process. This is a material limitation that may be circumvented by some creative engineering. The current calibration process looks sideways through a calibration apparatus that has holes on both sides. As the Teflon heats, gravity is constantly pulling down. When the viscosity gets too low, the flowing material can drip down the outside of the apparatus. Figure 5.1 shows a schematic of a calibration test that changed the orientation of the calibration apparatus to horizontal such that the Teflon would pool instead of dripping. Unfortunately, the ZnSe window was heated by proximity to the special hotplate being used and began to emit in the infrared. This invalidated the calibration in that design. However, if a method can be devised where the calibration apparatus can be turned such that the exposed Teflon surface faces upwards, any liquid phase that forms may simply pool without dripping. This could allow higher temperature calibrations to be achieved.

In the current calibration setup there are some practical hints that ease the operation of this diagnostic. The Teflon sheet used for calibration must be thick enough to drill into the side. Slightly under-sizing the thermocouple hole helps ensure a solid contact with the Teflon. Also, the back copper plate is tapped $\frac{1}{4}$ "-20 to hold the Teflon against the front plate. The bolts used to hold the apparatus together should only be screwed finger tight such that the Teflon has some room to expand as it heats. If the apparatus is tightly connected, the Teflon tends to deform earlier in the heating cycle. It was noted that the voltage vs. temperature heating and cooling curves must match to ensure a valid calibration. Any offset between these is usually explained by a couple of problems. If the heating curve shows a higher voltage than the cooling curve, the problem is usually traced to either Teflon deformation (TC measures different location than the detector), or the thermocouple may have contacted the copper. The copper plate cools faster than the Teflon due to radiation. In the case where the heating curve is lower voltage than the cooling curve, the thermal environment shielding should be checked. If the vacuum chamber heats during the test and the detector can view it, even peripherally, then the calibration is compromised.

In these experiments, the curve fit calibration data matches with the calculated detector voltage using the estimated Teflon emissivity. The thermographic theory even describes the emissive differences between virgin and plasma-exposed Teflon while retaining the dominant emissive structures in the Teflon bonds. This is significant because while there is an assumed temperature dependence for Teflon emissivity, it is likely that the dominant emissive structures will remain until the polymer is unzipped and the dissociated Teflon is liberated from the solid. Therefore, the prediction of surface temperature above the measured calibration limit is probably fairly accurate. This is further supported by the good agreement with simulation shown in Figure 4.45. Temperatures both near and far from the arc constriction immediately after the pulse are within a realistic range and close to those expected from the model. The cooling rates show similar trends, and the differences are not unexpected due to the omission of radiative and conductive physics. This demonstrates a strong likelihood that the calibration method can be accurately relied upon to provide surface temperatures for real-time operation of this diagnostic.

5.1.3.2 Thruster Application

The thermographic diagnostic is useful for measuring surface temperature on the face of a microPPT that is still flat and flush with the exit plane. A significant limitation of the diagnostic is the need for a smooth consistent surface for measurement. If the microPPT pulses more than about 1500 times, the conical recession shape that develops could render the calibration useless. Because of this, the thermography diagnostic may be more applicable to classic PPTs, which tend to retain a flatter propellant face over more discharges.

The unique high-temperature behavior of Teflon is also enabling for this diagnostic. Since Teflon ablates in small amounts and the surface actually gets smoother with operation, the infrared emission remains constant as the thruster operates. This is unlikely to occur with many other materials. Therefore application of this diagnostic to other rockets will depend on the material characteristics of the propellant being investigated.

Application of this diagnostic to an operating thruster has allowed some calculations of thruster performance due to the late-time surface temperature measurements. An estimate of the post-pulse mass loss as well as an exhaust velocity and two estimates of the impulse bit due to late-time ablation were carried out in Section 4.2.3.5. A critical appraisal of the assumptions required to make these calculations is required.

The calculations for the post-pulse performance are based on the assumption that the measured surface temperature within the arc-constricted region (claimed by comparison with the model prediction shown in Figure 4.46a) can be applied to the entire surface area of the propellant face. This is obviously not the case since a number of firings showed much lower surface temperatures as the arc likely moved around the propellant face. However, the lower temperatures measured do not indicate that the entire propellant case sees lower temperatures on a shot-to-shot basis. The low temperatures demonstrate the temperature of the propellant not directly covered by the arc. The high temperature curve is present during every shot at an undetermined location on the propellant face. The small size of the detector element disallows measurements of the highest temperature areas of propellant face over repeated pulse because of arc

migration. The assumption that the highest temperature curves apply to the entire area is used because there is no evidence indicating the dimensions of the arc from shot-to-shot. This assumption then allows determination of an upper limit for post-pulse mass loss and impulse bit.

Also, long-term coning suggests that the area near the central electrode ablated more rapidly than near the outer electrode. Since the temperature measurements were made halfway between the two electrodes, an assumption of temperature averaging in the radial direction is probably not unreasonable. However, in the angular direction, it is more likely that arc spoking causes a fraction of the total propellant surface area to reach the temperatures used for the above calculations. There is no good method to estimate the fraction of surface area covered by the arc. Emission in the visible portion of the spectrum can indicate possible anode spots, but there is no guarantee that visible emission correlates with current density. Alternatively, a statistical method can be proposed. Measuring surface temperature over a large number of pulses and calculating the fraction of total shots that follow the predicted temperatures from the constricted area could allow an estimate of how often the area in question sees high ablation rates. This could then be divided by 360 degrees to give an estimate of the angular surface area the arc may cover. However, there are two problems with this approach. It is entirely possible that the arc locates based on jagged edges at the outer electrode and can remain in a single location until the sharp edges of the electrode are worn away. This would skew a statistical analysis. Also, large numbers of pulses can begin to deform the propellant face causing a systematic error that would ruin any statistical description. In light of these restrictions, the assumption that the arc constricted temperature measurement can be used to describe the total surface temperature as when a symmetric current sheet is present is used. The practical result of this assumption is that the performance numbers calculated here represent an upper limit to the expected contribution from post-pulse Teflon ablation.

5.1.4 Surface Temperature During the Pulse

It is difficult to assess a surface temperature during the pulse of the microPPT for a variety of reasons. The first reason is limitations in the data taken. There is a significant amount of electrical noise present at the low voltages where these measurements were

made. Figure 4.20 shows a characterization of that noise signal without any emissive contribution from the plasma or surface of the thruster. There is both a high-frequency component as well as a low frequency part that follows the current oscillation in the thruster. Sources of electromagnetic noise include the reversing thruster current and the reversing current of the nearby sparkplug. While some of the high-frequency noise can be filtered out, the background noise on the timeframe of the current oscillations is too slow to be filtered effectively. For the present data sets, this cannot be removed, and requires an experimental setup with a much larger signal-to-noise ratio to reduce this noise source to a negligible level.

The second issue is the low voltage nature of the post-pulse surface signal. The high frequency noise early in the pulse often dwarfed the post-pulse voltage. The practical solution to this problem was to adjust the voltage measurement levels on the oscilloscopes to compensate for this large difference. The end-result is a loss of the peak and some high frequency noise data during the pulse due to clipping of the signal by the oscilloscope. Figure 5.2 shows the data from Pulse 20 along with the unfiltered data to illustrate the level of clipping involved. This information loss can cause the filtered peaks during the pulse to be of lower magnitude than they normally would be. It is for this reason that the in-pulse data has been excluded to this point.

However, were these not a problem, there are remaining issues with arc spoking, plasma emission, and solid Teflon emission that still need to be considered. The plasma emission was characterized by positioning the focal point of the viewable cone above the surface of the thruster at locations varying from 1-7 mm as discussed in Section 4.2.3.2. Figure 4.21 shows the difference between these contributions in an optical configuration that maximizes the signal-to-noise ratio. This optical configuration was not available for calibrated testing because of constraints from the heating equipment. Additionally, this configuration had a much higher thruster inductance than calibrated testing presented above, resulting in a lower likelihood of arc spoking. Some information about the plasma properties may be deduced from this data set. Figure 5.3 shows a schematic comparison of the 1 mm and 3 mm measurement locations in the plume along with the viewable cone used for surface measurements. (The cone half-angle for each is 3.05° , so the schematics are not to scale.) Figure 5.4 shows 6 traces of each plume measurement from multiple

pulses. The x-axis has been adjusted to focus on the early pulse emission signals. (These data were shown on long timeframes in Figure 4.21.) It is clear that emission from the plume contributes to the total emission measured during surface temperature measurements. The question of how much is difficult to assess. There is speculation that when the current reversal passes through zero (zero power into the arc) the plasma may provide a clear window to surface emission. However, close examination of the plume measurements in Figure 5.4 shows that while the emission minimizes with zero power conditions, the actual emission nadir is non-zero and even non-constant from 1 mm to 3 mm measurements. Figure 5.5 shows the emission minimums with standard deviations showing uncertainty. During the first emission minimum, the 3 mm case is 18 ± 2 mV or about 1/5 the magnitude of the first peak. For the 1 mm case, the emission minimum is 8 ± 3.5 mV (also about 1/5 of the emission peak). Since these amounts do not fall within the uncertainty of each other, it is clear that the emission is not a constant through the plasma volume. This cannot be attributed to spherical expansion or de-focusing because the 3 mm case shows stronger emission than the 1mm case.

Arc spoking can affect the measurements of the plume emission. For a single pulse there is no guarantee that a spoke will or will not occur, and without some indicator of the presence and dimensions of the spoke, it is difficult to make statements about any plasma emission that will be seen during a separate test measuring surface temperature. This limitation is best illustrated with an example. Figure 5.6 shows a case where a spoke may occur a.) outside the viewable measurement cone, and b.) inside the cone. While the arc usually attaches to the full surface of the central electrode, it is apparent that case b.) contributes more total emission due to the larger plasma volume measured. If the plasma is optically thick, the surface will not be viewable at all. Therefore we assume for the purposes of this discussion that the plasma is optically thin.

Finally, the IR emission from the hot solid Teflon largely emanates at discrete wavelengths in the IR. Figure 4.17b shows the estimated Teflon emissivity from these experiments where the main emissive contributions are at $8.4 \mu\text{m}$ and $4.4 \mu\text{m}$. Because the emissivity is so strongly wavelength dependent, the question of plasma optical thickness becomes critical. If the plasma is optically thick, then photons emitted from the surface cannot penetrate the plume to be collected by the detectors during the pulse. If

the plume is optically thin at those wavelengths the surface photons may be collected during the pulse.

If we assume here that the plasma is optically thin during the pulse, then it may be possible to subtract the plume emission from the surface emission. This would be best applied at the plasma emission minimums when the current passes through zero. It is worth noting that the viewable cone for the surface measurements traverses only a fraction of the volume viewed through the plume. This combined with the fact that the minimums in emission measured in Figure 5.4 are already small (1/5 of the peak voltage) suggests that the plasma emission could be neglected if the surface measurement sees only a tiny portion of the emission at 1 and 3 mm above the surface. A volume factor can be calculated to consider what percentage of the total surface viewable cone volume sees emission measured by the 1 mm or 3 mm cases. The intersection volume of the 1 mm viewable volume with the surface measurement volume is about 2% of the total surface measurement volume. Likewise, the intersection of the 3 mm viewable volume with the surface measurement volume is about 6% of the total surface measurement volume. For the purposes of this approximation, these amounts will be considered negligible. If all these assumptions are carried to their logical end, then the surface temperature should be visible through the plasma shortly after the current crosses zero (accounting for delay times inherent in the measurement).

A new challenge is determining what level of filtering to use for data during the pulse. Because of the high amount of noise, different filtering levels result in varying minimum values at a given time. Figure 5.7 shows filtering of Pulse 20 at varying cutoff frequencies during the pulse. It is apparent that the 300 kHz cutoff frequency misses some of the emission minimums and cannot be used. The measurements for 450, 500, and 700 kHz show roughly the same levels for the first two minimums. Using the logic above, picking off data at the minimums (arbitrarily choosing the 500 kHz cutoff frequency) might give surface temperature values. Figure 5.8 shows data points from the minimums during the pulse plotted along with the prediction for surface temperature near the arc-constriction. The minimums match to a certain degree, but it must be remembered that there is a large number of assumptions inherent in stating that these may indicate a surface temperature measurement. The uncertainties for the data points during

the pulse, though not shown, are very large due to the assumptions included. It is difficult to give exact uncertainties due to the unknown extent of noise and plasma emission levels, though they could be as high as ± 200 K. Additionally, one would expect that the surface temperature during the pulse might be at least as high as post-pulse temperatures. This is clearly not the case for all the in-pulse data points.

An in-depth exploration of surface temperature measurements during the pulse would require an infrared plume spectrum during the pulse to determine whether the plasma is emitting and absorbing at the same lines as the solid Teflon propellant. If the plasma does not emit at the same lines, a redesign of the optics to increase the signal-to-noise ratio coupled with a line filter for the $8.4 \mu\text{m}$ C-F stretching band could provide accurate surface temperature measurements during the pulse. An in-depth calculation of the optical thicknesses involved is also recommended. Unfortunately, because this effort was focused on characterizing the post-pulse cooling curves, the data taken during the pulse of the microPPT is not suitable for this type of study.

5.2 Implications of Experiment and Theory

The calibration, calibration theory, analysis, and reproducibility of the surface temperature measurements validate the measurements shown here. The agreement of the data with the model helps to validate the K-B model. There are some areas that can be modified slightly for improved description of details, but the trends predicted are well matched by experiment. This section describes some possible reasons for discrepancies in details between measurements and predictions, and reasons why theoretical description may be lacking in some areas.

5.2.1 Plume Characteristics

5.2.1.1 Flush Propellant Operation

The Keidar-Boyd theory shows excellent agreement with measured plume properties for operation with a flush propellant face. Electron and neutral densities during the pulse match in time and magnitude. This is a significant improvement over the old predictions of electron and neutral density (Figure 1.2 and Figure 1.4). This level of improvement is enabled by the two-color interferometry measurements in Figure 4.37

that utilize focusing of the beams onto the detector face. Keidar's attempt to match both electron and neutral density to unfocused two-color data (Figure 3.12) was forced to include a fudge factor (electron temperature gradient) because the uncertainties were so large. Using the focusing method, the uncertainties are reduced to a manageable level and the fudge factor becomes irrelevant. This demonstrates that the inclusion of non-equilibrium physics in the Knudsen layer was a valid step for describing the operation of this device. From this perspective, the description of the plume for a thruster with flush fuel face is validated. These results move theoretical development from attempting to match large trends to understanding thruster physics at a more detailed level including polarity effects and recombination times for the plasma.

5.2.1.2 Recessed Propellant Operation

As the microPPT operates over time, the recession characteristics become important from the standpoint of thruster performance and spacecraft contamination. The Keidar-Boyd model considers the effects of recession on a single-pulse basis by predicting the electron density at the thruster exit plane. Neutral density is also predicted, but experimental measurements to date have been unable to address the neutral density recession problem. The behavior of neutrals within the tube could be affected by development of a boundary layer along the tube walls. Therefore it is recommended that experimental analysis of neutral densities after the pulse be performed in the future.

Electron density is indicative of plasma behavior with the added constraint of propellant recession. Keidar hypothesized that ions could either reflect from the outer tube as the anode, or neutralize through interaction with the tube. Figure 4.42 showed the comparison of the electron density for these hypotheses. Experiment demonstrates that ion reflection must occur while the outer electrode acts as the anode. Ions can only extinguish while the outer electrode acts as cathode. Since the Debye length is small for this plasma ($\sim 0.1 \mu\text{m}$), this may indicate that inclusion of a non-reversing current pulse where the outer electrode is the anode could increase total ion flux and therefore increase thruster performance as the propellant recedes.

The prediction departs from experimentally observed behavior at the end of the pulse. The simulation suggests electron density does not extinguish with the current

pulse. In fact, the predicted trace suggests a time-of-flight for electrons associated with the distance traveled before exiting the thruster tube. While this seems to make sense, the experimental data for electron density shows an end to measurable density when the current pulse ends. This suggests that the recombination time for free electrons is being under-predicted by the theory. It is also possible that axial spreading is causing the low signal after the pulse.

To enable further analysis into recession effects Appendix A is included. This shows measurements of electron density in the plume of a microPPT for 7.8 J at 2.95 μF capacitance. Both polarities are measured for the case of the fuel face flush with the exit plane of the thruster and propellant recession depths of 0.25 cm, 0.5 cm, 1 cm, and 2 cm.

5.2.2 Surface Temperature and Ablation

This data demonstrates that Keidar's theory predicts thruster operation fairly well. Experimental curves show faster cooling, but beginning temperatures are within the same temperature range as the predictions. This model includes ablation as the only cooling mechanism. This neglects thermal conduction into and across the propellant face as well as radiation from the propellant into space. Figure 4.18 shows that in the LWIR Teflon radiation can be characterized as approximating a grey body with emissivity 0.113. Slight modification of the model to account for radiation and thermal conduction will increase the rate of cooling and likely bring it much closer to experimentally determined values.

Since there is no data concerning propellant temperature during the pulse, no claims can be made concerning the validity of the theoretical predictions of surface temperature at those times. However, Keidar and Boyd's model assumes that the bulk of propellant heating occurs as a result of particle convection. Radiation is considered in the model, but there is no accounting for subsurface heating effects by radiation penetration through the Teflon.

Ultraviolet radiation may play an important part in heating and propellant use. Ruchti and Niemeyer⁶⁸ introduce a threshold wavelength λ_p (~300 nm) that distinguishes between types of radiation inducing separate photochemical reactions in Teflon. A portion of the arc radiation is transferred such that $\lambda > \lambda_p$ and can penetrate deeply into the

material. For white PTFE they cite evidence of radiation damage several millimeters deep in the polymer face indicating the formation of high vapor pressure bubbles and eruptive discharge of material. A similar investigation conducted by Seres⁶⁹ shows that the transmission of radiation by Teflon increases substantially below 450 nm wavelengths. Data from Philipp et al.⁷⁰ show the absorption coefficient to be about 1.2 mm^{-1} in this regime. From 300-400 nm, it is approximately 0.1 mm^{-1} . Radiation between 300-400 nm is penetrating beneath the surface of the fuel. The possibility that either the molecular structure may be changing during arc exposure, or that sub-surface ablation may play a role in the amount of mass consumed by these thrusters, is not considered by the ablation models currently being used.

This could contribute to mass loss after the pulse through macro-particle ejection. Since Teflon is fabricated through a sintering process, there are natural voids and a level of porosity. Sub-surface radiation damage could be the result of radiation impinging on foreign particles or gases within these voids. Accounting for such a process theoretically would present a significant challenge. But an experimental analysis of macro-particle size and substance could yield significant information regarding that portion of late-time mass loss.

Over repetitive pulses, the Keidar-Boyd model predicts coning through multiplication of the single pulse ablation prediction by the total number of pulses. Figure 4.6c shows the initial recession after $\sim 12,000$ firings from a frontal perspective. Figure 2.27 shows a cutaway of a microPPT fired at 6 J for 6 hours at 1 Hz. The outer copper electrode was removed exhibiting the coning profile created by the extended pulsing. Figure 4.40 shows measurements of this profile along with a prediction by Keidar's model.³³ The red and black curves are the experimental measurements from both above and below the central electrode. The green is the prediction by Keidar. The predicted and measured coning profiles show good agreement considering the uncertainties discussed in Section 4.5.1.2. This demonstrates the predictive power of Keidar's model for describing the long-term effects of thruster operation. Note that the actual thruster surely came to some steady-state operating temperature that could have influenced the total amount of material ablated according to Spanjers theory. The slight under-prediction of the recession depth shown in Figure 4.40 could implicate this

increase in propellant base temperature (not accounted for by Keidar) as a possible explanation.

Unfortunately, the surface temperature measurements do not provide a direct validation or refutation of the Spanjers theory. Achieving a steady state operating temperature requires repetitive pulsing over long time periods which ultimately deforms the propellant face. Using an external heating coil may present a possible approach to this problem, but the Teflon tends to expand out the front end of the thruster at higher temperatures. Experimental validation of this theory may need to wait until a means of obtaining spatially resolved surface temperatures across the microPPT face is developed.

5.3 Chapter 5 Figures

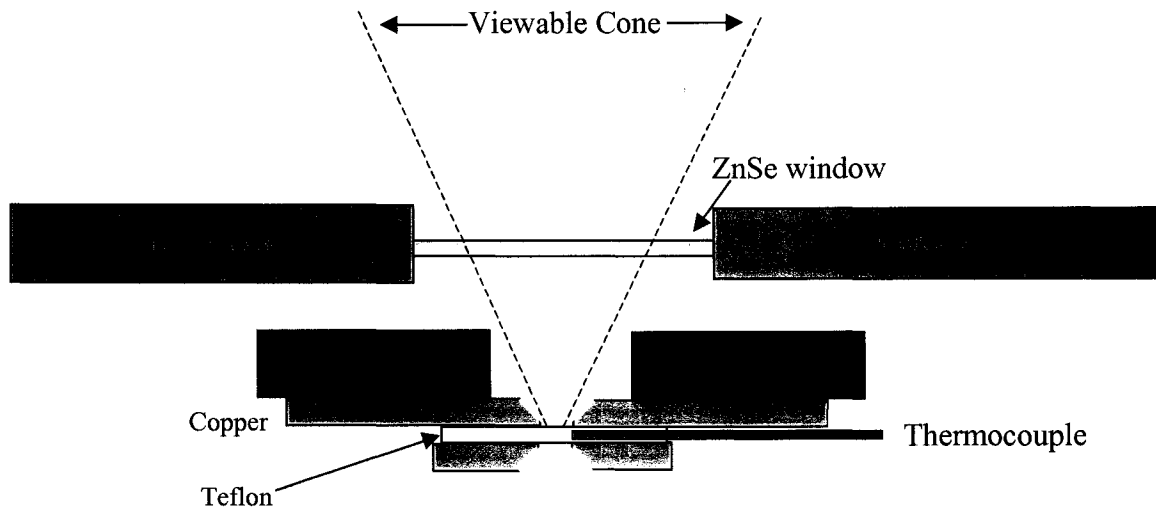


Figure 5.1: Schematic showing an attempt to keep Teflon from flowing during calibration using a horizontal orientation for the calibration apparatus. The ZnSe window was inadvertently heated and began emitting in the IR. This invalidated the calibration.

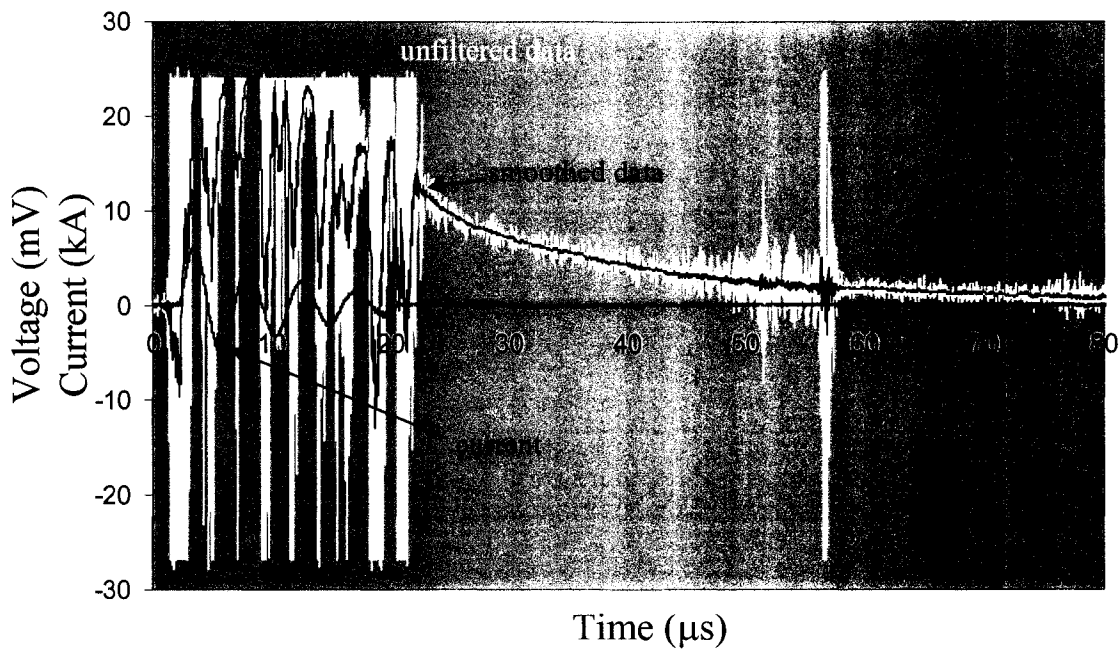


Figure 5.2: Unfiltered data for Pulse 20 shows data clipping above 25 mV during the pulse. This was done intentionally to increase the measurement resolution for post-pulse cooling data. However, this makes peak data values unreliable during the pulse when filtering is applied.

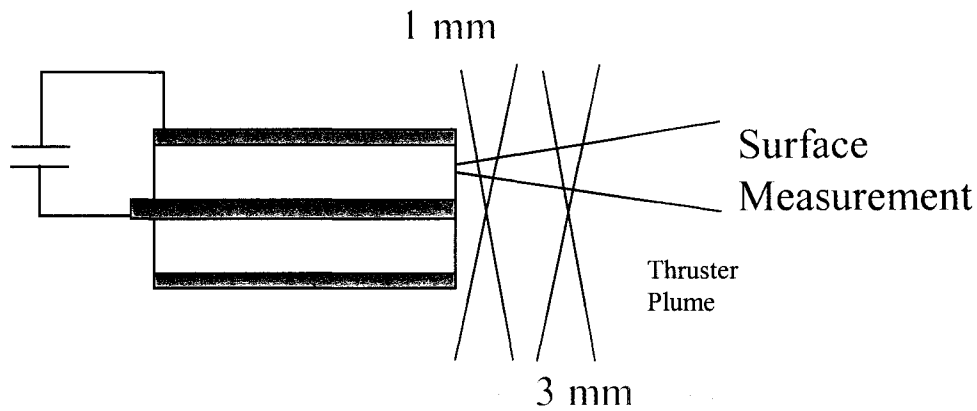


Figure 5.3: Schematic showing the viewable cone locations and orientations within the plume for plume emission measurements and surface temperature measurements. The focal point of the viewable cone is located at 1 mm and 3 mm away from the propellant face. The surface measurement sees emission from the plume during the pulse.

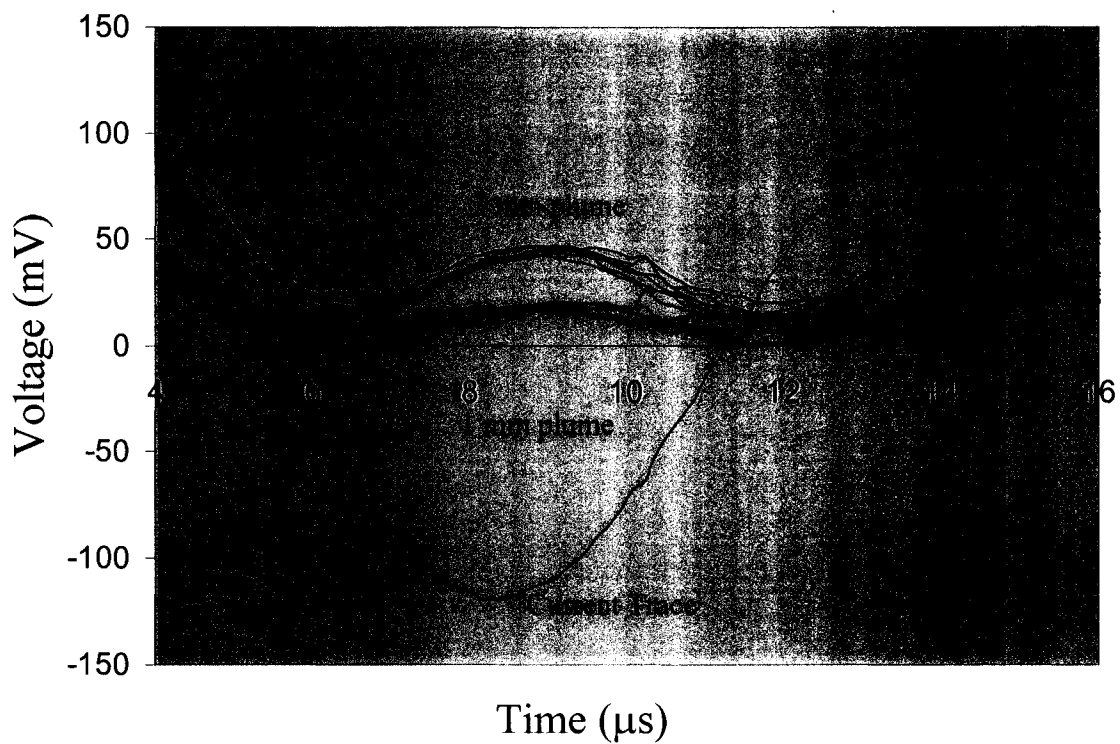


Figure 5.4: Six measurements at the 1 mm plume location and six at the 3 mm plume location are shown early in the pulse. The repetitive nature of the plasma emission is clear.

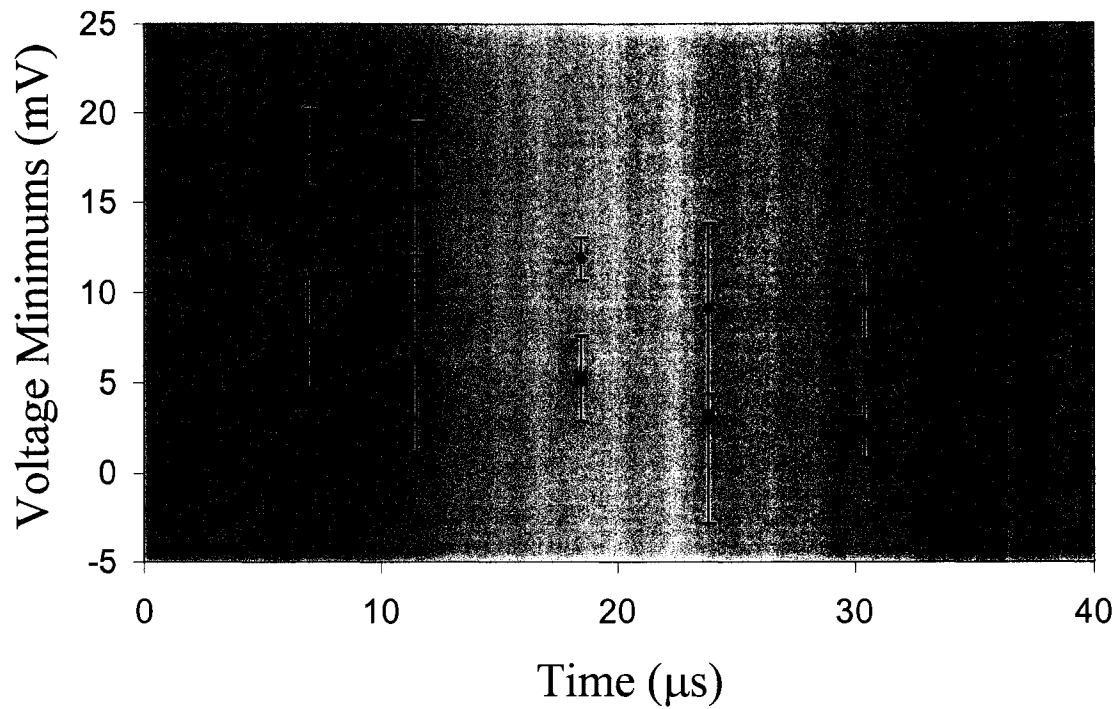


Figure 5.5: The emission minimums from Figure 5.4 are shown with uncertainty bars.

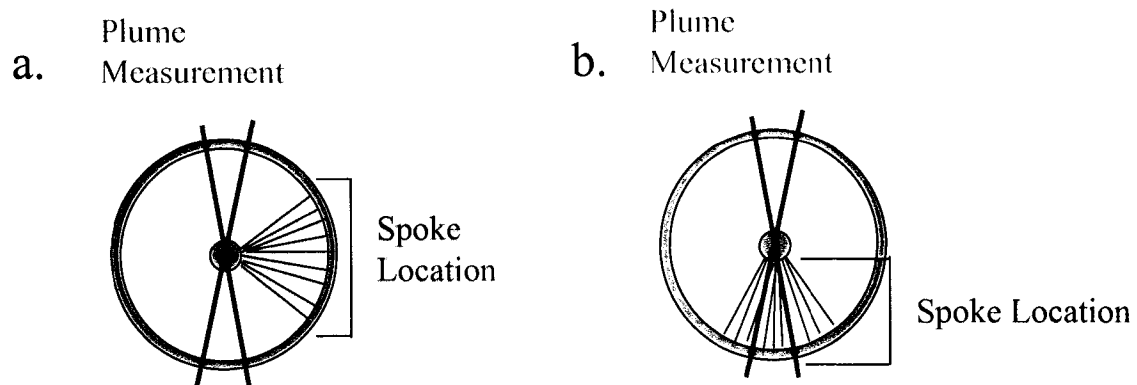


Figure 5.6: Thruster face showing the viewable cone of a plume measurement above the surface (red). If the arc spokes a.) outside of the viewable cone, the emission measurement will be minimized. If it spokes b.) within the viewable cone, the emission measurement will be maximized.

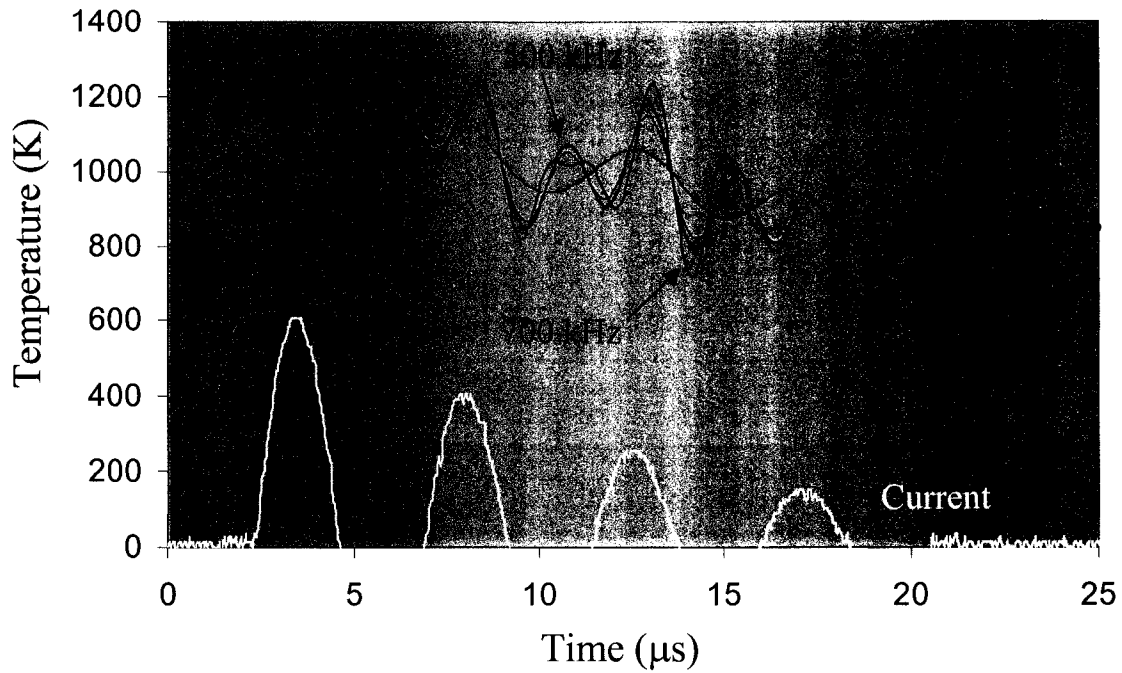


Figure 5.7: Due to high noise levels, varying the filtering frequency results in a number of values for the voltage when the current passes through zero. This makes it difficult to discern whether the surface is actually being measured.

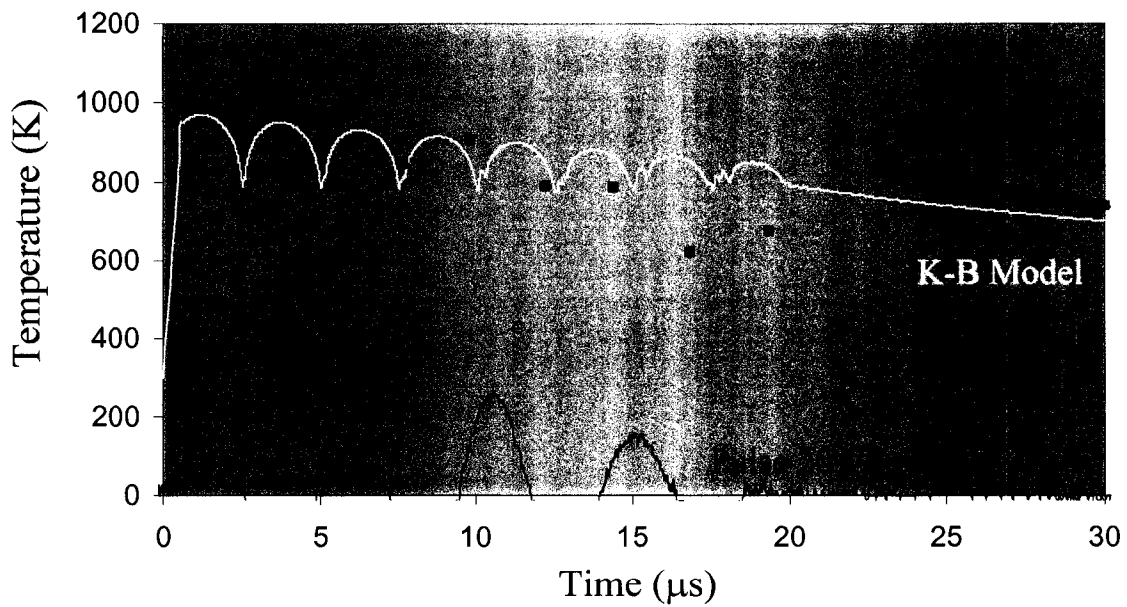


Figure 5.8: Using the 500 kHz cutoff frequency, the minimums during the pulse are plotted along with the prediction from the K-B model. These may be indicative of surface temperature during the pulse.

6. Conclusions

This work has described the construction, calibration, and application of HgCdTe photovoltaic detector diagnostic to determine the surface temperature of Teflon propellant during and after the pulse of a microPPT. This diagnostic is shown capable of measuring Teflon surface temperature in real-time after the completion of the current pulse. A theoretical description was developed to predict the detector output. This theory was confirmed by predicting experimental calibration data and then used to estimate a wavelength-dependent emissivity of Teflon in the LWIR. The significant achievements in the field of IR thermography include the following:

- A new calibration procedure was created for materials with wavelength dependent emissivity and high transmissive character. This allows application of emissive temperature measurements to materials that until now have been difficult to characterize.
- Using data from infrared spectroscopy and infrared thermography, a method of estimating the wavelength-dependent emissivity has been developed.
- The first measurements of Teflon surface temperature with infrared thermography are performed here.
- These experiments are the first application of high-speed thermography to discharge physics for analyzing plasma-wall interactions.

Although data during the pulse of the microPPT is not resolved due to plasma interference, the cooling curve of the propellant is characterized immediately after the pulse. The post-pulse cooling curve allowed calculation of post pulse performance for the microPPT. Using a pressure gradient calculation for post-pulse impulse bit, a value of $0.8 \pm 0.4 \mu\text{N}\cdot\text{s}$ is obtained. Using a centered expansion wave description, the post-pulse impulse bit for a 4.35 J microPPT is $1.1 \pm 0.5 \mu\text{N}\cdot\text{s}$. The estimated post-pulse mass loss is $1.2 \pm 0.6 \mu\text{g}$. The assumptions required for these calculations suggest that they define the upper boundary of possible performance. This is due to limited information on arc spoke dimensions and location.

This diagnostic, along with interferometry and other diagnostics, was compared to the model proposed by Keidar and Boyd. Significant improvements in the theoretical

description of microPPT physics are a result of the experiments performed here. These include the following:

- Two-color interferometry highlighted a shortfall in the ability of the Keidar-Boyd theory to describe neutral density during the pulse. The theory was modified to include non-equilibrium physics, which then showed excellent agreement with experiment. This is perhaps the most significant example of experiment helping to shape theory presented in this paper.
- Measurements of electron density for propellant recessed thruster operation indicated that the ion-reflection hypothesis applies. Ions reflect from the outer tube when acting as the anode. However, a more detailed description of plasma recombination may be required to describe accurately the post-pulse plume features.
- Measurements of coning profiles from operating thrusters provide a validation of Keidar's description of repetitive pulsing including recession ablation and current densities around the central electrode.
- Intensified images of the microPPT face during thruster firings provide evidence of anode spotting. Keidar has been able to calculate when spotting should occur and has initiated a new phase in his theory addressing arc constriction.
- Predictions of surface temperature near and far from a current constriction give an expected range of temperatures for propellant cooling after the pulse considering ablation as the main heat loss mechanism. This prediction shows good agreement with the cooling curves measured through infrared thermography, lending credence to both the experiment and theory. The differences between experiment and prediction suggest the inclusion of radiation losses and thermal conduction would improve the level of agreement.

A more detailed understanding of thruster physics in the recessed regime is suggested as a follow on to this research. The experiments presented in this paper lend credence to the K-B Model describing thruster operation. More work is needed to accurately describe the physics involved in recession operation. Appendix A provides a starting point for this next step of detailed model development. These plots show measurements of electron density in the plume of a microPPT for 7.8 J at 2.92 μF

capacitance. Both polarities are measured for the case of the fuel face flush with the exit plane of the thruster and recessions of 0.25 cm, 0.5 cm, 1 cm, and 2 cm. This data is provided to allow future analysis of detailed recession operation of these thrusters.

A number of avenues for future research with the infrared detector are also available. To increase the validity of surface temperature measurements and extend their usefulness, an investigation into the ability of the IR detectors to distinguish surface emission from plasma emission during the pulse is recommended. This is possible because the dominant emissive structure for Teflon in the wavelength range of the HgCdTe detectors is the C-F stretching mode at 8.4 μm . This mode reaches black-body emissivity which may be detectable independent of the plasma emissions. To know whether this is possible, IR spectroscopic imaging of the plume is required to show whether the plasma is emitting at 8.4 μm . If not, then it is possible to use line filters for 8.4 μm (commercially available for CO₂ lasers) to isolate the emission from the surface where it is strongest. This would allow real-time measurements of the surface temperature during the current pulse. An alternative theoretical approach would be to calculate a detailed optical thickness for all the species in the plasma to characterize whether emission from the Teflon has a high likelihood of being absorbed in the plasma. For either approach, the chances of success are good considering that plasma temperatures experienced above the propellant surface are high enough to dissociate the Teflon polymer and create doubly ionized species.

References

1. Jahn R. G., *Physics of Electric Propulsion*, McGraw-Hill Book Co., New York, NY 1968
2. R. L. Burton, P. J. Turchi, "Pulsed Plasma Thruster," *Journal of Propulsion and Power*, Vol. 14, No. 5, 1998, pp. 716-735.
3. Bromaghim, D. R., Leduc, J. R., Salosovich, R. M., Zimmerman, J. A., et al, "An Overview of the On-Orbit Results from the Electric Propulsion Space Experiment (ESEX)," *26th International Electric Propulsion Conference*, IEPC Paper 99-192, Kitakyushu, Japan, October 1999.
4. Christensen, J., et al, "Design and Fabrication of a 2.3 kW Ion Thruster for the Deep Space 1 Mission," *34th AIAA/ASME/SAE/ASEE Joint Propulsion Conference and Exhibit*, AIAA Paper 98-3327, Cleveland, OH, July 1998.
5. Spanjers, G. G., Birkan, M., Lawrence, Maj. T. J., "The USAF Electric Propulsion Research Program," *36th AIAA/ASME/SAE/ASEE Joint Propulsion Conference and Exhibit*, AIAA Paper 2000-3146, Huntsville, AL, July 2000.
6. Vondra, R. J., "The MIT Laboratory Pulsed Plasma Thruster," *AIAA International Electric Propulsion Conference*, IEPC Paper 76-998, Key Biscayne, Florida, 1976.
7. Guman, W. J., Williams, T. E., "Pulsed Plasma Microthruster for Synchronous Meteorological Satellite (SMS)," AIAA Paper 73-1066, Nov. 1973.
8. Ebert, W. L., Kowal, S. J., Sloan, R. F., "Operational Nova Spacecraft Teflon Pulsed Plasma Thruster System," AIAA Paper 89-2497, July 1989.
9. Vondra, R. J., Thomassen, K., Solbes, A., "Analysis of Solid Teflon Pulsed Plasma Thruster," *Journal of Spacecraft*, Vol. 7, No. 12, 1970, pp. 1402-1406.
10. Vondra, R. J., Thomassen, K. I., "Performance Improvements in Solid Fuel Microthrusters," *Journal of Spacecraft*, Vol. 9, No. 10, 1972, pp. 738-742.
11. Thomassen, K. I., Tong, D., "Interferometric Density Measurements in the Arc of a Pulsed Plasma Thruster," *Journal of Spacecraft*, Vol. 10, No. 3, 1973, pp. 163-164.

12. Spanjers, G. G., Malak, J. B., Leiweke, R. J., Spores R. A., "The effect of propellant temperature on efficiency in a pulsed plasma thruster," *Journal of Propulsion and Power*, Vol. 14, No. 4, July-August 1998.
13. Kamhawi, H., Turchi, P. J., "PPT Thermal Management," IEPC 97-125, Cleveland, OH, August 1997.
14. Spanjers, G. G., Bromaghim, D. R., Lake, Capt. J., Dulligan, M., White, D., Schilling, J., Bushman, S. S., "AFRL MicroPPT Development for Small Spacecraft Propulsion," IEPC 01-166, Pasadena, CA, July 2001.
15. Spanjers, G. G., Lotspeich, J. S., McFall, K. A., Spores, R. A., "Propellant losses Because of Particulate Emission in a Pulsed Plasma Thruster," *Journal of Propulsion and Power*, Vol. 14, No. 4, 1998, pp 554-559.
16. Spanjers, G. G., McFall, K. A., Gulcinski, F. S., Spores, R. A., "Investigation of Propellant Inefficiencies in a Pulsed Plasma Thrusters," 32nd *AIAA/ASME/SAE/ASEE Joint Propulsion Conference and Exhibit*, AIAA Paper 96-2723, Lake Buena Vista, FL, July 1996. Note in Reference 16 that the units on Eq. 3 are erroneously stated as MKS-degrees. The units should be MKS-radians.
17. Antonsen, E. L., Burton, R. L., Spanjers, G. G., "High Resolution Laser Diagnostics in Millimeter-Scale Micro-Pulsed Plasma Thrusters," IEPC-01-157, Pasadena, CA, 2001.
18. Antonsen, E. L., Burton, R. L., Engelman, S. F., Spanjers, G. G., "Herriott Cell augmentation of a quadrature heterodyne interferometer," *Rev. Sci. Instrum*, Vol. 74, No. 1, January 2003, pp 88-93.
19. Antonsen, E. L., *Herriott Cell Interferometry for Pulsed Plasma Density Measurements*, MS Thesis, University of Illinois U-C, 2001. Note that in Ref. 19 Figure 2.4 is incorrect: The bandpass and low pass filters are missing.
20. Antonsen, E. L., Burton, R. L., Spanjers, G. G., Engelman, S. F., "Herriott Cell Interferometer for Unsteady Density Measurements in Small Length Scale Thruster Plasmas," AIAA Paper No. 2000-3431, Huntsville, AL, July 2000.
21. Vondra, R. J., Thomassen, K., Solbes, A., "A Pulsed Electric Thruster for Satellite Control," *Proceedings of the IEEE*, Vol. 59, No. 2, 1971, pp. 271-277.

22. Bushman, S. S., Burton, R. L., "Heating and Plasma Properties in a Coaxial Gasdynamic Pulsed Plasma Thruster," *Journal of Propulsion and Power*, Vol. 17, No. 5, 2001, pp. 959-966.
23. Spanjers, Gregory G., "Pulsed Plasma Thruster with Electric Switch enabling the use of Conductive Propellants," Patent Number US 6,153,976, awarded Nov.28, 2000.
24. Spanjers, Gregory G., "Micro Pulsed Plasma Thruster having Coaxial Cable Segment Propellant Modules," Patent Number US 6,269,629 awarded Aug 7, 2001.
25. Spanjers, Gregory G., Schilling, John, and White, David, "Methods to Increase Propellant Throughput in a Micro Pulsed Plasma Thruster," Patent pending, U.S. provisional application No. 60/304,219 filed on Jul. 9, 2001.
26. Spanjers, G.G., Bromaghim, D.R., Lake, Capt. J., Dulligan, M., White, D., Schilling, J.H., Bushman, S.S., Antonsen, E.L., Burton, R.L., Keidar, M., Boyd, I.D., "AFRL MicroPPT Development for Small Spacecraft Propulsion," 38th AIAA/ASME/SAE/ASEE Joint Propulsion Conference, AIAA Paper No. 2002-3974, Indianapolis, IN, July 2002.
27. Keidar, M., Boyd, I. D., "Ionization non-equilibrium and ablation phenomena in a micro-Pulsed Plasma Thruster," AIAA Paper No. 2002-4275, Indianapolis, IN, July 2002.
28. Gatsonis, N. A., Yin, X., "Axisymmetric DSMC/PIC simulation of quasineutral partially ionized jets," AIAA Paper No. 97-2535, 1997.
29. Boyd, I. D., Keidar, M., McKeon, W., "Modeling of a pulsed plasma thruster from plasma generation to plume far field," *Journal of Spacecraft and Rockets*, Vol. 37, No. 3, 2000.
30. Keidar, M. Boyd, I. D., "Device and plume model of an electrothermal pulsed plasma thruster," AIAA Paper No. 2000-3430.
31. Keidar, M., Boyd, I. D., "Electromagnetic effects in the near field plume exhaust of a pulsed plasma thruster," AIAA Paper No. 2001-3638.

32. Keidar, M., Boyd, I. D., Gulczinski, F. S., Antonsen, E. L., Spanjers, G. G.,
“Analyses of Teflon Surface Charring and Near Field Plume of a Micro-Pulsed
Plasma Thruster,” IEPC Paper 01-155, October 2001.
33. Keidar, M., Boyd, I. D., Antonsen, E. L., Spanjers, G. G., “Progress in
Development of Modeling Capabilities for a Micro-Pulsed Plasma Thruster,” 39th
Joint Propulsion Conference, AIAA Paper No. 2003-5166, Huntsville, AL, July
2003.
34. Keidar, M., Boyd, I. D., Gulczinski, F. S., Antonsen, E. L., Spanjers, G. G.,
“Propellant Charring in Pulsed Plasma Thrusters,” *J. Prop. Power*, Accepted for
Pub. 2004.
35. Keidar, M., Boyd, I. D., Antonsen, E. L., Spanjers, G. G., “Electromagnetic
Effects in the Near Field Plume Exhaust of a micro-Pulsed Plasma Thruster,” *J.*
Prop. Power, Accepted for Pub. 2004.
36. Keidar, M., University of Michigan, Ann Arbor, MI, private communications,
March 2002.
37. Tipler, P. A., *Physics for Scientists and Engineers*, Worth Publishers, Inc., 1991.
38. The Cooke Corporation, Auburn Hills, MI, www.cookecorp.com
39. Zehnder, A. T., Rosakis, A. J., “On the temperature distribution at the vicinity of
dynamically propagating cracks in 4340 steel: experimental measurements using
high-speed infrared detectors,” *Journal of the Mechanics and Physics of Solids*,
39 (3), 385-417, 1991.
40. Mason, J. J., Rosakis, A. J., “On the dependence of the dynamic crack tip
temperature fields in metals upon crack tip velocity and material parameters,”
Mechanics of Materials, 16 (4), 337-350, 1992.
41. Bjerke, T. W., *Thermal Dissipation of Mechanical Work During Opening and
Shear Dominated Dynamic Fracture of Amorphous Polymers*, Ph.D. Dissertation,
University of Delaware, 2002.
42. Hodowany, J., Rachivandran, G., Rosakis, A. J., Rosakis, P., “Partition of plastic
work into heat and stored energy in metals,” *Experimental Mechanics*, 40 (2),
113-123, 2000.

43. Zehnder, A. T., Rosakis, A. J., "Temperature rise at the rip of dynamically propagating cracks," in: *Experimental Techniques in Fracture III* (Ed. Epstein), Society for Experimental Mechanics, Bethel CT, 125-169.
44. Li, Z., Lambros, J., "Strain rate effects on the thermomechanical behavior of polymers," *International Journal of Solids and Structures*, Vol. 38, pp. 3549-3562, 2001.
45. The Mathworks, Natick, MA, www.mathworks.com
46. Wentink, T. Jr., "High Temperature Behavior of Teflon," AFBMD-TN-59-15 Research Report 55, Avco-Everett Research Laboratory, Everett, MA, July 1959.
47. Micropyretics heaters International, Cincinnati, OH, www.mhi-inc.com.
48. Antonsen, E. L., Burton, R. L., Rysanek, F., "Energy measurements in a Coaxial Electromagnetic Pulsed Plasma Thruster," AIAA Paper 99-2292, Los Angeles, CA, June 1999.
49. Fermionics, Simi Valley, CA, www.fermionics.com.
50. Spanjers, G., Air Force Research Laboratory, Kirtland, AFB, NM, private communication, June, 1998, 2002.
51. Ion Physics Corporation, Fremont, NH, www.ionphysics.com.
52. <http://ioc.unesco.org/oceanteacher/resourcekit/M3/Toolbox/datathief.htm>.
53. Judson Technologies, Montgomery, PA, www.judsontechnologies.com.
54. Planck, M., *Theory of Heat Radiation*, Dover Publications, New York, 1959.
55. Dr. Bro, "Analysis of Polytetrafluoroethylene," DuPont Corp., Private Conversations.
56. Holman, J.P., *Heat Transfer 5th Ed*, McGraw-Hill Book Company, 1981.
57. Wertz, J. R., *Mission Geometry; Orbit and Constellation Design and Management*, Microcosm Press, El Segundo, CA, 2001.
58. Insulator Seal, Sarasota, FL, www.isi-seal.com.
59. Ebnesajjad, S. *Fluoroplastics Volume 1: Non-Melt Processible Fluoroplastics*, Plastics Design Library, 2000.
60. Hiyama, T., *Organofluorine Compounds*, Springer-Verlag Berlin Heidelberg, 2000.

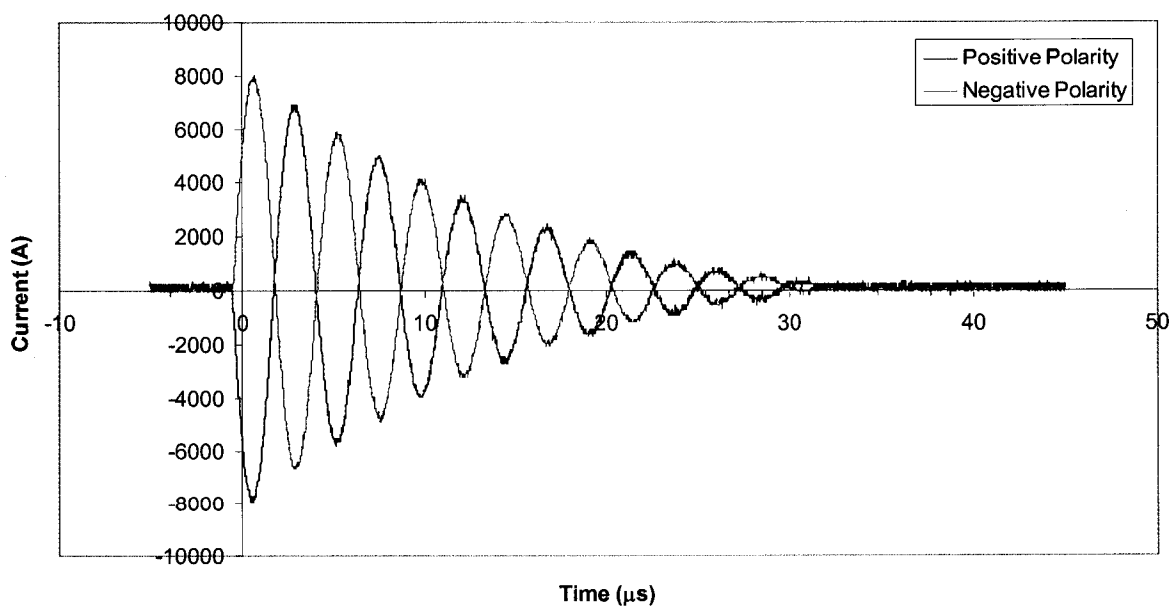
61. Book, D. L., *Revised and Enlarged Collection of Plasma Physics Formulas and Data*, NRL Memorandum Report 3332, 1977.
62. Unison Industries, Jacksonville, FL, www.unisonindustries.com
63. Wheeler, A. J., Ganji, A. R., *Introduction to Engineering Experimentation*, Prentice-Hall, Inc., New Jersey, 1996.
64. Turchi, P. J., "Directions for Improving PPT performance," *Proceedings of the 25th International Electric Propulsion Conference*, Vol. 1, Electric Rocket Propulsion Society, Worthington, OH, 1998, pp. 251-258.
65. Madou, M. J., *Fundamentals of MicroFabrication: The Science of Miniaturization 2nd Ed.*, CRC Press LLC, Boca Raton, FL, 2002.
66. Anderson Jr., J. D., *Modern Compressible Flow 2nd Ed.*, McGraw-Hill Publishing Company, 1990.
67. Kreith, F., Bohn, M. S., *Principles of Heat Transfer 4th Ed.*, Harper & Row Publishers, New York, 1986.
68. C. B. Ruchti and L. Niemeyer, "Ablation Controlled Arcs," *IEEE Trans. On Plasma Science*, Vol. PS-14, No. 4, August 1986.
69. Z. Seres, A. Alonsky, K. Ieki, J. J. Kruse, P. D. Zecher, "Optical Transmission of Mylar and Teflon Films," *Optical Engineering*, Vol. 33, No. 9, Sept. 1994.
70. H. R. Philipp, H. S. Cole, Y. S. Liu, T. A. Sitnik, "Optical Absorption of some polymers in the region 240-170 nm," *Appl. Phys. Lett.*, 48 (2), 13 January, 1986.
71. ANSYS Inc., Canonsburg, PA, www.ansys.com

Appendix A

This data is included to allow future investigations of thruster operation with recessed propellant. For these tests, a 6.35 mm diameter microPPT is used. All data are taken with a capacitance of 2.92 μF . The thruster is fired with a capacitor voltage of 3 kV which gives a discharge energy of 7.8 J. The propellant recession depth is marked on each plot along with the thruster polarity. Data is shown for 0 cm recession (propellant is flush with the thruster exit plane), 0.25 cm, 0.5 cm, 1 cm, and 2 cm. Positive polarity denotes the central electrode hot and positively charged (anode). Negative polarity denotes the central electrode hot and negatively charged (cathode). Data was taken using single color interferometry. The wavelength used is 1152 nm.

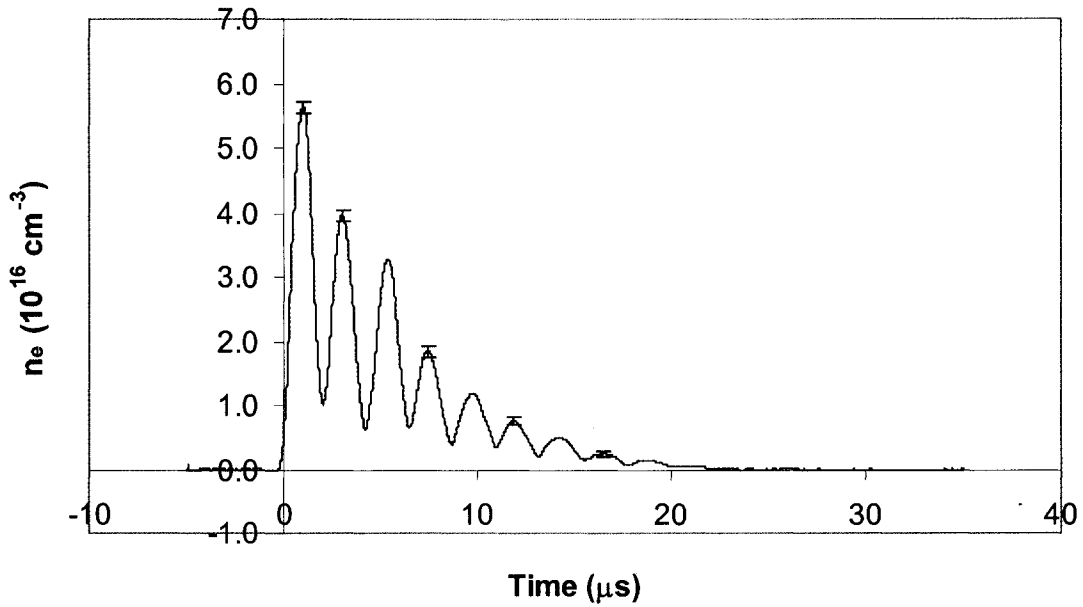
This first plot shows current pulses for both polarities. The Rogowski coil is left in the same physical position throughout testing, so the pulses are inverted for opposite polarities. These current traces are typical for all pulses shown here. This demonstrates a good level of comparability for the different plume measurements.

Rogowski Current Trace Polarity Comparison (7.8 J)

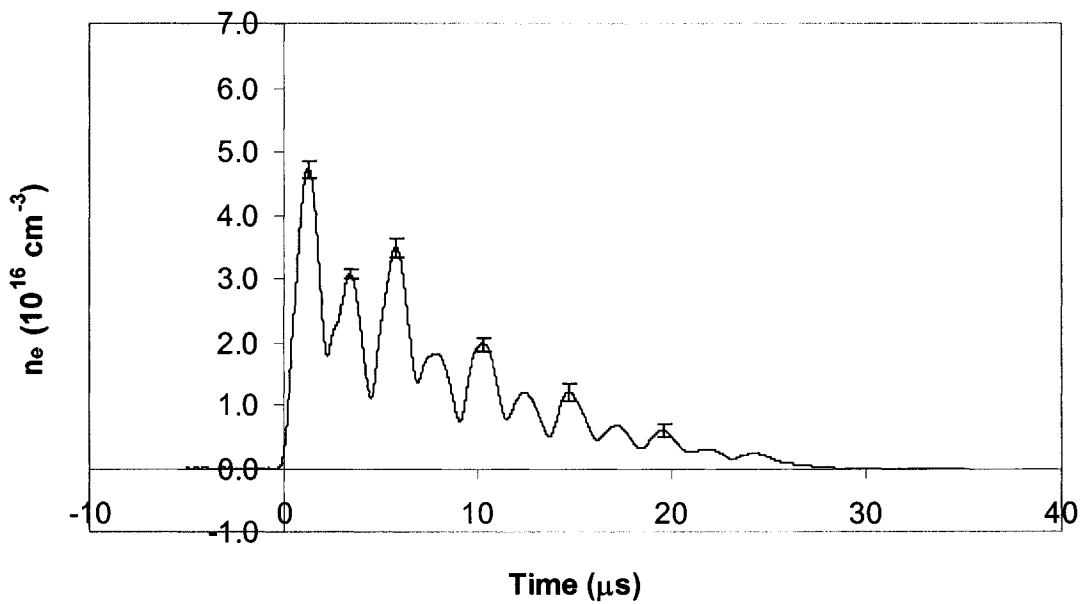


For each of the following plots, the trace shown is an average of 30 pulses. The uncertainty is defined by the standard deviation of those 30 individual measurements. This set of data is for Positive polarity.

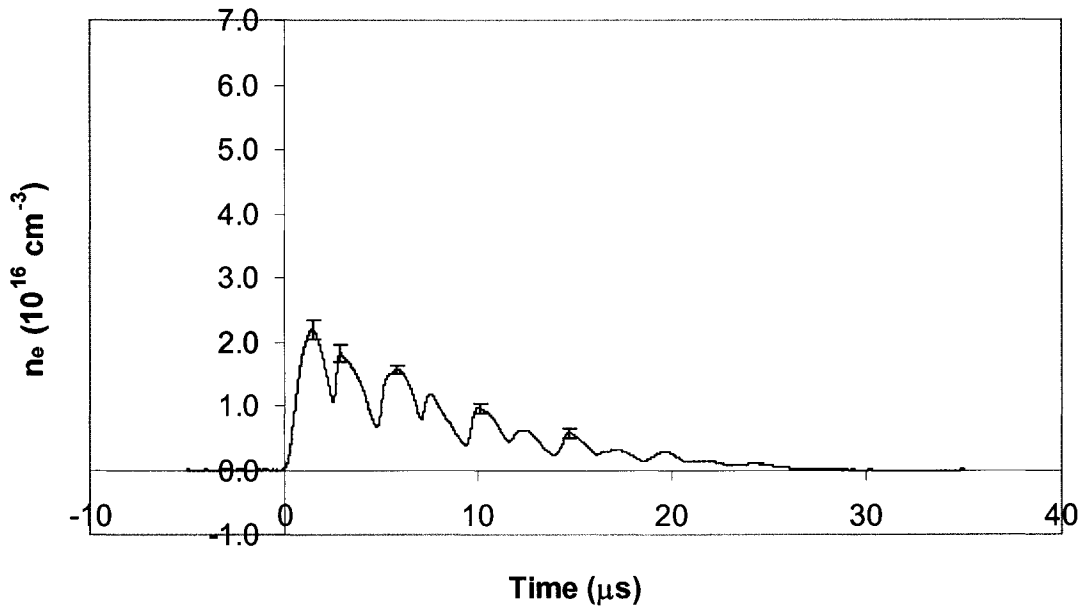
**0 cm Recession Electron Density
Positive Polarity, 7.8 J**



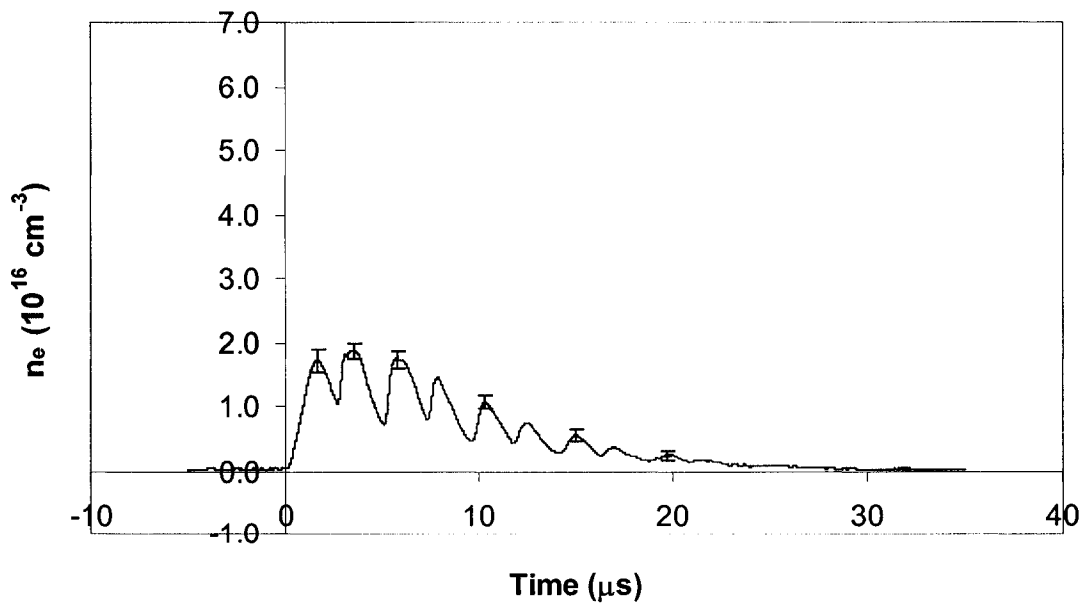
**0.25 cm Recession Electron Density
Positive Polarity, 7.8 J**



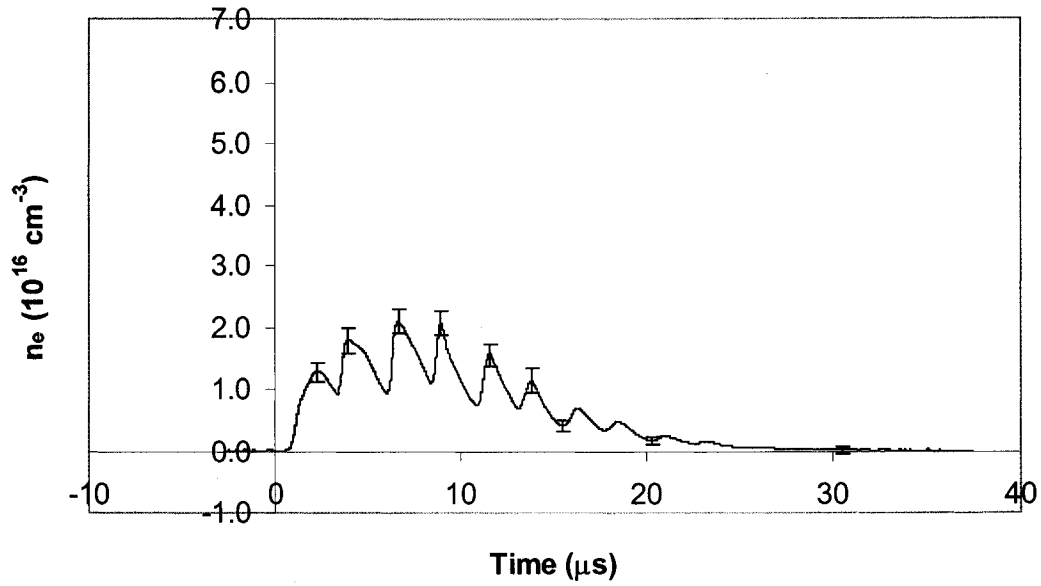
**0.5 cm Recession Electron Density
Positive Polarity, 7.8 J**



**1 cm Recession Electron Density
Positive Polarity, 7.8 J**

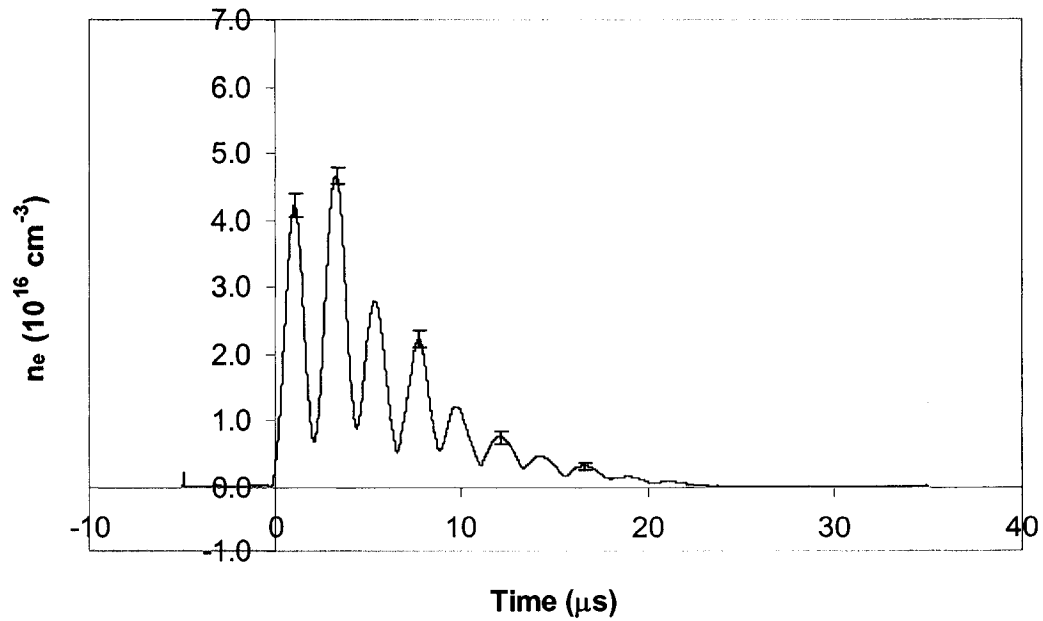


**2 cm Recession Electron Density
Positive Polarity, 7.8 J**

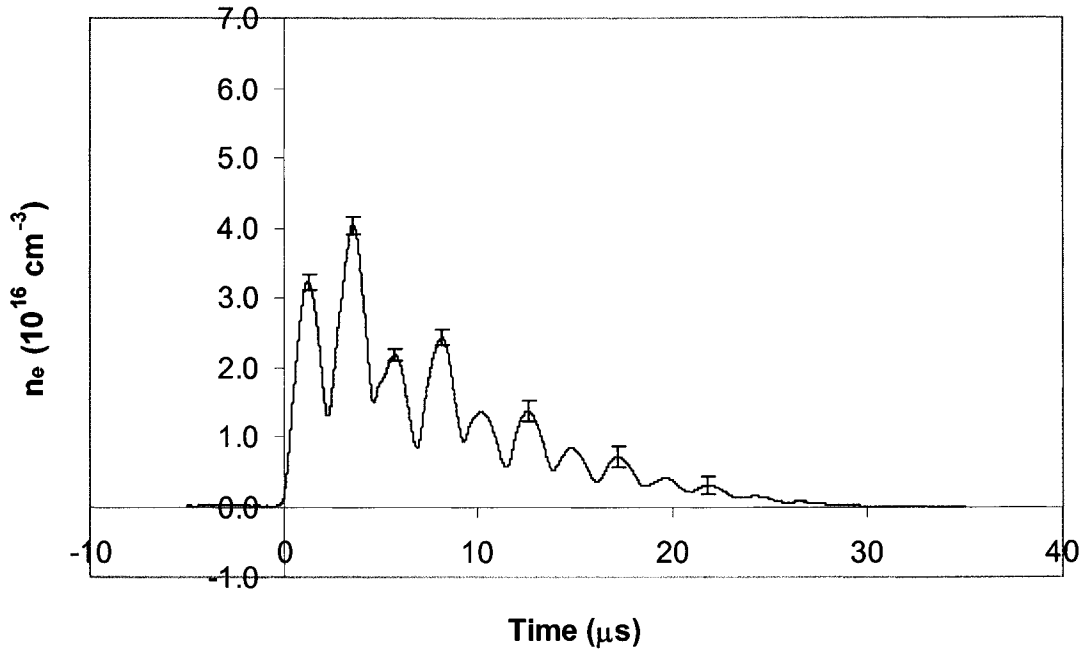


The following plots are for Negative polarity. Typical uncertainties are shown.

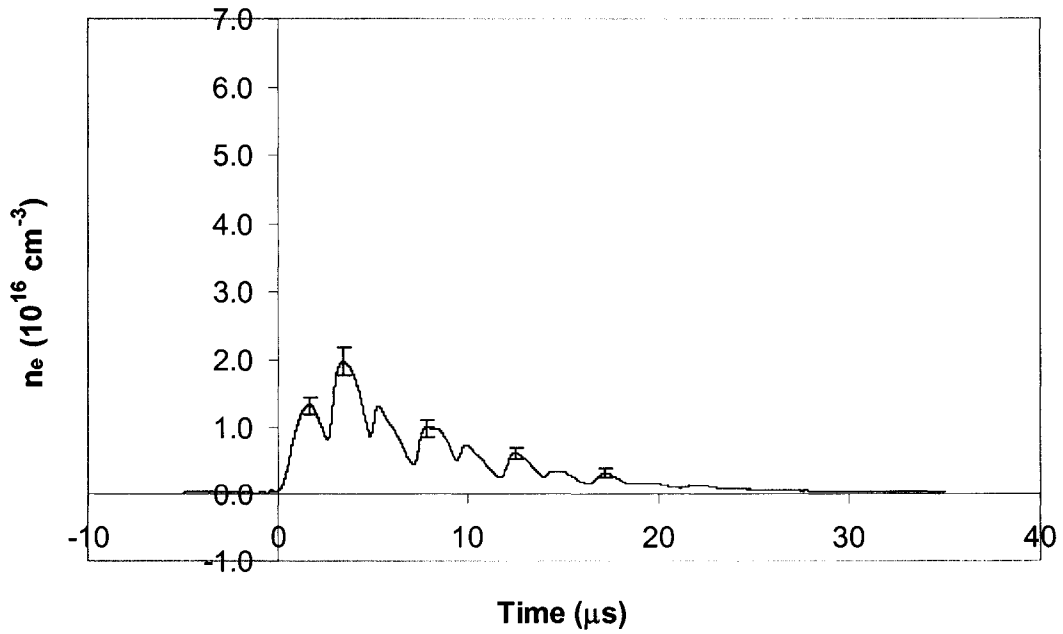
**0 cm Recession Electron Density
Negative Polarity, 7.8 J**



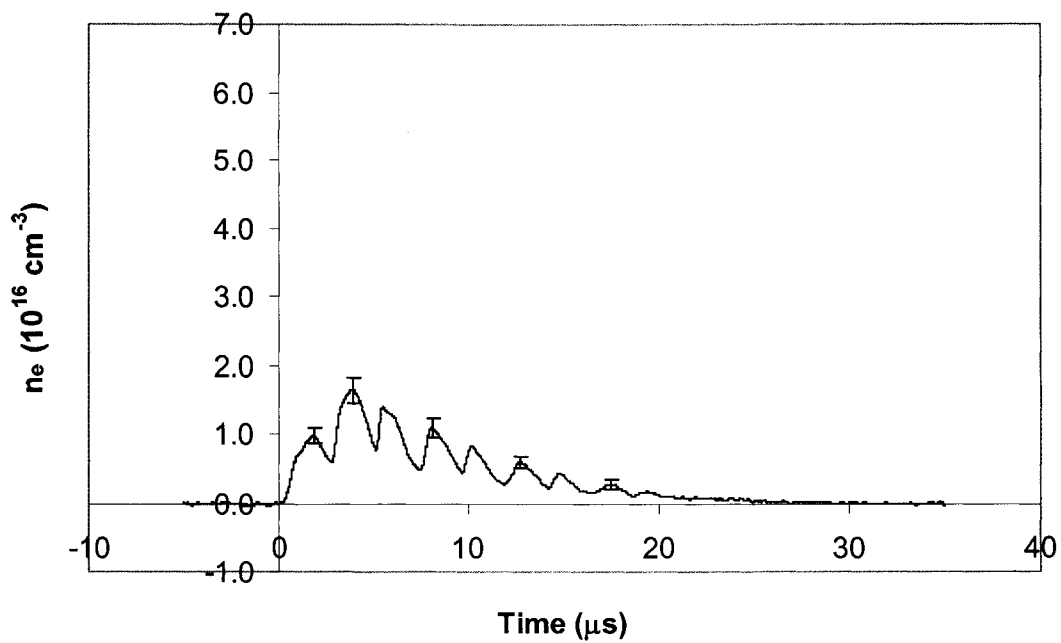
**0.25 cm Recession Electron Density
Negative Polarity, 7.8 J**



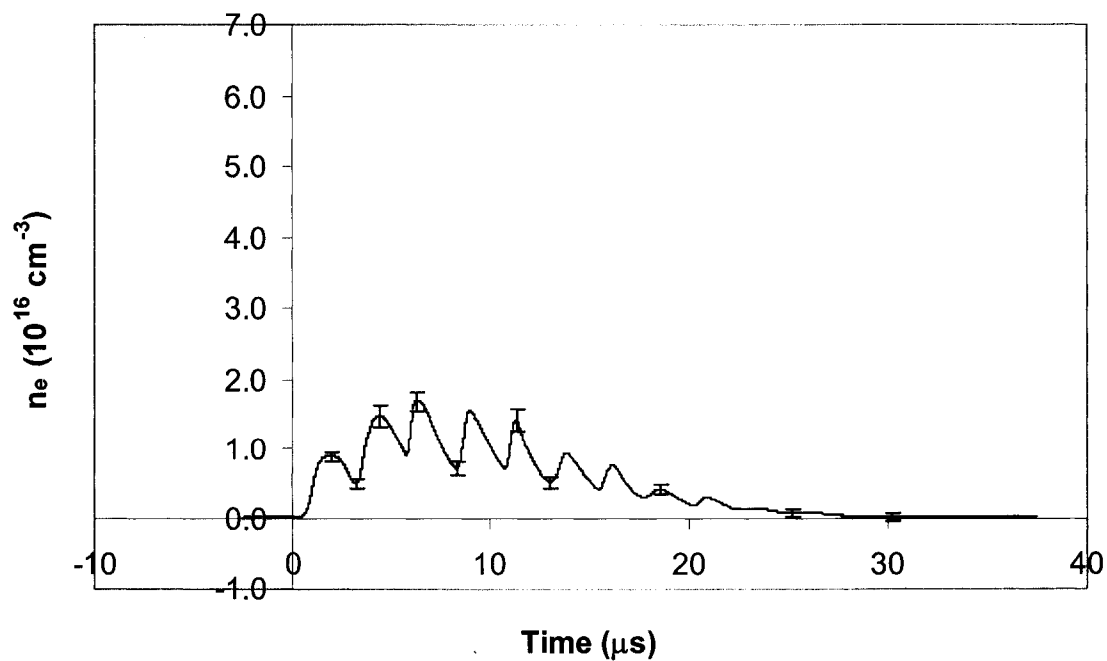
**0.5 cm Recession Electron Density
Negative Polarity, 7.8 J**



**1 cm Recession Electron Density
Negative Polarity, 7.8 J**



**2 cm Recession Electron Density
Negative Polarity, 7.8 J**



Vita

Erik Lawrence Antonsen was born in Chicago Heights, IL, on January 19, 1975. He graduated from the University of Illinois at Urbana-Champaign in 1997 with a Bachelor of Science degree in aeronautical and astronautical engineering. In May 1997 he started graduate study in aerospace engineering and became a graduate research assistant for the Electric Propulsion Laboratory at the University of Illinois Department of Aeronautical and Astronautical Engineering. He also began working at the Electric Propulsion Laboratory of the Air Force Research Laboratory at Edwards AFB in California. He completed a Master of Science in aerospace engineering at the University of Illinois at Urbana-Champaign in 2001. Following completion of his Ph.D., Erik will begin medical school at the University of Illinois at Chicago.